Hydrodynamics of tidal stream energy devices with two rows of blades

Peter B Johnson

University College London

Thesis submitted in partial fulfillment of the
requirements for the degree of Doctor of Philosophy

I, Peter Benjamin Johnson, confirm that the work presented in this thesis is my own. Where information has been derived from other sources, I confirm that this has been indicated in the thesis.

Abstract

Tidal stream energy is an emerging low-carbon technology which could meet 5% of UK electricity demand. Current developments use 'axial-flow' rotors, which are efficient but limited in size, to generate electricity from ocean currents. This thesis investigates the hydrodynamics of a previously undeveloped rotor concept which has two rows of blades and also has no inherent size limit, hence it might achieve greater economies of scale. The rotor concept, called the 'Moonraker', is a cross-flow device with an oval blade path in the horizontal plane. This thesis presents research into the hydrodynamic performance of the Moonraker, focussing on the forces exerted on the blades by water currents and thereby deriving the thrust on and power generated by a Moonraker.

The point vortex method was used to model the Moonraker and predicted high power coefficients when compared to a conventional cross-flow turbine with a circular blade path. A lab-scale Moonraker device was built and tested in the towing tanks at UCL and QinetiQ. The device was 2 m wide, 0.5 m high, with up to six blades and was towed at up to 0.7 m/s (blade Reynolds numbers were in the range 65,000–112,000). One of the blades was instrumented with strain gauges so that two components of blade loading could be recorded. Comparisons of predictions and measurements of blade loading showed some encouraging agreement, but also some disagreement, leading to suggested improvements in the modeling of the blade forces.

The vortex model was subjected to further verification and validation tests in order to explore the issue of double actuator surfaces in close proximity. The extension of this work could help optimise the spacing between the two rows of blades on a Moonraker.

Acknowledgments

While I take responsibility for this work it would not have been possible without the help and support of a lot of wonderful people, some of whom I would like to thank here.

Adam Wojcik and Kevin Drake were joint supervisors of this work from the initial funding application to the final submission and through all the ups and downs in between. I am grateful for their generous and unwavering support and commitment; for the space they gave me to be creative and follow unusual ideas; for always engaging in debate; for being so helpful and supportive when things didn't work (and when they did!); for their practical help with experiments and help with this thesis; and for not saying they told me so, even when they had told me so.

Thanks to Ian Eames for his encouragement, support and inspiration, without which I would not have pursued the work in Chapter 5. Tristan Smith and Tim McDonald got a raw deal sharing the office with me: always helping me, always engaging in my whiteboard dramas, and never asking for (or getting!) anything back. Thanks to Jo Whelan for her support throughout and for reading and commenting on this thesis. Thanks to Gareth Gretton for his support, collaboration, and for sharing his data; and to Tom McCombes for his contributions in our collaborative work. Thanks to Sam Harding, Rowan Dennison, and Christian Jonsson for reading and commenting on this thesis. Thanks to Peter Fraenkel for his helpful advice.

Special thanks to Christian Klettner for good times within and without the office (and elsewhere): endless helpful conversations, suggestions, whiteboard sessions and especially the tea breaks. Thanks to Andre Nicolle, in particular for suggesting the split-blade concept. Dave Western helped me a lot during our tea breaks, I appreciate the time he always had for me.

For help in the lab I would like to thank Savvas Achilleos, Mike Johnson, Sapna Halai, and Christian Jonsson. I thank Sinan Hasan for his extraordinary help with the PII experiments at QinetiQ; thanks to Arthur Pecher for helping with PII assembly; and thank you to Dan Fone for his generosity and support in the lab, from rescheduling to mopping to equipment tutorials, and general good company.

Thanks to Neil Collins for his welding, machining work, and practical advice; also to Richard Winn and John Inns for their machining and design tips, and to Peter Kelly and the rest of the workshop staff. Thanks to Ben Tompsen for his emergency soldering help. Thanks to Chris Pike at QinetiQ, and Steve Lowry at Transmission Dynamics for help with the Microlog. Thanks to everyone in the department of Mechanical Engineering at UCL for such an enjoyable and

enriching eight-plus years. Thanks to lunch club i.e. Dara McCutcheon, Adam Harman-Clarke, Phil Reardon, Doug Lazenby, Dave Western, Christian Klettner et al.

EPSRC funded this work, and the PII project was funded by NESTA and Kevin Drake. Thanks to Joachim Baumgaertner for his help with the NESTA funding. Thanks to NCGE for funding my time on leave at the Kauffman Foundation, and to Nazarbayev University School of Engineering for their support during the last stage. Thanks also for the support from INORE, UKERC, SUPERGEN marine, and the Royal Academy of Engineering.

Finally I want to thank my parents Mark and Ros, my sibs Daniel, Laura, Hannah, Mike, and brother-in law Mike, for a lifetime of endless support, encouragement and good times. I could not have done this without them and could not imagine a better family.

Contents

List of principal symbols

Listed below in alphabetical order are the principal symbols used in this thesis.

Latin characters, lower case

a	Induction factor in actuator disc theory
a_0	Gradient of the lift coefficient with respect to angle of attack (rads^{-1}) *or* mean of a signal
c	Chord length (m)
d	Perpendicular distance (m)
d	Derivative symbol
e	The base of natural logarithms
e	Prandtl's efficiency factor
$\hat{\boldsymbol{e}}$	Unit vector
f	Load per unit length (Nm^{-1}) *or* real part of the lift coefficient
g	Gravity (ms^{-2}) *or* Imaginary part of the lift coefficient
g_{M}	Geometric ratio of a Moonraker blade path
h	Blade length or device height (m)
i	$\sqrt{-1}$
k	Wave number or reduced frequency
$\boldsymbol{k}_1$, $\boldsymbol{k}_2$, ...	Runge-Kutta differences (ms^{-1})
l	Length (m)
m	Mass (kg) *or* volume source strength per unit length and depth (ms^{-1})

n	Distance in the normal direction (m) *or* integer for summing *or* number of vortices
p	Pressure (Nm^{-2})
q	Speed (ms^{-1})
r, $\boldsymbol{r}$	Distance or radius (m)
s	Non-dimensional streamwise spacing between actuator surfaces
s, $\boldsymbol{s}$	Spacing, length (m)
t	Time (s)
u, $\boldsymbol{u}$	Local fluid speed or velocity (ms^{-1})
$\boldsymbol{u}_E$	External fluid velocity (ms^{-1})
u_i	Induced velocity (magnitude) (ms^{-1})
u_{0i}, $\boldsymbol{u}_{0i}$	Speed or velocity induced at the origin (ms^{-1})
u_s	Non-dimensional fluid speed at an actuator surface
u_w	Non-dimensional streamwise fluid speed in the wake
v, $\boldsymbol{v}$	Blade speed or velocity (ms^{-1})
w, $\boldsymbol{w}$	Relative speed or velocity between blade and fluid (ms^{-1})
w	Wake width (m)
x, $\boldsymbol{x}$	Direction, distance or position (m)
y	Direction, distance or position (m)
z	Direction, distance or position (m)

Latin characters, upper case

A, $\boldsymbol{A}$	Representative area (m^2)
AR	Aspect ratio
B	Blockage ratio
C	Loop (m)
C_D, $C_{\mathrm{D_i}}$	Drag coefficient, induced drag coefficient
C_L, $C_{\mathrm{L_{3D}}}$	Lift coefficient, three-dimensional lift coefficient

C_{P}	Power coefficient
C_{Q}	Torque coefficient
C_{T}	Thrust coefficient
C_{n}	Normal force coefficient
C_{t}	Tangential force coefficient
D	Drag force (N)
D	Total derivative symbol
E	Young's modulus of elasticity (Nm^{-2})
F	Force (N)
$\boldsymbol{F}$	Force field (Nm^{-3})
$\boldsymbol{F}^{+}$	Non-dimensional total force on a blade
F_{n}	Normal force (N)
F_{n}^{+}	Non-dimensional normal force
F_{t}	Tangential force (N)
F_{t}^{+}	Non-dimensional tangential force
F_{t}'	Net tangential force (N)
Fr	Froude number
H	Heaviside step function
I	Second moment of area (m^4)
Im	Imaginary part of a complex number
$\boldsymbol{J}$	Transformation matrix
L	Lift force (N) *or* length of bending member or wake (m)
$\boldsymbol{L}$	Lift force (N)
L_{p}	Length of Moonraker blade path (m)
L	Dimension of length
LF	Load factor

N	Number of blades
P	Power (W)
$\boldsymbol{P}$	Position (m)
Q	Torque (Nm)
$\boldsymbol{Q}$	Position (m)
R	Radius (m)
Re, Re_c	Reynolds number, blade Reynolds number
Re	Real part of a complex number
S	Area (m^2) *or* streamwise spacing between rows of blades or actuator surfaces (m)
T	Time period (s)
T	Dimension of time
U, $\boldsymbol{U}$	Speed, velocity (ms^{-1})
U_s	Fluid speed at an actuator surface (ms^{-1})
U_∞, U_w	Fluid speed far upstream, fluid speed in the wake (ms^{-1})
W	Device width (m)

Greek characters, lower case

α	Angle of attack (rads or degrees)
β	Angle of relative velocity ($\boldsymbol{w}$) (rad or degrees)
γ	Circulation per unit length, i.e. vortex sheet strength (ms^{-1})
δ	Boundary layer thickness (m) *or* desingularising parameter *or* Dirac delta function
ϵ	Strain
θ	Angle (rads or degrees)
θ_1, θ_2	Angles (rads or degrees) between two vectors
κ	Pressure drop coefficient
μ	Friction coefficient *or* viscosity ($kgm^{-1}s^{-1}$)
ν	Kinematic viscosity (m^2s^{-1})

π	Ratio of circle circumference to diameter
ρ	Density (of mass) (kgm^{-3})
σ	Solidity (blade packing density)
τ	Non-dimensional time
ϕ	Pitch angle of blade (rads or degrees)
ω	Frequency ($\mathrm{rad.s}^{-1}$)

Greek characters, upper case

Δ	Difference
Γ, Γ_b	Circulation, bound circulation ($\mathrm{m}^2\mathrm{s}^{-1}$)
Θ	Normalised azimuth position *or* open area ratio
Λ	Blade speed ratio (blade speed / flow speed)
Ω, $\mathbf{\Omega}$	Vorticity (s^{-1})

Other symbols

∂	Partial derivative symbol
$\boldsymbol{\nabla}$	Nabla / gradient operator

List of abbreviations

2D, 3D	Two-dimensional, three-dimensional
AC	Alternating current
BEM	Blade element momentum
CFD	Computational fluid dynamics
CPU	Computer processing unit
DC	Direct current
NACA	National advisory committee on aeronautics (USA)
NASA	National aeronautics and space administration (USA)
NPV	Net present value
ODE	Ordinary differential equation
PCB	Printed circuit board
PC	Personal computer
PID	Proportional-integral-differential
PI, PII	First and second Moonraker prototypes
RANS	Reynolds averaged Navier-Stokes
RK4	Fourth-order Runge-Kutta
RMS	Root mean square
THAWT	Transverse horizontal axis water turbine
UCL	University College London
UK	United Kingdom

List of Figures

List of Tables

Chapter 1

Introduction

In the coming decade one third of the UK's electricity generating capacity will be retired and needs to be replaced. This new demand for generation capacity, combined with new government policies relating to climate change, has led to the development of new electricity generating technologies whose energy is sourced domestically and does not directly emit greenhouse gases. Among these emerging technologies is tidal stream energy which converts the kinetic energy of ocean currents into grid-ready electricity. It is estimated that tidal stream energy could meet 5% of the UK's electricity demand (Carbon Trust, 2005).

Figure 1.1 shows 'SeaGen', a pre-commercial tidal stream turbine installed in Strangford Narrows, Northern Ireland by Marine Current Turbines Ltd (MCT). This device was connected to the grid in July 2008 and generates 10 MWh per tide. It is accredited by OfGEM (the UK electricity regulator) as a power station and, at the time of writing, it was the only device with this status – licensed to operate for five years. The rotors on SeaGen are 'axial-flow' propellers, the conventional means of converting the kinetic energy into rotational motion, used to drive an electric generator.

This thesis investigates the hydrodynamics of an alternative rotor concept which has two rows of blades moving perpendicular to the water currents. The author first proposed this concept in December 2007 as a variant of the 'Darrieus' cross-flow turbine, with the suggestion that the blades follow an oval path as opposed to a circular path. The motivation for this configuration was to achieve high efficiencies in combination with the potential to be built on a much larger scale. In the absence of a convenient acronym the device became known as a 'Moonraker' and will be referred to as such throughout this thesis. Concepts very similar to the Moonraker were subsequently found in the patent literature (detailed later in this chapter); however no significant research or development work was found.

The aim of this thesis is to objectively study the hydrodynamic performance of a Moonraker, i.e. to establish a quantitative understanding of the forces that water would exert on the blades of the rotor, and subsequently the power that could be generated and the thrusts that must be resisted. This introductory chapter presents the fundamental hydrodynamic concepts relating

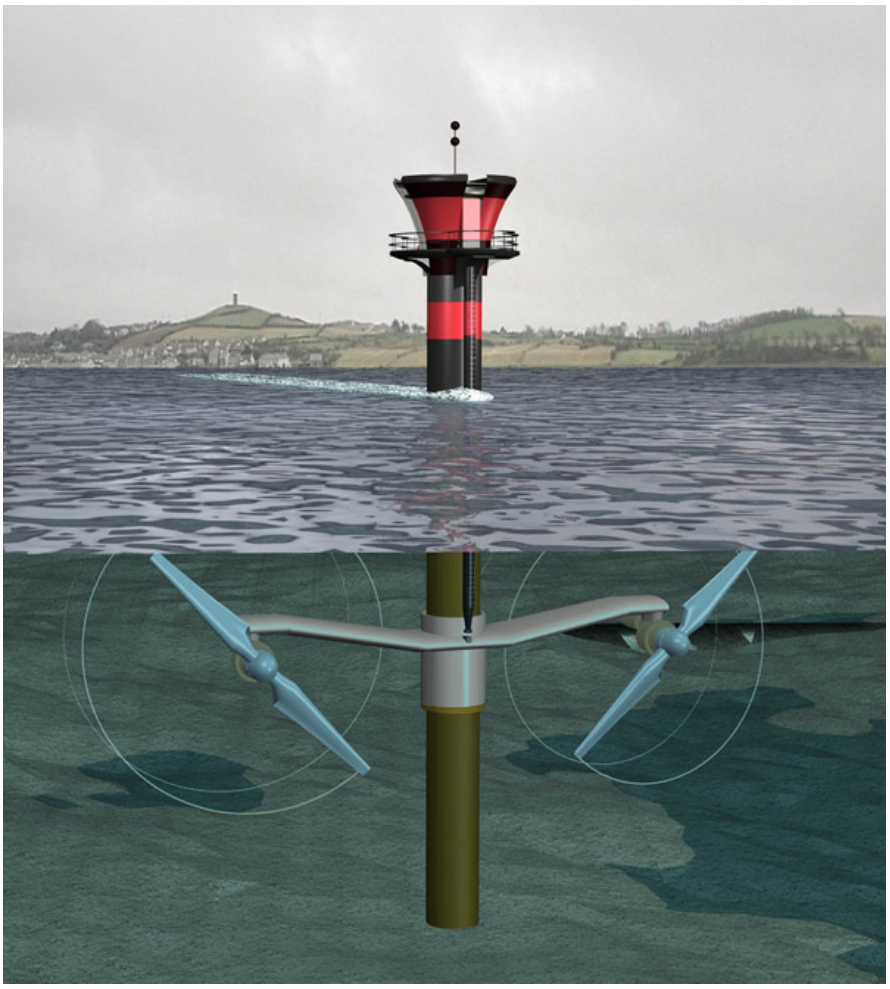

Figure 1.1: *'SeaGen', the most advanced tidal stream turbine in operation. Image from www.marineturbines.com.*

to tidal stream energy devices, introduces the Moonraker device, and outlines the specific aims of the thesis.

1.1 Fundamentals of tidal stream energy

The energy in ocean currents is predominantly quasi-steady kinetic energy, which is defined as the work required to accelerate a point mass, m, to a speed U:

$$\text{k.e.} = \frac{1}{2}mU^2.$$

For a constant water speed the rate of kinetic energy flow is $\frac{1}{2}\dot{m}U^2$ where $\dot{m} = \rho UA$ is the mass flow rate, ρ is the density of water, and A is the cross-sectional area of the water flow. Therefore the power in the flow due to kinetic energy is

$$\text{power} = \frac{\mathrm{d}}{\mathrm{d}t}\text{k.e.} = \frac{1}{2}\rho U^3 A, \tag{1.1}$$

where t is time. The estimate (1.1) neglects the potential energy of the hydraulic gradient that drives the system, which will not be considered in this thesis (see Draper et al. (2009) or Salter (2009) for further reading), where the kinetic energy of turbulence will also be neglected.

The speed of ocean currents is important and there are two reasons for this: firstly, the cubic dependency in (1.1) means that energy is much more densely available at faster sites, and secondly the thrust per unit power on a conversion device is inversely proportional to the speed of the currents:

$$\frac{\text{Thrust}}{\text{Power}} \propto \frac{1}{U},$$

(this will be shown in Section 2.6). The large thrust on a tidal stream turbine – higher than that on a Jumbo Jet engine – is expensive to resist, while the power output generates revenue. Thus extracting energy from a higher speed current is more economical.

Returning to equation (1.1), once a location with satisfactory velocity has been chosen, energy capture can be maximised by increasing the cross sectional area, A, of the device. The rotor diameter is limited by the water depth, for example SeaGen has a 16 m rotor diameter in a water depth of 25 m, hence the cross-sectional area is limited and this is illustrated in Figure 1.2. In practice, even in deep waters, rotor diameters will not exceed approximately 20m as the bending moments at the blade root would be too high to resist. Each blade carries a load equivalent to about 4 lorries and the difficulties associated with this are evident in that most leading companies (e.g. MCT, Atlantis Resources Corporation Pte Limited, OpenHydro Group Ltd) have lost blades due to catastrophic failure during the testing and development process.

The key challenge in engineering a tidal stream energy device is to manage these large forces in a robust yet economic way. As can be seen from SeaGen's sizable structure, it is robust but not particularly economical. The installation of large structures in such energetic conditions is extremely challenging and consequently very expensive. Installation of SeaGen cost more than the device itself; the crane used to install it cost £90,000 per day to hire – a cost that will

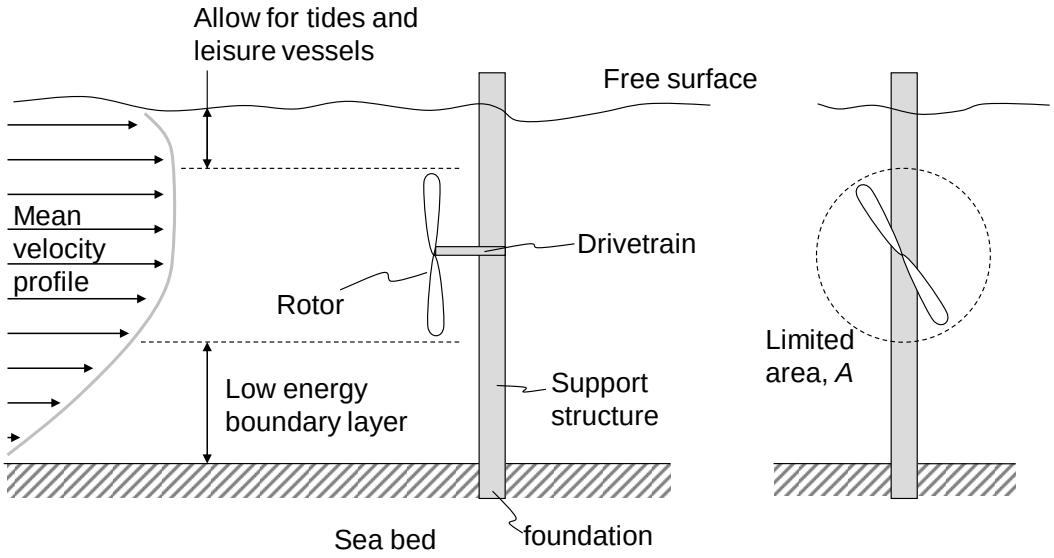

Figure 1.2: *Illustration of a generic single rotor on a monopile structure. The diameter of the rotor is limited by the water depth.*

only rise with oil prices due to competition with the oil and gas sector. Therefore, to maximise the energy capture and with limitations on the rotor diameter, two rotors are present on one installation, with a projected area of 402 m^2. Future deployments by MCT will have three devices per installation in order to further reduce the installation cost per unit power.

Once the location has been chosen, and the projected area of the turbine is fixed, the only remaining way of increasing power output, P, is through improvements in the performance of the device itself. A key measure of device performance is the hydrodynamic power coefficient, C_{P}, which is defined as

$$C_{\mathrm{P}} = \frac{P}{\frac{1}{2}\rho U^3 A}, \tag{1.2}$$

and depends on the design of the rotor, which is a carefully shaped body that is acted on by the moving fluid in a way that generates torque on a shaft. Conventionally the forces on an approximately two-dimensional body such as a turbine blade are decomposed into the component parallel to the relative fluid flow, known as 'drag', and the component perpendicular to the relative fluid flow, known as 'lift'. Rotor designs employ either the drag force (with negligible lift) or the lift force (with minimal drag) to generate all or most of the torque.

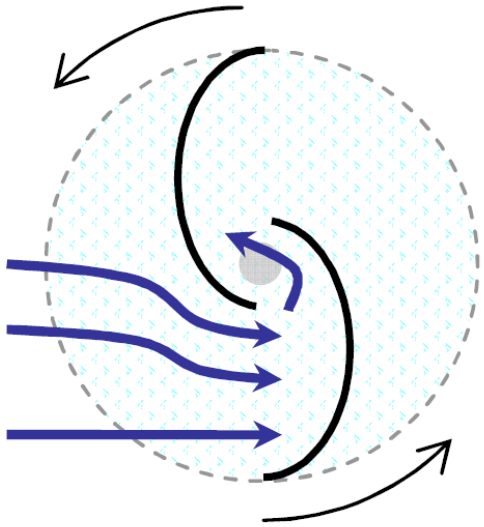

Figure 1.3: *Illustration of a Savonius-type turbine, which uses drag forces to generate torque.*

1.2 Rotor types

1.2.1 Drag based rotors

Drag based rotors are not used for commercial electricity generation principally because they are inefficient and suffer large forces per unit power; to justify this statement herein lies a basic analysis of the power generated by a drag-based device.

Bluff bodies can generate significant drag forces and this can be used to generate torque. Typical uses include water wheels and the 'Savonius' type turbine, which is illustrated in Figure 1.3. The benefit of this approach is that the drag is not very sensitive to the shape of the bluff body – simple shapes such as a plate or a cup can be used. Consider a fluid flowing at speed U. A body moving through the fluid at a speed ΛU, where Λ is the non-dimensional 'blade speed ratio', will experience a relative fluid velocity $U(1-\Lambda)$. The drag, D, on a body is described using a dimensionless drag coefficient, C_{D}:

$$D = C_{\mathrm{D}} \frac{1}{2} \rho U^2 (1-\Lambda)^2 A, \tag{1.3}$$

where ρ is the fluid density, and A is a representative frontal area of the bluff body. Only flows of high Reynolds number ($\Lambda U\sqrt{A}/\nu \gg 1$) will be considered here, where ν is the kinematic viscosity of the fluid. In practice, a large drag coefficient can be generated by a concave surface and can have a magnitude up to approximately 2.

If the body is not moving through the fluid then the drag force is not doing any useful work on the body. If the body is allowed to move in the direction that it is being forced (the

stream-wise direction) then the fluid is working on the body. The rate of work done by the fluid on the body will be the force on the body, multiplied by its speed:

$$C_{\mathrm{P}} = C_{\mathrm{D}} \left(1 - \Lambda\right)^2 \Lambda. \tag{1.4}$$

Differentiating this expression with respect to Λ, the optimum power coefficient is seen to occur at $\Lambda = 1/3$, i.e. the body moves at one third of the upstream flow speed, giving

$$C_{\mathrm{Pmax}} = \frac{4}{27} C_{\mathrm{D}}. \tag{1.5}$$

This puts an approximate limit on the power coefficient of $C_{\mathrm{P}_{\mathrm{max}}} \approx 0.3$. Most drag devices have some inherent drag that will reduce their power coefficient further. Some turbines improve on this efficiency, for example the Savonius turbine in Figure 1.3 will produce beneficial lift during a part of each revolution and that lift create a torque on the shaft.

1.2.2 Lift based rotors

Lift based rotors employ long blades with relatively short chords, and therefore the flow over the blade tends to be approximately planar in a plane normal to the span of a blade. Such a plane is illustrated in Figure 1.4 where the blade has a cross-section called an 'aerofoil' or 'hydrofoil', shaded in grey. The direction of blade motion is indicated in the diagram: the blade moves in a direction perpendicular to the direction of the fluid flow from which it extracts energy. There is a net force exerted by the fluid on the blade and this has been decomposed in Figure 1.4 into the conventional components lift, L, and drag, D. Hydrofoils are designed to attain a high ratio of lift to drag - but a relatively modest ratio is illustrated in Figure 1.4 for the purposes of illustration.

The local fluid velocity is denoted $\boldsymbol{u}$ (it may be distinct from the upstream velocity) and the blade velocity is denoted $\boldsymbol{v}$. The fluid flow relative to the blade is given by the vector subtraction

$$\boldsymbol{w} = \boldsymbol{v} - \boldsymbol{u}. \tag{1.6}$$

The vector $\boldsymbol{w}$ forms an angle with the blade's velocity $\boldsymbol{v}$

$$\beta = \arcsin\left(\frac{\boldsymbol{w} \times \boldsymbol{v}}{|\boldsymbol{w}|\,|\boldsymbol{v}|}\right), \tag{1.7}$$

where the cross-product is used to preserve the sign of the angle. If the blade is pitched at an angle ϕ relative to its motion, then angle of attack of the flow relative to the blade (the hydrodynamic angle of attack) is

$$\alpha = \beta - \phi. \tag{1.8}$$

The lift force is defined as the component of force that is perpendicular to the relative fluid flow, and is described using a lift coefficient:

$$L = C_{\mathrm{L}} \frac{1}{2} \rho \left| \boldsymbol{w} \right|^2 A, \tag{1.9}$$

where A is a representative area over which the lift is obtained - this is usually the product of the chord, c and span of the hydrofoil, h. The magnitude of the lift force is very sensitive to the angle of attack, α. For a blade with symmetric section and a very long span, the lift can be approximated as

$$C_{\mathrm{L}} \approx 2\pi\alpha, \tag{1.10}$$

where α is in radians and $\alpha \lesssim 0.2$ ($\sim$12 degrees); above that angle (which is dependent on Reynolds number) 'stall' occurs due to boundary layer separation and the drag will increase dramatically and the lift will not increase any further (in steady conditions). At $\alpha = 0.2$ we have $C_{\mathrm{L}} \approx 1.26$ and in practice the steady lift coefficient will not exceed this magnitude. In high Reynolds number flows ($Re \gtrsim 10^6$) the accompanying drag coefficient can be as low as $C_{\mathrm{D}} = C_{\mathrm{L}}/50$ (Lighthill, 1986).

If a blade is stationary ($\Lambda = 0$) then the lift force is perpendicular to the direction of oncoming flow U. The stationary blade cannot do any work but if it is allowed to move, say perpendicular to the oncoming flow at a velocity, $\boldsymbol{v}$, then work will be done but also the angle of attack will change and this is sketched in Figure 1.4. The forces tangential and normal to the blade's movement are defined as

$$C_{\mathrm{t}} = C_{\mathrm{L}} \sin\beta - C_{\mathrm{D}} \cos\beta, \tag{1.11}$$

$$C_{\mathrm{n}} = C_{\mathrm{L}} \cos\beta + C_{\mathrm{D}} \sin\beta, \tag{1.12}$$

respectively, where $\beta = \alpha - \phi$ and ϕ is the attitude of the blade chord relative to its direction of motion, also known as the pitch. The tangential and normal forces are often re-normalised for easier comparison at different blade speeds:

$$F_{\mathrm{t}}^{+} = C_{\mathrm{t}} \Lambda^2, \tag{1.13}$$

$$F_{\mathrm{n}}^{+} = C_{\mathrm{n}} \Lambda^2. \tag{1.14}$$

The rate of useful work done by the fluid on the blade is the product of F_{t}^{+} and Λ. It is evident from (1.11) that a high ratio of lift-to-drag is important in order to create a high tangential force on the blade. For N blades, with chord c and covering a projected area W per unit height

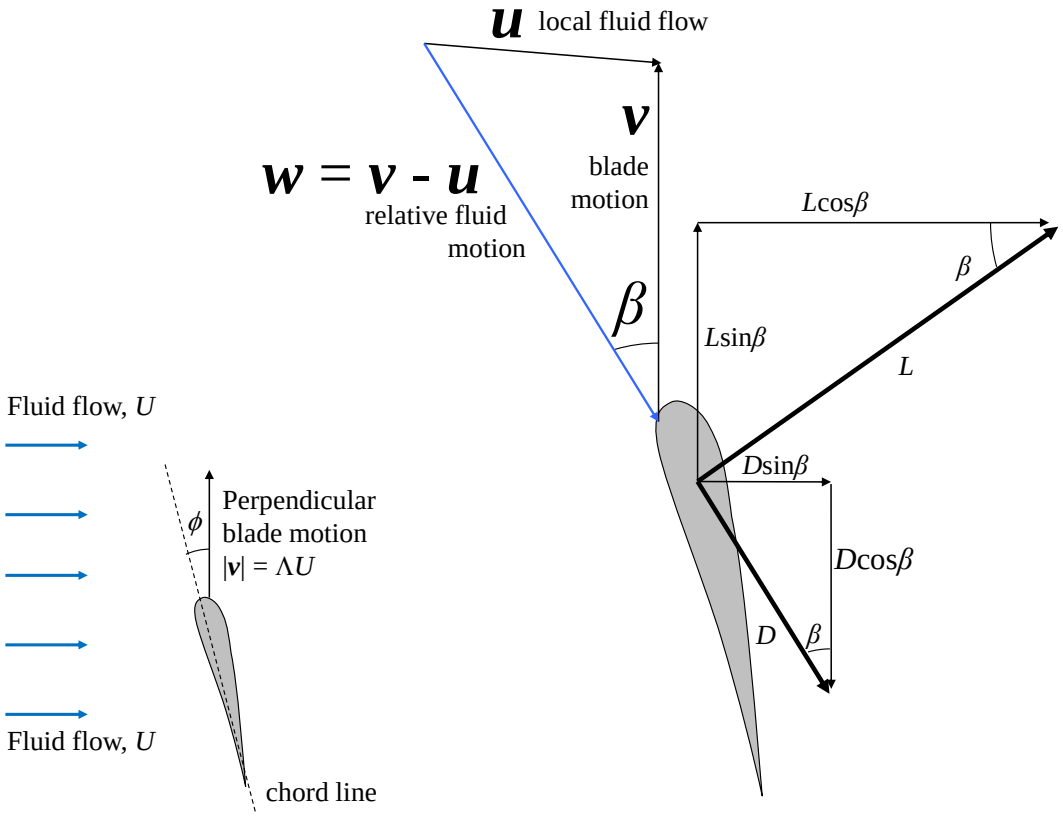

Figure 1.4: *The blade velocity triangle of a lifting blade. The blade is pitched at an angle ϕ from its direction of motion, and experiences the flow at a relative angle β. The angle of attck of the blade is then $\alpha = \beta - \phi$.*

of the device, the power coefficient is

$$C_{\mathrm{P}} = NF_{\mathrm{t}}^{+}\Lambda\frac{c}{W}, \tag{1.15}$$

$$= F_{\mathrm{t}}^{+}\Lambda\sigma, \tag{1.16}$$

where $\sigma = Nc/W$ is the 'solidity' or packing density of the blades.

Increasing the solidity is only beneficial up to the point that the local velocity $\boldsymbol{u}$ reduces too much; in other words the blades have to share the same energy resource. Fundamentally the energy is extracted by causing a pressure drop across the blade. The time averaged effect of a cascade of blades is that they have a high pressure on their upstream side and a low pressure on their downstream side. The average pressure drop across the plane through which the blades translate is defined as

$$\Delta p = \kappa\frac{1}{2}\rho u^2, \tag{1.17}$$

where u is the local fluid speed through the plane of energy extraction and κ is the 'pressure drop coefficient'. Far upstream and far downstream the pressure will be atmospheric, so there must be a gradual increase in pressure as the fluid approaches the turbine, and following a discontinuous drop at the turbine below atmospheric, the pressure will subsequently recover in the fluid as it flows downstream. According to Bernoulli's theorem this corresponds to a reduction in velocity upstream of the turbine. The local fluid speed u is therefore less than the upstream speed U and 100% energy extraction is impossible. The study of this effect is called 'actuator disc theory' and is presented in detail in Chapter 2. The optimum pressure drop coefficient is $\kappa = 2$, causing a thrust coefficient $C_{\mathrm{T}} = 8/9$ and a power coefficient

$$C_{\mathrm{Pmax}} = \frac{16}{27} = 0.5926... \tag{1.18}$$

This is known as the Lanchester-Betz limit and is derived in Chapter 2. It results from the fact that fluid can flow around the device in preference to flowing through it. The pressure drop coefficient κ will be a function of the solidity of the device, the rotational speed of the device, and the shape, attitude and Reynolds number of the blades.

A lifting device has a theoretical maximum power coefficient that is approximately twice as high as that of a drag based device with the same cross-sectional area. The lift device will require smaller blades, and the forces on those blades per unit of extracted power will tend to be less.

A translating lifting blade is therefore the most efficient mechanism for converting fluid kinetic energy into a moving mechanical force. Figure 1.5a shows an ideal translating lifting blade which would be spaced some distance from its neighbouring blades such that the solidity σ is optimum for a given blade speed, Λ. Such an ideal device can achieve power coefficients very close to the Lanchester-Betz limit. However, all practical means of implementing this ideal blade motion bring inherent inefficiencies.

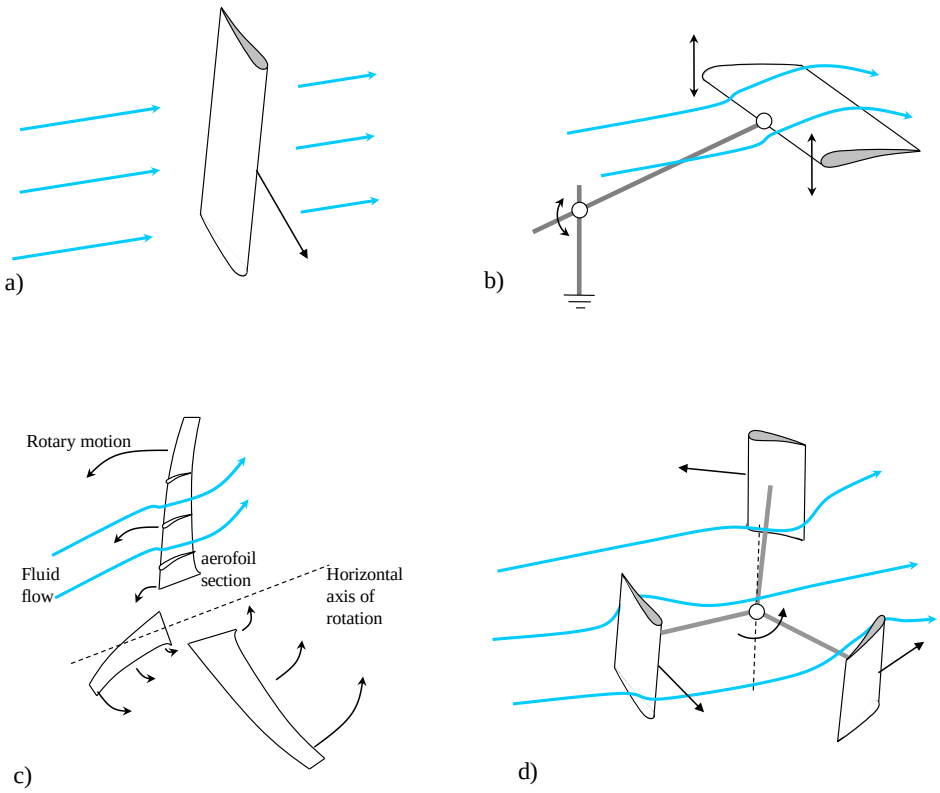

Figure 1.5: *Types of lift devices: a) ideal translating lifting blade, b) oscillating foil, c) axial flow rotor, d) cross-flow rotor.*

1.2.2.1 Oscillating hydrofoils

A lifting blade can translate back and forth on a finite path and this is known as an oscillating hydrofoil, illustrated in Figure 1.5b. This concept was pioneered in the tidal environment by The Engineering Business Ltd (2005), including installing a device rated at 150 kW. The blade can be neutrally buoyant in the water, which is not an option in wind turbines. The conclusion reached by the private company (Engineering Business Ltd, 2005) was that it was not a commercially viable concept, due mostly to the low efficiency of the device.

The oscillating foil has to reverse in direction so does not always travel at an optimum speed. For a path length l and blade chord c, in the limit $l/c \to \infty$ the blade will spend all its time at an optimum speed. However in that case, with only one blade, the solidity of the device tends to zero, $\sigma = c/l \to 0$, hence the optimum can never be reached. This is the inherent limitation of an oscillating device with a single blade.

The oscillating hydrofoil has seen renewed interest recently: Pulse Tidal Ltd are developing a device with two oscillating foils, one downstream of the other: this increases efficiency and can smooth out power delivery. At the time of writing their 100 kW test device was installed in the River Humber in the UK but data was not publicly available; a 1MW device was in development.

1.2.2.2 Axial-flow lift devices

The axial-flow device, illustrated in Figure 1.5c, is the most popular and the most advanced example of tidal stream technology. These devices, which look like propellers, are also the established standard device type for large scale commercial wind energy.

The blades of an axial-flow device move at a constant speed, always perpendicular to the oncoming flow. The blade-speed ratio varies along the span of the blade, so that a different blade section and attitude are required. Although optimum performance cannot be achieved along the entire length of the blade, it is near optimum. Average hydrodynamic power coefficients of 0.48 have been reported for SeaGen (Fraenkel, 2010)[1].

1.2.2.3 Cross-flow (Darrieus) lift devices

The blades on a cross-flow turbine move in a circle about an axis perpendicular to the oncoming flow, hence they are called cross-flow turbines. The blades spend the majority of their time moving in a direction approximately perpendicular to the flow. Hence the fluid dynamic mechanism of generating a useful force is the same as with any other lift device. This is distinct from drag-based cross-flow machines, such as the Savonius turbine. The main advantage of the cross-flow concept is that operation is independent of flow direction. This is of great benefit in the wind industry where significant amounts of energy yield come from a large range of angles. In tidal flows, which are usually rectilinear, this advantage is less but still significant: the device

[1] The maximum efficiency was 0.52. Note that these figures include the benefits of the close proximity of the sea bed and sea surface, and are also subject to an appropriate determination of U_∞ given the variable upstream conditions and non-uniform and unsteady velocity profile. The key point is that these are very efficient devices, with low inherent losses.

will not need to be altered in order to capture the reversing currents. Cross-flow wind turbines have the advantage that their generating systems can be at ground level. The analogy in tidal devices is that the generation system can be above water if the shaft is vertically orientated.

The cross-flow concept was patented by French engineer George Darrieus (Darrieus, 1926) but not developed significantly until South and Rangi (1973) independently invented the concept for use in wind energy. The blades can be straight, i.e. along the span the radius is constant; alternatively the radius can change, for example it can be reduced towards the ends of the blade. This 'skipping rope' or 'troposkein' shape helps reduce blade bending moments caused by centrifugal forces but reduces the power coefficient due to a non-optimum blade speed ratio on some parts of the blade. Centrifugal forces are less significant in tidal stream devices because they are proportional to the square of the blade speed, which is considerably less.

The Darrieus concept reached commercialisation in the 1980s as a wind turbine, but its use was short lived. Gipe (1995) attributes this to the higher cut-in and lower cut-out speeds compared to axial-flow machines, so that when placed on the same site an axial-flow machine will generate more electricity. The slightly higher performance coefficient of an axial-flow rotor compounds this difference.

More recently these machines have found a new commercial life as urban wind turbines, providing at least token 'green' power on buildings. These devices tend to have a constant blade radius, but a varying azimuth position along the span, i.e. helical blades. This helix shape, at the cost of a small efficiency drop, means that torque is delivered much more smoothly. A variant of the Darrieus concept is also now being considered for very large scale ($\sim$10MW) offshore wind turbines under the name NOVA (publications were not available at the time of writing).

An excellent explanation of the operation of a Darrieus turbine is found in Pawsey (2002). In summary Darrieus devices are distinct from axial-flow turbines for the following reasons:

- They operate independent of flow direction (omnidirectionality).
- Their cross-section is not limited to any particular aspect ratio (they can be very wide).
- The blades pass the flow twice per revolution (potentially higher theoretical efficiency).
- The blades travel into and away from the flow during some parts of each revolution (in practice this leads to a reduced efficiency).
- The blade loadings are reversed during every revolution (causing fatigue issues).
- Most practical implementations have some parasitic drag associated with the blade fixtures.
- The device does not self-start except in very unusual inflow conditions.

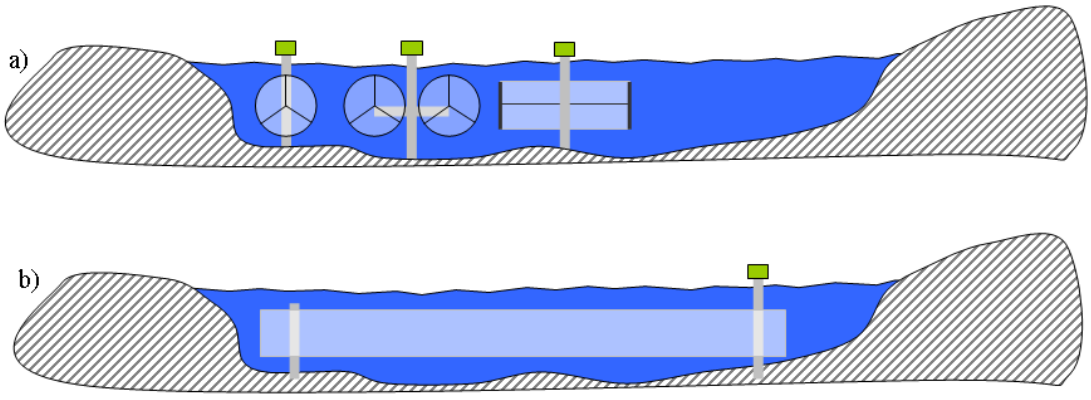

Figure 1.6: *A typical cross section of a tidal strait, which is much wider than the water depth. a) left-to-right: a single axial-flow rotor, twin axial-flow rotors, and a cross-flow rotor. b) conceptually a device that can be very wide, while maintaining high efficiency, will have a reduced installation cost per unit power.*

There are some current projects to develop cross-flow turbines for tidal stream energy, for example the Kobold project (Calcagno et al., 2006) and the work by Edinburgh Designs Ltd (Edinburgh Designs Ltd, 2006).

1.3 Moonraker concept

Figure 1.6a is a sketch of a cross-section of a tidal strait. The strait is much wider than the water depth and this is a characteristic of all tidal stream energy sites. To extract power on an economic scale an area much wider than the water depth must be captured. Conventional axial-flow turbines cannot achieve this because their diameter is limited by the water depth, and is also practically limited to about 20 m. Therefore multiple devices will be necessary, each with their own support structure, incurring high installation costs. These costs could be reduced – per unit power installed – if larger devices were possible. This is illustrated conceptually in Figure 1.6b, showing an ideal 'letterbox' shaped cross-section.

1.3.1 Principles of the Moonraker

The Moonraker is a relatively undeveloped hydrodynamic rotor concept that projects a letterbox cross-section as sketched in Figure 1.6b. The blades are arranged vertically and travel at a constant speed around an oval path, illustrated in Figure 1.7. In addition to its scalability,

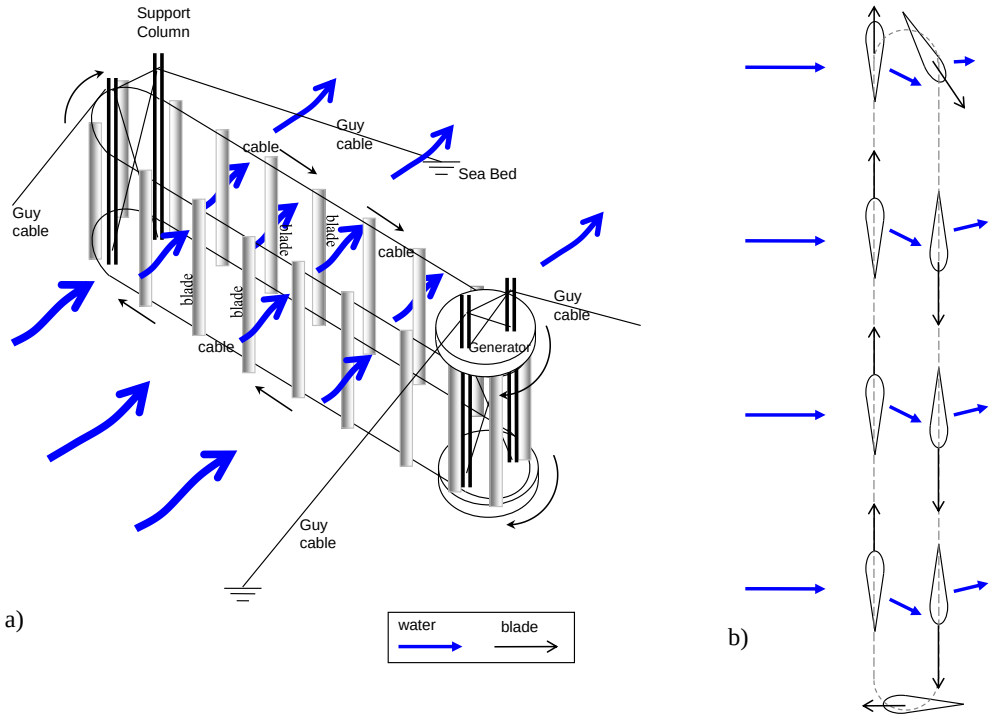

Figure 1.7: *A sketch of the Moonraker concept.*

the key beneficial hydrodynamic features of a Moonraker are:

1. The blades move almost entirely in the optimum direction (as with an axial-flow turbine).
2. The entire blade moves at the optimum speed (as with a cross-flow turbine).
3. The blades pass the flow twice, potentially increasing the efficiency beyond the Lanchester-Betz limit.
4. The blades are supported at both ends, allowing longer blades (longer blades can have a higher aspect ratio, resulting in less induced drag).
5. The blades will not experience fluctuating hydrostatic pressure (a benefit common to the cross-flow turbine).
6. Yawing of the device in a rectilinear flow is not necessary.
7. Shaft torque generation is smooth (as with an axial flow turbine).

In summary the Moonraker is the practical implementation which is the closest approximation to the ideal translating lifting blade that can fill a wide cross-section; in addition it incorporates two rows of extraction in one device.

The aim of this thesis is to quantify the hydrodynamic performance of a Moonraker: the blade forces F_{t} and F_{n}, and the resulting net power and thrust.

The blades will not necessarily need pitching on a Moonraker, however blade pitching can reduce the maximum forces on the blades and the structure, it can improve efficiency, and offers more control - e.g. rapid shutdown without use of a large brake. Pitching of the Moonraker is not addressed in this thesis.

1.3.2 Inherent problems with the Moonraker

Many of the problems associated with conventional devices still apply to the Moonraker. The dominant forces on the blades of the Moonraker (F_{n}) will reverse twice per revolution, causing fatigue issues (also a problem with other cross-flow devices). Control of the speed of rotation, and conditioning of the electrical power generated, are issues common to all devices and the Moonraker is not an exception.

The following new problems, which are not encountered by conventional devices, also arise with the Moonraker:

1. The structure and mechanics of the system are new, and may be inherently more expensive and less reliable

Bearing type	μ
Deep-groove ball bearings	0.0015
Self-aligning ball bearings	0.0010
Angular-contact ball bearings	0.0020
Cylindrical roller bearings: with cage	0.0011
Cylindrical roller bearings: full-complement	0.0020
Spherical roller bearings	0.0018
Thrust ball bearings	0.0013
Spherical roller thrust bearings	0.0018

Table 1.1: *Typical friction coefficients for roller bearings (Smith, 1998, p.54)*

2. If the blades are secured on a cable, forces in the system will be very high (and expensive)
3. If the blades run on tracks (therefore avoiding cables) the total bearing friction is likely to be higher than for an axial-flow machine

Regarding the first problem listed above, the mechanics of the Moonraker are undesirably complicated and from an engineering perspective it would require a lot of development work before reaching satisfactory levels of reliability when operating in the ocean. This thesis focuses on the hydrodynamics of the Moonraker and therefore a discussion of the mechanics of such a device is not included.

The second problem listed above can be avoided by using tracks instead of cables - this is discussed in more detail in Section 4.3 of this thesis.

The third problem listed above is addressed as follows. Each blade on a Moonraker is assumed to experience a negligible net force in the vertical direction. The force on each blade will therefore have one component in the direction of the blade's motion - called the tangential force, F_t – and one component normal to the blade's motion - called the normal force, F_n. If the blade is running along a track, then it will inevitably experience a rolling resistance equal to $F_\mathrm{n}\mu$ where μ is the friction coefficient. Some values of friction coefficients of rolling bearings are given in Table 1.1 showing a typical value of $\mu \approx 0.0015$. So the net tangential force on the blade will be

$$F'_\mathrm{t} = F_\mathrm{t} - \mu F_\mathrm{n}.$$

The power coefficient is proportional to the net tangential force, F'_t, so the 'efficiency' of the track system could be defined as:

$$\frac{F'_\mathrm{t}}{F_\mathrm{t}} = 1 - \mu \frac{F_\mathrm{n}}{F_\mathrm{t}}.$$

Evidently it is important to reduce the coefficient μ, which largely depends on available 'best' technology, and to reduce the ratio $F_\mathrm{n}/F_\mathrm{t}$, which is a hydrodynamic parameter. Here we make an order of magnitude estimate of the ratio $F_\mathrm{n}/F_\mathrm{t}$. The thrust is shared between the blades and

neglecting the curved parts of the blade path we can approximate $F_\mathrm{n} = C_\mathrm{T}/\sigma$ (see Section 2.6). The power will also be shared between the blades: $F_\mathrm{t} = C_\mathrm{P}/(\sigma\Lambda)$(see Section 2.6). We therefore estimate that

$$\frac{F_\mathrm{n}}{F_\mathrm{t}} \approx \frac{C_\mathrm{T}\Lambda}{C_\mathrm{P}}. \tag{1.19}$$

This says that the ratio of normal force to tangential force on each blade is equal to the blade speed multiplied by the ratio of thrust to power. In an ideal device we have $C_\mathrm{T} = 8/9$ and $C_\mathrm{P} = 16/27$ so we estimate that

$$\frac{F_\mathrm{n}}{F_\mathrm{t}} = \frac{3}{2}\Lambda. \tag{1.20}$$

The blade speed ratio is likely to be $3 < \Lambda < 5$ and we see here an incentive to reduce the blade speed ratio. Taking a typical value of $\Lambda = 4$ and $\mu = 0.0015$ we estimate that

$$\frac{F'_\mathrm{t}}{F_\mathrm{t}} = 99.1\%, \tag{1.21}$$

which indicates that at least 1% of the power is likely to be unavoidably lost through bearing friction - in addition to the bearings on the vertical shafts of the Moonraker. This does not compare favourably to axial-flow rotors, where the bearings operate at the centre of blade rotation and are likely to offer much less resistance. The bearings on an axial flow rotor are resisting the same thrust but their speed is much less than Λ because their radius of rotation is much smaller. In this sense the Moonraker is analogous to an axial-flow rotor with bearings of very large diameter around the path of the tip of the blades. This is the case for the OpenHydro concept, whose motor is located on the path of the blade tips in order to give a high rotor/stator speed and avoid the need for a gearbox (a similar benefit could be possible with the Moonraker; power take-off will not be covered in this thesis).

The purpose of the Moonraker design as an alternative to current developments is to reduce the cost per installed unit of power. The Moonraker enables this by being inherently scalable, but must also have a power coefficient that is competitive with conventional rotors, for example SeaGen's power coefficient of 0.48, otherwise the benefits will be lost. The conclusion in this section is that the Moonraker is inherently at a mechanical loss by design: according to this analysis its power coefficient will be reduced by an amount on the order of 1%. It is also important to note that the analysis leading to (1.21) is more important than the result because at this stage, with no detailed mechanical design for a full scale device, it is not clear what a realistic friction coefficient will be. This thesis aims to quantify the hydrodynamic benefits of the Moonraker, which could offer higher power coefficients as well as scalability.

1.3.3 Potential development of the Moonraker

The Moonraker is a novel device for an industry that is still in its early stages. It is therefore conceivable in principle that the Moonraker could be developed as a commercial technology. The basic process, which is no different to any other type of device, would be as follows:

1. The hydrodynamic benefits of the Moonraker need to be assessed quantitatively.
2. A mechanical and structural solution for the Moonraker needs to be developed in detail.
3. An ocean scale proof-of-concept could be built.
4. The technology could be developed on an industrial scale.

The aim of this thesis is to meet the first requirement above. The thesis is a scientific exploration of the hydrodynamic performance of the Moonraker.

1.3.4 Review of similar projects

The purpose of this section is to put the Moonraker concept in context. Firstly projects currently under development are reviewed, followed by a patent search for similar concepts regardless of their development status. The concept of a very wide installation for tidal stream energy extraction is not new: this is already in practice with SeaGen, which has two rotors, and future versions will have more rotors per installation, as illustrated in Figure 1.8a.

Alternatively, cross-flow devices with a vertical axis can be much wider than their height, as illustrated in Figure 1.6a on the right. Such use of traditional cross-flow turbines offers limited benefits: the blade speed is constant, so that with a large radius the rotational speeds are very low, leading to high torque. Further, with low power coefficients compared to axial-flow turbines, and further parasitic losses from the necessarily large support arms, this strategy offers only limited benefits. One exception to this is Salter's 'Polo' concept (Salter and Taylor, 2007), illustrated in Figure 1.8b. This innovative structure is built solely out of rings, so that there is no shaft and no arms. This concept uses ring cams and hydraulic power take off: the power take off is at high speed, and is located at the water surface so that it can be sealed by lightly pressurising the upper ring. This concept is yet to be implemented.

If cross-flow devices are arranged with a horizontal axis then they can be very wide, matching the letterbox section illustrated in Figure 1.6b. This is the strategy being followed by researchers at Oxford University with the THAWT device (Figure 1.8c), and also the University of Maine. These devices can be very large. Their main drawbacks are the limited power coefficient of a cross-flow device. At the time of publication, the University of Maine had tested their device in a lake.

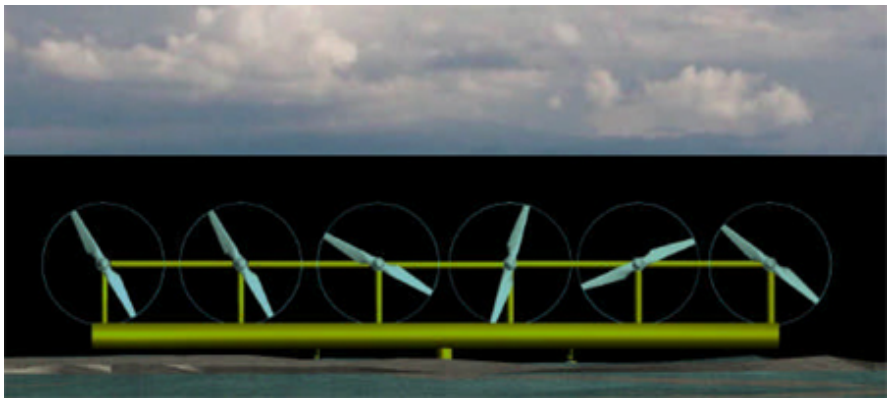

(a) *Multiple axial-flow turbines on a single installation, patented by MCT (image from www.marineturbines.com).*

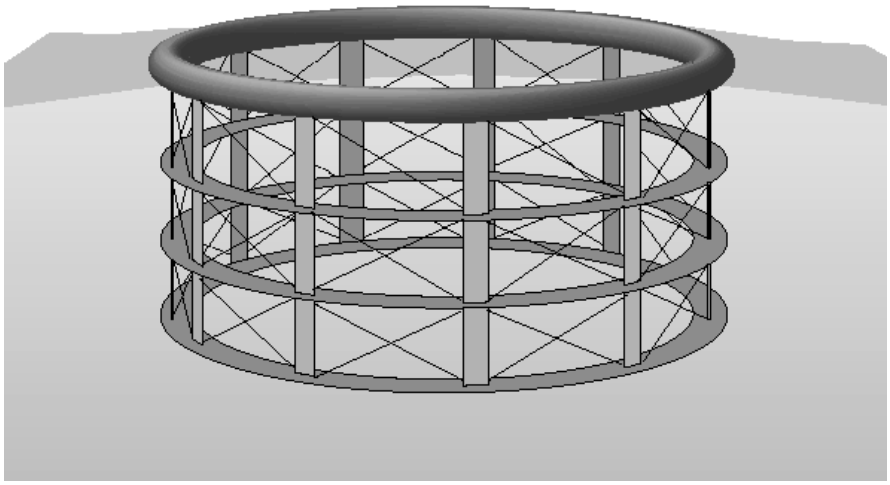

(b) *Salter's (2007) 'polo' vertical axis turbine, with hydraulic power take off using ring cams.*

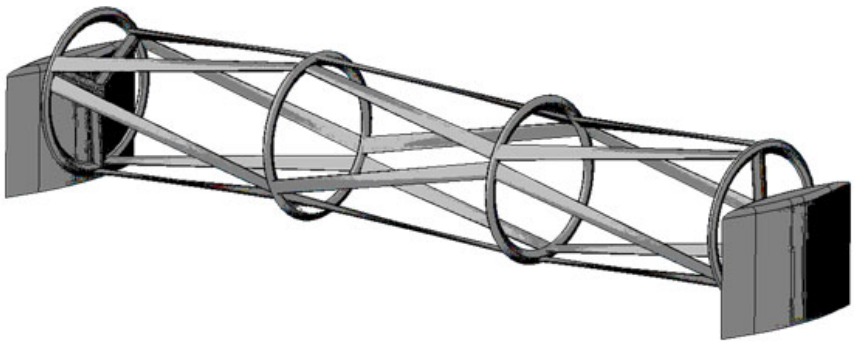

(c) *Oxford University's patented 'THAWT' device, with blades arranged for increased stiffness (image: University of Oxford).*

Figure 1.8: *Candidates for larger power per installation.*

Patent Number	Year	Title
US7075191	2006	Wind and water power generation device using a rail system
WO2005054669	2005	A TIDAL POWER STATION DEVICE
US6809430	2004	Conveyor-type fluid energy-harnessing apparatus
US6435827	2002	Apparatus for generating a fluid flow
US6498402	2002	Wing energy catchment device
DE10162516	2002	Turning blade dam for energy conversion in flowing ...
US6081043	2000	Eolian energy production systems
US6072245	2000	Wind-driven driving apparatus employing kites
US5744871	1998	Wind system for electric power generation
US5684335	1997	High-efficient hydraulic torque generator ...
US4878807	1989	Relating to energy conversion apparatus
US4572962	1986	Apparatus for extracting energy from winds at high altitudes
US4536125	1985	Wind lift generator
US4494008	1985	Wind-driven generator
GB2131491	1982	Device for extracting energy from wind or water
US4302684	1981	Free wing turbine
US4303834	1981	Cable wind mill
US4186314	1980	High efficiency wind power machine
US4175910	1979	Windmotor as a windbreak
US4163905	1979	Electric generating water power device
US4113205	1978	AERODYNAMIC LIFTING MECHANISMS
US4049300	1977	Fluid driven power producing apparatus
US3730643	1973	Wind Power Machine
US3504988	1970	MEANS FOR HARNESSING NATURAL ENERGY
US763623	1904	WIND OR WATER MOTOR
US443641	1890	WIND-ENGINE

Table 1.2: *Patents with features similar to or the same as the Moonraker. For patents filed in multiple countries the US number is given if possible.*

There are numerous examples in the public domain of concepts which are similar to the Moonraker and following a patent search 120 patents have been identified that resemble the Moonraker concept. These were then classified by their key features so that a filter could be applied based on the following criteria: use in water, lift based operation, high blade speed (greater than the flow speed). The number of relevant patents then reduces to 26 and these are listed in Table 1.2.

The patents listed, most of which have expired, cover the key aspects of the Moonraker. Figure 1.9 shows two examples of key Moonraker aspects. Patent application GB2131491 from 1982 clearly shows the concept of two rows of translating lifting blades, in this case secured on cables. The patent US7075191 shows a sketch where a track system is employed. There are also many examples of patents with methods of pitching the blades so that their angle of attack can be controlled. The conclusion of the patent search was that the concept of the Moonraker was not in itself novel. However, at least according to information that was publicly available at the outset of this research, the concept had not been subject to significant scientific research

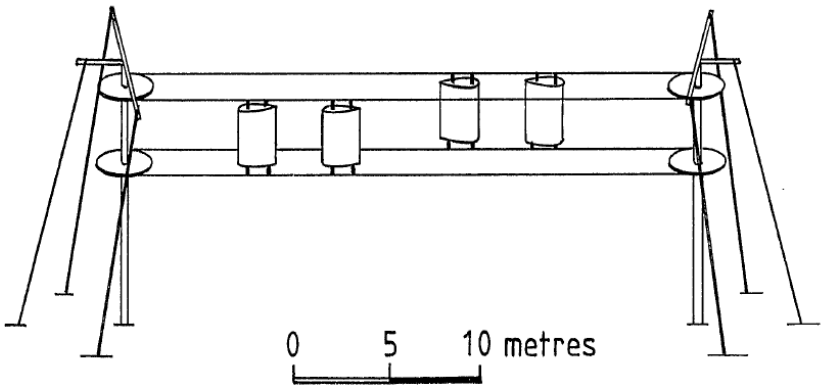

(a) *Sketch from patent application GB2131491 filed in 1982.*

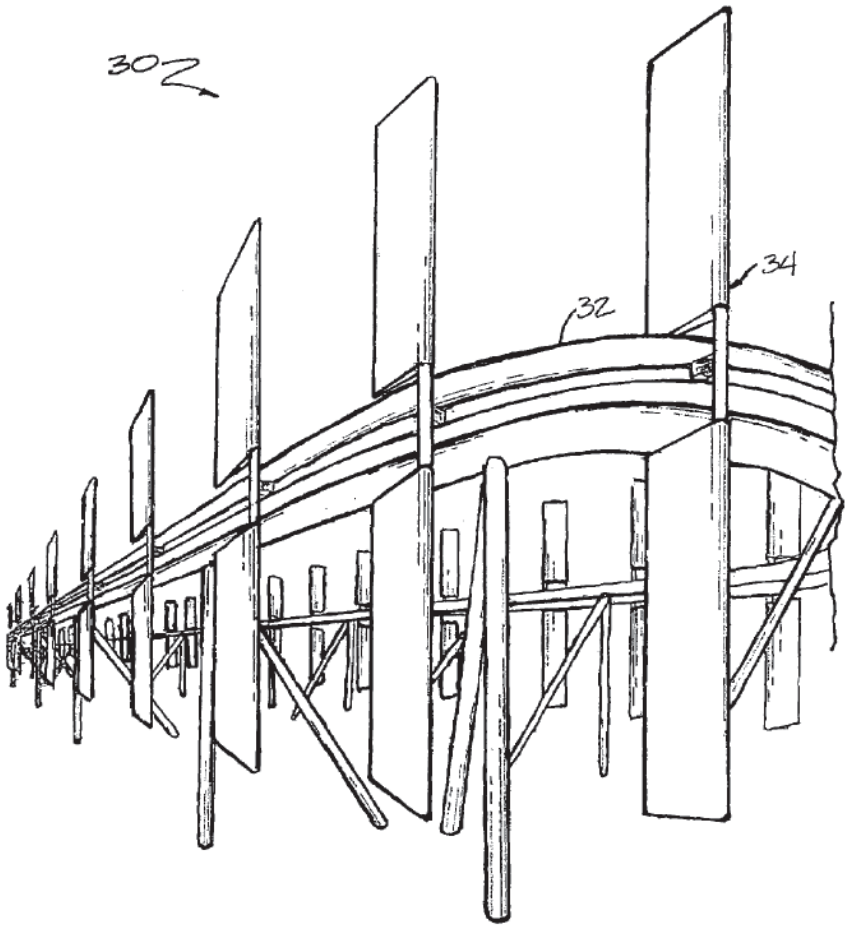

(b) *Sketch from patent US7075191, 2006, showing a system with a track.*

Figure 1.9: *Examples of patents that cover the key aspects of the Moonraker.*

or development. Therefore the purpose of this thesis was to carry out such research, and in particular to analyse the hydrodynamics of such a device.

During the course of this research two similar projects were discovered, firstly the aerodynamics of a Darrieus turbine with oval blade trajectory was investigated by Ponta et al. (2007). Ponta et al. (2007) investigated a wind turbine with many discrete blades travelling along ground-based train tracks. Ponta et al. (2007) used the blade element momentum (BEM) method to investigate the device, and this is reviewed more in Chapter 3. Also the author was contacted by Arthur Pecher, a researcher at Aalberg University, who is developing a similar device for wind energy though no publications were available at the time of writing.

1.4 Overview of the thesis

The thesis chapters are structured as follows:

1. Introduction
2. Theory and literature review
3. Prediction of blade forces
4. Experimental Moonraker device
5. Vortex model of actuator surfaces
6. Conclusions

Chapter 2 reviews the theory and research relevant to this thesis and serves as a reference for later chapters. In particular the tidal energy resource, the mechanics of fluid flow over turbine blades, and the study of 'actuator disc theory' are reviewed.

In Chapter 3 the forces on the blades of cross-flow devices are predicted using hydrodynamic models. The standard blade element momentum method (BEM) is used to show the effectiveness of a blade translating across the flow. Following this, the vortex method is presented: this is a fairly well established technique and was implemented here in Matlab and first applied to a Darrieus turbine. Results of the vortex model are first compared to the original work of Strickland et al. (1981) showing close agreement. The vortex model was then applied to the same configuration of Darrieus turbine that was studied by Gretton (2009) with a BEM model and using a commercial Computational Fluid Dynamics (CFD) code; results from vortex model are compared directly with those of the BEM and CFD models to give insight into the physical effects which are captured, or not, by the BEM and vortex models.

Finally in Chapter 3 predictions of the Moonraker are presented, i.e. a cross-flow turbine with an oval blade path. The BEM method was not used for these predictions because there is no available theory for two rows of energy extraction in close proximity. Progress towards

the development of such a theory was pursued, and is presented separately in this thesis in Chapter 5. Therefore in Chapter 3 only the vortex model is applied to the Moonraker. The vortex model can be applied in two- or three-dimensions and it is argued in Chapter 3 that in many cases the three-dimensional model is important; however due to time constraints only the two-dimensional model was implemented here.

Results from the two-dimensional vortex model presented in Chapter 3 predict that the Moonraker can achieve favourable power coefficients when compared to the Darrieus turbine. Chapter 3 concludes that experimental measurements of blade forces on a Moonraker are required for comparison with the predictions of the vortex model and this is pursued in Chapter 4. In addition, Chapter 3 concludes that a theory for double actuator surfaces would be valuable and recommends further investigation into the vortex model's suitability for this – a task which is pursued later in the thesis, in Chapter 5.

Chapter 4 presents the design, experimental method, and results from a lab-scale Moonraker device – in particular two-axis blade force measurements. The device was tested in the towing tanks at UCL for development purposes, and at QinetiQ where the blockage ratio was very low and the results should be comparable to predictions from the vortex model. Measured and predicted blade forces are compared, as are averaged torque and power measurements which were derived from blade force measurements. There is some encouraging agreement between predictions and measurements, but also some disagreement which is mostly attributed to the short comings of the predictions.

Chapter 5 investigates two complementary issues which are highlighted in Chapters 3 and 4 for further research. The chapter investigates the vortex method in more detail and studies the time averaged affect of the blades of a Moonraker or other device with the concept of an 'actuator surface'. This is useful firstly because Chapter 3 presents predictions from the vortex model of power coefficients which exceed the limits derived from linear momentum theory; by simplifying the vortex model to that of an actuator surface the vortex method itself can be tested against linear momentum theory. A convergence study is presented, and comparisons are made with theory, published experiments and new experiments conducted in the towing tank at UCL. Once the vortex model had been tested it was suitable for use in the other issue highlighted by Chapters 3 and 4, to investigate the dynamics of two rows of energy extraction with arbitrary separation. An initial study is presented in Chapter 5, the extension of which may facilitate the use of the BEM model for two rows of energy extraction in a manner which accounts for the separation between the rows.

Chapter 2

Theory and literature review

2.1 Introduction

This chapter reviews the theory and literature relevant to this thesis beginning with the tidal energy resource. The Biot–Savart law, which relates fluid vorticity to velocity is briefly described as it is used throughout the thesis. Following this the fluid dynamics of hydrofoils is reviewed, and then 'actuator disc theory' which is a key tool in analysing devices with multiple hydrofoils.

This thesis is a study in hydrodynamics and therefore is always employing the concept of a continuum to model water. The water is always assumed to be incompressible, to have a constant (Newtonian) viscosity, and to be of single phase. Except where stated otherwise the fluid is assumed to be unbounded - with no influence from rigid external boundaries or free surfaces. Internal boundaries are frequently considered: a hydrofoil constitutes an internal boundary.

This thesis assumes a working knowledge of calculus, vectors, and the theory of incompressible fluid flow. Theory that is covered by standard texts such as Batchelor (1967) is not referenced specifically.

All of the flows considered in this thesis are inertially dominated, and so the effect of viscosity will be limited to the boundaries of solid objects, as first suggested by Prandtl (1904). Assuming the fluid flows considered were impulsively started and therefore are initially irrotational except in the thin boundary layers, the main body of fluid therefore behaves as an irrotational fluid. An irrotational fluid is free of vorticity (the curl of the velocity vector field) and therefore free of the effects of viscosity. It can therefore be treated as a potential flow. Some vorticity may later be present in the main body of the fluid if it is shed from the boundary layer, and this is discussed below after the introduction of the Biot–Savart law, which relates vorticity to velocity.

Modeling methods for wind turbines are used interchangeably with water turbines and here a brief comparison is made. The lower speed but higher density of the water means that, in

practice, Reynolds numbers are broadly similar for both fluids. The energy is more densely available in water by a factor of about four, leading to smaller devices per unit power. The main differences in water are: the water speed and therefore blade speed is lower; effects of gravity can be countered with buoyancy; cavitation is a potential problem; corrosion and fouling are also potential problems but are not discussed here.

The implications of the lower blade speed in water are firstly that forces are higher per unit power, and secondly that centrifugal forces are much lower and so, for example, solutions like the skipping rope ('troposkein') blade shape on cross-flow turbines are less relevant.

Cavitation is the vaporisation of a liquid due to very low pressure, which is a result of the high speeds occurring over the lifting surfaces. If cavitation does occur the bubble(s) tend to quickly collapse, causing extremely high local pressures and 'pitting' the blades, ruining their surface. In general cavitation is avoided by finding, and then always staying below, the blade speed at which it occurs. Cavitation is not addressed in any more detail in this thesis.

2.2 Tidal stream resource

The common method of assessing a tidal stream energy resource is to estimate the rate of quasi-steady kinetic energy flowing through a given site per unit of cross-sectional area, based on the density, ρ, and speed, U, of the ocean currents. In this section some typical values are used to show by example how the tidal energy resource is calculated and how the very basic economics of a tidal stream energy device work. The instantaneous power available is then the rate of kinetic energy per unit area, multiplied by the projected cross-sectional area of any conversion devices, A, multiplied by some power coefficient, C_{P}:

$$\text{Power} = C_{\mathrm{P}} \frac{1}{2} \rho U^3 (t) A, \tag{2.1}$$

where C_{P} is a property of the conversion device. Here we have used mass flow rate $\dot{m} = \rho U A$, and kinetic energy flow rate $\frac{1}{2}\dot{m}U^2$. This is the instantaneous power, and the average power will depend on the distribution of speed as a function of time. We define the load factor as

$$LF = \frac{1}{T U_{\mathrm{rated}}^3} \int_0^T U^3 (t) \, \mathrm{d}t, \tag{2.2}$$

where U_{rated} is the 'rated' speed at a given site and T is a time period that is long enough not to effect the value of LF. For a tidal system this will be fairly accurate for $T \sim 28$ days. It is important to note that the load factor is dependent on the rated speed. Manufacturers may choose a high rated speed, so that their device looks powerful, or likewise a low rated speed, so that their load factor looks higher. The annual energy yield of a conversion device or farm is then

$$\text{Annual energy yield (Wh)} = 8760 \, LF \, C_{\mathrm{P}} \, \frac{1}{2} \rho U_{\mathrm{rated}}^3 A. \tag{2.3}$$

where 8760 is the number of hours in a non-leap year and kWh is a standard unit of energy. The

density of sea water is typically 1025 kg/m^3 and load factors are site dependent but will tend to be around 0.4. The electrical power depends on the 'water-to-wire' efficiency of the device, which is the energy in the flow, multiplied by the power coefficient, multiplied by mechanical and electrical efficiencies; this will tend to be around 0.4. A typical rated speed is 2.6 m/s, and a turbine with an 18m diameter will will have a project area of 254 m^2. This represents a rated power of 1 MW and an annual energy yield of 3.4×10^9 Wh. Wholesale electricity is typically worth £50 / MWh, so the turbine given in this example is generating about £170k per year. The net present value (NPV) of this income over 20 years - assuming steady electricity prices and an 8% discount rate - is £1.45m. This simplified example, which neglects the not insignificant cost of maintaining the machines, suggests that at a constant electricity price of £50 / MWh, the cost of installing a tidal stream energy device at a site with a rated speed of 2.6 m/s must be less than £1.45m / MW. This is a rough estimate which excludes subsidies and therefore gives a guide for the cost targets for tidal stream energy if it is to be economically sustainable. The estimate also illustrates how sensitive the economics are to the rated speed and its associated load factor: this highlights the importance of an accurate resource assessment, which is equivalent to a power-plant requiring an accurate assessment of the energy content of its fuel.

Figure 2.1 shows the magnitude of peak flow speeds in UK waters. This is part of the data that was used by Black & Veatch (2005a,b) on behalf of the Carbon Trust (2005) to assess the UK's potential to generate tidal stream energy. They applied a limiting factor so that at a given site no more than 20% of the energy flowing through the site was extracted. The total technically feasible potential was estimated at 18 TWh/yr, or 5% of annual UK demand. This represents half of the known European resource and is estimated at 10-15% of the global resource.

Equation (2.3) shows that the energy yield of a site is most sensitive to the rated speed, because it is proportional to the cube of the rated speed. The data in Figure 2.1 shows peak speed but when plotted in terms of energy yield the results are very similar. It is clear that the areas for economic tidal stream energy extraction are very geographically concentrated. The Pentland Firth, between northern Scotland and Orkney, represents about 60% of the UK's resource (Carbon Trust, 2005). It is this region that was leased by the Crown Estate in March 2010 for 600 MW of tidal stream energy farms.

Of the resource estimated by the Carbon Trust (2005), 21.3% is in water depths less than 40 m, and the remainder is deeper than 40 m. This has important implications for the design of structures to hold conversion devices in place. Deeper water installations require more expensive installation vessels, and more expensive installed structures, making the installed cost on a per MW basis much higher.

There is some controversy over the method of kinetic energy flux for assessing the tidal stream energy resource. In the kinetic energy flux method the resource is assumed to be a source of kinetic energy, but disregards the fact that this kinetic energy arises originally in the form of potential energy: the tide. Tidal streams are actually shallow waves moving across the globe. If a resistance is placed in the stream, then the head difference across the site is unaffected.

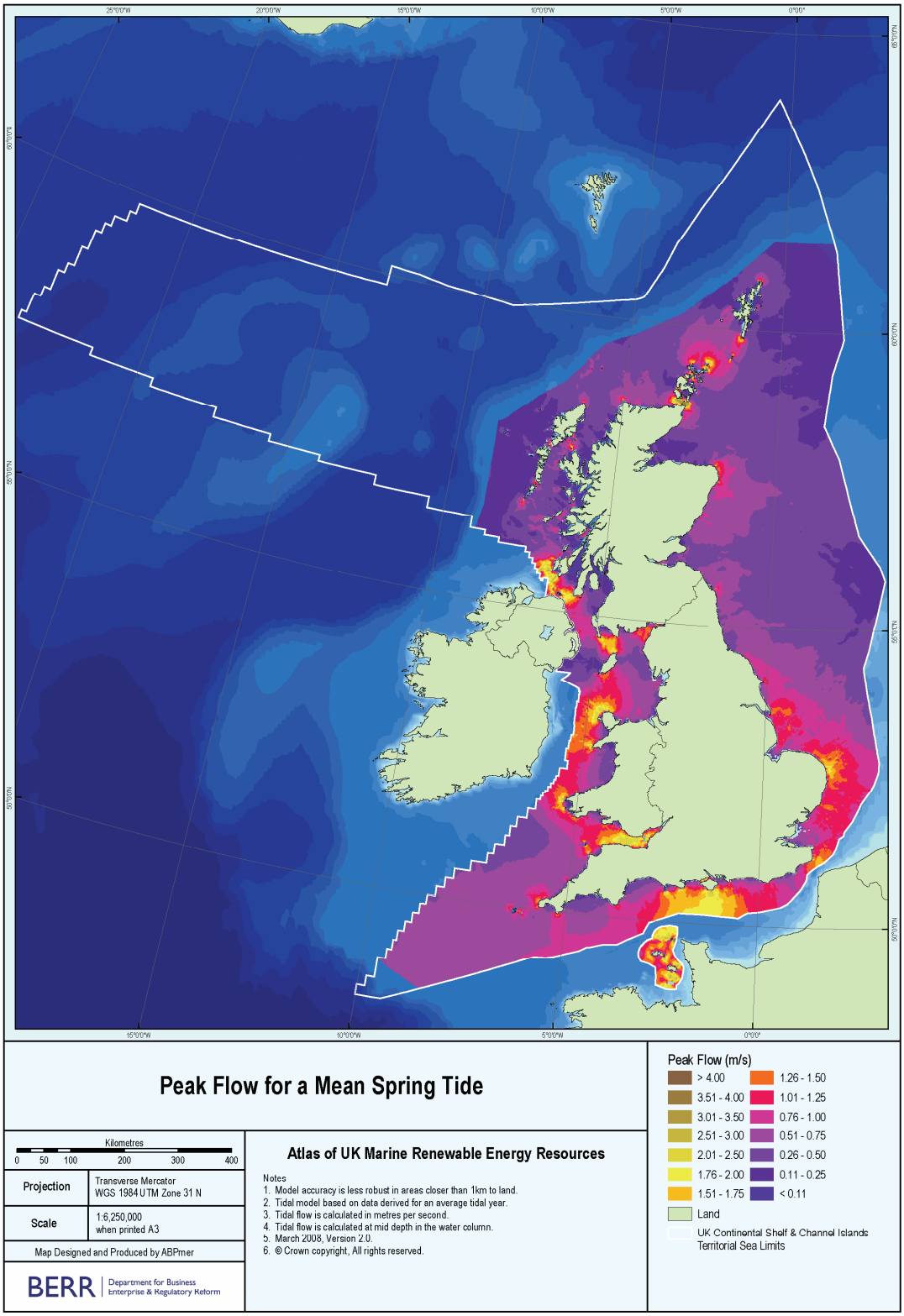

Figure 2.1: *Peak spring flow speeds around the UK, from the Renewables Atlas BERR (2008).*

The head difference continues to drive the tidal streams and it is not unreasonable to expect the stream to continue its motion even in the presence of a resistance. This implies that extra energy is available. This argument is made by MacKay (2009) and Salter (2009). Salter goes on to predict that the extraction of energy could push the tidal system closer to resonance, and the head difference driving the system could actually increase as a result of energy extraction. Both MacKay (2009) and Salter (2009) predict a tidal stream energy resource that is at least an order of magnitude higher than the popularly cited figure provided by the Carbon Trust.

This thesis is concerned with device scale hydrodynamics, and assumes that the energy extraction will not be large enough to have a significant effect on the resource itself: no interaction with the resource will be considered.

There will still be some energy available in addition to the kinetic energy. If a device occupies a significant proportion of the water column then the problem of 'blockage' is introduced, and this is addressed in Section 2.6.

2.3 Biot–Savart law

The Biot–Savart law relates a vorticity field to a velocity field and it is used frequently in this thesis. Assume a vorticity vector field $\boldsymbol{\Omega}$ which is solenoidal ($\boldsymbol{\nabla}\cdot\boldsymbol{\Omega}=0$) and is concentrated in vortex tubes of cross-sectional area $\boldsymbol{A}$ (vortex tubes are the analogue of streamtubes in a velocity vector field). The Biot–Savart law is presented here for a vortex filament, which is a vortex tube where $|\boldsymbol{\Omega}|\to\infty$ while $\boldsymbol{A}\to 0$. The circulation around the filament $\Gamma=\boldsymbol{\Omega}\cdot\boldsymbol{A}$ is finite and for an inviscid fluid it is constant. Consider a straight segment of this vortex filament located at a position $\boldsymbol{Q}$ and denoted $\mathrm{d}\boldsymbol{s}$, as illustrated in Figure 2.2. The Biot-Savart law gives the velocity 'induced' by the element $\mathrm{d}\boldsymbol{s}$ of the vortex filament at a point $\boldsymbol{P}$ as

$$\Delta\boldsymbol{u}=\frac{\Gamma}{4\pi r^3}\mathrm{d}\boldsymbol{s}\times\boldsymbol{r}. \tag{2.4}$$

where $\boldsymbol{r}=|\boldsymbol{Q}-\boldsymbol{P}|$ and $r=|\boldsymbol{r}|$. The conventional term 'induced' is slightly confusing: the relation (2.4) is derived from the solution to Poisson's equation for some vector field whose curl represents the velocity field $\boldsymbol{u}$ (Karamcheti, 1980, ch. 18). The Biot-Savart law is a relation between two kinematic descriptions of the fluid flow (the vorticity field and the velocity field). The word 'induce' suggests that vorticity causes velocity but actually the velocity given by (2.4) is that which is *associated* with the vorticity field. It is the inverse of the equation $\boldsymbol{\Omega}=\nabla\times\boldsymbol{u}$.

The angle between $\mathrm{d}\boldsymbol{s}$ and $\boldsymbol{r}$ is defined as θ for $0<\theta<\pi$ and illustrated in Figure 2.2. Expressed in scalar form, the magnitude of the induced velocity is

$$\Delta q=\frac{\Gamma}{4\pi d}\sin\theta\mathrm{d}\theta, \tag{2.5}$$

where we have used $|\mathrm{d}\boldsymbol{s}|=r\mathrm{d}\theta/\sin\theta$ and $d=r\sin\theta$ which is the perpendicular distance from the filament to the point $\boldsymbol{P}$ and d does not vary with θ. Integrating between θ_1 and θ_2 gives

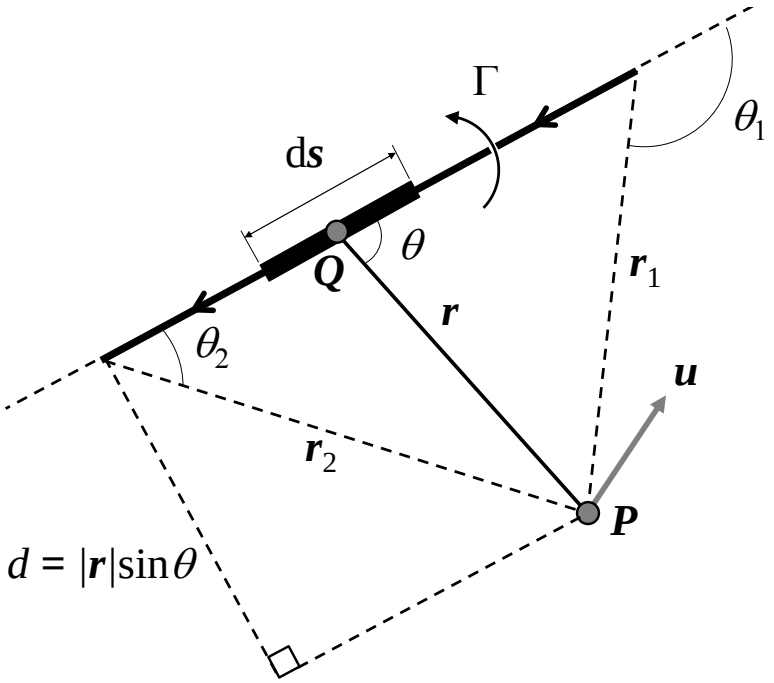

Figure 2.2: *A segment* ds *of a vortex filament of strength* Γ*, which induces a velocity* $\boldsymbol{u}$ *at a point* $\boldsymbol{r}$ *from the vortex.*

$$q = \frac{\Gamma}{4\pi d}\left(\cos\theta_2 - \cos\theta_1\right). \tag{2.6}$$

Two simplified results in particular are of interest: the infinite, straight vortex filament ($\theta_1 = \pi$, $\theta_2 = 0$) induces a planar velocity field of magnitude

$$q = \Gamma/2\pi d$$

in a plane normal to $\boldsymbol{s}$ and containing $\boldsymbol{Q}$; the semi-infinite vortex ending at the point $\boldsymbol{Q}$ (where $\theta_1 = \pi$, $\theta_2 = \pi/2$) produces a velocity

$$q = \Gamma/4\pi d$$

in a plane normal to $\boldsymbol{s}$ and containing $\boldsymbol{Q}$.

2.4 Static hydrofoils in steady flow

Lift-based rotors have discrete blades which are slender (i.e. large span to chord ratio, or aspect ratio, AR) and have carefully selected cross-sections known as hydrofoils. The hydrofoils move in a direction perpendicular to the oncoming flow, as illustrated in Figure 1.4. Because the blades are slender and the cross-section changes smoothly, the flow over a small section of the blade is often considered as two-dimensional. Traditionally, the force on the blade is decomposed

into the lift and drag, which are perpendicular and parallel to the relative fluid flow, respectively, and this is illustrated in Figure 1.4. For an energy device, the more relevant components are the force tangential and normal to the blade's motion, F_{t} and F_{n} respectively. The tangential force generates useful work; the normal force causes the majority of the momentum reduction in the flow (and is the dominant force when considering structural design). The tangential and normal forces can be found from the velocity triangle in Figure 1.4, and are given in equations (1.11-1.14) where it is clear that the lift force is beneficial, and the drag force always acts againts the motion of the blade.

2.4.1 Drag, separation and streamlining

Hydrofoils with high lift and low drag are desirable. In two-dimensional flow drag is composed of skin friction, due to the boundary layer, and 'pressure' or 'form' drag due to any difference in pressure in the fluid surrounding the blade. The combination of skin friction and pressure drag is called profile or total drag and can be dramatically reduced by avoiding boundary layer separation.

Figure 2.3a illustrates a foil submerged in an oncoming flow: the foil is symmetric and its chord is parallel to the flow. The flow stagnates at the front of the blade and the streamlines split in two, flowing over the surface of the blade and gradually growing a boundary layer due to the no-slip condition and the action of viscosity, before meeting again at the trailing edge. The foil increases in thickness quite quickly, but reduces its thickness gradually: the negative gradient has been limited in order to prevent the boundary layer from separating and hence avoiding the associated large form drag.

Downstream of the thickest part of the foil, the diverging streamlines indicate slowing flow; in the absence of an external pressure gradient and any viscous effects Bernoulli's equation suggests that the pressure is increasing along the foil.

The 'adverse' pressure gradient is, from Newton's second law, associated with a rate of change of momentum per unit volume, which for an incompressible fluid means a reduction in velocity. This velocity reduction is experienced all across the boundary layer because the pressure field is approximately uniform across the boundary layer (Batchelor, 1967, §5.7).

Near the boundary the velocity is very low so the reduction in velocity causes a reversal in the velocity: this is the separation of the boundary layer. Fluid that separates becomes unstable and breaks into a series of turbulent eddies: this results in rotational flow downstream of the body. This rotational 'wake' has angular momentum which, from energy considerations must have been gained at the expense of the fluid pressure and the result is significant pressure drag. Hence boundary layer separation is to be avoided. This is achieved by streamlining which consists of restricting the geometrical gradient of the boundary so that the adverse pressure gradient is limited to such a small magnitude that separation can be avoided. This is perhaps best explained by appealing to a different explanation of boundary layer separation, which will now follow.

The velocity is zero at the boundary but at a small distance, δ, away from the surface

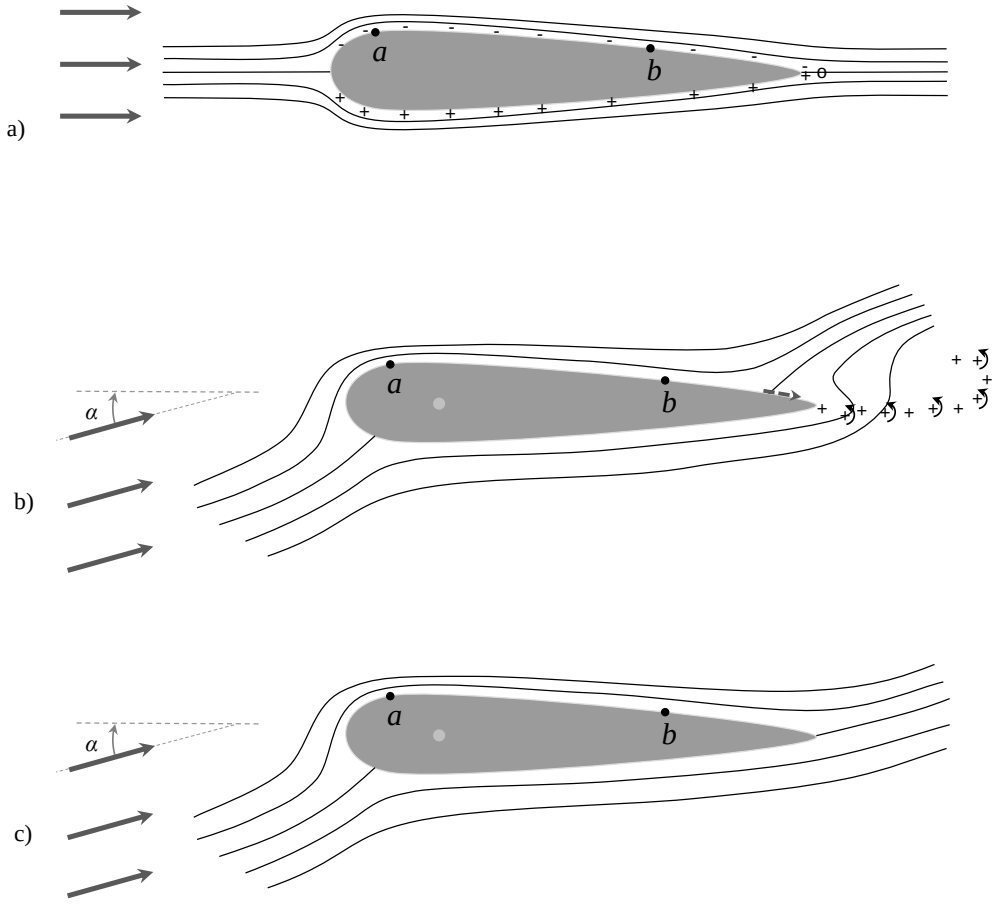

Figure 2.3: *Sketch of a non-cambered hydrofoil, showing streamlines which when upstream are equally spaced.*
a) foil parallel to flow,
b) foil with flow at relative angle α (during start-up),
c) foil with flow at relative angle α (steady state).

it is finite: this 'boundary layer' is therefore a shear layer and hosts vorticity in an otherwise irrotational flow; this vorticity is illustrated by the '+' and '-' characters in Figure 2.3a: counter-clockwise vorticity is positive. The action of viscosity, which opposes shear, will cause the boundary layer to grow. Dimensional considerations show that the boundary layer will grow in proportion to $(\nu t)^{\frac{1}{2}}$ where ν [L^2T^{-1}] is kinematic viscosity and t [T] is a characteristic time; for a flow speed U [LT^{-1}] and chord length c [L] we can approximate $t = c/U$ so that $\delta \sim (\nu c/U)^{\frac{1}{2}}$ and the relative thickness of the boundary layer is $\delta/c = (\nu/cU)^{\frac{1}{2}}$. This shows that in high Reynolds number flows (say, $Re = Uc/\nu \gtrsim 10^4$) the boundary layer is very thin compared to the length of the foil ($\delta/c \ll 1$) and in the limit of infinite Reynolds number the boundary layer becomes an infinitely thin vortex sheet around the surface of the foil.

To study the vortex sheet bounding the foil we introduce a coordinate system (x_1, x_2, x_3) where x_1 is tangential to the foil surface, x_2 is normal to the foil surface, and x_3 parallel to the span of the foil, the vorticity in the boundary layer is

$$\boldsymbol{\Omega} = \nabla \times \boldsymbol{u} = \begin{bmatrix} \partial u_3/\partial x_2 - \partial u_2/\partial x_3 \\ -\partial u_3/\partial x_1 + \partial u_1/\partial x_3 \\ \partial u_2/\partial x_1 - \partial u_1/\partial x_2 \end{bmatrix}. \tag{2.7}$$

The 'strength' of a thin boundary layer is denoted γ:

$$\gamma = \int_0^\delta \boldsymbol{\Omega} \mathrm{d}x_2 \tag{2.8}$$

where $x_2 = 0$ indicates the foil surface. The strength γ has the units m/s which can be interpreted as circulation per unit length, or as a velocity. For two-dimensional flow ($\partial/\partial x_3 = 0$) and for a thin boundary layer ($\partial/\partial x_2 \gg \partial/\partial x_1$) the only significant term in the vorticity is $\boldsymbol{\Omega} = -\partial u_1/\partial x_2 \hat{\boldsymbol{e}}_1$. This is the velocity gradient in the boundary layer. So (2.8) becomes

$$\gamma = u_1, \tag{2.9}$$

and the boundary layer can be thought of as a vortex sheet with strength (circulation per unit length) equal to the local flow speed, u_1 (see Lighthill 1986, p.75). It is useful to think of the boundary layer as a vortex sheet because vortex models, which are applied in the following chapter, are based upon the representation of a hydrofoil in potential flow by vortex sheets.

We will now use this model of the boundary layer as a vortex sheet to explain how separation on a hydrofoil in high Reynolds number flow can be avoided. A foil that is parallel to ambient, irrotational flow is illustrated in Figure 2.3a. The streamlines are initially equally spaced so that their spacing downstream indicates the local fluid speed. Consider a point, a, on the foil surface, which has a local speed u_a; the no-slip condition therefore requires a boundary layer (vortex sheet) strength of u_a and vorticity will be generated at the boundary layer, by viscous action, such that this is the case. At another point b, further downstream on the foil surface, the local speed is u_b, and this is the strength of vortex sheet required to meet the no slip condition.

However, the local speed at b is less than at a, because the foil thickness has reduced:

$$u_a > u_b$$

Some of the net circulation generated at a (of strength u_a) will diffuse through the boundary layer by viscous action while the remainder will be advected downstream and will reach b:

$$\gamma_{\text{advected}} = u_a - \gamma_{\text{diffused}} \tag{2.10}$$

Therefore at location b, in order to meet the no-slip condition, the additional circulation generated by the boundary layer will be

$$\gamma_b = u_{\text{b}} - \gamma_{\text{advected}} \tag{2.11}$$

$$\gamma_b = u_b - u_a + \gamma_{\text{diffused}} \tag{2.12}$$

Therefore as long as the rate of diffusion of circulation by the boundary layer (γ_{diffused}) is greater than the velocity gradient along the foil, the action of viscosity in the boundary layer will be to generate circulation of the same sign as at a point upstream; in Figure 2.3a this would be clockwise on the top surface.

If the velocity gradient along the foil is too high, then the circulation generated by the boundary layer will be of the opposite sense: the no-slip condition can only be met if the flow reverses, and this implies that the streamlines will separate from the surface (because they will remain tangential to the surface but switch directions). In that case vorticity is shed from the boundary layer and a wake forms, continually accruing vorticity until it becomes a large region of rotational flow; this familiar disordered pattern in the wake is full of rotational energy which is gained at the expense of a drop in pressure. Hence the profile drag is high.

To avoid separation and therefore to minimise drag, the foil must therefore keep any adverse velocity gradients shallow, i.e. the gradient of the foil itself must be shallow.

In the limit of a very shallow foil gradient the friction drag will increase and so an optimum needs to be found: this tends to be a foil thickness of between about 10% and 25%.

2.4.2 Theory of lift

Following the previous argument, the flow around the foil is essentially that of a uniform irrotational flow, plus the effect of a vortex sheet around the foil. All viscous actions are accounted for by the use of vortex sheets - this is the limiting case of infinite Reynolds number. The vortex sheets are related to the velocity field via the Biot–Savart law, and this in turn gives the local pressure from Bernoulli's equation. In the case of steady flow, anywhere on a streamline in irrotational flow:

$$p + \frac{1}{2}\rho u^2 = \text{const.}, \tag{2.13}$$

where p is pressure, ρ is fluid density, and u is the local fluid speed.

Therefore the net force due to pressure on the foil, per unit length, is:

$$L = \oint_C p \mathrm{d}x \tag{2.14}$$

where C is the boundary of the blade and $\mathrm{d}x$ is the component of a small segment of the boundary that is parallel to the relative fluid flow. This leads to the familiar Kutta-Jouwkowski equation:

$$L = -\rho U_\infty \oint_C \gamma \mathrm{d}C, \tag{2.15}$$

where the integral in (2.15) is the 'bound' circulation:

$$\Gamma_\mathrm{b} = \oint_C \gamma \mathrm{d}C. \tag{2.16}$$

For high Reynolds number the term γ is essentially the fluid speed on the foil surface. The velocity in Figure 2.3a is the inverse of the spacing between the streamlines, which is symmetric hence the integral in (2.15) will be zero and there is no net lift force.

However, in Figure 2.3b, the flow is at an angle α to the chord, and the flow around the blade is asymmetric. The streamlines that are predicted by irrotational flow with no circulation have been sketched, however it is clear that at the trailing edge the gradient is extremely adverse and the boundary layer will separate. The positive (counter-clockwise) vorticity of the boundary layer is shed into wake at the trailing edge. This strong collection of vorticity which collects in a spiral shape (Graham, 1983) is known as the start-up vortex: it will induce a velocity at the blade which will encourage the separation point on the top edge of the foil to move towards the trailing edge - this is indicated in Figure 2.3b by the dashed arrow. If the separation point moves beyond the trailing edge to the lower side, the opposite will happen: the top layer will shed negative vorticity and encourage the separation point back towards the trailing edge where it will settle: this is illustrated in Figure 2.3c and is the steady state of a foil in flow at a small angle of attack. On a body with a sharp trailing edged the flow will always tend to separate at the sharp edge, and this is known as the Kutta condition. In this case the vortex sheets on the top side of the foil are longer and stronger and the lift (2.15) becomes non-zero.

2.4.3 Analytical models

The lift on a particular blade section can, in some cases, be closely approximated using analytical techniques for example 'thin airfoil theory' which assumes that the foil has zero thickness and is in two-dimensional flow. Thin airfoil theory is outlined here and given in more detail in e.g. Katz and Plotkin (2001, Ch. 5). Thin airfoil theory brings physical insight and is also a useful building block when correcting two-dimensional blade loads for three-dimensional effects.

For low angles of attack (below stall) the assumption of zero foil thickness often produces a

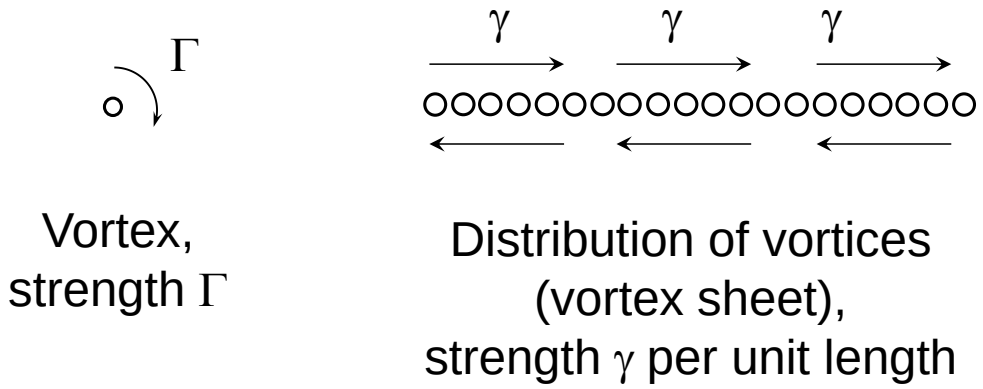

(a) *Symbols for a vortex and a distribution of vortices.*

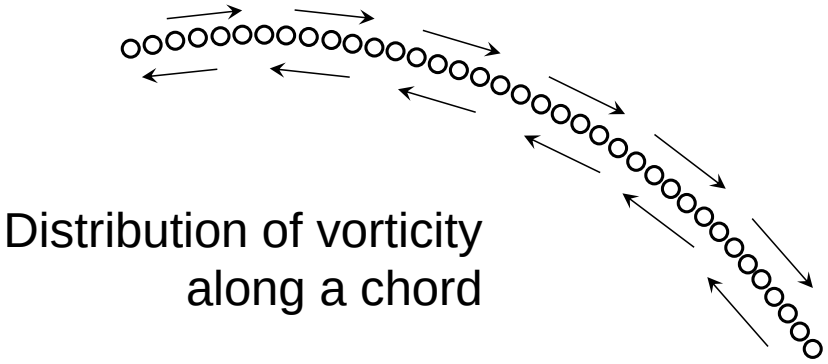

(b) *Vortices distributed along the chord, with distribution γ to meet the boundary conditions.*

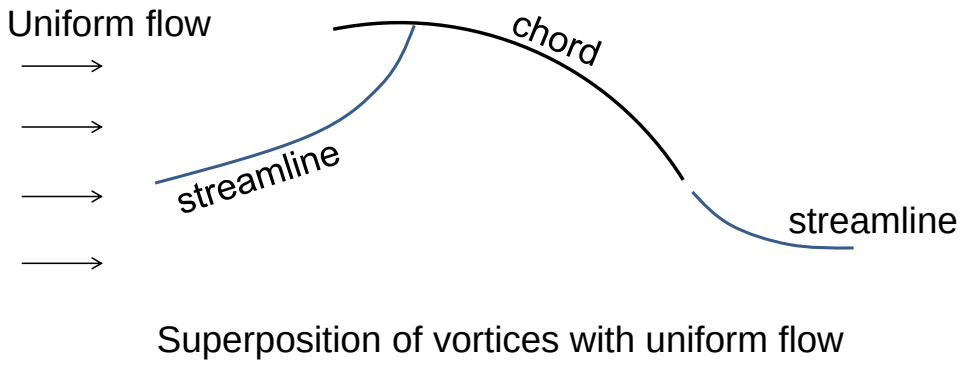

(c) *Superposition of the vortices with a uniform flow.*

Figure 2.4: *Illustrations for thin airfoil theory.*

close approximation because aerofoils and hydrofoils tend to have a small thickness compared to their chord length. Thin airfoil theory assumes zero thickness and represents the foil as a distribution of vortices along the chord line. The problem consists of finding the vorticity distribution, γ, along the chord which meets the boundary condition that there is no flow normal to the chord, and also the Kutta condition that flow stagnates at the trailing edge. The Kutta condition is necessary because the flow is doubly connected. Conceptual illustrations for this are given in Figure 2.4. For a flat plate (no camber) the vorticity distribution is classically solved using a Fourier series. The result (see e.g. Katz and Plotkin, 2001, Ch. 5) is that the centroid of vorticity is located on the chord a distance of one quarter of the chord length downstream from the leading edge; this is therefore also the point of centre of lift and the point about which the moment on the foil is zero. Thin airfoil theory produces a result which agrees fairly well with experiment, except at the leading edge where the solution is singular. The lift coefficient from the theory is

$$C_{\mathrm{L}} = 2\pi \sin\alpha. \tag{2.17}$$

where for small angles $2\pi\alpha$ is a close approximation if α is in radians. The flow field far from the foil (multiple chord lengths away) can therefore be approximated by a point vortex located at the quarter chord point and of strength

$$\Gamma = \frac{L}{\rho U} = \frac{1}{2} C_{\mathrm{L}} U c. \tag{2.18}$$

In that case the boundary condition of zero velocity normal to the chord is only satisfied at the three-quarter chord point.

An alternative way to reach the same solution is to split the blade into a finite number of 'panels', each hosting a vortex. The vortex is located a quarter of the way along each panel (known as the 'lumped vortex' method), and the boundary condition of no flow through the panel is set at the three-quarter point along the panel. For n panels there will be n vorticies (of unknown strengths) and n equations (from the boundary condition on each panel). The Kutta condition is automatically met by using this lumped vortex method. The n equations are solved using standard methods, for example the inversion of a matrix. The results agree with (2.17) but the method can be used on a more comprehensive set of problems. The simplest case of one panel yields the result in (2.17) without needing any calculations.

The simplest representation of a blade in potential flow is to use a vortex at the quarter chord point and this is most appropriate when the blades are far apart (multiple chord lengths), which is the case in tidal stream energy devices. This is the essence of the 'vortex method' for simulating turbines. The method relies on determining the blade section lift coefficient, C_{L}, either from empirical measurements or from theory, for example thin airfoil theory (2.17) or the panel method.

2.4.4 Empirical blade section data

The prediction by thin airfoil theory (2.17) that the gradient

$$a_0 = \frac{\mathrm{d}C_\mathrm{L}}{\mathrm{d}\alpha} = 2\pi, \tag{2.19}$$

where α is in radians, is a useful guide. However this becomes less accurate as the angle of attack increases. The flow on the upper side of the foil is subject to increasingly strong adverse gradients in the boundary layer: this increase in vorticity production on the top surface can cause the separation point on the upper side to move upstream. Meanwhile the flow around the underside of the foil will continue to separate at the trailing edge. The result is less lift (because there is less area over which the low net pressure is acting), and more drag. This is known as 'light stall'. Light stall can be approximated reasonably well by using boundary layer theory, although that theory is not discussed in this thesis as empirical blade data is used instead.

If the angle of attack is increased further, the separation point moves further up the foil causing a further reduction in lift and an increase in drag. Eventually, if the angle of attack becomes too high, the flow will separate near the leading edge, causing a large drag and considerable loss in lift. This is known as 'deep stall' and is relatively difficult to predict theoretically. The stall angle is highest at high Reynolds numbers because the boundary layer is turbulent, more energised, and more able to diffuse vorticity thus avoiding separation. To predict the behaviour (steady lift and drag) of blades when they stall it is common to use empirical data, for example measurements from wind tunnel tests.

Catalogues of blade section data, for example Abbott and Doenhoff (1959), are widely available and selecting the most appropriate data set(s) to use when modelling a Moonraker is now discussed, beginning with the identification of the most relevant blade section geometries. There are many standard families of aerofoil (or hydrofoil) geometries, for example the NACA four-digit series (NACA, the National Advisory Committee on Aeronautics, was the predecessor to NASA). The four digits indicate the geometry, for example: the NACA2412 indicates a maximum camber of 2% (first digit), located 40% along the chord (second digit multiplied by 10), with a maximum thickness of 12% (last two digits).

For cross-flow devices such as the Darrieus or Moonraker the blades will experience positive and negative angles of attack and therefore symmetric (uncambered) blade sections are of most interest. Any attention to cambered profiles was postponed until after the basic research with symmetric profiles is complete as it is considered second order; such research is beyond the scope of this thesis. Hence only symmetric profiles are considered here.

Among the many symmetric profiles that could be used in this research, the NACA four-digit series was used in the present research (i.e. NACA00XX where XX is the percentage thickness). This family is well defined, well researched by others, and reasonably efficient (in terms of lift and drag) so it is a natural starting point for research on a cross-flow device.

The distribution of the thickness of the NACA00XX profile is defined more completely by

Data set	NACA Profile		α	$Re_{\min}$	$Re_{\max}$
1 Sheldahl et al.	0012, 0015	2D	0-180^o	1.0×10^4	1.0×10^7
	0018, 0021, 0025	2D	0-180^o	1.0×10^4	5.0×10^6
2 Abbott and von Doenhoff	0012	2D	0-20^o	3.0×10^6	9.0×10^6
3 Critzos et al.	0012	2D	0-360^o	5.0×10^5	1.8×10^6
4 Loftin and Smith	0012	2D	0-18^o	7.0×10^5	9.0×10^6
5 Jacobs and Sherman	0012	3D	0-28^o	1.7×10^5	3.0×10^6
	0015, 0018	3D	0-28^o	4.0×10^4	3.0×10^6
6 Althaus	0012	2D	0-12^o (C_{L}) 0-9^o (C_{D})	4.0×10^4	1.5×10^5

1. Sheldahl and Klimas (1980), partly numerical (PROFILE code) partly from Wichita State wind tunnel, closed return, 0.91 m x 2.13 m 2D section with floor-to-ceiling end plates, within the main 3.05 m x 2.13 m closed section. Turbulence levels not given, 'turbulence correction factors' were used, with reference to Pope and Harper (1966).
2. Abbott and Doenhoff (1959), from NASA Langley 2D low-return turbulence pressure tunnel, closed return, 0.9 m x 2.29 m, 0.02% turbulence.
3. Critzos et al. (1955), from NASA Langley 2D low-turbulence tunnel, closed return, closed section, 0.9 m x 2.29 m, 0.03% turbulence.
4. Loftin and Smith (1949), from same facility as no. 3 above.
5. Jacobs and Sherman (1937), from NASA Langley Variable-density tunnel, closed return, closed section 1.5 m circular, 2% turbulence.
6. Althaus (1980), IAG der Universitat Stuttgart open return tunnel, closed section 0.37 m x 0.6 m, 0.08% turbulence.

Table 2.1: *Summary of relevant blade data in the literature (all except the last entry are reviewed by Gretton and Bruce, 2007).*

the polynomial equation

$$y\left(x\right) = \frac{t}{0.2} c \left(0.2969 x^{\frac{1}{2}} - 0.1260 x - 0.3516 x^2 + 0.2843 x^3 - 0.1015 x^4\right), \tag{2.20}$$

where $0 < x < 1$ is the position along the chord, and t is the maximum thickness of the foil (e.g. $t = 0.12$ for a 12% thickness).

Gretton and Bruce (2007) discuss the use of the NACA 4-digit series for modelling cross-flow tidal stream turbines and list the data available in the literature (which tends to come from research programs in aeronautics - aeroplanes and helicopter blades - and also research applied to cross-flow Darrieus wind turbines). Gretton and Bruce (2007) found that the NACA0012 profile is the section most commonly included in experimental measurements and is therefore effectively a benchmark. NACA0015 and 0018 are also fairly commonly used; these thicker profiles offer greater strength and stiffness. Increasing the thickness also increases drag and above 20% thickness the drag is significantly higher, and above 25% it is excessively high and it is unusual to use profiles above 25% thickness.

Table 2.1 lists data available in the literature for the NACA0012 and similar profiles. This table is taken from Gretton and Bruce (2007, Table 1) and the data of Althaus (1980) (which can also be found in Miley et al. 1982) has also been added. In the data from Althaus (1980) the

Re	$\alpha_{\max}$ for C_{L}	$\alpha_{\max}$ for C_{D}
4.0×10^4	11^o	9^o
6.0×10^4	16^o	10^o
8.0×10^4	16^o	10^o
1.5×10^5	15^o	10^o

Table 2.2: *Range of data available in Althaus (1980).*

maximum angle at which lift and drag are available varies slightly with the Reynolds number; at the higher Reynolds numbers a slightly larger range is available and this is given in detail in Table 2.2.

The relevant Reynolds number for the Moonraker will now be discussed, for which the chord length, c, and blade speed, ΛU, need to be approximated;

$$Re_c = \Lambda U c/\nu.$$

Unlike conventional devices, the chord of the Moonraker will not be limited by the solidity of the device (to be discussed in more detail in Section 2.6). The two limiting factors of the chord will be firstly the minimum aspect ratio of span-to-chord (to be discussed in Section 2.4.5), and cavitation (which is not discussed in detail in this thesis). Roughly speaking the blades are likely to be 20m long with a chord of about $c = 1$ m. The blade speed will be between about three and six times the flow speed ($3 < \Lambda < 6$), which is in the region of $U = 3$ m/s. Taking the kinematic viscosity of water to be $\nu = 10^{-6}$ m^2/s, this gives a rough Reynolds number of $Re_c = 10^7$.

Meanwhile, for research purposes, smaller scale devices will be required, and in particular the device described in Chapter 4 uses a NACA0015 blade with $4 \times 10^4 < Re < 2.5 \times 10^5$ - although in the experiments reported in Chapter 4 a maximum Reynolds number of $\sim 1.2 \times 10^5$ was achieved.

So data on NACA0012, NACA0015, NACA0018 is required, with $4 \times 10^4 < Re < 10^7$. Referring to Table 2.1 the data by Sheldahl and Klimas (1980) looks appropriate (and was measured for this specific purpose), as does the data of Jacobs and Sherman (1937); all of the other data is suitable for large scale modelling only, except for Althaus (1980) which is suitable for small scale only.

The data of Jacobs and Sherman (1937) includes a comment that the data is unsatisfactory, partly due to the correction from 3D to 2D, and partly due to the significant influence of the turbulence; in accordance with that comment and the review by Gretton and Bruce (2007), the data of Jacobs and Sherman (1937) was not used in this research.

The data of Sheldahl and Klimas (1980) is included in Appendix A.1 and some examples of the data are plotted in Figure 2.5. The measurements by Sheldahl and Klimas (1980) were made in a wind tunnel on NACA0009, NACA0012 and NACA0015 sections (among others), covering angles of attack of $\pm 180^o$, and at Reynolds numbers of 0.36x10^6 and 0.69x10^6. Mea-

surements over angles $-20 < \alpha < +30$ were also made on the NACA0012 at $0.86\text{x}10^6$ and $1.76\text{x}10^6$. Sheldahl and Klimas (1980) present their experimental results in graphical form, and also tabulated results from numerical predictions created using the open source prediction code PROFILE (which uses a combination of conformal mapping, vortex panels, and boundary layer theory). The numerical data is compared to the experimental data in terms of the drag coefficient at zero lift, showing reasonable agreement; however this is not sufficient to validate the data, especially at low Reynolds numbers. Hence the tabulated data from Sheldahl and Klimas (1980) - including data at the Reynolds number relevant to laboratory scale measurements - is actually just numerical predictions. The data of Althaus (1980) is experimental measurements and is included in Appendix A.1 and also plotted in Figure 2.5 for comparison.

For high Reynolds numbers the data of Sheldahl and Klimas (1980) is adequate and covers a good range of Reynolds numbers up to 5 million. For modelling at full scale, this data was used.

At low Reynolds numbers (say, $Re < 500,000$) the data of Sheldahl and Klimas (1980) shows good agreement with Althaus (1980) for drag. However the lift data of Sheldahl and Klimas (1980) is of questionable accuracy: Figure 2.5 shows that the data is not smooth, and also that the lift is very low - even negative - after stall, which is dubious.

The data of Althaus (1980) is preferable at low Reynolds number because it is from genuine physical measurements, and also on inspection the data is smooth. The difficulty with this data is that it is limited in range, both in terms of angle of attack and maximum Reynolds number.

The approach in this work was therefore to create a hybrid data-set, using the data of Althaus (1980) where possible, and otherwise using the data of Sheldahl and Klimas (1980). The exception is in the lift data in the range $15 < \alpha < 20$, where a constant lift coefficient has been used, to ensure smooth data; this is indicated in Figure 2.5 by the grey circles. Also lift at zero angle of attack was set to zero and data for negative angles of attack was neglected.

2.4.5 Three dimensional effects - theory

The previous section described lift on a blade of effectively infinite span, h, in planar flow. If the blade span is finite, with an aspect ratio of

$$AR = h/c, \tag{2.21}$$

where c is the chord, then it will have free ends and the flow will be three-dimensional. For sufficiently high aspect ratios ($AR \gtrsim 4$) then a close approximation is found by assuming that each section of the blade behaves as a section in two-dimensional flow but the inflow at each section is augmented by three-dimensional considerations, i.e. the flow caused by the three-dimensional wake. This is known as wing theory, introduced by Prandtl (1924).

Consider the bound vorticity, Γ_b on the blade to be a bundle of multiple vortex filaments, where the sum of the circulation of each vortex filament gives the total bound circulation. According to Helmholtz's second vortex theorem these vortex filaments must keep a constant

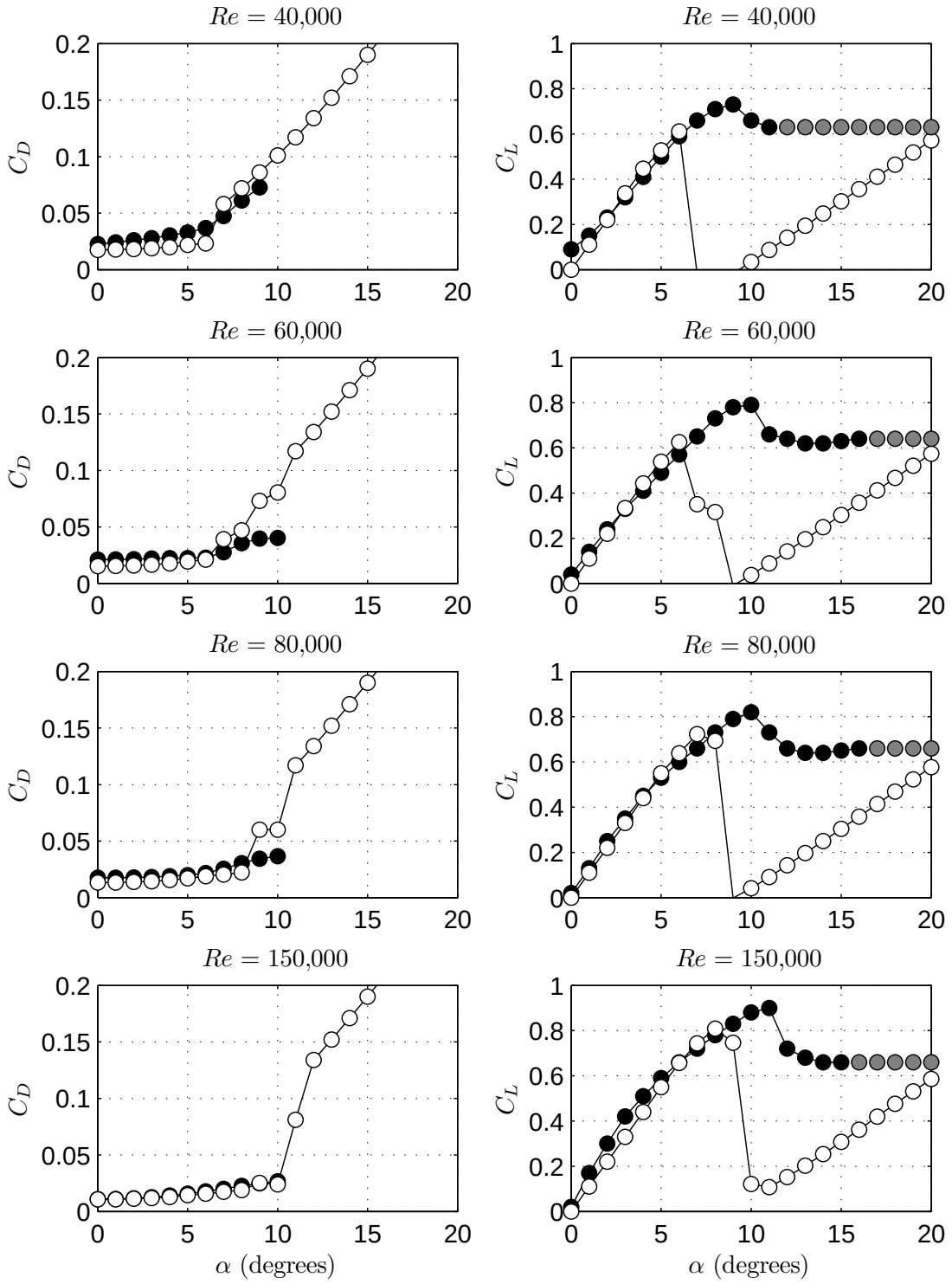

Figure 2.5: *Lift and drag on a NACA0012 blade section at low Reynolds number.*
(○) Sheldahl and Klimas (1980) - numerical results.
(●) Althaus (1980) - experimental data.
(●) Data created to join the two sets together and create a hybrid.

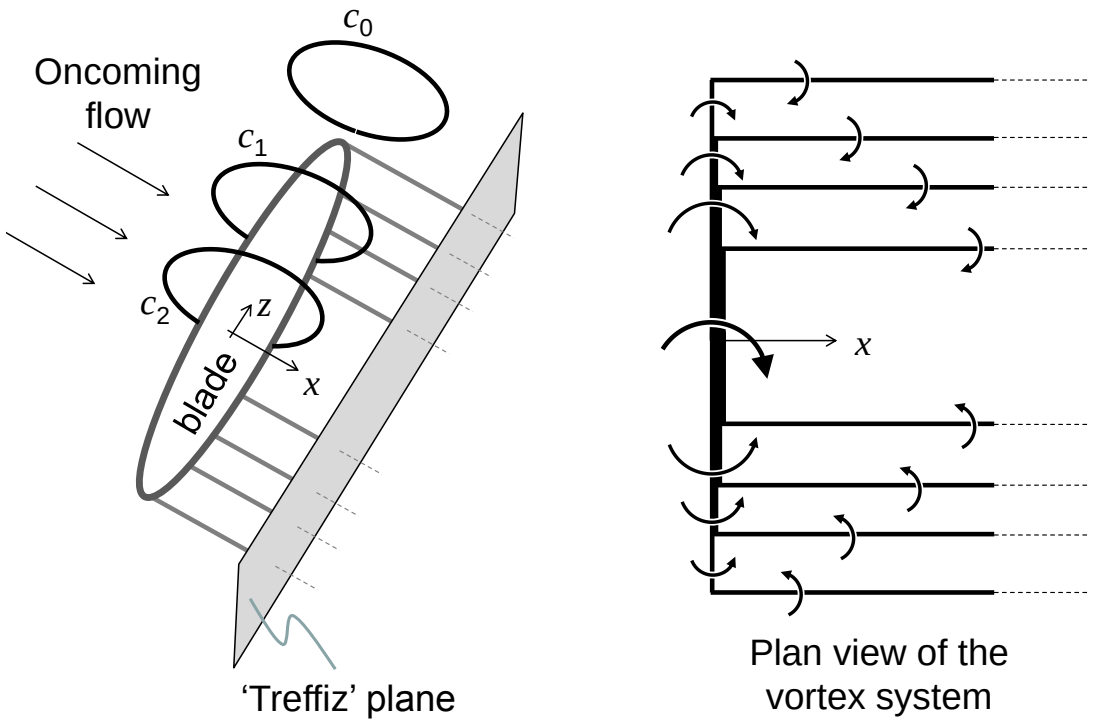

Figure 2.6: *Schematic of the vortex system of a finite wing in steady flow where the wake is assumed to be planar (its intersection with the Treffiz plane is a straight line). On the left is a blade with elliptic plan form in an oncoming flow; three closed loops, c_0, c_1, c_2 are illustrated, and vortices are shown trailing from the wing and parallel to the flow. On the right a plan view of the vortex system illustrates equation (2.22), which comes from Helmholtz's theorem that vortex lines do not end in the fluid.*

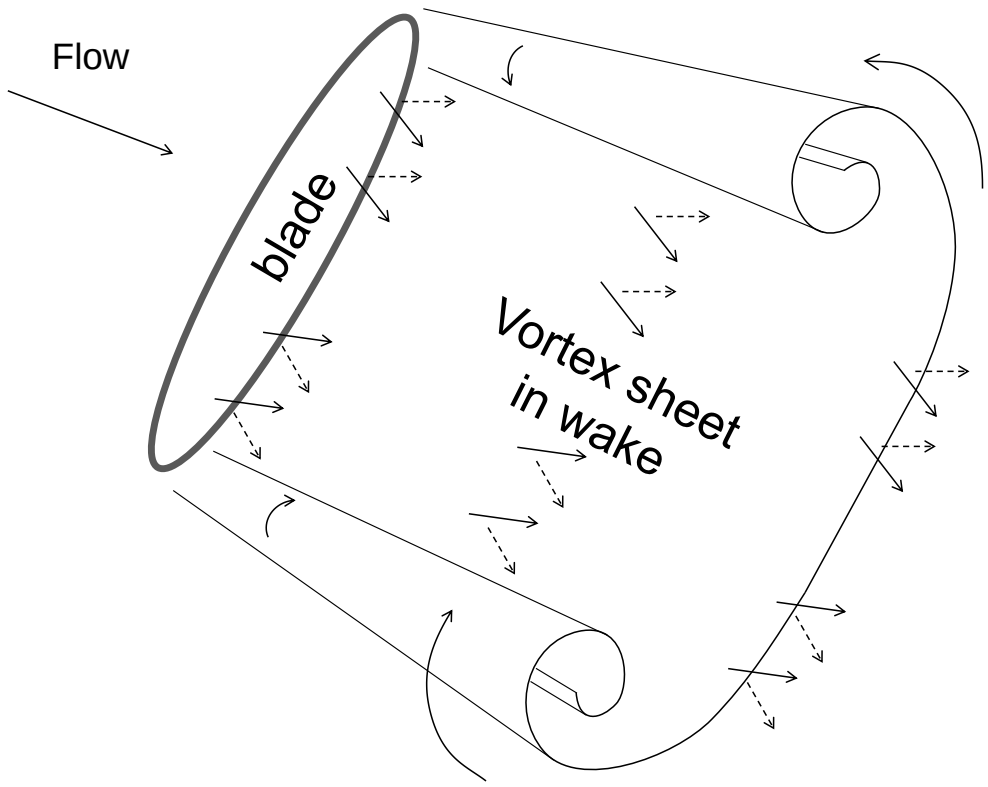

Figure 2.7: *Sketch of the vortex sheet downstream of a finite wing, with a cross-section taken in the 'Treffiz plane' normal to the oncoming flow, showing the vortex sheet curling into two spirals. Dashed arrows are the flow on the under side of the wake, solid arrows are the flow above the wake.*

circulation along their length - and therefore cannot end in the fluid. If the total circulation along the blade span reduces, then some of the filaments that were bound must become free; i.e. they cannot end in the fluid, so instead change direction and are no longer parallel to the span of the blade. These vortex filaments have become 'free' and will be advected by the flow. This is illustrated in Figure 2.6, where the closed loop c_2 encompassing the blade has some circulation Γ_2, while the circulation around c_1 is some value Γ_1; the circulation around c_0, which is beyond the tip of the wing, is zero so that the shedding of trailing vortices is inevitable in this three-dimensional system.

The vorticity which is shed into the wake is called trailing vorticity. There will be a continuous sheet of stream-wise vorticity in the wake with strength γ_t (per unit length in the z direction)

$$\gamma_\mathrm{t}(z) = \frac{\mathrm{d}\Gamma_\mathrm{b}(z)}{\mathrm{d}z}. \tag{2.22}$$

This system can be modelled as discrete trailing vortices and this is illustrated in Figure 2.6. The trailing discrete vortices have strength equal to the integral of (2.22):

$$\Gamma_\mathrm{t} = \Delta\Gamma_\mathrm{b}(z),$$

where $\Delta\Gamma_\mathrm{b}$ is the difference in bound circulation on either side of the trailing vortex, Γ_t.

The vortex system is such that most of the wake is advected downwards as it is carried downstream but near the edges of the wake the vortex system is such that the wake will curl up and this is illustrated in Figure 2.7. For small angles of attack and small lift these wake movements are not significant until far downstream ($x \gg h$) so wing theory makes the assumption that the wake is planar, as illustrated in Figure 2.6.

Trailing vortices induce a velocity at the blade known as 'down-wash', u_i, which alters the effective angle of attack of the local flow. The down-wash due to a planar wake is calculated from the Biot-Savart law (2.4):

$$u_i(z) = \frac{1}{4\pi}\int_{-\frac{h}{2}}^{+\frac{h}{2}} \frac{1}{z}\frac{\mathrm{d}\Gamma(z)}{\mathrm{d}z}\mathrm{d}z, \tag{2.23}$$

$$= \frac{1}{4\pi}\int_{-\frac{h}{2}}^{+\frac{h}{2}} \frac{\mathrm{d}\Gamma(z)}{z}. \tag{2.24}$$

The inflow at each segment is therefore augmented by the small down-wash:

$$\alpha_\mathrm{e} = \alpha - \alpha_\mathrm{i}, \tag{2.25}$$

$$= \alpha - \arctan\left(\frac{u_i}{U}\right), \tag{2.26}$$

where subscript e is 'effective' and i is 'induced' by the trailing vorticity. The down-wash causes the lift slope, $a = \mathrm{d}C_\mathrm{L}/\mathrm{d}\alpha_\mathrm{e}$, to be less than the two-dimensional value of 2π: the lift is reduced

because the effective angle of attack is less. Also, the lift force is at a different angle than it would be in two-dimensional flow: it is shifted back by an angle α_{i}. There will also therefore be extra drag associated with the lift, called 'induced' drag:

$$C_{\mathrm{D}_i} = C_{L_{3D}} \arctan \alpha_{\mathrm{i}}. \tag{2.27}$$

A numerical solution to the lift and drag distribution along the span can be found by using the 'panel' method, where the blade is split into n span-wise segments, each with a bound vortex and a trailing vortex on each side – i.e. there are $n+1$ trailing vortices. An example of this is illustrated in Figure 2.6 for seven segments where the vortex filaments are positioned at the quarter chord point.

The boundary condition on the blade is that the velocity normal to the chord must be zero (invoked at the three-quarter chord point), and for a single bound vortex the Kutta condition is automatically satisfied (as reviewed briefly in Section 2.4.3) so that there are n unknowns (bound vortex strength on each panel) and n equations from the boundary conditions on each blade. The strengths of the trailing vortices are given by (2.22). The problem is solved by standard methods; details of the method are given in Katz and Plotkin (2001, ch. 12) and are employed here.

Figure 2.8 shows the distributions of lift and induced drag along a blade with a uniform chord distribution as from calculations using 30 panels along the span and a single bound vortex on the quarter chord point. The lift is highest in the centre and drops to zero at the tips while the induced drag is maximum at the tips and minimum at the centre. The higher aspect ratio blade has a higher lift and lower drag.

This was explored by Prandtl (1924) in his 'lifting line theory', where he expresses the modified (quasi three-dimensional) lift in the following form:

$$C_{\mathrm{L_{3D}}} = \frac{a_0}{1 + \frac{a_0}{e\pi AR}} \left(\alpha - \alpha_0\right), \tag{2.28}$$

where $e \leq 1$ is some efficiency factor. This is the *mean* lift coefficient. This can be simplified for a symmetric thin foil using $a_0 = 2\pi$ and $\alpha_0 = 0$:

$$C_{\mathrm{L_{3D}}} = 2\pi\alpha \frac{eAR}{2 + eAR}. \tag{2.29}$$

The lift to drag ratio is maximised when the down-wash is uniform along the span, and this is achieved with an elliptical lift distribution (see e.g. Batchelor, 1967, §7.8) which gives $e = 1$.

The result for an elliptical lift distribution ($e = 1$) is analytical however the experimental device detailed in chapter 4 uses blades of rectangular plan-form and uniform pitch angle and for such a blade there is no closed-form analytical solution, hence the use of the panel method here.

The mean lift and mean induced drag for a range of aspect ratios are presented in Figure 2.9a

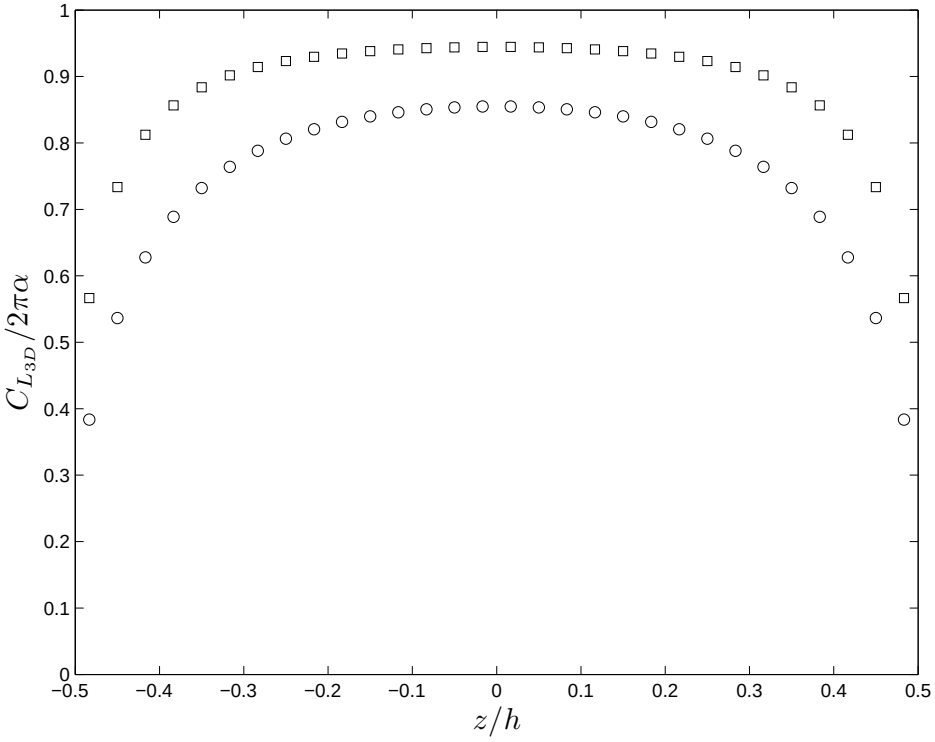

(a) *Lift.*

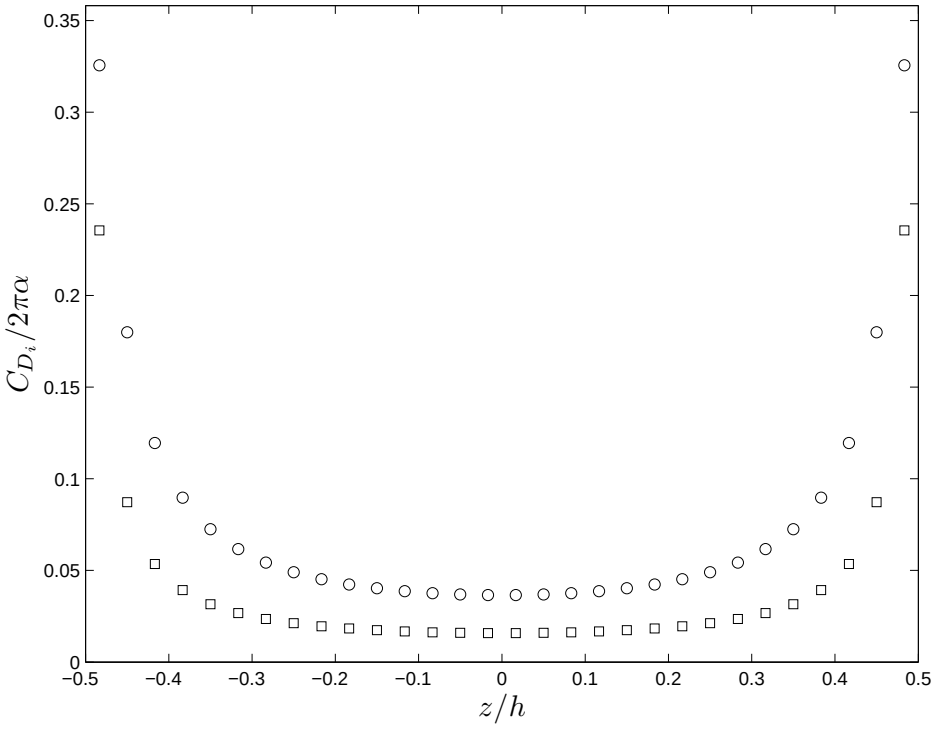

(b) *Induced drag.*

Figure 2.8: *Distribution of lift and induced drag along the span of a blade with uniform chord distribution, calculated with a single bound vortex along the span using 30 panels and assuming a planar wake. (□) - $AR = 20$, (○) - $AR = 8.33$.*

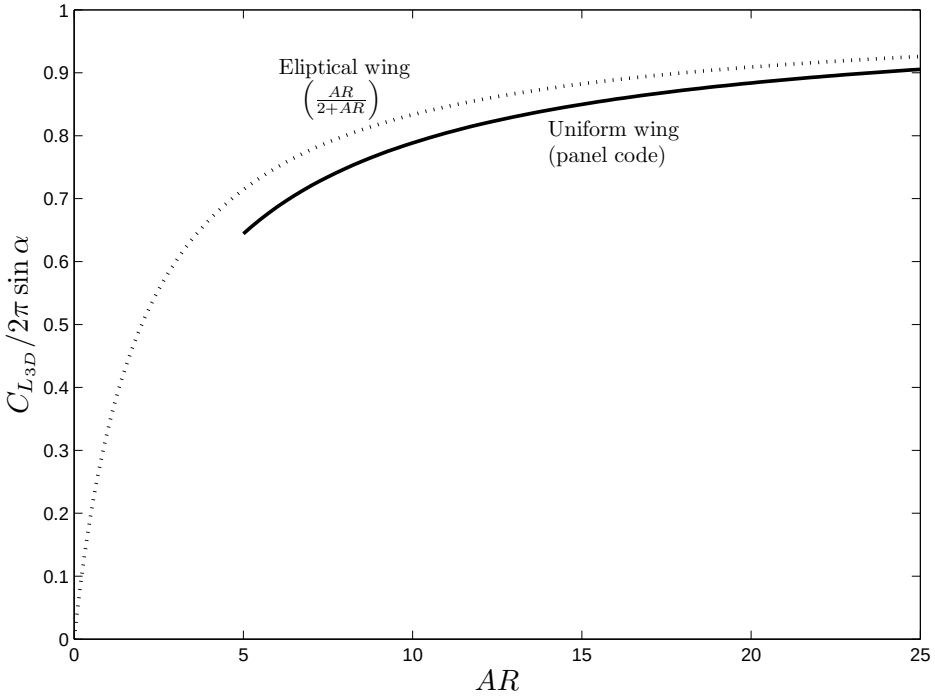

(a) *Mean lift.*

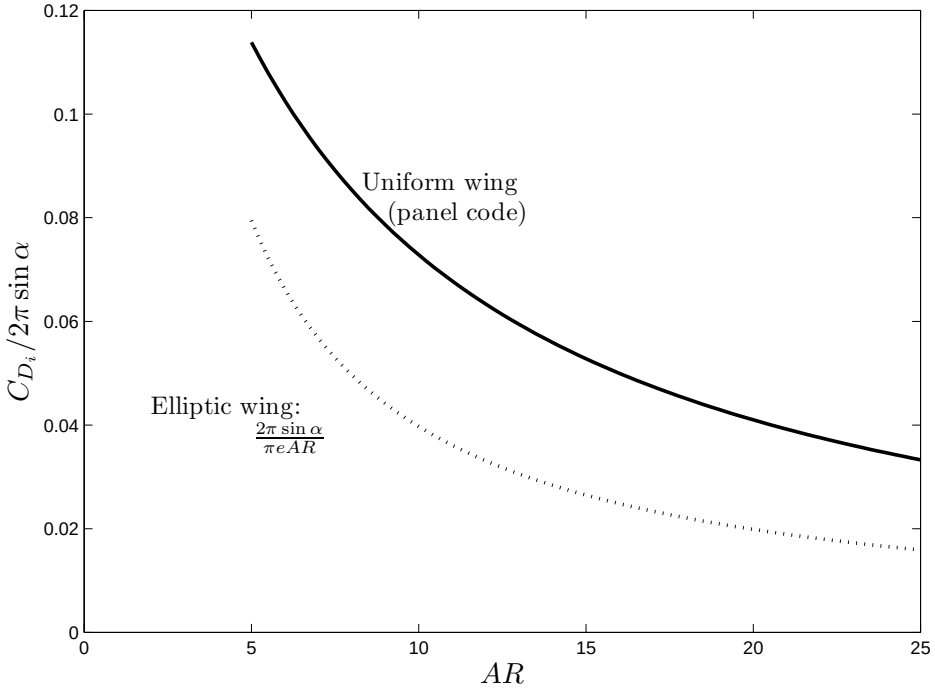

(b) *Mean induced drag.*

Figure 2.9: *Effects of a finite aspect ratio, AR, on a thin airfoil:*
· · · elliptical plan-form (Prandtl's theory),
— rectangular plan-form (numerical calculation with panels)

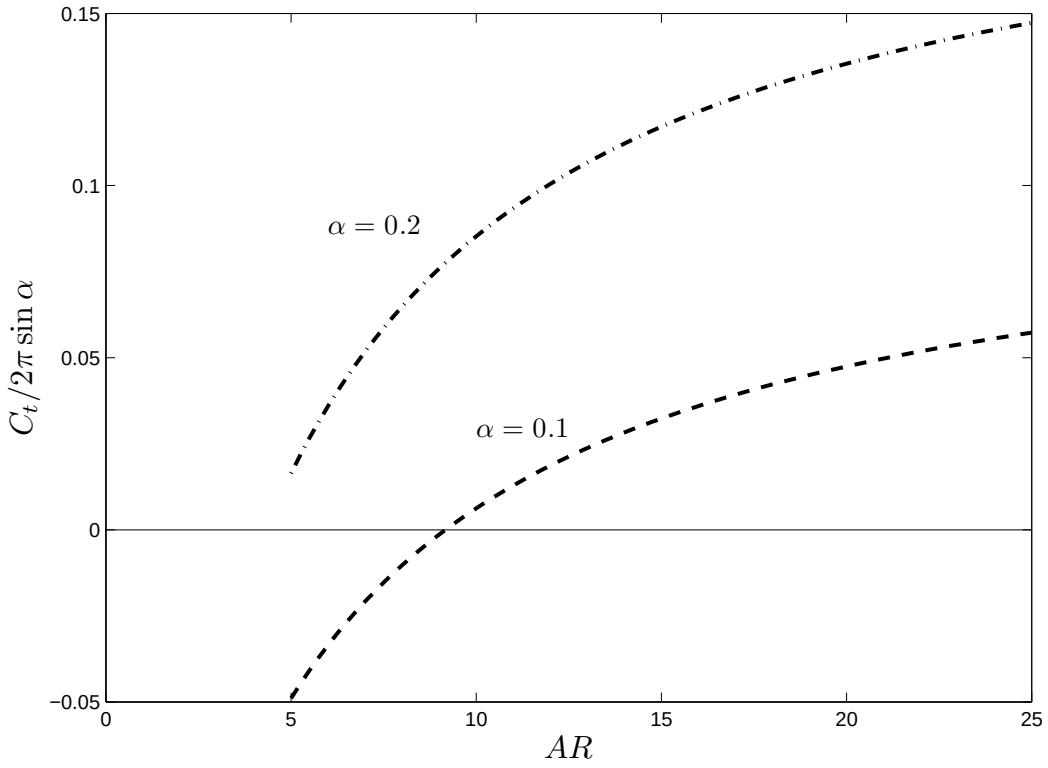

Figure 2.10: *Effect of finite aspect ratio, AR, on the tangential force ($C_\mathrm{t} = C_\mathrm{L}\sin\alpha - C_\mathrm{D}\cos\alpha$) of a thin airfoil with rectangular plan-form, calculated using the panel method:* ·-·- $\alpha = 0.2$ *rad,* - - - $\alpha = 0.1$ *rad.*

AR	$C_{\mathrm{D_i}}/2\pi \sin\alpha$
8.33	0.1036
10	0.0909
15	0.0659
20	0.0512

Table 2.3: *Notable results for $C_{\mathrm{D_i}}$ using the panel code for a wing of rectangular plan-form.*

and Figure 2.9b respectively for blades with rectangular plan-form. Results for both an elliptical and rectangular plan-form are plotted, the former from (2.29) and the latter using 20 panels. The calculated lift on a wing with rectangular plan-form is closely approximated by using an efficiency factor $e = 5/7$ in (2.29). The calculated drag on a wing with rectangular plan-form is not easily expressed analytically so for later use notable results are given in Table 2.3.

Figure 2.10 shows the tangential force coefficient (1.11) for a finite blade. The effect of finite AR on the tangential force - even neglecting profile drag - is quite dramatic. Even at an angle of attack of $\alpha = 0.1 = 5.7^o$ a wing of $AR = 8$ does not produce a positive tangential force.

In conclusion, firstly a large aspect ratio blade is desirable for energy conversion devices. Secondly for two-dimensional prediction models, three-dimensional effects of free wing tips in the fluid can be approximated by altering the lift coefficient (2.29) with an appropriate efficiency factor e, where $e = 5/7$ for $AR = 8.33$; and the drag coefficient can also be approximated using the data in Table (2.3).

2.4.6 Three dimensional effects - implementation in models

For blades with a finite length, defined by their aspect ratio $AR = h/c$, Section 2.4.5 showed that for a thin foil

$$C_{L_{3D}} = \underbrace{2\pi\alpha}_{\text{2D lift}} \cdot \underbrace{\frac{eAR}{2 + eAR}}_{\text{3D correction}}, \tag{2.30}$$

(see (2.29)) where α is in radians. This result is important for cross-flow energy extracting devices because it shows a significant change in the blade loading compared to the use of uncorrected two-dimensional blade section data. However the three-dimensional correction (2.30) is the result of a linear analysis and includes the assumption of a planar wake. The difficulty with applying a similar correction to a model of a cross-flow energy extracting device is firstly that the wake is not even approximately planar, and secondly that the lift does not vary linearly with angle of attack (i.e. the '2D lift' term in (2.30) is different and non-linear). The validity of this correction in the case of a cross-flow device therefore requires further interrogation. This is important for the BEM model (described in Section 3.3) and the two-dimensional vortex model (described in Section 3.4).

The near wake of a blade has the greatest influence on the induced lift and drag; for a Moonraker the near wake will tend to be approximately planar (see Figure 3.8b later in the

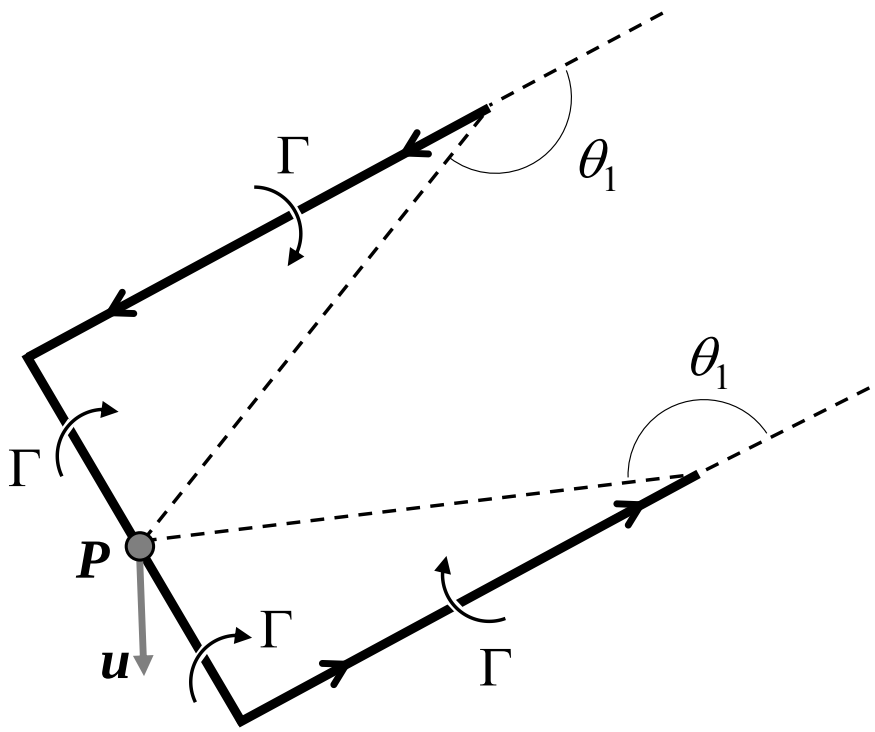

Figure 2.11: *The velocity, $\boldsymbol{u}$, induced at the centre of a blade (point, $\boldsymbol{P}$) by trailing vortices of finite length ($\theta_1 < \pi$).*

next chapter). In the model that produced (2.30) the down-wash is calculated from a pair of semi infinite vortices using (2.24) which in turn uses the Biot–Savart law (2.6) with $\theta_1 = \pi$ and $\theta_2 = \pi/2$. To explore the influence of the near wake, we keep θ_2 unchanged but reduce θ_1, as illustrated in Figure 2.11. For example if the length of the blade's wake is equal to its span then for the central section of the blade $\theta_1 = 3\pi/2$. The induced velocity in (2.24) is then $1/\sqrt{2} \simeq 70\%$ of that given by a semi-infinite wake. The '3D correction' in (2.30) would therefore be 70% (because lift is linearly related to angle of attack) of the correction for a semi-infinite wake. The remainder of the wake is still present and has the same type of effect so that the remaining 30% of the correction factor is likely to be restored as well (see in particular Figure 3.8b later to understand this) although with less accuracy regarding the geometry and therefore the influence of the far wake. Therefore the full correction should be applied but with a note that it is less accurate in the case of a blade on an energy extraction device due to the complicated and, more importantly, different wake shape.

The three-dimensional vortex model (discussed in Section 3.5) does not need a correction.

The approach used here is to apply the correction factor – the term '3D correction' in (2.30) – to the lift coefficient from empirical data, i.e.

$$C_{L_{3D}} = C_{L_{2D}} \frac{eAR}{2 + eAR}. \tag{2.31}$$

The drag coefficient also requires correction due to the 'induced' drag, $C_{\mathrm{D_i}}$, which was defined in (2.27):

$$C_{D_{3D}} = |C_{D_{2D}}| + |C_{D_i}|\,. \tag{2.32}$$

The value of C_{D_i} is taken from the calculations using the panel method described in Section 2.4.5, plotted in Figure 2.9, and tabulated in Table 2.3. In particular,

$$C_{D_i} = 0.1036 C_{L_{2D}}, \qquad \text{for } AR = 8.33. \tag{2.33}$$

There is a fundamental flaw in this type of correction when applied to a blade within a model for an energy extractor: the component of trailing vorticity which is normal to the upstream flow will induce a velocity which is also accounted for by the linear momentum theory and therefore the implementation of such corrections in any model based on combining blade element and momentum (BEM models) theory is incorrect.

Alternatively, the implementation of such corrections in a two-dimensional vortex model leads to an inconsistency because the span-wise vorticity shed into the wake is assumed to have infinite length, while the correction factor assumes that the length of the span-wise shed vortex elements are finite, hence the importance of the trailing vorticity which would otherwise be an infinite distance away and have no influence. The result is likely to be a prediction that the velocity at the rotor is reduced by more than is physically realistic, and hence a lower power coefficient would be predicted. The only way to account properly for the three-dimensional

vorticity in the wake of the device and this is the essence of the vortex model described later in the next chapter, in particular Section 3.5.

2.5 Dynamic effects on hydrofoil loading

This section considers unsteady loading on a blade. In the absence of stall the unsteady loading of a hydrofoil can be described in terms of 'circulatory' effects due to the unsteady Kutta condition and the effect of vorticity in the wake, and 'non-circulatory' effects due to fluid inertia. When boundary layer separation occurs the combination of effects are generally grouped together as 'dynamic stall' and treated separately.

In this section the inertia and circulatory terms derived by Strickland et al. (1981) for general unsteady translation and rotation of a foil without separation are presented. All of these terms appear in Theodorsen's (1935) analytical solution to the particular case of an oscillating foil; Theodorsen's (1935) solution is discussed in order to show the type of effect the unsteady terms will have on the predictions for a Moonraker, concluding that the effects are at most the same order of magnitude as the uncertainty in the empirical blade data, and therefore these corrections will not be employed. Finally, dynamic stall is discussed.

2.5.1 Inertia effects

Strickland et al. (1981) considered the inertial (added mass) effects by approximating the foil as a flat plate. Using local Cartesian axes x_f, y_f fixed relative to the flat plate, where y_f is parallel to the plate, the complex plane is

$$z = x_\mathrm{f} + iy_\mathrm{f}.$$

The plate, and therefore the origin of the complex $z-$plane, moves and rotates with respect to an inertial reference frame which is fixed in the fluid at infinity. The plate translates with respect to the inertial reference frame at a velocity expressed in the $z-$plane as

$$V = v_x + iv_y,$$

so that $|V| = \sqrt{v_x^2 + v_y^2}$ and $\tan\alpha_\mathrm{f} = v_y/v_x$. The plate rotates at an angular rate ω_f with respect to the inertial reference frame. The system described here is illustrated in Figure 2.12.

Strickland et al. (1981) derive the force on the plate as

$$X + \mathrm{i}Y = \mathrm{i}\rho\Gamma V + \frac{\pi\rho c^2}{4}\left(\omega_\mathrm{f} v_y - \mathrm{i}\frac{\mathrm{d}v_y}{\mathrm{d}t}\right). \tag{2.34}$$

where X and Y are the components of force tangential and normal to the blade's chord respectively. The first term on the right hand side of (2.34) is the steady lift and is identical to the Kutta-Joukowski relation (2.15). For unsteady flows the second term in (2.34), in brackets, is non-zero and this is the 'added mass' or 'non-circulatory' unsteady term (the first term in brackets is recognised as the added mass of a flat plate accelerating normal to its chord).

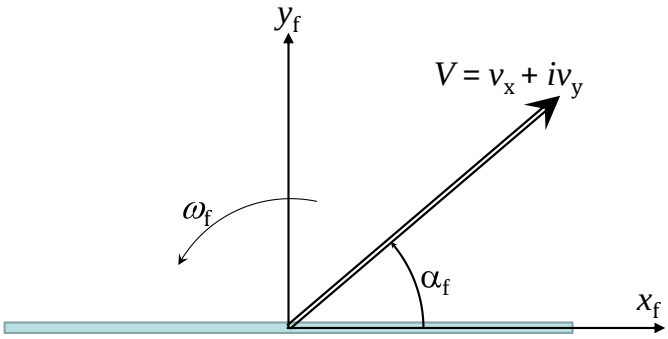

Figure 2.12: *A flat plate with local coordinate system (x_f, y_f). The plate is moving at complex velocity V with respect to an inertial reference frame fixed in the fluid at infinity. The velocity V has an angle α_f with respect to the local coordinates. The plate is rotating with respect to the inertial reference frame at an angular velocity ω_f.*

2.5.2 Bound circulation

The bound circulation in steady flow is given from the Kutta-Joukowski relation (2.15) and it is the circulation required to meet the condition that flow separates at the trailing edge:

$$\Gamma_{\text{steady}} = \frac{1}{2} C_{\text{L}} c V. \tag{2.35}$$

If the blade is rotating about the centre of the chord at a rate ω_{f} then an additional circulation will be required to ensure zero velocity at the trailing edge and this is given by Strickland et al. (1981) as

$$\Gamma = \frac{1}{2} C_{\text{L}} c V + \frac{1}{4} c^2 \omega_{\text{f}}. \tag{2.36}$$

For a discussion of the Kutta condition in unsteady flows, see Crighton (1985).

2.5.3 Circulation in the wake

A foil with a changing angle of attack tends to have a changing lift and, importantly, a changing bound circulation, $\Gamma(t)$. According to Kelvin's theorem, the conservation of angular momentum means that the total circulation in the fluid must not change; therefore any change in circulation around the foil must lead to an equal and opposite change in circulation in the body of fluid. This is manifest as span-wise vorticity being shed by the foil into its wake. This vorticity is then, according to Helmholtz's theorem, advected passively in the flow. The vorticity in the wake will affect the angle of attack at the foil. Circulation in the wake is considered in more detail in Chapter 3.

2.5.4 Oscillating foil without separation

As an example of both circulatory and inertial effects on the loading of an unsteady hydrofoil, this section presents Theodorsen's (1935) linearised analytical solution to the problem of an oscillating foil in steady uniform flow.

Theodorsen (1935) considered a linearised thin airfoil subject to small pitching and small heaving. Here we neglect heaving and consider the simple case of sinusoidal pitching: $\alpha = \sin(\omega t + \phi)$ where ω is some frequency (rad/s) and ϕ is some phase (rads). We adopt a non-dimensional frequency known as the 'reduced frequency':

$$k = \frac{\omega c}{2U}. \tag{2.37}$$

Theodorsen's (1935) solution assumes a thin foil, small oscillations, and a planar vortical wake that is advected at the free stream speed:

$$C_{\mathrm{L}} = \frac{2\pi}{U} C(k) \underbrace{\left[\underbrace{U\alpha}_{\text{steady lift}} + \underbrace{\left(\frac{3}{4} - \frac{a}{c}\right) c\dot{\alpha}}_{\text{unsteady lift}} \right]}_{\text{Circulatory}} + \frac{\pi c}{2U^2} \underbrace{\left[\underbrace{U\dot{\alpha}}_{\text{damping}} + \underbrace{\left(\frac{1}{2} - \frac{a}{c}\right) c\ddot{\alpha}}_{\text{added inertia}} \right]}_{\text{Non-circulatory}} \tag{2.38}$$

where a is the centre of oscillation and is the distance along the chord from the leading edge, and $C(k)$ is the Theodorsen function, which is a complex function. Under steady conditions $\dot{\alpha} = 0$ and only the steady lift term is present; in that case $C(0) = 1 + \mathrm{i}0$ and the steady lift $C_{\mathrm{L}} = 2\pi\alpha$ is recovered.

Theodorsen's function is defined in terms of Hankel functions, which are defined as $H_a^{(2)}(k) = J_a(k) - \mathrm{i}Y_a(k)$, where a is an integer and J_a is a Bessel function of the first kind and Y_a is a Bessel function of the second kind:

$$C(k) = \frac{H_1^{(2)}(k)}{H_1^{(2)}(k) + \mathrm{i}H_2^{(2)}(k)} = F(k) + \mathrm{i}G(k), \tag{2.39}$$

where F and G are real functions.

In the case of simple harmonic oscillation the pitch angle is defined as:

$$\alpha = \mathrm{e}^{\mathrm{i}kt} = \sin kt + \mathrm{i}\cos kt. \tag{2.40}$$

So the real part of Theodorsen's equation, $F(k)$, will affect terms that are in phase with the oscillation (the first and fourth terms in (2.38)) and the imaginary part, $G(k)$, will affect the terms that are out of phase (the second and third terms in (2.38)). The functions F and G are plotted in Figure 2.13a, and they are combined to make Theodorsen's complex function in 2.13b. The lift coefficient is plotted in Figure 2.14a where $f = Re(C_{\mathrm{L}})$ and $g = Im(C_{\mathrm{L}})$. The unsteady lift (2.38), is a simple harmonic of magnitude $|C_{\mathrm{L}}(k)| = \sqrt{f^2 + g^2}$ and phase

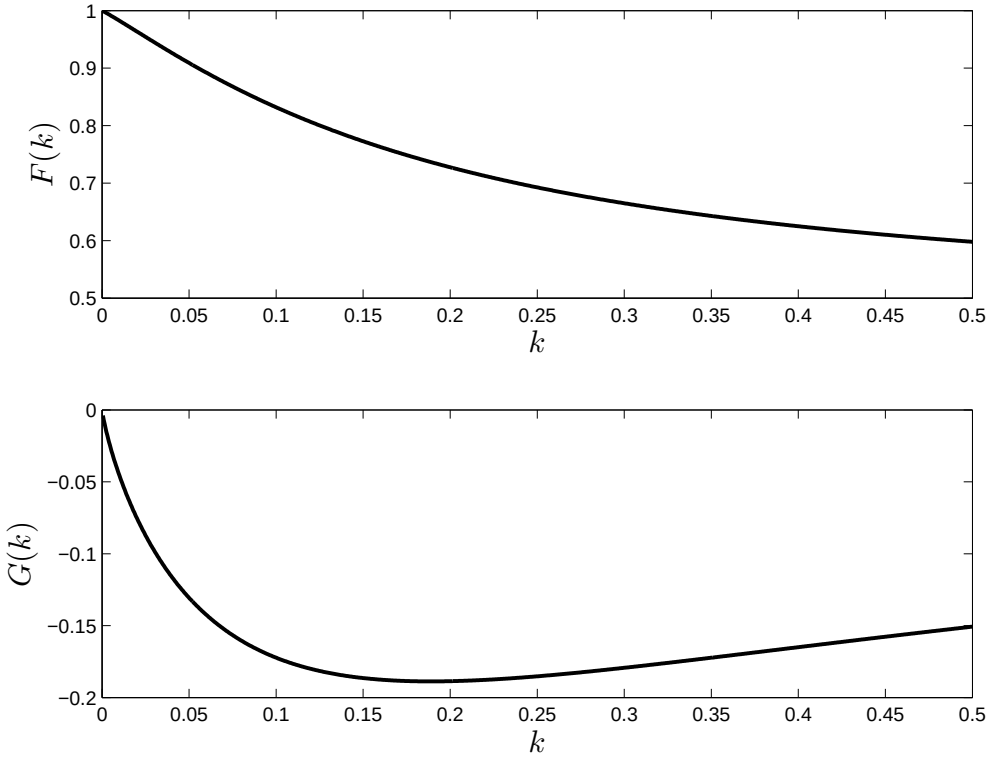

(a) *The functions F and G from (2.39).*

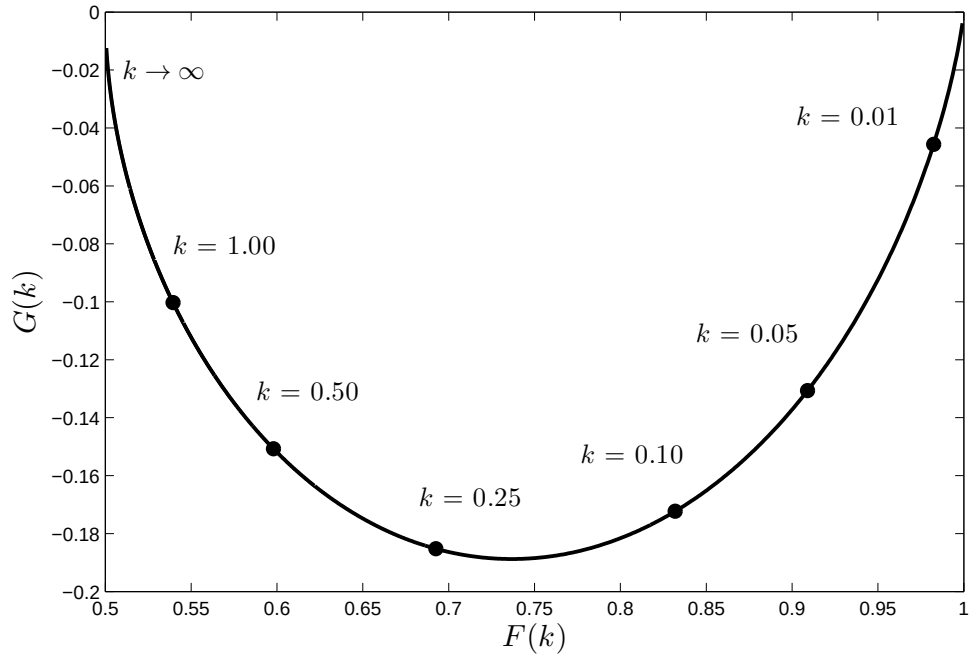

(b) *Theodorsen's function, $C(k) = F + iG$.*

Figure 2.13: *Theodorsen's model for an oscillating foil.*

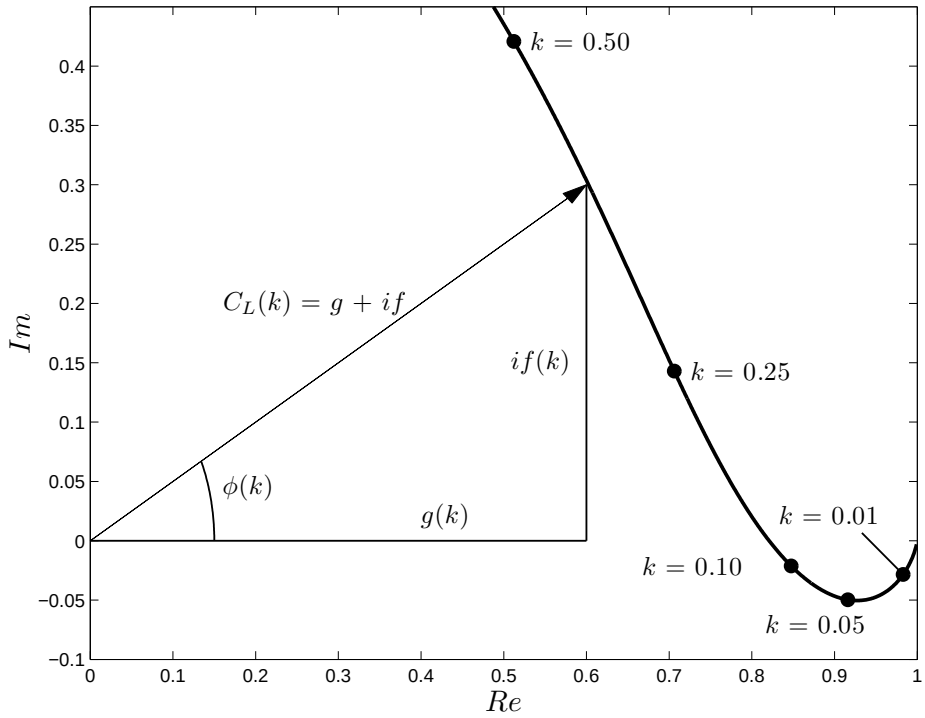

(a) Unsteady lift coefficient from equation (2.38), where $\alpha = \mathrm{e}^{\mathrm{i}kt}$.

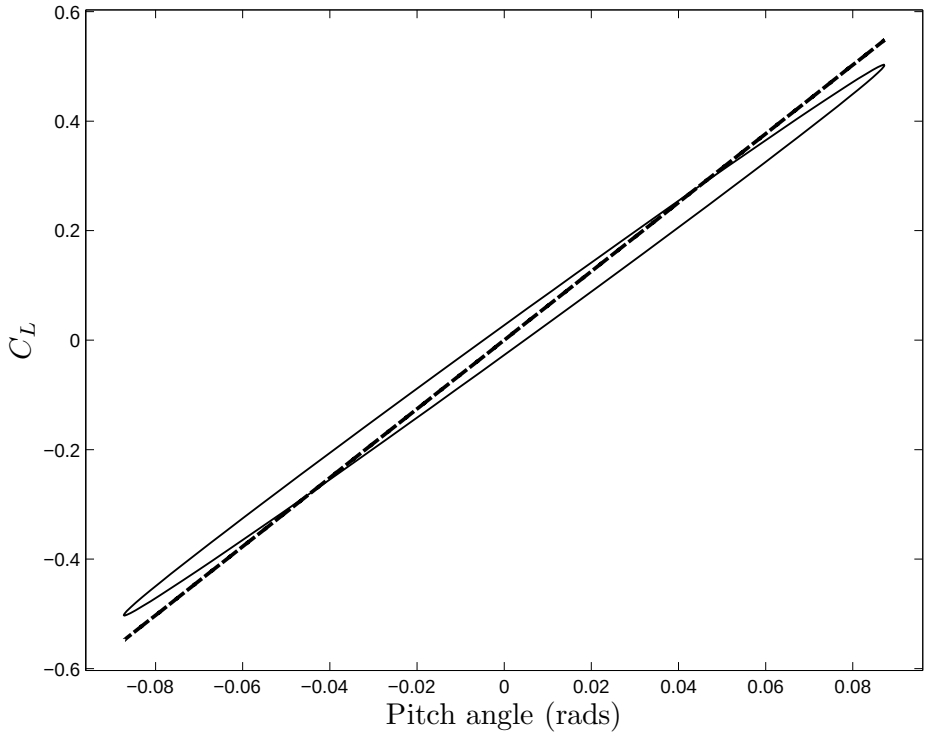

(b) Example of a reconstructed lift coefficient from (2.38) using $k = 0.05$. — Theodorsen's theory (2.38), - - - $C_\mathrm{L} = 2\pi\alpha$.

Figure 2.14: *Lift on an oscillating foil.*

$\phi(k) = \arctan(f/g)$ relative to the pitching of the foil. In the practical range of k considered here, the unsteady lift will be smaller than the steady lift. It will lag the pitch angle of blade up to $k = 0.15$, beyond which it will lead.

The lift coefficient can be reconstructed as a time series:

$$C_{\mathrm{L}}(t) = |C_{\mathrm{L}}(k)| \, \mathrm{e}^{\mathrm{i}(kt+\phi)}. \tag{2.41}$$

When the time series is combined with the pitch angle (2.40) then the $C_{\mathrm{L}} - \alpha$ plot can be recovered and an example is given in Figure 2.14b, for $k = 0.05$, showing a reduced magnitude and small hysteresis effect in the unsteady lift. The ellipse is counter-clockwise in this case, because $\phi < 0$.

For cross-flow turbines the range of relevant values of k is approximately $k < 0.2$: on a cross-flow turbine, for example a Darrieus turbine with a circular path, the angle of attack is oscillating in an almost sinusoidal manner and the reduced frequency of a Darrieus turbine is

$$k = \frac{\omega R}{U}\frac{c}{2R} = \Lambda\sigma/N.$$

Broadly speaking, for $\sigma \sim \frac{1}{6}$ and $N = 3$, we expect $\Lambda \sim 4$; for higher solidities (σ) the blade speed (Λ) will drop so that k remains similar in magnitude. These numbers are drawn from the data in Chapters 3 and 4. We therefore expect, in terms of order of magnitude, $k \sim 0.1$.

Figure 2.14a shows that in this range the magnitude of lift decreases with increasing reduced frequency; and the phase lag increases up to around $k = 0.05$ beyond which it decreases. The results are seen in Figure 2.14b which represents the most extreme effects of phase lag and a typical reduction in magnitude of the lift.

In summary, in the range of frequencies relevant to the Moonraker the magnitude of inertial effects on the lift of the blade in pure pitching is expected to be similar or less than the uncertainty of the empirical data for steady lift and drag. For this reason the vortex model used in this work neglected the terms derived in Sections 2.5.1 and 2.5.2.

2.5.5 Dynamic stall

Dynamic stall refers to the loading on an unsteady hydrofoil when the boundary layer separates. When the angle of attack is changing the process of boundary layer separation and re-attachment depends both on the angle of attack and its rate of change: it takes time for the boundary layer to separate and also to re-attach, leading to a hysteresis in the loading. The hysteresis in blade loading is illustrated in Figure 2.15, taken from Oates (1989, Ch. 7), showing the normal force coefficient, C_{n}, on the blade as it oscillates. In Figure 2.15, top-left, for small angles we see 'light stall', which vaguely resembles the un-stalled unsteady loading hysteresis curve (Figure 2.14). In Figure 2.15 top-right, for larger angles, 'heavy stall' occurs, showing a deep drop in lift before reattachment. In Figure 2.15 bottom-left, for higher angles still, a similar deep stall is evident. Finally in Figure 2.15 bottom right, for a higher frequency,

the behaviour is distinctly different. McCroskey (1982) distinguishes between 'light' and 'heavy stall' and sketches typical flow patterns, illustrated here in Figure 2.16, and the connection between the flow phenomena and the loading patterns is illustrated in Figure 2.17, taken from Carr (1988).

There are a number of models for dynamic stall, for example Gormont (1973), based on the phenomena illustrated here. The approach taken in this work, explained in more detail in Chapter 3 (in particular Section 3.6.2.5), was not to employ a dynamic stall model because of the focus on the blade's behaviour during the straight part of the track, where unsteadiness is limited. However the conclusions of this work are that dynamic stall models should be employed in any future work.

2.6 Actuator surfaces

The energy extracted by a single lifting surface in an unbounded flow is the scalar product of the force on the blade and its velocity. However if there are multiple blades, each affecting the flow around each other, then the local flow at each blade will differ from the upstream flow. A common model for this is the 'actuator surface': a permeable surface of the same area as that swept by the blades, and imposing a pressure drop on the fluid equivalent to the time-averaged effect of the blades - i.e. the loading is 'smudged' across the surface. Actuator surfaces are a standard tool in wind and tidal turbine engineering. It is common in the literature to use the term actuator 'disc' with reference to the circular projected area of a conventional wind turbine or helicopter rotor, however the term actuator 'surface' is used hereafter in this thesis because it is more general and because the Moonraker does not sweep a circular area.

In this section an actuator surface is defined and its treatment using linear momentum theory is described, followed by a review of further work on actuator surfaces. The purpose of presenting theories on actuator surfaces is that they are used in Chapter 3 in the so-called blade element momentum (BEM) model, and in more detail Chapter 5 to explore the general concept of two rows of energy extraction.

2.6.1 Formulation

Assume an unbounded planar flow, i.e. $\frac{\partial}{\partial y} = 0$, of an ideal (inviscid, incompressible) fluid where the velocity in the far field is uniform:

$$\lim_{|\boldsymbol{x}|\to\infty} \boldsymbol{U} = \frac{\mathrm{d}\boldsymbol{x}}{\mathrm{d}t} = U_\infty \hat{\boldsymbol{x}}. \tag{2.42}$$

We introduce a surface, perpendicular to the upstream flow, across which there is a uniform pressure discontinuity (energy extraction) and this is illustrated in Figure 2.18. The pressure discontinuity over the surface gives rise to a thrust force on the fluid, which is alternatively described as a rate of momentum loss of the fluid.

The surface is called an 'actuator surface' and is formulated here to be parallel to the $y-z$ plane, with infinite width in the $y-$direction, of height h in the $z-$direction, and thickness 2ϵ in

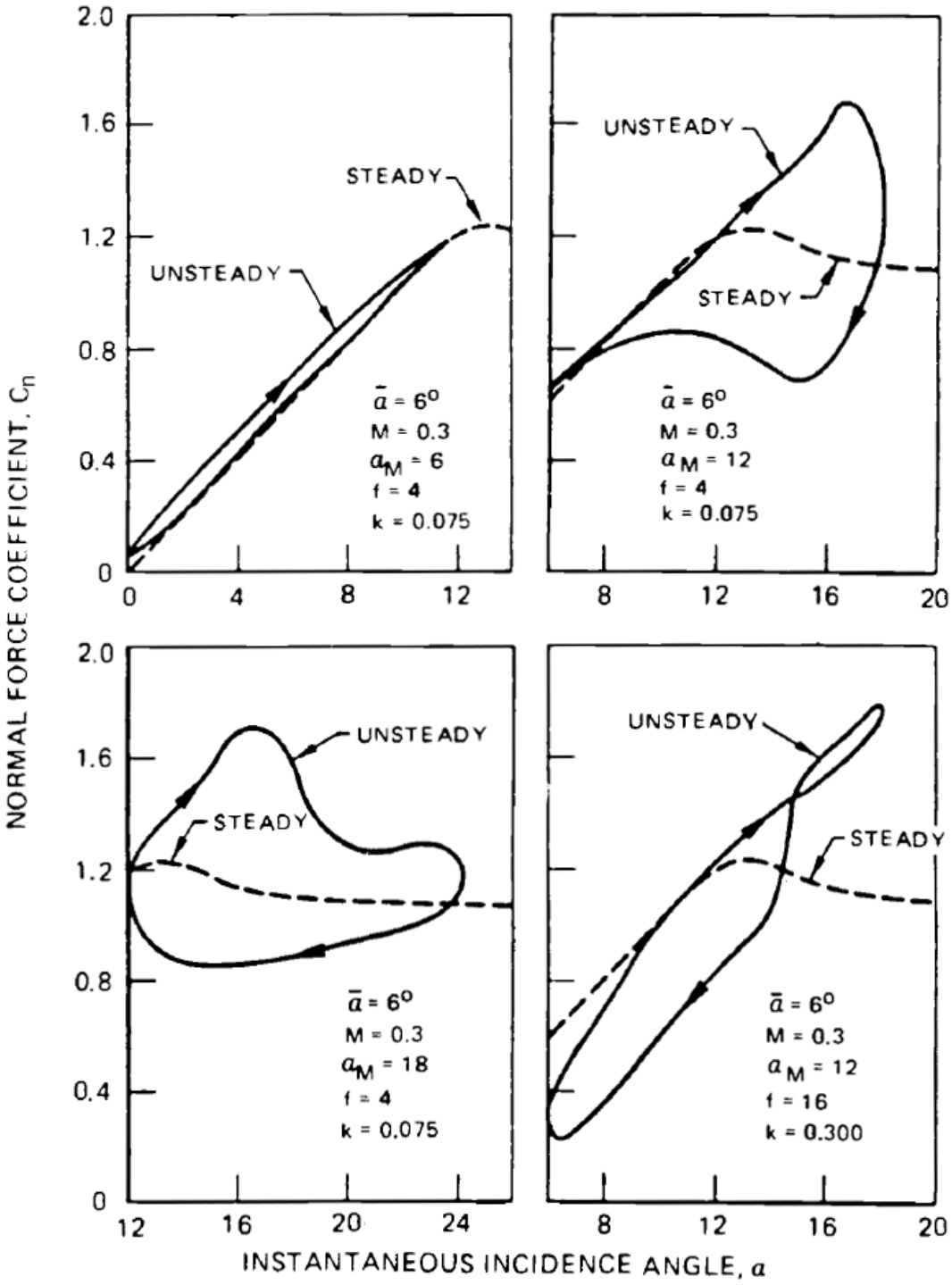

Figure 2.15: *Four examples, from Oates (1989, Ch. 7), of the normal force coefficient, C_n vs angle of attack $\alpha = \alpha_M + \overline{\alpha}\sin\omega t$, for reduced frequency, k, where M is the Mach number (not used elsewhere in this thesis).*

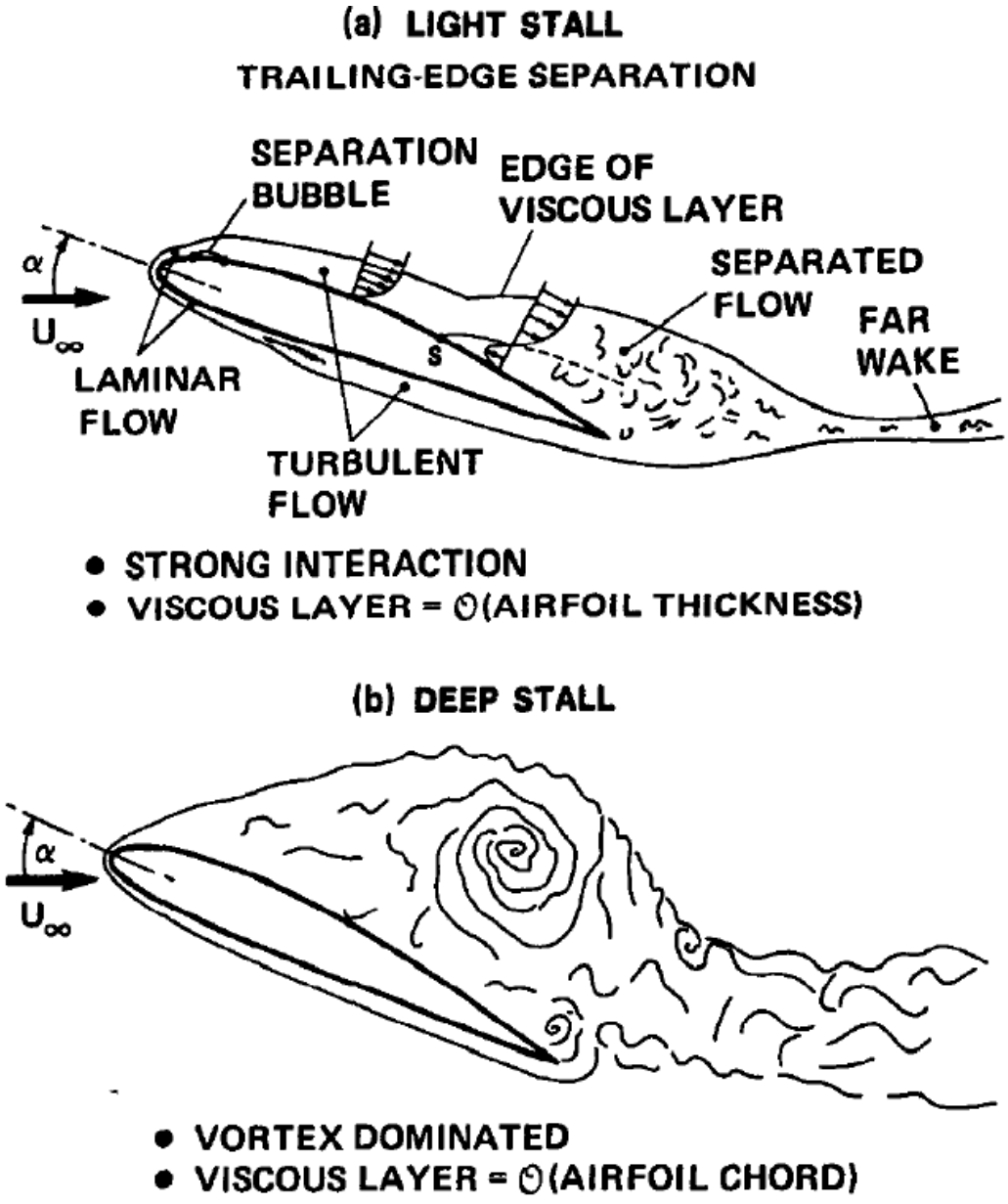

Figure 2.16: *Sketches of 'light' and 'deep' stall, from McCroskey (1982).*

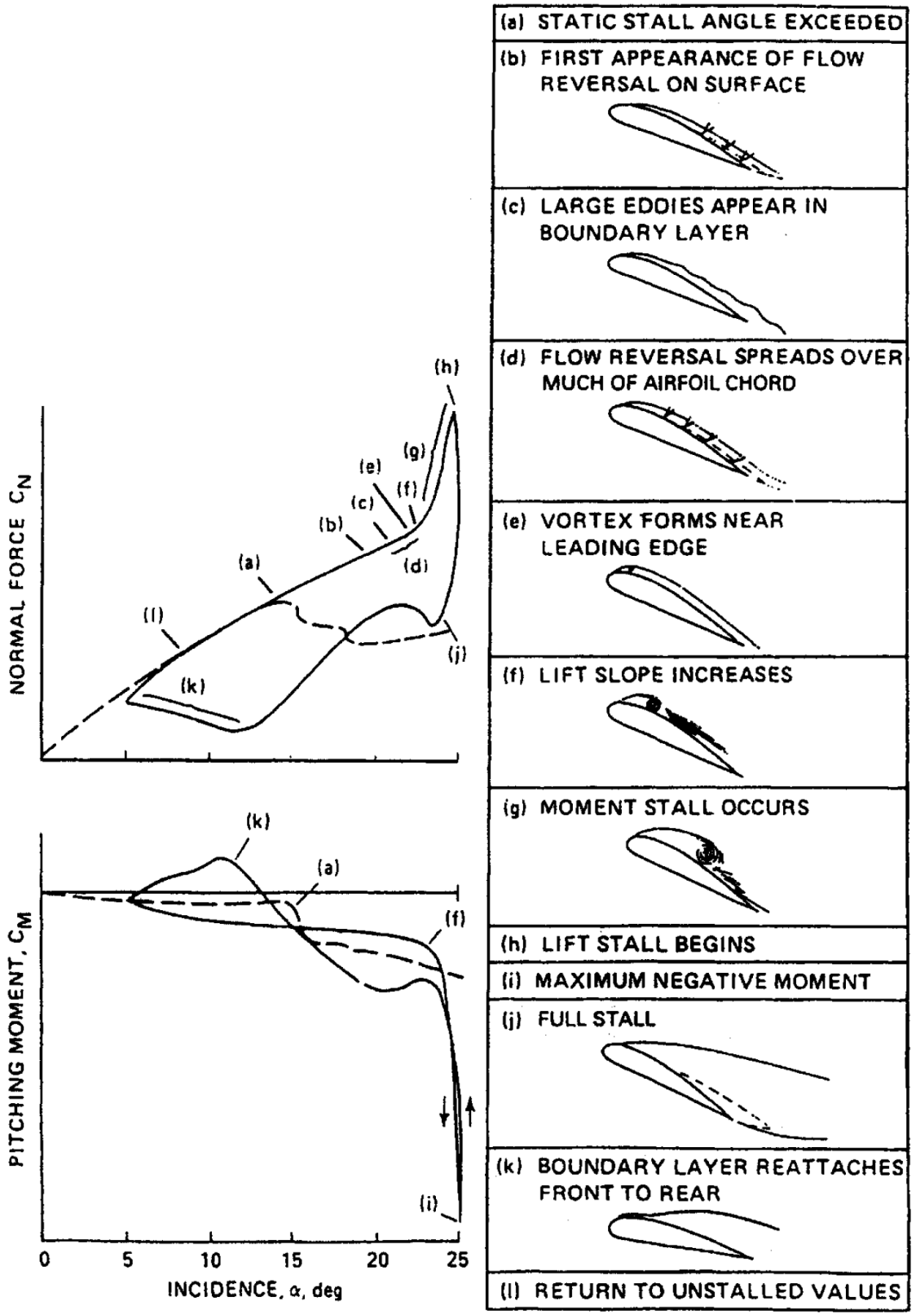

Figure 2.17: *The connection between flow phenomena and blade loading in dynamic stall, taken from Carr (1988).*

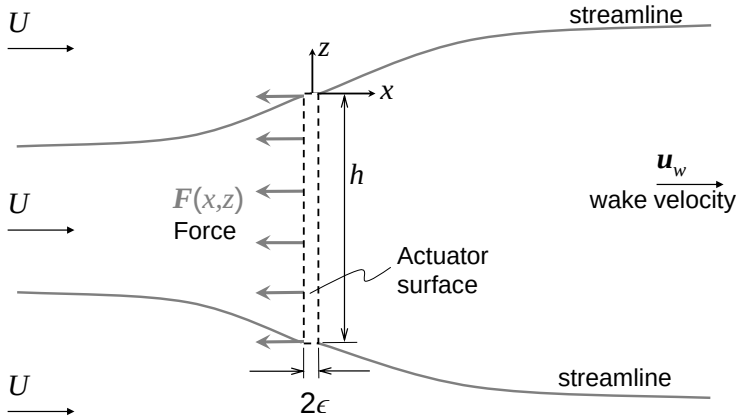

Figure 2.18: *Cross-section of an actuator surface which is normal to the upstream flow, has thickness* 2ϵ *and creates a permeable force field* $\boldsymbol{F}$ *(*Nm^{-3}*).*

the $x-$direction, sustaining a pressure drop (force per unit area) Δp. The pressure drop across the surface is coupled to the flow that it induces and is defined using the velocity normal to the surface, U_{s}:

$$\Delta p\left(t\right)=\frac{1}{2}\kappa\rho U_{\mathrm{s}}^{2}\left(t\right), \tag{2.43}$$

where κ is the dimensionless pressure drop coefficient, which defines the strength of the actuator surface. The normal velocity at the surface is taken either at the centre of the surface, or the root mean square (RMS) of the normal velocity across the surface; the choice depends on the type of analysis because the edges of the surface can have singularities.

The coupling in (2.43) between the pressure drop and the flow field it induces is representative of a typical turbine, for which the thrust (normal force) generated is approximately proportional to the square of the normal velocity, and is not strongly related to the tangential velocity component.

To represent the load on a real rotor, we assume a uniform load due solely to (2.43), i.e. neglecting tangential surface forces, and the force field, $\boldsymbol{F}$ (Nm^{-3}), generated by the actuator surface is:

$$\boldsymbol{F}\left(x,y,t\right)=\kappa\frac{1}{2}\rho U_{s}^{2}\left(t\right)\delta\left(x\right)\left[H\left(z\right)-H\left(z-h\right)\right]\hat{\boldsymbol{x}}, \tag{2.44}$$

per unit span, where δ is the Dirac-delta function, H is the Heaviside step function, and the origin is at the top of the surface. Equation (2.44) describes a force field of height h and width 2ϵ, generating a uniform, normal force of magnitude $F_{n}\left(t\right)=\int\boldsymbol{F}dx=-\frac{1}{2}\kappa\rho U_{s}(t)^{2}$, where positive κ represents an energy sink, and negative κ is an energy source.

The equations governing the fluid flow through and around an actuator surface are incompressibility and Euler's equation (with added force term) :

$$\nabla \cdot \boldsymbol{u} = 0, \tag{2.45}$$

$$\rho \frac{\mathrm{D}\boldsymbol{u}}{\mathrm{D}t} = -\nabla p + \boldsymbol{F}, \tag{2.46}$$

where $\boldsymbol{u}$ is the vector velocity field and $\frac{\mathrm{D}}{\mathrm{D}t} = \frac{\partial}{\partial t} + \boldsymbol{u} \cdot \nabla$ is the total acceleration, or 'material derivative', in a Eulerian frame of reference. Typically a tidal turbine will have a Reynolds number based on diameter of above 10^7 so that the associated flow is inertially dominated. The effect of viscosity is negligible except close to solid boundaries, i.e. on the blades. The effects of solid boundaries are accounted for by the actuator surface approximation, which represents the average forces on the blades (those forces arise due to action of viscosity in the boundary layer of the turbine blades). The important effects of viscosity are therefore accounted for in the force field $\boldsymbol{F}$ which is the last term on the right-hand-side of equation (2.46), and this effectively replaces the viscous term that would be present in the Navier-Stokes equation. The inertially dominated flow will still have the capacity to break down into smaller motions, and smaller motions again, until eventually the scale is such that viscous action is important and will dissipate energy. However, the assumption here is that the time scale for this energy cascade (turbulence) is so large that those fluid elements will be swept far from the device, do not significantly affect the flow in the vicinity of the actuator surface, and can be neglected.

We will use the vorticity equation (curl of Euler's equation):

$$\rho \frac{\mathrm{D}\boldsymbol{\Omega}}{\mathrm{D}t} = \nabla \times \boldsymbol{F}, \tag{2.47}$$

where $\boldsymbol{\Omega} = (\nabla \times \boldsymbol{u})$ is the vorticity; for two-dimensional flow, the vorticity field is a scalar and there is no stretching of vorticity.

Equation (2.47) states that vorticity generation is equal to $\nabla \times \boldsymbol{F}$. This term, the curl of the force-field, can be found from (2.44): vorticity will be shed at the strip edges, creating a pair of vortex sheets.

When an actuator surface is used to represent an energy extraction device, the thrust and power coefficients, C_T and C_P respectively, are defined as

$$C_\mathrm{T}(t) = \frac{\Delta p.S}{\frac{1}{2}\rho U_\infty^2 S} = \kappa u_\mathrm{s}^2, \tag{2.48}$$

$$C_\mathrm{P}(t) = \frac{\Delta p.S.U_s}{\frac{1}{2}\rho U_\infty^3 S} = \kappa u_\mathrm{s}^3, \tag{2.49}$$

where S is the area of the surface and $u_\mathrm{s} = U_\mathrm{s}/U_\infty$. The power coefficient, C_P, is a measure of power extraction with respect to the kinetic energy that would otherwise flow through the area S.

2.6.2 Linear momentum theory

Froude (1889) introduced the actuator surface, as described in Section (2.6.1), originally to consider ship propellers. In Froude's classical theory, an actuator surface is characterised by its induction factor, a:

$$U_\mathrm{s} = U_\infty (1 - a) . \tag{2.50}$$

Froude's concept was an extension of the work by Rankine (1865) which included an important finding about the relationship between the mean normal velocity at the surface, U_s, and the velocity far downstream in the wake, U_w. When considering only the stream-wise momentum of the fluid it is easily shown that (see e.g. Burton et al. 2001):

$$U_\mathrm{s} = \frac{U_\infty + U_\mathrm{w}}{2}, \tag{2.51}$$

which yields the thrust and power coefficients:

$$C_\mathrm{T} = 4a(1 - a), \tag{2.52}$$

$$C_\mathrm{P} = 4a(1 - a)^2, \tag{2.53}$$

The optimum C_P value occurs at $a = \frac{1}{3}$ yielding $C_{\mathrm{P}_\mathrm{max}} = 16/27$ and $C_\mathrm{T} = 8/9$. This was first shown by Lanchester (1915) and independently by Betz (1920) hence it is known as the Lanchester-Betz limit and is a useful guide for the performance of an ideal energy extractor. The remaining $\frac{11}{27}$ of the power is found partly outside of the wake due to flow diversion ($\frac{9}{27}$) and also in the energy remaining in the wake ($\frac{2}{27}$).

Taylor (1944) investigated the air-resistance of flat, very porous plates and idealised them as actuator surfaces. Taylor (1944) represents an actuator surface as a uniform distribution of centres of resistance with elemental drag (or thrust) δT per unit area. The flow outside the wake is then represented by a distribution of volume sources each of strength:

$$\delta T / \rho U_\mathrm{s}, \tag{2.54}$$

per unit area. From Newton's second law, the total resistance is equal to the momentum flow rate deficit in the wake, which in incompressible flow equates to a volume flow rate deficit. From continuity of mass means, the flow outside the wake must account for this volume flow rate deficit. A resistance according to (2.43) must therefore produce the same flow outside the wake as that by a plane of volume sources of strength:

$$m = \frac{1}{2}\kappa\rho U_\mathrm{s}^2 / \rho U_\mathrm{s} = \frac{1}{2}\kappa U_\mathrm{s}, \tag{2.55}$$

per unit area. The resulting velocity field will have components (Taylor, 1944):

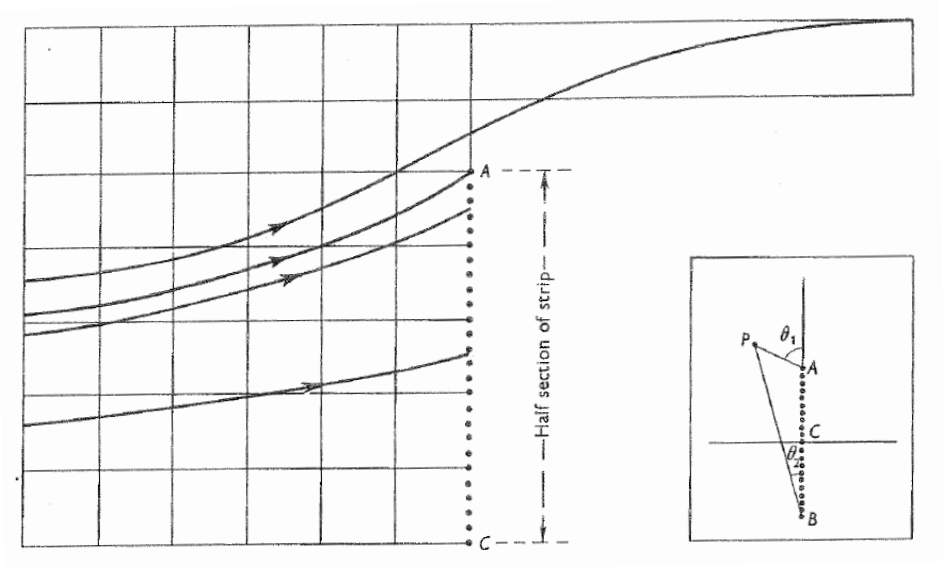

Figure 2.19: *Figure from Taylor (1944) showing streamlines around a uniform source distribution for the case of $k = 4$. The streamlines show how flow originally destined for the surface is diverted due to the surface's resistance.*

$$u_x = 1 - \frac{\kappa U_\mathrm{s}}{4\pi}\left(\theta_1 - \theta_2\right), \tag{2.56}$$

$$u_z = \frac{\kappa U_\mathrm{s}}{4\pi}\ln\left(\frac{\sin\theta_1}{\sin\theta_2}\right), \tag{2.57}$$

with θ defined as in Figure 2.19. The velocity field inside the wake is not valid, because mass is not conserved across the actuator surface (Koo and James, 1973).

At the actuator surface, i.e. $\theta_1 = \pi$ and $\theta_2 = 0$, there is a flow away from the plate with speed $\frac{1}{4}\kappa U_\mathrm{s}$. When superposed with an upstream flow, $U_\infty = 1$, this yields an expression for the flow at the plate:

$$U_\mathrm{s} = 1 - \frac{1}{4}\kappa U_\mathrm{s}, \tag{2.58}$$

$$U_\mathrm{s} = \left(1 + \frac{\kappa}{4}\right)^{-1}. \tag{2.59}$$

Equation (2.59), from Taylor (1944) is equivalent to Froude's (2.50) and yields a relationship between the pressure drop coefficient, κ, and Froude's induction factor, a:

$$a = \frac{\kappa}{4+\kappa}, \quad \text{or} \quad \kappa = \frac{4a}{1-a}. \tag{2.60}$$

Further, we can define the thrust and power coefficients:

$$C_{\mathrm{T}} = \kappa \left(1 + \frac{\kappa}{4}\right)^{-2}, \tag{2.61}$$

$$C_{\mathrm{P}} = \kappa \left(1 + \frac{\kappa}{4}\right)^{-3}, \tag{2.62}$$

which is identical to (2.53) and yields the Lanchester-Betz limit for $\kappa = 2$. Taylor's work, as well as yielding identical results to classical theory, provides information about the flow field outside of the wake (Figure 2.19).

The classical theory of Lanchester (1915) and Betz (1920) is equivalent to Taylor's theory and together they will be called 'linear momentum theory' in this thesis, which is consistent with the literature, e.g. Conway (1995).

Linear momentum theory for energy sinks becomes invalid outside the range $0 \leq a \leq 0.5$ or $0 \leq \kappa \leq 4$ where the equations break down because the flow reverses through the actuator surface. For negative values of a or κ the surface acts as an energy *source*, which is beyond the scope of this thesis.

Within the limits of the validity of Linear momentum theory, it is for lower values of a or κ, i.e. lightly loaded surfaces, that the theory is more accurate because the linearisation is less extreme. This is evident, for example, in the experiments of Taylor and Davies (1944) who used a mesh to represent an actuator surface. Meshes exert a force normal to the local flow, which for higher loading will not be parallel to the upstream flow (Conway, 1995, §6). O'Neill (2006) suggests that the assumption of a normal flow at the surface breaks down in the region of $\kappa = 2.5$ ($C_{\mathrm{T}} = 0.95$). The validity of linear momentum theory is discussed in more detail in Chapter 5.

2.6.3 Literature review

Since the theories of Froude, Lanchester, Betz, and Taylor, more general solutions to the problem of an actuator surface have been produced, for example for a wider range of κ, for non-uniform loading, or for unsteady effects. This section reviews work on both steady and unsteady work in the literature, with particular attention to the ability of models to study multiple actuator surfaces, and also reviews available experimental data.

Taylor and Davies (1944) performed experiments with planar metal gauzes in steady, unbounded flow. They approximated the value of κ by spanning a wind tunnel with the gauze and measuring the pressure difference on either side of the gauze for various materials. They measured the drag on meshes in either air or water or both, showing that it is fairly constant with varying Reynolds number. However the spread of estimated values for κ was on the order of 5%.

Kuchemann and Weber (1953, p. 38) pose the problem in terms of the steady vortex sheets that delimit the wake. The vortex sheets are described in terms of their shape and vorticity distribution which, if both are known, fully determine the velocity field via the Biot–Savart law. The two boundary conditions along the vortex sheets are: zero normal flow (kinematic

condition), and zero pressure difference (dynamic condition). Kuchemann and Weber did not solve their general problem, however among their simplified solutions was that of the uniformly loaded actuator surface. It is shown that, outside of the wake, this solution is the same as the source distribution of Taylor (1944), and that the solution inside the wake does not agree well with experiments. It is therefore not possible to use this solution to study multiple actuator surfaces.

Castro (1971) performed experiments with a series of porous plates spanning a wind tunnel. The open area ratios of the plates are given, and the thrust on the surfaces in uniform flow is measured by two methods: pitot-static wake traverse, and a mass balance. The open area ratio, Θ, is the ratio of open area to total area of the plate, and can be used to roughly approximate the pressure drop coefficient, κ, using the approximation (Taylor and Davies, 1944):

$$\kappa = \frac{1}{\Theta^2} - 1. \tag{2.63}$$

Koo and James (1973) present a more comprehensive model for meshes of arbitrary shape and loading in a uniform two-dimensional flow in a channel. The channel has infinite length, infinite width (two-dimensional flow) and is of arbitrary height. Their model uses a non-uniform distribution of sources at the mesh and determines the source strengths based on matching conditions through the mesh: continuity of mass and energy. The fluid is split into two regions – inside and outside the wake – and the matching conditions at the mesh permit an approximate solution of the whole fluid domain. Their solution is subject to an error in the dynamic boundary condition on the edge of the wake so that there is a pressure difference across the wake edge – but the error is only up to 2%. Their model can be solved numerically and shows very good agreement with their experiments, as well as good agreement with the experiments of Taylor and Davies (1944). In the special case of the normal velocity at the surface being much greater than the tangential velocity at the surface ($u_\mathrm{s} \gg w_\mathrm{s}$), the source distribution becomes constant. This approximate model – with uniform loading – has an analytical solution:

$$C_\mathrm{T} = \frac{\kappa}{(1 + \frac{1}{2}m\kappa/U_\infty)^2[1 - Bm\kappa/U_\infty(2 + m\kappa)]^2} \tag{2.64}$$

where m is the source-strength per unit area and B is the height of the surface as a proportion of the channel height. The factor B is an expression of the 'blockage', i.e. the mesh area as a proportion of the channel area. For unblocked flow, $B = 0$, the solution is the same as Taylor's (1944). Equation (2.64) can also be recovered as follows: using Taylor's model but assuming a finite channel height, the surface has a height B as a proportion of the channel height. The source strength is given in (2.55), and equation (2.59) gives the normal velocity at the surface. Far upstream, where the streamlines are parallel, the velocity is the sum of the upstream flow and the source flow (spread uniformly across the channel area):

$$[U_\infty]_\mathrm{blocked} = 1 - \frac{\kappa U_\mathrm{s} B}{4}. \tag{2.65}$$

Substituting (2.59) into (2.65) gives

$$[\mathrm{U}_\infty]_{blocked} = 1 - \frac{\kappa B}{4+\kappa}, \tag{2.66}$$

hence the thrust, normalised with the modified upstream velocity (2.66) is:

$$[C_T]_{\mathrm{blocked}} = \frac{\kappa U_s^2}{[U_\infty^2]_{\mathrm{blocked}}} = \frac{\kappa}{(1+\kappa/4)^2\,[1-\kappa B/(4+\kappa)]}, \tag{2.67}$$

which is identical to (2.64) and can also be found in Garrett and Cummins (2007). Koo and James's method cannot describe multiple actuator surfaces without major adaptations, as it would require the introduction of a third fluid region. The problem of blockage is also addressed by Whelan et al. (2009), including accounting for the disturbance at the free surface. The results of that model show that, for practical Froude numbers the free surface blockage effect will be very similar to the rigid surface blockage effect expressed above and in Koo and James (1973) and Garrett and Cummins (2007).

O'Neill (2006) provides derivations and a comparison of the works of Taylor (1944), Taylor and Davies (1944), and Koo and James (1973), which all use similar source distribution models. O'Neill also reviews the work of Cumberbatch (1982), which provides a solution to some cases where the actuator surface is only partially permeable, however the solution is provided for a pressure drop that is proportional to the flow through the actuator surface (Darcy's law). The forces on turbine blades do not follow Darcy's law, but follow a square law as per (2.43). Howells and Waechter (1995) reach Cumberbatch's solution through simpler means and also develop a solution for a jet impinging on a mesh, i.e. subject to a square law pressure drop, but the mesh is not totally immersed in the fluid.

Madsen (1982) introduced the 'actuator cylinder' concept which is a surface of revolution designed to represent a Darrieus-type turbine, where blades follow a circular path around an axis which is perpendicular to the oncoming flow. The actuator cylinder is therefore a type of double-actuator surface. Madsen solved the inviscid, two-dimensional flow field for a prescribed pressure distribution around the infinitely long cylinder. The analysis, which assumes steady flow, is essentially that of a non-uniformly loaded actuator surface of circular shape. It is restricted to loads that are normal to the flow across the surface, i.e. the load is zero where the streamlines are parallel to the surface. Madsen's technique could be used to study double actuator surfaces in general, however it was not adopted for this research because it is limited to steady flow. Further, Madsen's technique is applied to a circular surface, with non-uniform load, so that the load tends gradually to zero towards the outer sides of the cylinder. If this method were used to study flat, uniformly loaded surfaces, the velocity gradients at the edge of the surfaces would be extreme and Madsen's method may not be adapted to these extreme spacial gradients – this problem was encountered in the numerical simulations of van Kuik (1991).

Lee and Greenberg (1984) investigated the ejection of cooling water from electric power stations which amounted to analysing a uniformly loaded actuator surface in two-dimensional

ideal fluid flow. The method of Lee and Greenberg is similar to that of Kuchemann and Weber (1953); a numerical method is developed which iteratively solves the shape and vorticity distribution of the vortex sheets that delimit the wake. Although their analysis applies to an energy source, it is valid for an energy sink. Lee and Greenberg provide a helpful tabulation of their results, which aids comparison. It is conceivable that their method could be adapted to multiple actuator surfaces (if they are energy sinks), although this was not pursued due to the steady-state nature of the solution.

Van Kuik's (1991) PhD thesis, *On the Limitations of Froude's Actuator Disc Theory*, is a critical analysis of the classical theory outlined in Section 2.6.2 of this thesis. Van Kuik's key observation is that classical theory provides a consistent undeprediction of velocity at the surface, for both energy sources and energy sinks. This under prediction is with respect to more accurate models including those of Lee and Greenberg (1984) and Madsen (1982), as well as his own rotor experiments. His conclusion is that there is an edge force on the actuator surface which is normal to the local flow (so does no work) and whose absence in the classical model makes it an inconsistent model. The effect of the edge force is to concentrate the flow, hence a higher velocity at the surface. The addition of this edge force improves predictions - but there is still an under prediction.

Van Kuik (1991) goes on to study the steady flow field of a uniformly loaded actuator surface (in both 2D and axisymmetric-3D) using a finite element calculation with increasing Reynolds number, in order to extrapolate the inviscid solution. Results show a 3.5% increase in velocity at the surface compared to classical theory, which is similar to the 4% increase he found in experiments.

Finally, van Kuik (1991) rigorously explains the origin of vorticity in an inviscid flow, and also investigates the nature of the singularity at the edge of the actuator surface. The singularity is a semi-infinite spiral which provides an edge force but of unknown (and possibly zero) magnitude, hence the edge forces are an issue still to be resolved. A point vortex is a useful approximation for the spiral vortex (Moore, 1974).

Many parts of van Kuik's research have been helpful in forming the present research. For further details about actuator surfaces generating vorticity in an inviscid fluid, see van Kuik (2004b). For more on the edge singularity, see van Kuik (2003; 2004a; 2009).

Conway (1995) provides an analytical solution to a circular actuator surface of arbitrary non-uniform loading, including the special case of a uniform load which corresponds to that studied by Lee and Greenberg (1984) and Kuchemann and Weber (1953). The variation in width of the wake downstream is accounted for in Conway's approach, though most of the solutions are for the linearised actuator surface. The solution does not include the case of multiple actuator surfaces. It could conceivably be adapted to do so, but this would only be a steady state solution, hence this course was not pursued as part of this research. Although Conway's solution includes all 'heavy loads' (subject to incompressibility assumptions), it is considered as an energy source, not sink. In the case of a heavily loaded energy sink, the recirculating flow in the wake (the propeller brake state) may not be captured by Conway's method.

Harrison (2011) used a commercial Reynolds-Averaged Navier-Stokes solver (CFX) to solve the flow field associated with a single actuator surfaces and multiple actuator surfaces. Harrison (2011) used a uniformly loaded actuator surface as formulated here, and also a circular surface whose load is determined by blade element data. Harrison (2011) systematically varied the parameters of the simulation, and the turbulence model used, to investigate the accuracy of the RANS model. Experimental velocity measurements in the wake of a steel mesh in water flumes were used to validate the RANS model and the principal comparison was the velocity along the centreline in the wake. When ambient turbulence was low, the RANS model predicted velocities within $<3\%$ of the experimental values, with the error attributed to discretisation error. For higher ambient turbulence, the error was 9% and the necessary higher resolution to reduce this accuracy was stated to be impractical.

2.6.4 Unsteady actuator surfaces

Sorensen and Kock (1995) generated a numerical solution to the unsteady Navier-Stokes equations for an axisymmetric fluid domain which included an actuator surface. The loading of the circular actuator surface, which represented a wind turbine, was determined by blade element data and a prescribed turbine configuration i.e. the solidity and the distribution of chord vs radius. It is therefore a simulation of a non-uniformly loaded actuator surface whose loading is coupled to the flow field it induces. This type of analysis could be used to study multiple actuator surfaces – see Mikkelsen et al. (2007), below. In a later paper Sorensen et al. (1998) performed a similar analysis but for an actuator surface with fixed loading, i.e. not coupled to the flow they induced. This was to study wake states for comparison with classical theory.

Mikkelsen et al. (2007) simulated axial-flow wind turbines using the actuator line technique coupled with an unsteady Navier-Stokes solver using large eddy simulation (LES). The study focuses on the effect of an upstream wind turbine on a downstream turbine. This analysis could be simplified and used to study the effect of two generic actuator surfaces on each other.

With modern computational fluid dynamics (CFD) widely available there is a wealth of literature, such as the above two examples, showing solutions to particular problems such as wind turbines or actuator surfaces, in both steady and unsteady flow. Research into helicopter aerodynamics makes extensive use of actuator surfaces in CFD (for example Le Chuiton, 2004). An exhaustive review is not included here. In summary CFD could be used to investigate double actuator surfaces but optimisation is required for a range of parameters and this would be too computationally expensive.

2.7 Double actuator surfaces

Figure 2.20 illustrates double actuator surfaces, i.e. an additional surface sits in the wake of the first surface. In this scenario the normal velocities at the upstream and downstream surfaces, U_1 and U_2 respectively, will be functions of the upstream pressure drop coefficient,κ_1,

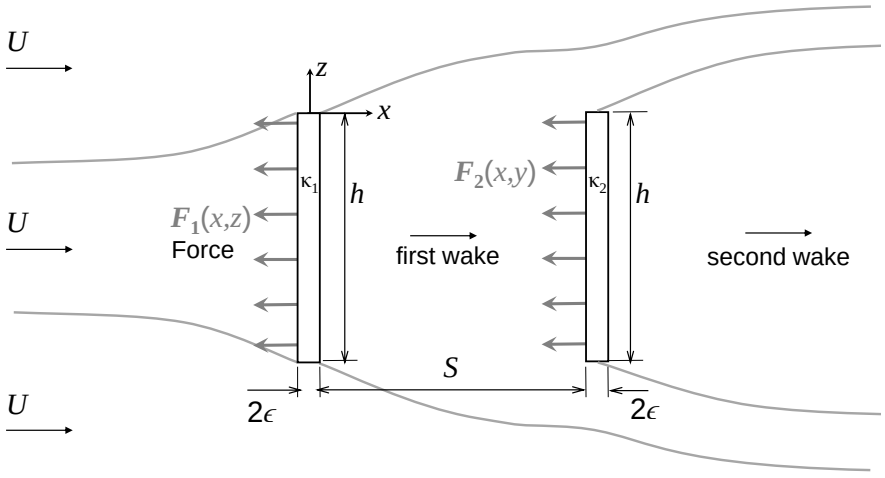

Figure 2.20: *Double actuator surfaces normal to the upstream flow.*

the downstream pressure drop coefficient, κ_2 and the streamwise spacing between the surface, S. By non-dimensionalising the spacing with a length representative of the lateral size of the actuator surface, l:

$$s = S/l,$$

we have

$$\begin{aligned} U_1 &= f(\kappa_1, \kappa_2, s), \\ U_2 &= f(\kappa_1, \kappa_2, s). \end{aligned}$$

Depending on the streamwise spacing, s, there are some solutions for double actuator surfaces while other cases remain unsolved. These available solutions for double actuator surfaces are illustrated with examples in Figure 2.21 and each case will now be discussed.

2.7.1 Coincident surfaces

In the limit $s \to 0$ the surfaces will be coincident and they will experience the same velocity field:

$$\lim_{s\to 0} U_1 = U_2 = U_\infty \left(1 + \frac{\kappa_1 + \kappa_2}{4}\right)^{-1}, \tag{2.68}$$

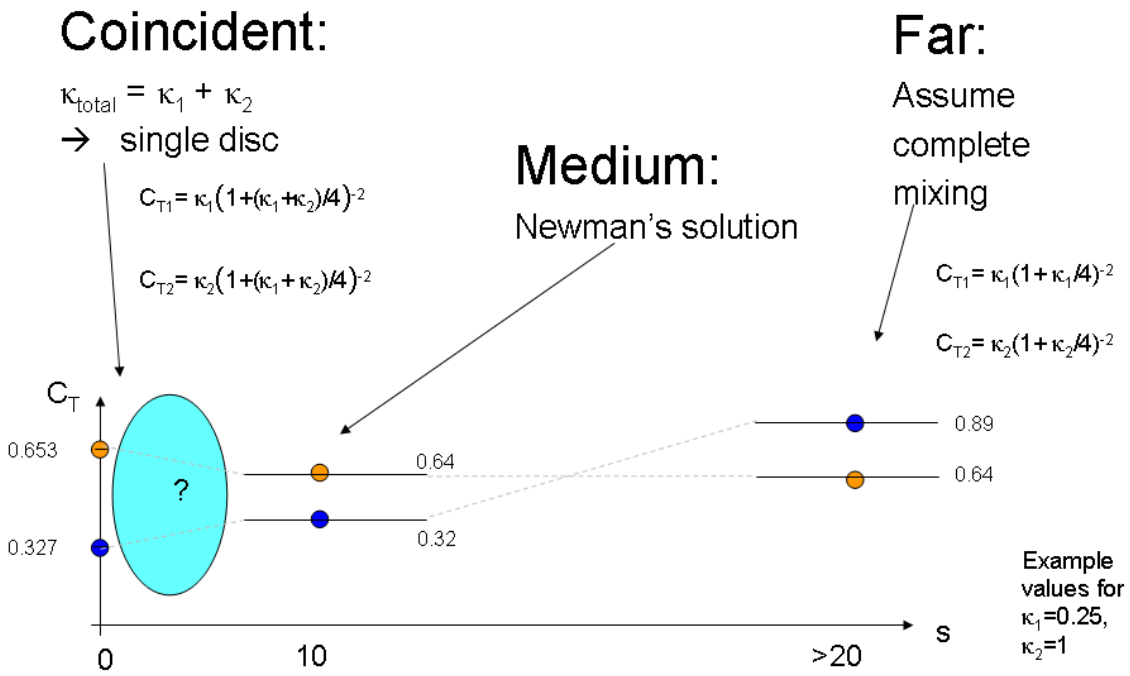

Figure 2.21: *Thrust on tandem actuator surfaces of separation $s = S/l$ where l is the lateral size of the actuator (e.g. h). Three solutions are readily available: coincident ($s \to 0$), medium distance ($1 \lesssim s \lesssim 15$), and large distance after mixing ($s \gtrsim 25$). There is no obvious solution for $0 < s < 1$.*

in which case each surface will experience a thrust:

$$C_{T_1}|_{s=0} = \kappa_1 u_1^2 = \kappa_1 \left(1 + \frac{\kappa_1 + \kappa_2}{4}\right)^{-2}, \tag{2.69}$$

$$C_{T_2}|_{s=0} = \kappa_2 u_2^2 = \kappa_2 \left(1 + \frac{\kappa_1 + \kappa_2}{4}\right)^{-2}, \tag{2.70}$$

where $u_1 = U_1/U_\infty$ and $u_2 = U_2/U_\infty$.

2.7.2 Surfaces in 'close' proximity

There is no known solution to this problem and it is identified by the question mark in Figure 2.21. Chapter 5 researches this problem. The approach in those chapters is to use a point vortex representation of the vortex sheets that define the flow field, and to validate these calculations with physical measurements of the drag on steel meshes.

2.7.3 'Medium' spacing

There is a range of spacing, which will be called 'medium' spacing, where an analytical solution is available and was first presented by Newman (1983). We introduce a length scale, l, to denote the diameter or height or width of the actuator surfaces: in the range $1 \lesssim s \lesssim 10$ the second surface will sit in the wake of the first surface. Newman suggested that, in this medium range of actuator surface spacing, the downstream surface will effectively experience an 'upstream flow' speed that is equal to the speed in the wake of the upstream actuator surface. This assumes that the downstream wake is no longer expanding in width, and that the downstream action will not affect the upstream action. The first of these assumptions was validated by Newman (1983) by visualising flow in a wind tunnel with gauzes positioned accordingly. The streamlines between the gauzes were shown to be parallel when $s > 2/3$. For distances $s > 10$ the wake will have broken down and the downstream surface will experience a complex, turbulent flow (e.g. Huang and Keffer 1996, Harrison et al. 2009, Rethore et al. 2009).

Using Newman's assumptions the performance of each momentum sink can be derived; given the classical result that the speed normal to the surface is the average of the upstream and wake speeds, we can express the wake speed as:

$$u_{\text{wake}_1} = \left(\frac{1}{2} + \frac{\kappa_1}{8}\right) - 1. \tag{2.71}$$

The downstream surface therefore has a normal velocity of:

$$u_2 = \left(2\left(1 + \frac{\kappa_1}{4}\right)^{-1} - 1\right)\left(1 + \frac{\kappa_2}{4}\right)^{-1}. \tag{2.72}$$

Thus the contributions to the thrust from each actuator surface are:

$$C_{\mathrm{T}_1} = \kappa_1 u_1^2 = \kappa_1 \left(1 + \frac{\kappa_1}{4}\right)^{-2}, \tag{2.73}$$

$$C_{\mathrm{T}_2} = \kappa_2 u_2^2 = \kappa_2 \left(2\left(1+\frac{\kappa_1}{4}\right)^{-1} - 1\right)^2 \left(1+\frac{\kappa_2}{4}\right)^{-2}. \tag{2.74}$$

Power is equal to thrust multiplied by velocity, and it can easily be shown that the power is optimised when $\kappa_1 = 1$ and $\kappa_2 = 2$ giving a total thrust and power of the system of actuator surfaces of $C_{\mathrm{T}} = 0.96$ and $C_{\mathrm{P}_{\max}} = 0.64$ respectively. This is a relative increase of 8% power and 8% thrust. This result was derived by Newman (1983).

2.7.4 Very large spacing

In the limit $s \to \infty$ the wake of the first actuator surface will have completely mixed with the unbounded flow, and the second surface will experience upstream flow conditions (assuming that turbulence is negligible):

$$C_{T_1}|_{S=\infty} = \kappa_1 u_1^2 = \kappa_1 \left(1+\frac{\kappa_1}{4}\right)^{-2}, \tag{2.75}$$

$$C_{2_1}|_{S=\infty} = \kappa_2 u_2^2 = \kappa_2 \left(1+\frac{\kappa_2}{4}\right)^{-2}. \tag{2.76}$$

The distance required for mixing is dependent on the ambient turbulence, and the turbulence created by the turbine (or actuator surface); it will tend to be completely mixed by approximately 20-25 diameters downstream (Huang and Keffer 1996, Harrison et al. 2009, Rethore et al. 2009).

2.7.5 Application to the Darrieus turbine

Consider a tall Darrieus turbine, illustrated in Figure 2.22a, with a large ratio of height to width: $h \gg W$. The flow is dominated by motion in the $x-y$ plane and so a two-dimensional model in the $x-y$ plane is appropriate. In the $x-y$ plane the time-averaged effect of the blades is that of an 'actuator cylinder', as illustrated in Figure 2.22b. The upstream and downstream parts of the actuator cylinder can be simplified further as double actuator surfaces, as illustrated in Figure 2.20 except that the surfaces will be normal the $x-y$ plane, *not* the $x-z$ plane as illustrated in Figure 2.20. The length scale of each surface is $l = W$, and the surfaces are separated by $s \sim 1$ hence they have 'medium' spacing and Newman's (1983) solution can be applied. It is common to use Newman's (1983) solution to model the two rows of energy extraction in a Darrieus turbine, and this is discussed more in Chapter 3.

2.7.6 Application to the Moonraker

The Moonraker has two distinct rows of energy extraction: one is in the wake of the other as illustrated in Figure 2.23. Each row can be considered as an actuator surface, as illustrated in Figure 2.23, so that double actuator surfaces in Figure 2.20 are again relevant but this time the surfaces *will be* normal to the $x-z$ plane, as illustrated in Figure 2.20. In this case (again contrary to the Darrieus turbine) the relevant length scale is $l = h$ so that $s = S/h$. The spacing, s, on a Moonraker could be anything from $s \to 0$ to $s > 1$, i.e. anything from very close and

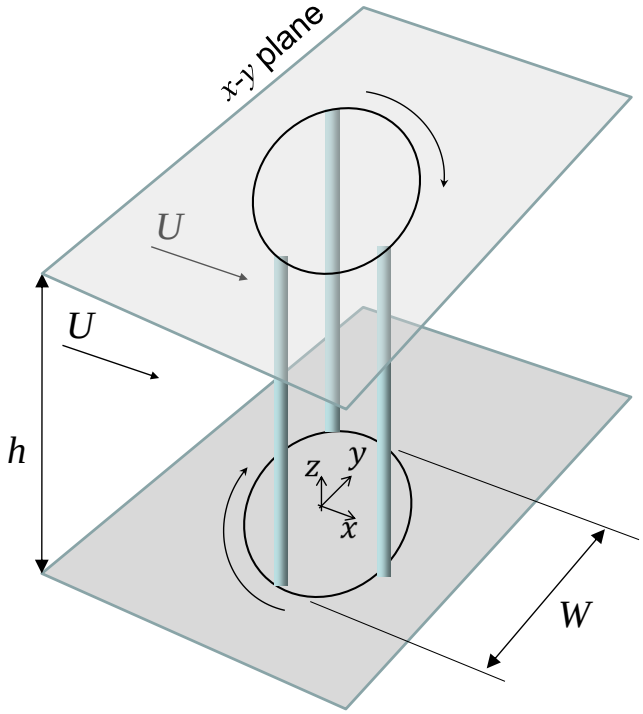

(a) *A tall Darrieus with $x-y$ planes highlighted at each end of the blades.*

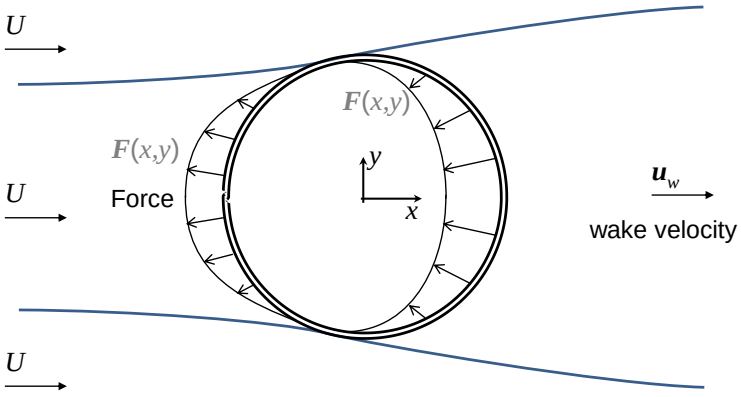

(b) *An actuator cylinder in the $x-y$ plane to represent a Darrieus turbine.*

Figure 2.22: *Approximations of a Darrieus turbine with $h \gg W$.*

effectively coincident spacing, to close proximity, to medium spacing. In practice, the spacing is likely to be finite but small, i.e. the rows will be in close proximity and the Moonraker cannot easily be modeled as double actuator surfaces without further solutions being developed. The approach to modeling the Moonraker in this thesis is therefore as follows:

- A single actuator surface and blade element momentum (BEM) theory will be used to illustrate the efficiency of a single row or coincident rows of blades (Chapter 3)
- For finite spacing, the theory of actuator surfaces and BEM are inadequate; the vortex model will be used to model a Moonraker with finite blade row spacing (Chapter 3).
- Further investigation of double actuator surfaces in close proximity, with the aim of developing a theory to be implemented, in future work, in the BEM model, is presented in Chapter 5.

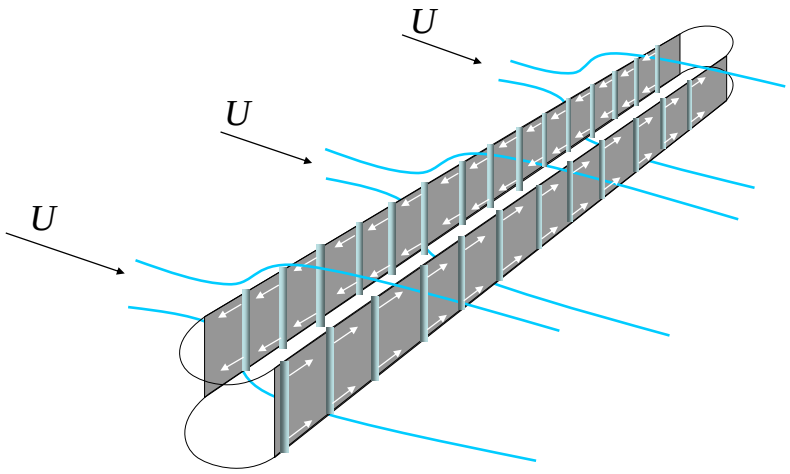

(a) *The predominant effects of a Moonraker on the fluid flow are highlighted in grey: the circular part of the blade path will have a minimal effect.*

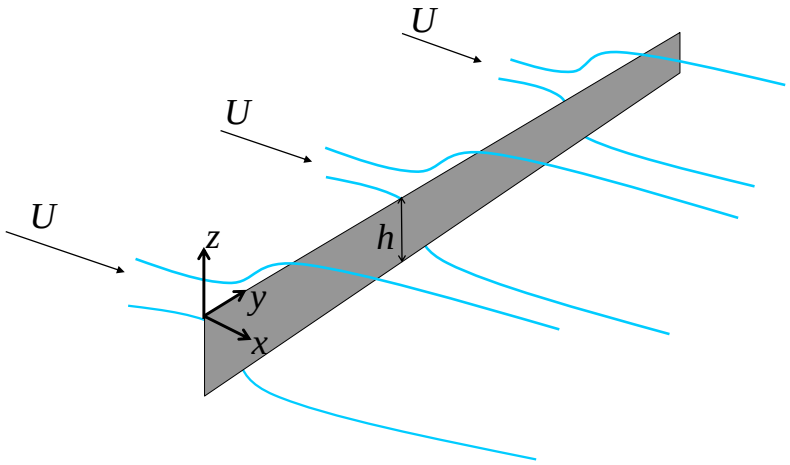

(b) *Each row of the Moonraker can be approximated by an 'actuator surface', illustrated here.*

Figure 2.23: *Representation of a Moonraker by actuator surfaces.*

Chapter 3

Prediction of blade forces

3.1 Introduction

This chapter presents predictions of the hydrodynamic performance of a Moonraker device. Hydrodynamic performance is defined here as the forces and moments acting on the blades over one period of rotation. The overall performance of the device is found by integrating the forces and moments on the blades over one representative rotation, yielding average values of thrust, shaft torque, and shaft power.

Although the hydrodynamics of the Moonraker has seen limited development, it can be modelled, with only minor modifications, in the same way as the 'Darrieus' cross-flow turbine, which saw extensive development from 1967 through to the late 1980s. The Darrieus was developed as a wind turbine but the modeling techniques are equally applicable in water because they are based on the assumption of an incompressible, isothermal Newtonian fluid, a definition that covers both water and air at low speeds.

This chapter begins with some definitions, which will be used throughout this and the next chapter, and then reviews of the blade element momentum (BEM) method, a standard tool for aerodynamic predictions in the wind energy industry. Results are presented for an idealised cascade of lifting blades moving perpendicular to the upstream flow, showing why this configuration is suggested for the Moonraker concept.

Following this the potential flow vortex model is reviewed and its implementation in Matlab is described. Results are presented firstly in comparison to those of the original model of a Darrieus turbine developed at Sandia Laboratories in the US, and also to the results from a recently published study of the Darrieus turbine from Edinburgh University which used a BEM model and a commercial Reynolds averaged Navier-Stokes (RANS) solver in two-dimensions. The RANS model is more physically comprehensive but also more computationally demanding; the comparison with the RANS model highlights the strengths and weaknesses of the BEM and vortex models, but further use of a RANS model was not practical due to time constraints. It

will be concluded that the BEM and vortex models agree closely, but that the vortex model offers more flexibility for the Moonraker so the vortex model was chosen as the tool for predicting Moonraker performance.

Vortex model predictions of the performance of a Moonraker are then presented for a large scale device for a range of aspect ratios and solidities (results for a laboratory scale device are presented in the following chapter when compared to experimental results). Finally a discussion of a three dimensional vortex model is presented, where it is argued that a three-dimensional model is essential for a Moonraker in unbounded flow and the extension of the vortex model to three-dimensions is recommended.

3.2 Definitions

3.2.1 Coordinates and geometry

A right-handed Cartesian coordinate system, x, y, z, is adopted where a fluid of density ρ is assumed to be flowing far upstream with a constant and uniform velocity $[U_\infty, 0, 0]$. The oval blade path of a Moonraker, which is in the $x-y$ plane, is illustrated in Figure 3.1a, showing a total width, W, and a spacing between each row of $2R$, where R is the radius of curvature of the oval. The ratio

$$g_{\mathrm{M}} = 2R/W \tag{3.1}$$

indicates the geometry of the path for a Moonraker: lower values indicate that the straight sections constitute a larger proportion of the path; for a Darrieus turbine, $g_{\mathrm{M}} = 1$ and the blade path is a circle. The total length of the path is

$$L_{\mathrm{p}} = 2\pi R + 2W - 4R. \tag{3.2}$$

In non-dimensional terms:

$$\frac{L_{\mathrm{p}}}{W} = \pi g_{\mathrm{M}} + 2 - 2g_{\mathrm{M}} \tag{3.3}$$

The position of a blade along the path is denoted Θ and ranges from zero to one. A blade at $\Theta = 0$ or $\Theta = 1$ is always facing directly into the flow, and a blade at $\Theta = 0.5$ is always facing the same direction as the flow. This is illustrated in Figure 3.1b for the case of clockwise blade rotation.

The device has a height, h, which is also the length of the N blades which have a chord, c, and the device therefore has a 'solidity'

$$\sigma = \frac{Nc}{W}. \tag{3.4}$$

3.2.2 Forces and moments

The horizontal force on the blades is initially defined in the blade's frame of reference. This

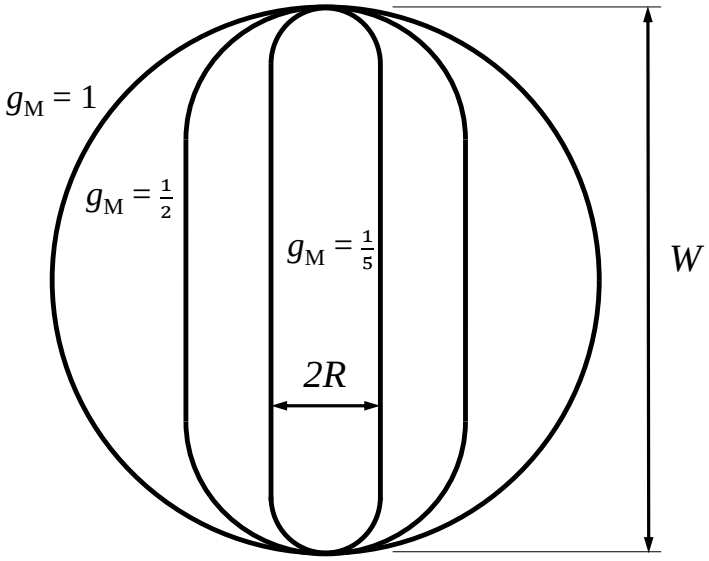

(a) *Geometry of the blade path in the $x - y$ plane.*

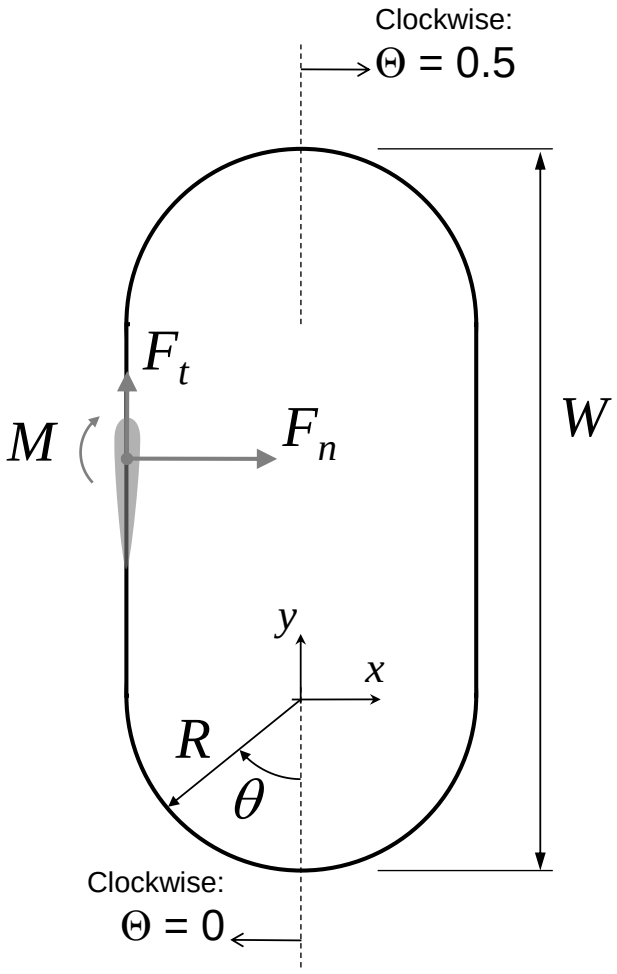

(b) *Coordinates, forces and azimuth in the $x - y$ plane.*

Figure 3.1: *Definitions for the Moonraker (for fluid flow left-to-right).*

horizontal force is decomposed into the component tangential to the blade path, F_t, and normal to the blade path, F_n, which is positive when pointing inside the blade path. The hydrodynamic moment about an axis parallel to the blade span and located on the blade chord $c/4$ from the leading edge, is M. These are non-dimensionalised as

$$F_\mathrm{n}^+ = \frac{F_\mathrm{n}}{\frac{1}{2}\rho U_\infty^2 ch}, \tag{3.5}$$

$$F_\mathrm{t}^+ = \frac{F_\mathrm{t}}{\frac{1}{2}\rho U_\infty^2 ch}, \tag{3.6}$$

$$M^+ = \frac{M}{\frac{1}{2}\rho U_\infty^2 c^2 h}. \tag{3.7}$$

The vertical forces on the blade are relatively small, constant, and do not do any work because the blade's vertical position does not change; therefore the vertical component of the force is neglected.

The fluid velocity in the vicinity of the blade is denoted $\boldsymbol{u} = [u_1, u_2, u_3]$ and is measured in a fixed frame of reference; the blade velocity in the fixed frame of reference is $\boldsymbol{v} = [v_1, v_2, v_3]$ and the non-dimensional blade speed is known as the blade speed ratio:

$$\Lambda = \frac{|\boldsymbol{v}|}{U_\infty} \tag{3.8}$$

The blade will experience a relative fluid velocity $\boldsymbol{w} = [w_1, w_2, w_3]$ which is the vector subtraction of the blade velocity from the local fluid velocity:

$$\boldsymbol{w} = \boldsymbol{u} - \boldsymbol{v}, \tag{3.9}$$

and will have an angle relative to the blade chord

$$\beta = \arcsin\left(\frac{(\boldsymbol{w} \times \boldsymbol{v}) \cdot \hat{\boldsymbol{z}}}{|\boldsymbol{w}|\,|\boldsymbol{v}|}\right). \tag{3.10}$$

Using the cross-product preserves the sign of the angle, β. The blade is pitched at an angle ϕ relative to the blade path, so that the hydrodynamic angle of attack experienced by the blade is

$$\alpha = \beta - \phi. \tag{3.11}$$

The blade Reynolds number is defined as

$$Re_c = |\boldsymbol{w}|\, c/\nu, \tag{3.12}$$

where ν is the kinematic viscosity of the fluid. The quasi-steady blade section lift and drag coefficients, C_L and C_D respectively, can be estimated from the speed of the relative fluid flow, $|\boldsymbol{w}|$, the hydrodynamic angle of attack, α, and the blade Reynolds number, Re_c. This yields an

estimate of the tangential and normal forces on the blade:

$$F_{\mathrm{t}}^{+} = \frac{|\boldsymbol{w}|^2}{U_\infty^2}\left(C_{\mathrm{L}}\sin\alpha - C_{\mathrm{D}}\cos\alpha\right), \tag{3.13}$$

$$F_{\mathrm{n}}^{+} = \frac{|\boldsymbol{w}|^2}{U_\infty^2}\left(C_{\mathrm{L}}\cos\alpha + C_{\mathrm{D}}\sin\alpha\right). \tag{3.14}$$

The lift and drag coefficients may need correcting due to the finite length of the blades, and this is discussed in Section 2.4.6.

3.2.3 Average torque, power, and thrust

The average performance of the device is defined by the torque and power, which are non-dimensionalised as C_{Q} and C_{P} respectively, and are derived from the blade forces as:

$$C_{\mathrm{Q}} = \frac{\text{torque}}{\frac{1}{2}\rho U_\infty^2 h W^2 g_{\mathrm{M}}} = \overline{F_{\mathrm{t}}^{+}}\sigma, \tag{3.15}$$

$$C_{\mathrm{P}} = \frac{\text{power}}{\frac{1}{2}\rho U_\infty^3 h W} = \overline{F_{\mathrm{t}}^{+}}\sigma\Lambda, \tag{3.16}$$

where the over-line is the average over a period of rotation. The equation for torque is missing the contribution of the hydrodynamic moment: $M^{+}c/R$; assuming the blade transfers torque via a flexible tension member such as a chain, wire, or belt during the straight portion of the track, then the moment, M, will only make a contribution to torque while on the curved path and the contribution will depend on the mechanical design of the Moonraker, which has not yet been determined. However, even at this stage it is reasonable to neglect this small quantity - this is justified later where, in Figure 3.11, the relative magnitudes of F^{+} and M^{+} are evident (from numerical predictions, at least).

The remaining average measure is the thrust, which is the streamwise component of the net force on all the blades, in a fixed frame of reference. The total force in the fixed frame of reference is denoted $\boldsymbol{F}^{+}$:

$$\boldsymbol{F}^{+} = \boldsymbol{J}\cdot\begin{bmatrix} F_{\mathrm{t}}^{+} \\ F_{\mathrm{n}}^{+} \end{bmatrix} + \text{dynamic forces}, \tag{3.17}$$

where $\boldsymbol{J}$ is a transformation matrix which depends on the section of the blade path:

$$\boldsymbol{J} = \begin{bmatrix} -\cos\theta & \sin\theta \\ \sin\theta & \cos\theta \end{bmatrix}, \tag{3.18}$$

where θ is the angle of rotation around the curved parts of the path as illustrated in Figure 3.1. For the straight part of the blade path $\theta = \pi/2$ on the upstream track and $\theta = 3\pi/2$ on the downstream track.

The 'dynamic forces' are due to centripetal acceleration of the blade and depend on the mass

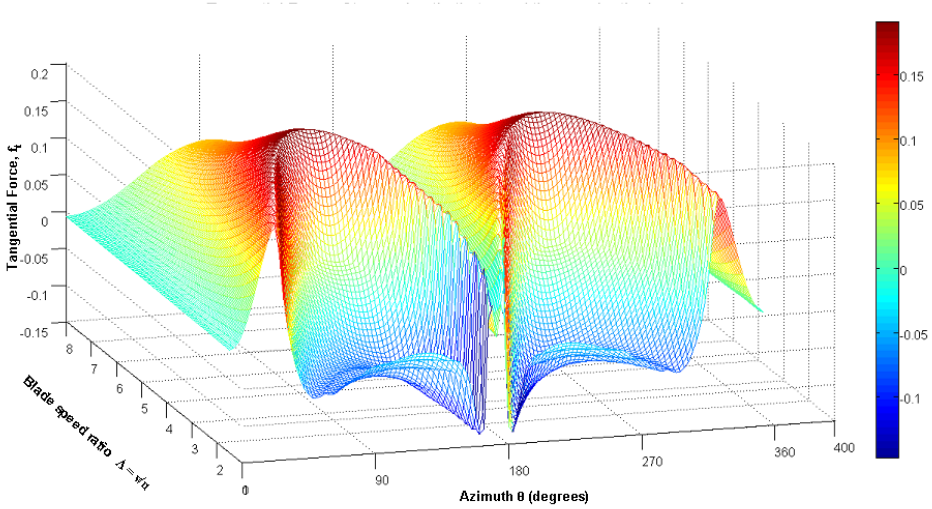

Figure 3.2: *Non-dimensional tangential force, F_t^+ vs azimuth θ on a single bladed Darrieus turbine ($\sigma \to 0$) using blade data from a NACA0018 section (Sheldahl and Klimas, 1980).*

of the blade. The dynamic fluid forces, such as added mass, are accounted for in the terms F_{t}^+ and F_{n}^+.

Having defined the total force on a blade in the fixed frame of reference, we assume periodic behaviour and then the average thrust on the device is

$$C_{\mathrm{T}} = \sigma \oint_{\Theta} \left(\boldsymbol{F}^+ \cdot \hat{x} \right) \mathrm{d}\Theta. \tag{3.19}$$

3.3 Blade element momentum (BEM) analysis

3.3.1 Analysis without momentum considerations

The tangential force F_{t}^+ (3.13) on a single blade rotating around a circular path ($g_{\mathrm{M}} = 1$) is illustrated in Figure 3.2, where it is assumed in (3.9) and (3.11) that $\boldsymbol{u} = [U_\infty, 0, 0]$ i.e. that the flow is unaffected by the presence of the blade. The lift and drag coefficients were obtained from blade section data for a NACA0018 section from Sheldahl and Klimas (1980), and assumed $U_\infty = 2$ m/s and $c = 0.5$ m.

This is effectively a linearised model and Figure 3.2 can be used to explore the parameter space of the dynamical system that consists of a fluid, and the blades of a device.

The tangential force, F_{t}^+, on the blade is the torque generating force. Following a blade over its rotation from left-to-right in Figure 3.2 the tangential force on the blade fluctuates as the angle of attack rises and falls twice - one 'hill' represents the upstream, the second 'hill' is the downstream half; the two halves are identical in this model because the flow is unaffected by

the forces on the blade.

At blade speeds below about $\Lambda = 4$ Figure 3.2 shows a depression in the middle of each 'hill' because the blade has stalled. At speeds below about $\Lambda = 3$ the net torque summed over one rotation is negative, hence such a device (a Darrieus turbine) cannot reach operational speeds without starting assistance – it cannot self-start. At operational speeds, i.e. $\Lambda \gtrsim 3$, the net torque is positive but the torque on the shaft fluctuates considerably and causes large fatigue loads. The torque is more smooth when using multiple blades that are out of phase, for example 3 or more blades.

The peaks of the 'hills' in Figure 3.2 occur when the blade is translating perpendicular to the oncoming flow: this is the peak in torque generation.

Figure 3.2 is for the limiting case of low solidity, $\sigma \to 0$; in other words it is assumed that the velocity is everywhere U_∞ and unaffected by the presence of the blade and there is no limit to the energy that can be extracted from the flow. In reality the rotor will interact with the flow and change the local velocity; as more blades are added and more power is taken from the flow, the assumption $\sigma \to 0$ will cease to be valid. The blade element momentum (BEM) method models these effects, which are non-linear and require an iterative approach to converge on an approximate solution.

3.3.2 BEM concept

The Blade Element Momentum (BEM) technique was introduced for cross-flow devices by Templin (1974) who applied the momentum balance technique presented in Section 2.6 to the streamtube of fluid passing through the turbine. In this technique an iterative calculation is performed as follows: firstly the local streamwise flow speed, u_1, is used to estimate blade forces, which in turn yields an estimate for the thrust (3.19); secondly, the thrust is used along with linear momentum theory (Section 2.6) to estimate the local streamwise flow speed, u_1, which will then be fed back into the first calculation. The iterations continue until the local speed converges.

In this section the BEM model is applied to a single row of blades – a 'cascade' – to illustrate the effectiveness of a blade moving perpendicular to the upstream flow. Extension to cross-flow turbines is discussed in Section 3.3.6 and is recommended as a future addition to this work.

3.3.3 BEM assumptions

The BEM model combines blade element section data with linear momentum theory (Section 2.6.2); any non-streamwise momentum is neglected. In multiple streamtube BEM models it is assumed that the streamtubes are independent: no matter how large the thrust (rate of change of momentum) is in one streamtube, the neighbouring streamtube is treated independently.

As a blade moves along its path the relative velocity is determined by the vector subtraction of the blade speed and the local flow speed (3.9). The second major assumption is that this relative velocity will have the same effect on the blade as if it were in an isolated flow of the same relative velocity. In other words, the blades do not interact with each other, except via

the influence on the time-averaged momentum deficit flowing through the device. This can later be corrected by considerations of centripetal force, added mass, and flow curvature. A further assumption is that the forces on a blade at any point along its path are independent of the forces at any point earlier or later. This is the assumption of quasi-steady flow and can be augmented by a dynamic stall model. None of the corrections for dynamic effects are included in this thesis, for reasons given in Section 3.6.2.5.

3.3.4 BEM method

To determine the local flow conditions at a blade, the following momentum considerations can be made:

- Make an initial estimate of the local flow speed, e.g. $a_n = 0$, $u_n = U_\infty$.
- Estimate blade forces, C_L, C_D, from $|\boldsymbol{w}|$ (3.9), α (3.11), Re (3.12) and using blade element data. Use these to estimate F_t^+ (3.13) and F_n^+ (3.14).
- The time-averaged thrust C_T is estimated from (3.19), integrated over the relevant range of Θ for each streamtube.
- A new induction factor is estimated by rearranging (2.52) as:

$$a_{n+1} = \frac{1}{4} C_\mathrm{T} + a_n^2.$$

- This gives a new estimate of the local flow speed:

$$u_{n+1} = U_\infty \left(1 - a_{n+1}\right).$$

- An iterative loop can be repeated until a convergence criterion is met, e.g.

$$|a_{n+1} - a_n| < 10^{-4}.$$

The limitations of the BEM model are:

- Steady flow assumption - blade interaction during passing is not captured; this can be improved slightly by using a dynamic stall model.
- One-dimensional momentum assumption - no transverse velocities accounted for
- Planar flow assumption - this can be improved using tip-loss corrections, but ultimately for short blades relative to the device width the flow will become three-dimensional.

- Reliance on linear momentum theory so, with few exceptions, cannot account for multiple rows of energy extraction.

All of the above limitations can potentially be improved by using a vortex model which is a higher order model, offering a more comprehensive physical simulation but at the cost of higher computational power requirements. The vortex model is explored in Section 3.4.

3.3.5 BEM results for a single row of blades

The BEM method is relatively undemanding on CPU power so can be used to generate data across the whole parameter space. The BEM method has been applied here to a cascade of translating lifting blades with solidity (or packing density), σ. Figure 3.3 shows the power coefficient, C_{P}, with contour increments of $\Delta C_{\mathrm{P}} = 0.05$, for a cascade of translating lifting blades with zero pitch ($\phi = 0$). Figure 3.3a shows a performance map for a range of solidities, σ, and blade speed ratios Λ. Figure 3.3b shows information all contained within Figure 3.3a but highlights the nature of the power curves which can be deduced from a performance map such as Figure 3.3a.

The $C_{\mathrm{P}} - \Lambda$ power curve is a conventional way of representing the performance of a device. Figure 3.3 shows that there is a steep increase in power above a certain blade speed - in this case $\Lambda \sim 2.5$ - which corresponds to the angle of attack dropping below the stall angle. Beyond the steep increase there is a gradual increase and then decrease in power with blade speed, as the angle of attack varies around its optimum. Figure 3.3 shows that increasing the solidity effectively squashes the power curve to the left: the blade speed for stall and for optimum power are both reduced as the solidity increases. According to these calculations, there is a fairly wide range over which a translating lifting blade can achieve a hydrodynamic power coefficient greater than 0.55, which is very close to the Lanchester-Betz limit. These results are consistent with those of Ponta et al. (2007).

Figure 3.4 shows a series of performance maps where the blade pitch angle has been varied between -0.5^o and 3.5^o at increments of 0.5^o. In this context it is seen that the performance with a zero pitch angle ($\phi = 0$) is fairly good. The effect of increasing the pitch angle is similar to the effect of increasing the solidity: the performance map is shifted to the left of the plot, and upwards slightly. So increasing the pitch angle reduces the blade speeds that correspond to stall and to optimum power. This point is important in later discussions of experiments, where mechanical difficulties led to a limit in blade speed.

3.3.6 Multiple streamtube BEM

The BEM method can be extended as per Strickland (1975) to account for multiple streamtubes, within each of which the calculation is independent and can account for different blade pitch angles and different blade directions. This facilitates a prediction of the Darrieus turbine, the result of which can be inferred approximately from the information in Figures 3.3 and 3.4.

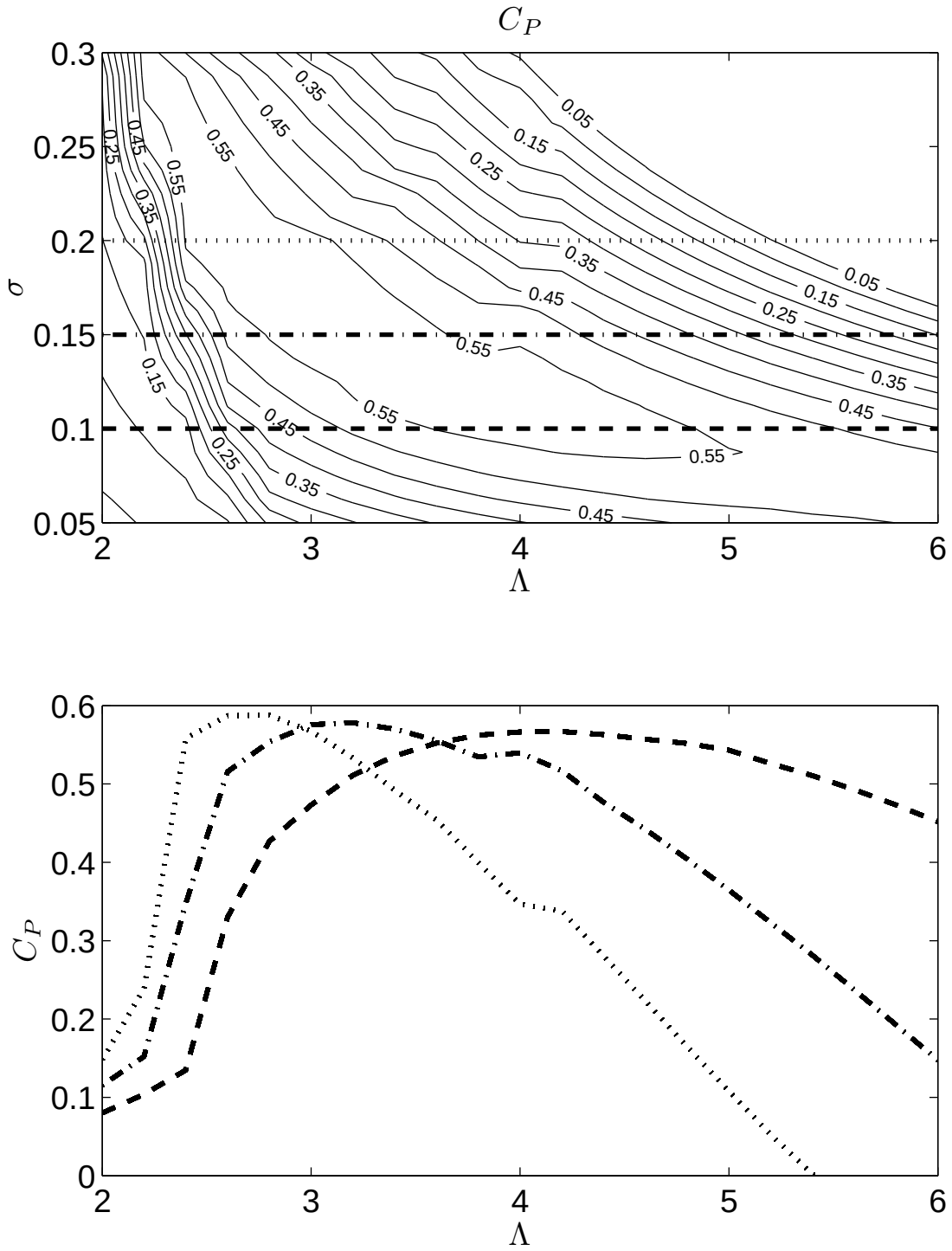

Figure 3.3: *BEM results: C_P for blades translating perpendicular to the flow with zero pitch, using section data for a NACA0018 from Sheldahl and Klimas (1980) with $U_\infty = 2$ m/s, $c = 1$ m, i.e. $Re = 3\Lambda \times 10^6$. Above: performance map for C_P with contours equally spaced at $\Delta C_P = 0.05$. Below: power curves ($C_P - \Lambda$) for $\sigma = 0.1, 0.15, 0.2$, taken from the performance map above and using the same line styles.*

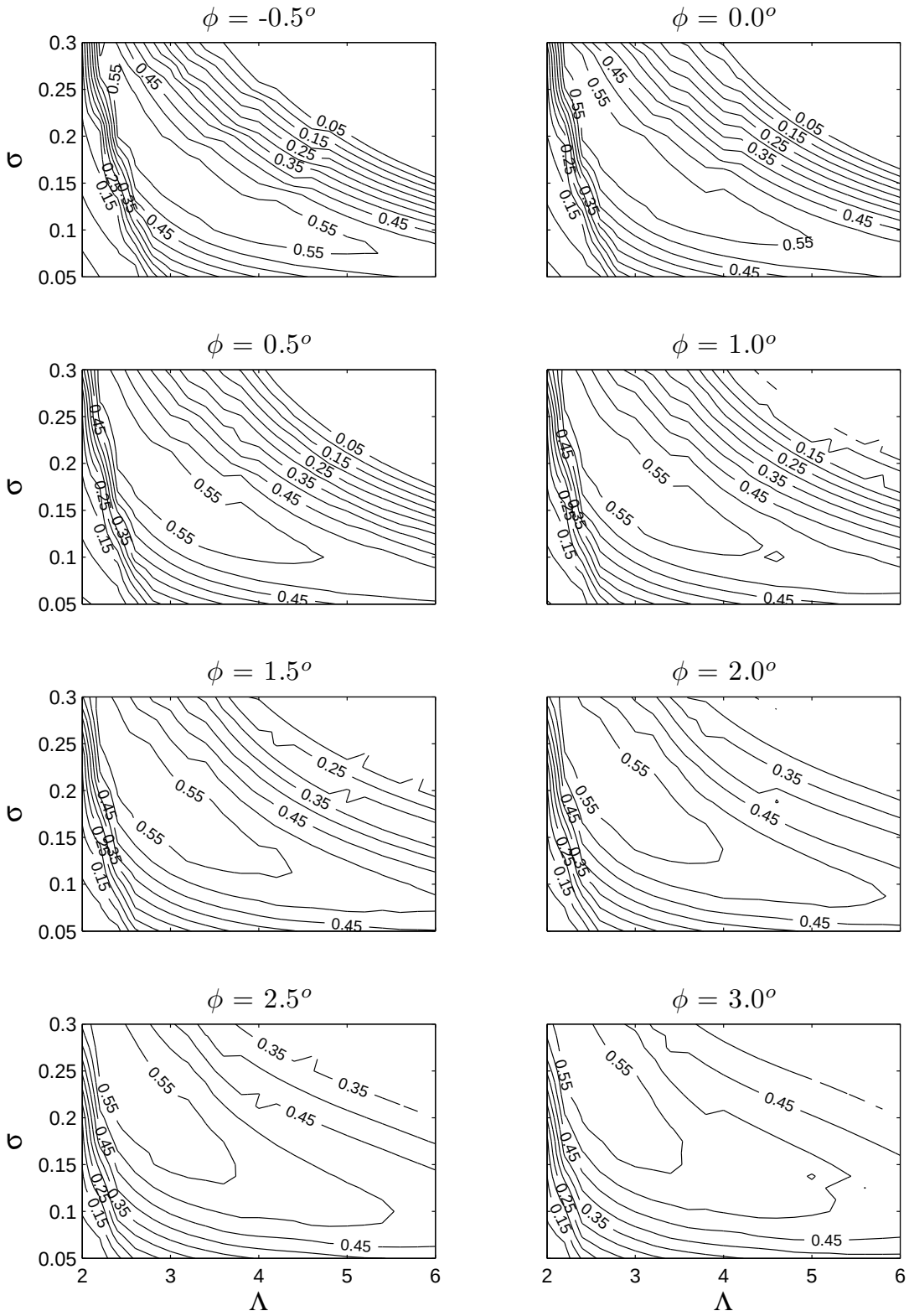

Figure 3.4: *As Figure 3.3 but for a variety of blade pitch angles, ϕ.*

Multiple streamtube models have been successful in research and industry because their prediction of the power coefficient, C_P, vs blade speed ratio, Λ, is fairly accurate, while the computational intensity of the models is minimal.

The BEM method was extended further by others including Read and Sharpe (1980) and Paraschivoiu (1981), both of whom formulated a double multiple streamtube model: a set of multiple streamtubes represents the front row of blades, and a second set represents the back row. The method of Read and Sharpe (1980) is limited to a circular blade path, while the method of Paraschivoiu (1981) is not and so would be more appropriate for use on a Moonraker. This was the approach of Ponta et al. (2007), who used the double multiple streamtube model of Paraschivoiu (1981) to investigate a cross-flow device with an oval blade path (effectively a Moonraker), showing that the part of the blade path where the blade moves perpendicular to the flow generates the most power.

The multiple streamtube BEM model could be applied to a Moonraker but the two rows of energy extraction would have to be modeled either as coincident, as per Strickland (1975), or using the theory of (Newman, 1983) for double actuator surfaces as per Paraschivoiu (1981). However, to account for an arbitrary separation between the two rows of extraction a new theory would be required (as discussed in Section 2.7) for double actuator surfaces in close proximity. During the course of this research progress was made towards this theory; that work is presented later in the thesis, in Chapter 5, because it is inconclusive.

In the mean time, the approach in this research was to use a vortex model to predict the performance of a Moonraker, as described in Section 3.4. This model has the flexibility of allowing effectively any blade path, including oval blade paths with arbitrary spacing between the rows.

3.4 Two-dimensional vortex model

The vortex model is a potential flow based prediction method capable of producing a time-series of the entire velocity field and blade forces, in two- and three-dimensions. It is more computationally intensive than the BEM method but it can produce more detailed and more comprehensive results and is more flexible than the BEM method in terms of multiple rows of energy extraction. The vortex model is described here in its two-dimensional form, assuming planar flow in the $x-y$ plane.

As illustrated in Figure 3.5, assuming planar flow in the $x-y$ plane is effectively placing a rigid wall above and below the Moonraker and forcing all flow through, or around the sides of, the device. This is a useful model if the Moonraker is near the sea bed and the water surface, but in the case of unbounded flow a three-dimensional model would be needed. The two-dimensional vortex model described here was developed as a stepping stone to the three-dimensional vortex model, which is discussed in Section 3.5 but unfortunately was not complete at the time of

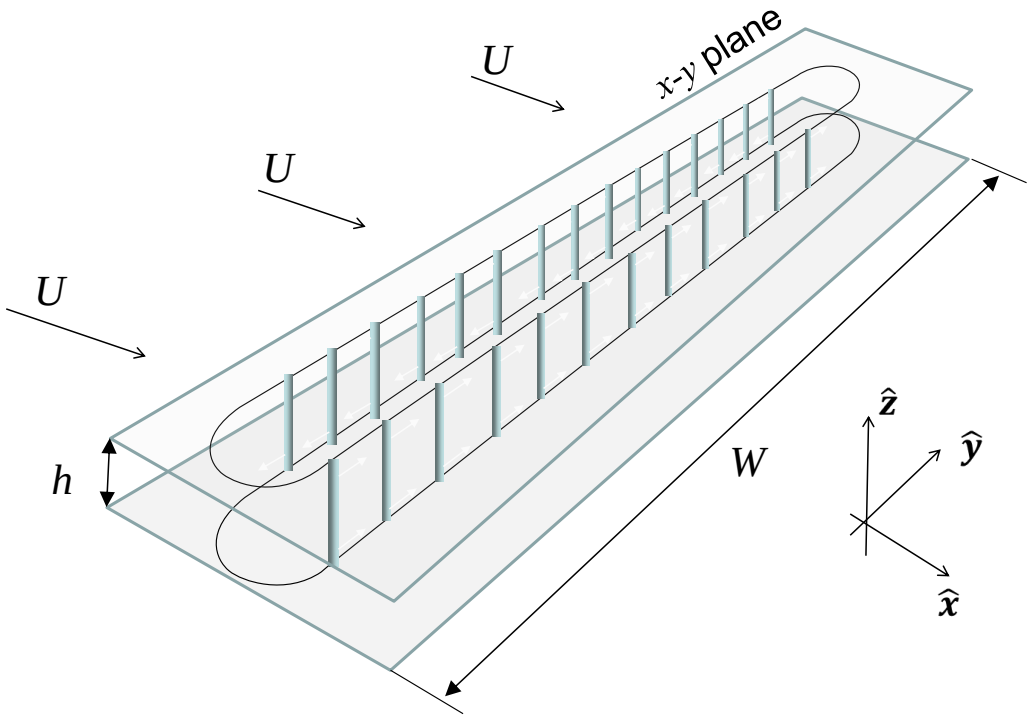

Figure 3.5: *A low, wide Moonraker with $x-y$ planes highlighted at each end of the blades. The two-dimensional model in the $x-y$ plane is equivalent to the highlighted planes being rigid, non-slip boundaries.*

writing.

3.4.1 Theory

A vortex model is a simulation of the unsteady, inviscid, incompressible fluid field associated with a turbine. The vorticity generated at the blades is introduced according to blade element data and the Kutta-Joukowski relation, and the fluid field is treated with potential flow theory and employing Kelvin's and Helmholtz's theorems for circulation and vorticity respectively. The model is purely kinematic and implicitly accounts for the conservation of mass via Laplace's equation and momentum via Kelvin and Helmholtz's theorems. The vortex model of a cross-flow turbine was introduced by Strickland et al. (1981) as part of the research at Sandia National Laboratories.

This thesis does not innovate upon the fundamentals of the vortex model, and there is no additional modeling theory presented here that is not presented by Strickland et al. (1981). The

purpose here is to adapt the model to simulate the hydrodynamics of a Moonraker device.

The fluid field is assumed to be planar in the $x-y$ plane:

$$\frac{\partial}{\partial z} \to 0 \quad -\infty < z < \infty, \tag{3.20}$$

where the blade span is in the $z-$ direction.

The governing equations are then Laplace's equation in 2D for an inviscid, incompressible fluid:

$$\nabla \cdot \boldsymbol{u} = 0, \tag{3.21}$$

and Kelvin's theorem stating the persistence of circulation, Γ, around a 'necklace', or closed curve C, of particles in a simply connected inviscid fluid[1]:

$$\frac{\mathrm{D}}{\mathrm{D}t}\left(\int_C \boldsymbol{u} \cdot \mathrm{d}\boldsymbol{x}\right) = \frac{\mathrm{D}\Gamma}{\mathrm{D}t} = 0, \tag{3.22}$$

where $\boldsymbol{x} = [x, y, z]$. A lifting blade carries an associated bound circulation according to the Kutta-Joukowski theorem:

$$\boldsymbol{L}(t) = \rho \boldsymbol{u}(t) \times \Gamma_{\mathrm{b}}(t)\, \hat{\boldsymbol{z}}, \tag{3.23}$$

where Γ_{b} is the bound circulation and $\hat{\boldsymbol{z}}$ is a unit vector in the z direction. Given the local velocity at a blade the lift force on the blade can be estimated from empirical blade element data, discussed in Section 2.4.4, which together with (3.23) gives the the circulation around the blade. Far from the blade (multiple chord lengths) the effect of the bound circulation on the blade can be represented by a single point vortex with equal total circulation, located at the blade's quarter chord (the centroid of the bound circulation). This representation of a blade by a point vortex at its quarter chord point is the most simple of vortex models; this topic is treated in more detail in Katz and Plotkin (2001).

If the flow conditions at the blade change, i.e. the flow is unsteady, then the lift can be expected to change, as will the bound circulation. Kelvin's theorem states that the total circulation of the fluid cannot change and hence if the circulation around the blade reduces, there must be an equal increase in circulation in the wake as illustrated in Figure 3.6a. A blade with attached flow at reasonably high Reynolds numbers ($\gtrsim 10^4$) will tend to shed that vorticity in a very thin layer that will be advected downstream. The thin wake can be treated as a vortex sheet, which in turn can be discretised.

[1] Only the fluid particles constituting the 'necklace' need to be inviscid. In Figure 3.6, for example, the foil boundary layer is generating circulation due to viscous effects, but Kelvin's theorem still holds around the curve C.

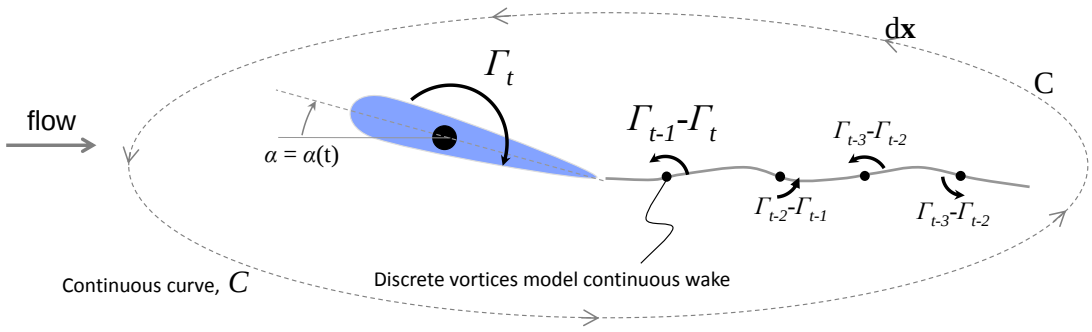

(a) *Unsteady aerofoil. The wake can be modeled by discrete vortices whose strength ensures that the circulation around the whole system is unchanged.*

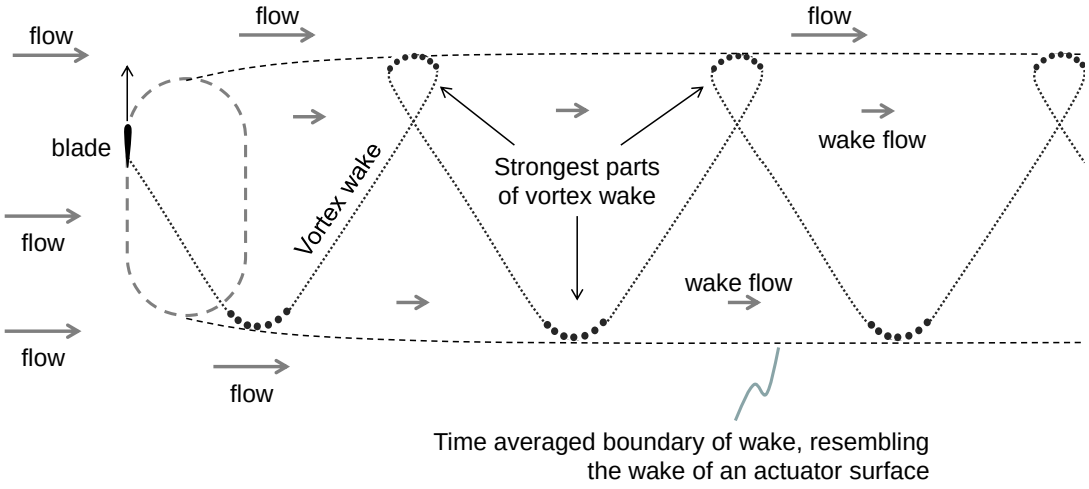

(b) *The wake vortex system in a two-dimensional model of a Moonraker.*

Figure 3.6: *Illustrations of the two-dimensional vortex model.*

3.4.2 Implementation

The model was implemented in Matlab following the work by Strickland et al. (1981) and the structure of the program is illustrated in Figure 3.7. The vortices are advected using a simple Euler integration method, and each time-step includes one correction step for the effect of the bound vortices once the lift has been calculated.

The model is purely kinematic, and the program used non-dimensional space and time. Velocity was normalised with the upstream velocity, U_∞, length was normalised with the width, W, of the Moonraker, and time was normalised as

$$\tau = tU_\infty/W.$$

The input dimensions are preserved so that the blade Reynolds number can be recovered.

The geometric factor g_M was usually set to 0.193 to match the experiments of Chapter 4, however this can take any value $g_\mathrm{M} \leq 1$. The track length (3.2) is

$$\frac{L_p}{W} = \pi g_M + 2 - 2g_\mathrm{M}. \tag{3.24}$$

To avoid the velocity, $\boldsymbol{u}$, induced by a point vortex of strength Γ at a distance r reaching very high values as $r \to 0$, the core is mollified by a small value δ:

$$\boldsymbol{u} = \frac{\Gamma}{2\pi r}\left(\frac{r^2}{r^2+\delta^2}\right). \tag{3.25}$$

The physical meaning and appropriate value of δ is discussed in more detail in Chapter 5 where the effect of different values is investigated. The effect of $|\delta| > 0$ is only significant for high resolution calculations where vortices are in close proximity, and this tends to be the case only when the blade passes a vortex sheet in the wake.

Alternatively each vortex can be treated as a 'Rankine' vortex which is described in detail by Strickland et al. (1981) and consists of a rotational core and irrotational outer, with the interface defined where the two velocities are equal:

$$\boldsymbol{u} = \begin{cases} \frac{\Gamma}{2\pi r} & r > \frac{\delta^2}{\pi^2} \\ \frac{\pi\Gamma}{2\delta^2} & r < \frac{\delta^2}{\pi^2} \end{cases}. \tag{3.26}$$

This velocity (3.26) was not used in the present work, but is important because it is the cause of minor differences when comparing the codes.

In order to reach periodic behaviour long simulations are desirable however calculation times are proportional to the cube of simulation times so a compromise is sometimes necessary. The original vortex model of Strickland et al. (1981) tended to be run for 5 to 10 revolutions and net performance was obtained by extrapolating the results; the more recent CFD work of Gretton (2009) used 60 revolutions as a standard for reaching an approximately periodic (steady) state.

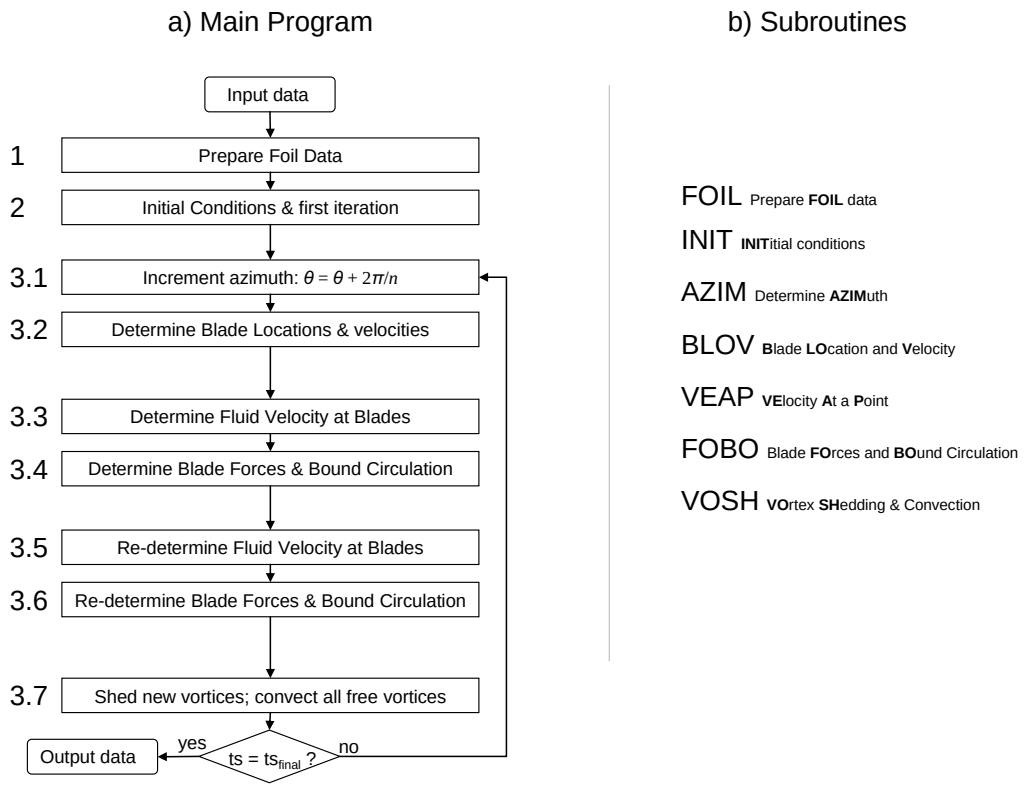

Figure 3.7: *Structure of a vortex model for cross-flow rotors.*

In practice it is the length of the wake that determines when the system becomes steady (not the number of rotations, which is dependent on the blade speed ratio, Λ), and this is studied in detail in Chapter 5 where calculations show that by $\tau = 50$ convergence within 1% is possible.

The time step was defined by fixing the proportion of a revolution that each blade advances between calculations. This implies that the time step $\Delta\tau$ is smaller for higher blade speed ratios, and they therefore take considerably longer to calculate. To achieve long simulation times a coarse time step was used until the final few revolutions. The wake far downstream is therefore at a lower resolution, which is acceptable because its influence on the device is less significant.

3.5 Three-dimensional vortex model

Sections 2.4.5 and 2.4.6 describe corrections for the finite length of blades for use if the two-dimensional model is used to predict performance in a three-dimensional scenario. A more physically realistic model of the effects of finite blade length would be implicitly included in a

three-dimensional vortex model, which was also developed by Strickland et al. (1981) for the Darrieus turbine. Such an implementation for the Moonraker was not complete at the time of writing this thesis. However, because a three-dimensional model is important when considering a Moonraker, this section explains in principle why such a model is so important and why the two-dimensional model presented here is not adequate for the Moonraker in unbounded flow.

3.5.1 Appropriate conditions for a two-dimensional model

The discussion begins by exploring when the two-dimensional model *is* appropriate and then goes on to show how this is often *not* the case for the Moonraker. Figure 2.22a shows a sketch of a three-bladed Darrieus turbine of height h and width (diameter) W. Two planes are sketched, both parallel to the $x-y$ plane and normal to the blades and the axis of rotation. In this sketch the ratio W/h is relatively small: the device is much higher than it is wide. In such a situation the predominant motion of the fluid will be in the $x-y$ plane, with only small changes in the $z-$ direction ($\partial/\partial z \ll \partial/\partial x$, $\partial/\partial y$). If a two-dimensional model were employed, then the planes highlighted in the sketch would effectively become rigid boundaries with zero normal velocity (but a finite slip velocity) and this would be a reasonably accurate approximation. Physically, the trailing vortices are far away from most of the device, so that their influence is diminished and negligible.

Figure 3.5 shows a sketch of a many-bladed Moonraker of height h and width W; once again a plane parallel to the $x-y$ plane is sketched at each end of the blades. In this case $W/h \gg 1$: the device is much wider than its height. If the highlighted planes are rigid boundaries, for example the sea bed and free surface, then the two-dimensional model is again reasonable.

3.5.2 Conditions for which a three-dimensional model is essential

If a Moonraker with $W/h \gg 1$ as illustrated in Figure 3.5 is in *unbounded* fluid then the energy extraction process causes the flow to diverge *over* the device in the vertical ($z-$wise) direction; this is in combination with the smaller scale motion in the $x-y$ plane associated with the circulation of the blades and explored in detail in Section 3.4 with a two-dimensional vortex model. Therefore, for a device in unbounded fluid with $W/h \gg 1$, three-dimensional considerations are essential.

3.5.3 Principles of the three-dimensional model

Figure 3.8a shows three sketches of a blade of finite span with a steady wake; on the left is a full wake, then to its right is a discretised, planar wake as discussed in Section 2.4.5; on the far right is a 'simplified discrete steady planar wake', which has amalgamated all of the trailing

vortices into two symmetric vortices. This simplified wake is appropriate because most of the trailing vorticity is shed near the tips of the blade. Below the three sketches of steady wakes is a sketch of a vortex model of the unsteady wake of single blade showing a vortex 'ladder'. As with the two-dimensional model, the strength of the wake vortices is conserved. However in three-dimensions the vortices can stretch - the distance, l, between two vertices on the ladder can change in time; hence the quantity Γl must be conserved. Just as in two-dimensions, where the point vortices are advected with the local flow, in three-dimensions the ladder vertices are advected with the local flow. The result is a wake as sketched in Figure 3.8b, showing significant motion in all directions, hence the necessity of the three-dimensional model. In Figure 3.8b the 'rungs' on each ladder (span-wise vorticity) have equal strength, so that the intensity of the wake can be seen by the packing density of the rungs; similarities with the two-dimensional wake can be seen (see Figure 3.6), however in the three-dimensional case the wake is free to diverge in all directions.

3.6 Results and discussion

This section presents results from the two-dimensional point vortex model. The initial focus is on the Darrieus turbine, i.e. a circular blade path, to verify the performance of the model. Results are presented in comparison to those of Strickland et al. (1981) from Sandia National Laboratories showing very close agreement; in addition a comparison is made between the vortex model and published results from both a BEM and a Reynolds Averaged Navier-Stokes (RANS) model for a Darrieus turbine (all in two-dimensions) and the results are discussed. Following this the vortex model is applied to the oval blade path of a Moonraker. Three cases of Moonraker are considered: large scale with infinite blades, large scale with finite blades, and lab scale. The large scale results are presented and discussed here, while the results for the lab scale Moonraker are not presented until the following chapter, where they are compared to experimental measurements and discussed further.

3.6.1 Comparison with Sandia code

The vortex model was first developed by Strickland et al. (1981), hereafter referred to as the 'Sandia' code, and has been re-written for the present research (hereafter referred to as the UCL code) with the additional facility to vary the blade path.

The first test of the UCL code is to compare results with those of the Sandia code using the same blade section data and parameters - as listed in Table3.1. There are two notable differences between the codes: firstly the Sandia code uses a 'fixed wake grid point' algorithm (see Strickland et al. 1981) and interpolates to find the velocity at each vortex, while the UCL code does not and is therefore more accurate but less time efficient; secondly close encounters

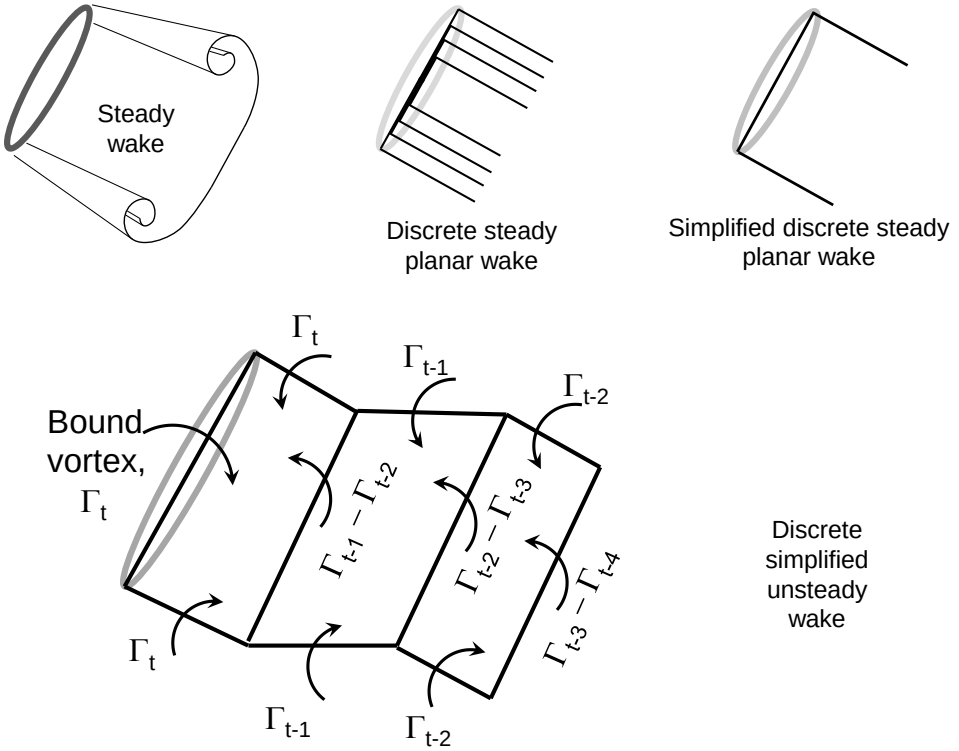

(a) *Illustration of the vortex ladder associated with a blade in unsteady conditions.*

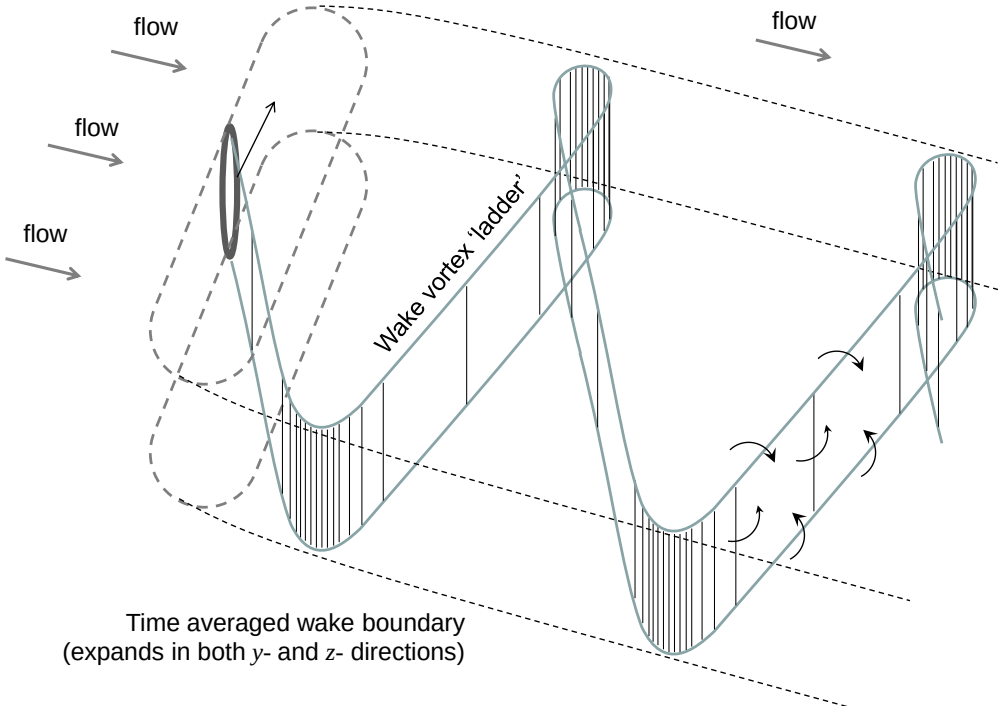

(b) *The three-dimensional wake of a Moonraker using vortex ladders.*

Figure 3.8: *Vortex models of three-dimensional wake systems.*

Parameter	Value
Time step, $\Delta\Theta$	$1/24 = 0.04167$
Blade profile	NACA0012
g_M	1
W	1.22 m
c	0.0914 m
Re_c	40,000 (fixed)
AR	∞
δ (3.25)	0.005
Λ	7.5
N	1 blade

Table 3.1: *Parameters used when comparing the UCL and Sandia (Strickland et al., 1981) vortex models. Blade section data from Strickland et al. (1981) was used.*

of vortices are treated differently: the Sandia code uses (3.26) while the UCL code uses (3.25).

The results for the tangential and normal force on the blades are shown in Figure 3.9 for the case of a single blade at a speed of $\Lambda = 7.5$. Results for $\Delta\Theta = 1/24$ are shown (solid line: Sandia; circles: UCL), and also results from UCL using the small time step $\Delta\Theta = 1/100$ are given (dots). The UCL results are evidently independent of the time step.

The agreement between the Sandia and UCL is mostly excellent - which is to be expected - with two significant differences. The first difference is in the phase at some stages of the cycle, however this is on the order of 1% and is likely to be due to the inaccuracy of the Sandia data, which was obtained from a 30 year old microfiche and enlarged on a photocopier before being scanned and digitised. The second and more significant difference between the Sandia and UCL results is on the downstream half of the blade's revolution: the forces on the blade as it cuts through its own wake are quite different. This is because the UCL code accommodates close encounters with vortices using (3.25), while the Sandia code uses (3.26), so this difference is to be expected. From the comparisons in Figure 3.9 we can conclude with reasonable confidence that the UCL code has been implemented satisfactorily. This is corroborated by a comparison of the vortex locations, which is shown in Figure 3.10.

It is important to note that the agreement shown in Figure 3.9 could only be obtained by carefully matching input data of the UCL code to that of the Sandia code; a small change in δ, or in the initial azimuth, or in the blade section data, can lead to large discrepancies between the two results. This means that any results from the vortex model should be used cautiously - because they are so sensitive to the input data.

3.6.2 Comparison with BEM and RANS method

A Moonraker can alternatively be simulated using BEM model, which would be subject to the limitations of theories on actuator surfaces; or a Reynolds-Averaged Navier-Stokes (RANS)

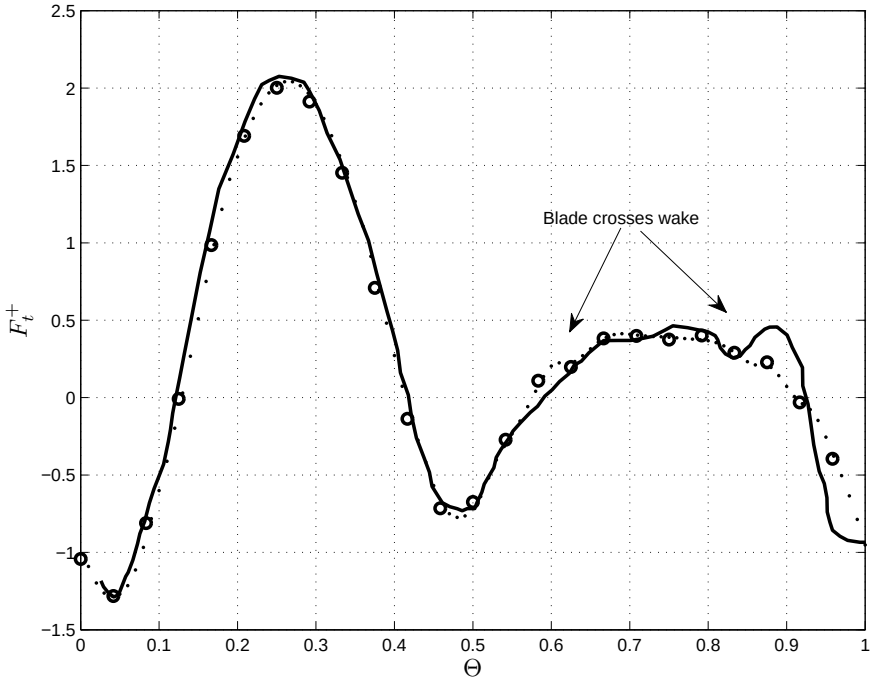

(a) *Tangential force on the blade,* F_t^+.

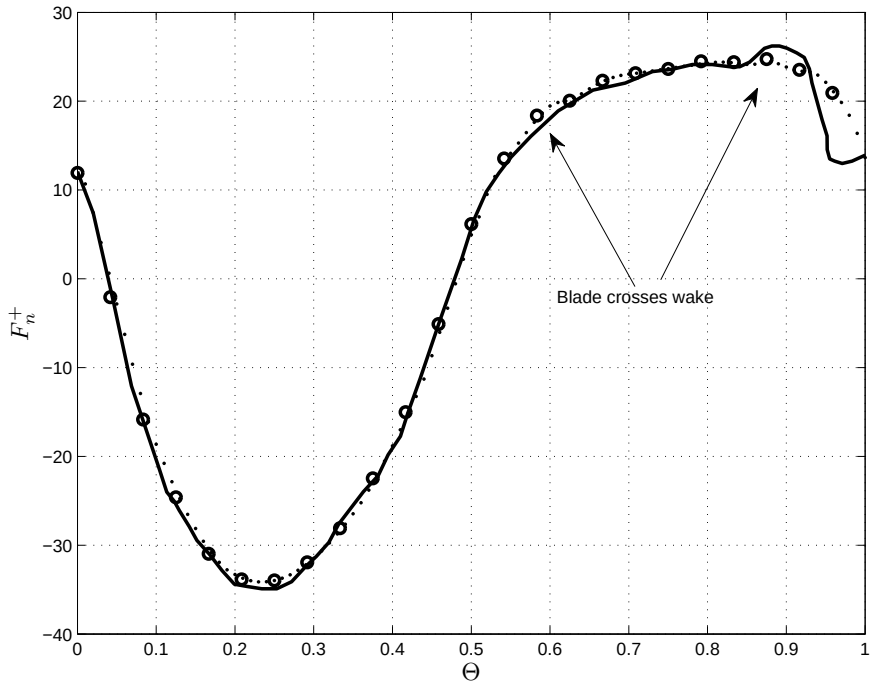

(b) *Normal force on the blade,* F_n^+ *(this plot uses the same sign convention as Strickland et al. (1981) which is opposite to that used elsewhere in this thesis).*

Figure 3.9: *Forces on a Darrieus turbine blade during its fifth rotation: comparison between UCL vortex model and Sandia model (Strickland et al., 1981) for the parameters in Table 3.1. (–) Sandia code; (○) UCL code,* $\Delta\Theta = 1/24$*; (·) UCL code,* $\Delta\Theta = 1/100$*;*

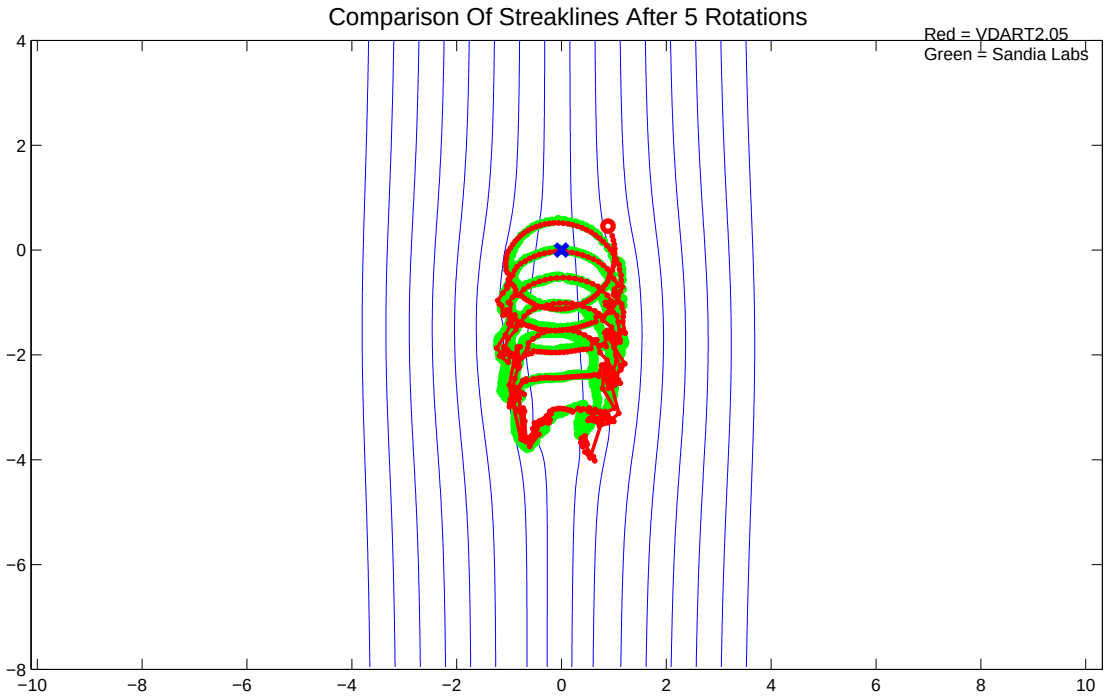

Figure 3.10: *Comparison of streaklines generated by the Sandia code (light green) and the UCL code (dark red). Streamlines have been added based on the UCL data.*

solver could be used but such a simulation would be excessively time consuming for the present research. In this section, as a benchmarking exercise, the vortex model is compared directly with the results of Gretton (2009) from a BEM model and RANS solution for a Darrieus turbine. The work in this section was presented at the 3rd International Conference on Ocean Energy (ICOE) (Johnson et al., 2010). The purpose of the comparison is to highlight the physical effects that each model (vortex, BEM, RANS) does or does not account for.

Data was generated from each model at tip speed ratios of $2.0 < \Lambda < 3.6$ at increments of $\Delta\Lambda = 0.2$. For each simulation results were taken between 55 and 65 revolutions (excluding BEM, which is quasi-steady). By this time results had become periodic in all models.

A comparison of the performance of each method is based primarily on predictions of blade forces on an isolated turbine with a standard configuration shown in Table 3.2. Given the high Reynolds number, even at this scale the results of the comparison are directly relevant to full scale.

The BEM and vortex methods rely on empirical data for blade section forces and moments. For this study, steady blade force data was generated using the RANS model – presented in Gretton and Bruce (2007) – and this data was used in the BEM and vortex models.

The results of the BEM model (following the method of Read and Sharpe (1980)) and the RANS model were kindly provided by Dr. Gareth Gretton. The RANS model is described here briefly and in more detail in Gretton (2009). The RANS simulations were run using the

Parameter	Value
Diameter ($W = 2R$)	2.5 m
Blade chord (c)	0.2 m
Blade section	NACA 0024
Flow speed U_∞	2.5 m/s
Number of blades (N)	3
Solidity ($\sigma = Nc/2R$)	0.24
Typical blade Reynolds number ($Re = wc/\nu$)	$\sim 10^6$

Table 3.2: *Configuration of the standard Darrieus turbine*

commercial code ANSYS CFX, this being selected because of its known strength in turbomachinery applications. The RANS equations were solved with the $k - \omega$ SST turbulence model, this choice being determined by the importance of accurately capturing the development of the boundary layers on the turbine blades. The stability of this model in CFX was also a determining factor. Two grids were used in the study: the first, a coarse grid, was used to allow the solution to be advanced through time relatively quickly, while the second, a medium grid, was used to improve the accuracy of the results. The result of the coarse grid simulation after 60 turbine revolutions was used to start the medium grid simulation which was then advanced for a further three revolutions. Both of these grids were one element thick extrusions of surface grids; a 3D grid being required by the CFX solver.

Figures 3.11 and 3.12 present data from all models. Figure 3.11 shows blade force coefficients plotted against azimuth for a whole revolution with each column representing a different blade speed ratio. The results will now be discussed in more detail.

3.6.2.1 Tangential force, F_t^+

The top rows of Figure 3.11 show the torque generating force, F_t^+. All models are well synchronised, and this is most evident at an azimuth of Θ 0, where the blade forces drop together to their minimum as the blade moves directly into the flow. For the lower blade speed ratios take the example of $\Lambda = 2.4$ where there is good agreement in the range $0 < \Theta < 0.15$, after which the BEM and vortex models, which rely on empirical data, predict blade stall while the RANS model differs by predicting a later stall because it accounts for dynamic stall effects. During the downstream half of the blade's rotation there is less agreement between the models. The vortex and BEM models agree fairly closely and predict quite high forces – this is because they did not capture as much energy while upstream, so that more is available downstream.

At higher blade speeds angles of attack are smaller and there is no stall. During this regime the RANS and vortex models agree more closely. The RANS model predicts more power extraction upstream, and less downstream, compared to the vortex model. The equations for the BEM model break down at high speed and high solidity, so no results are possible in this regime.

In summary, all four models predict similar general blade force behaviour at higher blade

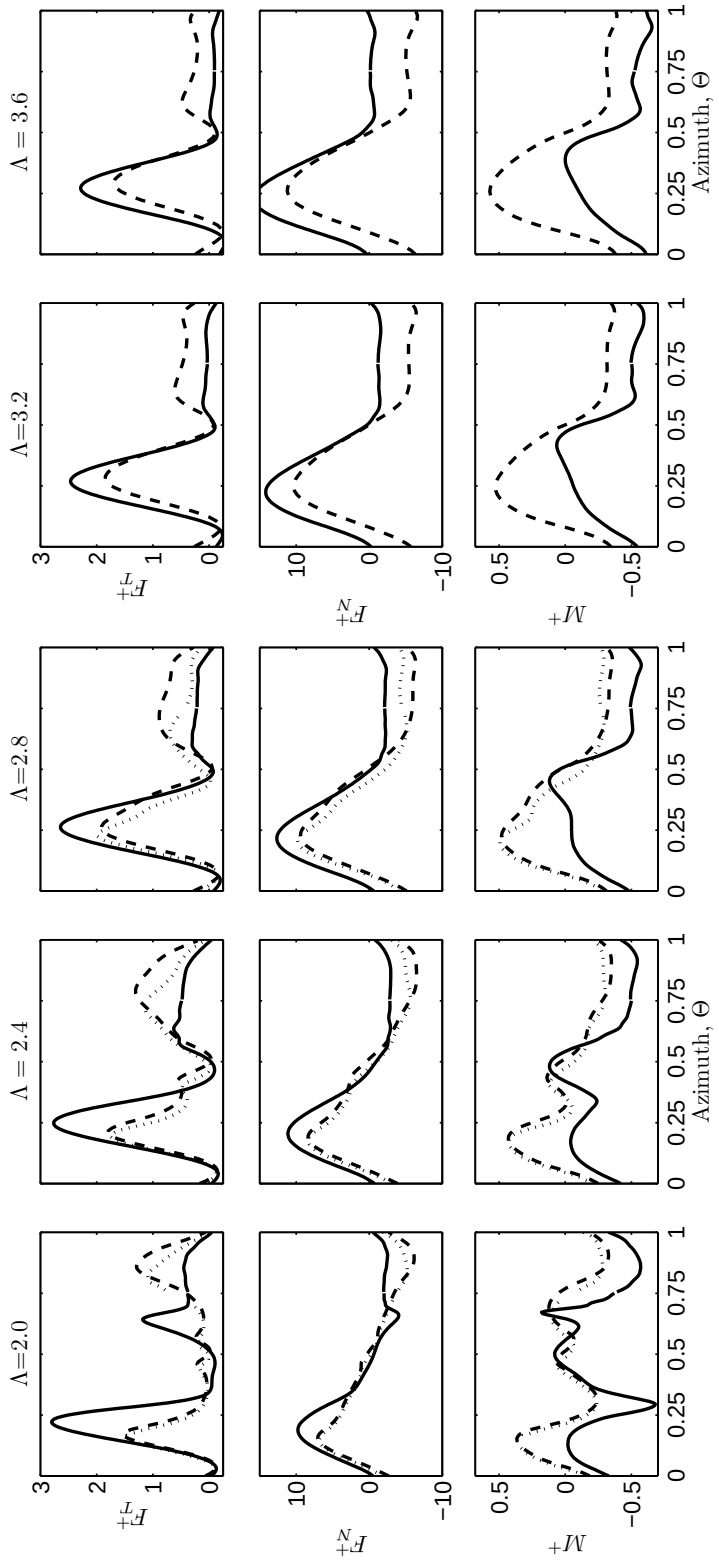

Figure 3.11: *Direct comparison of blade forces and moments over a quasi-steady revolution of a cross-flow (Darrieus) turbine, showing some agreement but also major differences due to stall at low blade speeds. — RANS, – – vortex, · · · BEM. The RANS and BEM results are from Gretton (2009).*

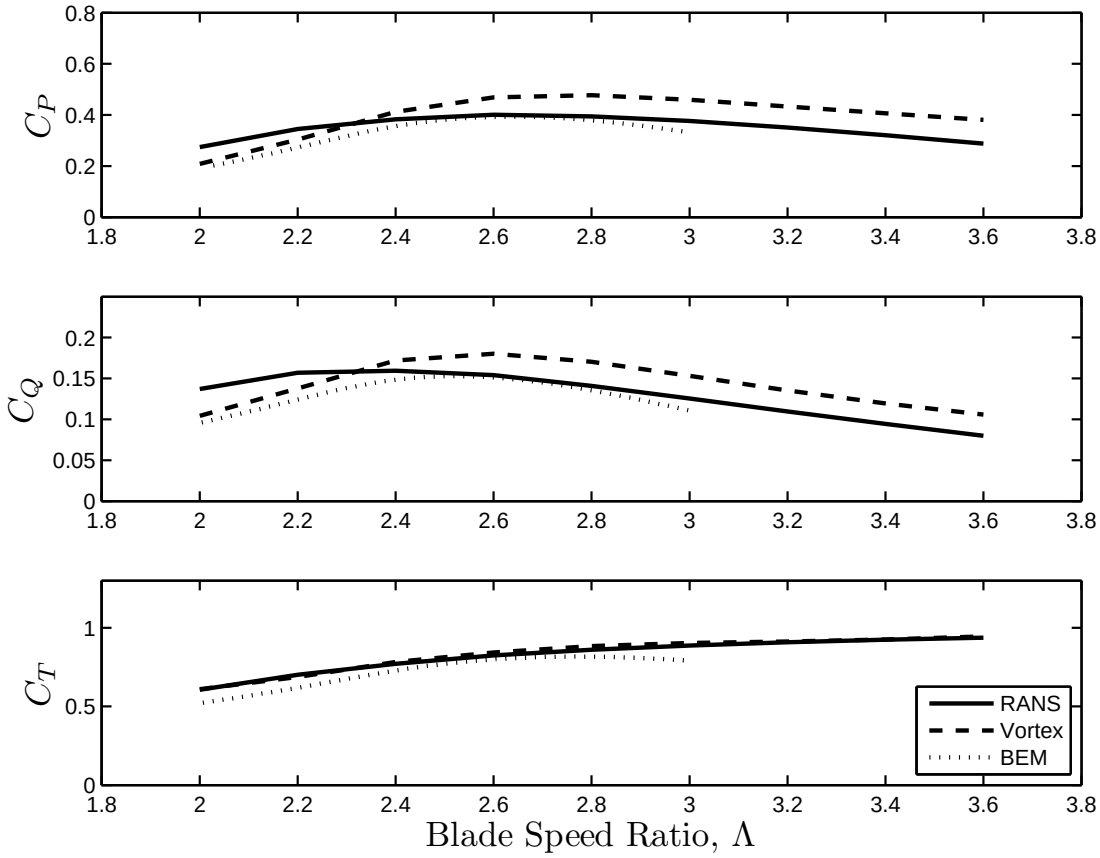

Figure 3.12: *Direct comparison of predictions of the average power, torque, and thrust, on a cross-flow (Darrieus) turbine for a range of tip speed ratios. — RANS, – – vortex, · · · BEM.*

speed ratios, however there are clear and quite serious differences in the way the models predict stall and therefore the results differ at lower blade speed ratios. The BEM and vortex models are heavily sensitive to modeling of dynamic stall. The RANS model predicts a later stall relative to the BEM and vortex models. Finally it is worth noting that the agreement between BEM and vortex models at all blade speed ratios is quite remarkable given initially quite different physical principles – one is dynamic and one is kinematic. This highlights the importance of empirical blade section data, and this is discussed by Gretton and Bruce (2007).

3.6.2.2 Normal force, $F_{\mathbf{n}}^{+}$

The middle rows of Figure 3.11 show the normal force, F_{n}^{+}, which is important because it is large and will dominate the structural design of blades including stress, deflection and fatigue considerations. Again very close agreement is found between the BEM and vortex models. At lower tip speeds the BEM and vortex models predict lower normal forces than RANS for the upstream half, and conversely BEM and vortex models predict larger normal forces than RANS for the downstream half. This corresponds to the effects seen in the tangential force: a stalling blade upstream results in reduced lift and therefore reduced normal forces over much of the blade's upstream pass; consequently high flow velocities in the downstream section result in more energy extraction and higher forces during that half.

In summary, as with the tangential force, at higher blade speed ratios there is good agreement between all models during the upstream half, and less agreement on the downstream half. Again there is surprisingly strong agreement between BEM and vortex results. Prediction of stall at low tip-speeds leads to the largest discrepancy in predictions from different models.

3.6.2.3 Blade moment, M^{+}

The bottom rows of Figure 3.11 show the blade moment, M^{+}, which brings insight into the unsteadiness experienced by the blade because moment stall occurs at lower angles of attack than lift or drag stall. Again there is very close agreement between BEM and vortex results. Again RANS results show a pattern of later stall prediction, and also in this case a shift to lower values of blade moment.

3.6.2.4 Time-averaged coefficients: $C_{\mathbf{P}}$, $C_{\mathbf{Q}}$, $C_{\mathbf{T}}$

Figure 3.12 shows results for the power, torque and thrust coefficient from all models over the range of tip speeds. The torque coefficient, C_{Q}, is dominated by the average value of F_{t}^{+}, because it is much larger than M^{+}. The torque curve in Figure 3.12 can be inferred from the plot of F_{t}^{+} in Figure 3.11. At low tip-speeds, the vortex model predicts lower torque than RANS, due to the differences in stall prediction. At higher tip-speeds, where stall is less important,

the vortex model predicts higher torque than RANS. This difference comes primarily from the higher downstream tangential force, F_t^+ , predicted by the vortex code. The power coefficient, C_P, can be inferred from the $C_Q - \Lambda$ plot in the centre of Figure 3.12 and illustrates the same relative differences. The thrust coefficient, C_T, shows relatively good agreement between all models. Slightly higher values of thrust for RANS and the vortex model correspond to slightly higher blade forces, and therefore larger thrust.

3.6.2.5 Summary

The two-dimensional vortex model has been used to simulate a Darrieus turbine with the parameters listed in Table 3.2 and the results were compared to the BEM and RANS models of Gretton (2009). The BEM and vortex models agree very closely.

The results of a RANS model highlight which physical effects are (or are not) picked up by the BEM and vortex models. The biggest differences are due to static stall models being used in the empirical data for the BEM and vortex models – therefore the differences are most evident at low blade speed ratios, where angles of attack are higher. This highlights the importance of dynamic stall considerations for models using empirical blade section data. The vortex and BEM models – in their current form – are not suitable for predicting behaviour at low blade speeds, but agree reasonably well with RANS predictions at high blade speeds (in the absence of stall).

It is important to note, however, that, in the context of the Moonraker design, focussing on the Darrieus turbine emphasises the dynamic blade forces. For the Moonraker, dynamic effects are only significant on the circular parts of the path. The comparison presented here shows that the vortex model agrees well with the RANS model except when dynamic blade loading is important; therefore the vortex model was considered suitable for predicting the forces on a blade moving *along the straight part* of the Moonraker blade path, while results for the curved part of the track, particularly for low blade speeds, should be treated very cautiously.

Additionally, Chapter 4 goes on to describe an experiment for which blade force measurements are only valid on the straight sections of the track (because it is only during these parts that the blade support conditions are relatively well known). The straight part of the track is most important in the research of a Moonraker because it is the majority of the blade's path and because it is essentially the novelty; given this emphasis on the straight part of the track, and the fact that the experiments in Chapter 4 only yield useful measurements on the straight part, the focus from here onwards will be limited to the forces on the blades *on the straight part of the track*. Dynamic corrections were not included in the vortex method due to time constraints, however it is recommended that a dynamic stall model is implemented in further work.

	Case A (ideal)	Case B (practical)	Case C (lab. scale)
Width, W (m)	40	40	2
Height, h (m)	∞	10	0.5
'Letterbox' ratio, W/h	0	4	4
Geometric ratio, $g_{\mathrm{M}} = S/W$	0.193	0.193	0.193
Chord, c (m)	1	1	0.06
$AR = h/c$	∞	20	8.33
Blades, N	3, 4	3, 4	3, 6
Solidity, $\sigma = Nc/W$	0.075, 0.10	0.075, 0.10	0.09, 0.18
Flow speed, U_∞ (m/s)	2.5	2.5	0.4, 0.5, 0.6, 0.7

Table 3.3: *Configuration of Moonrakers for which results of the vortex method are presented.*

3.6.3 Moonraker blade path

This section presents results from the vortex model for a Moonraker. A blade path with geometry $g_{\mathrm{M}} = 0.193$ has been considered because this corresponds to the experimental device, PII, described in the following chapter. Details of the configuration for each test case are given in Table 3.3, and for all simulations the hybrid data for the NACA0012 section was used (see Section 2.4.4 for discussion and Appendix A.1 for data). Results are presented here for an ideal high performance case (case A) and a more practically realisable case (case B). A laboratory scale case has also been simulated (case C) and these results are presented in Chapter 4 where they are compared to experimental measurements.

3.6.3.1 Convergence

Simulations were run until blade forces were periodic, which tended to require $\tau = tU/W > 40$. Further investigations of the time required to reach steady conditions are presented in Chapter 5. To ensure that the blade forces are resolved the time-step is measured in terms of the incremental change in azimuth, $\Delta\Theta$. Therefore the actual time-step, $\Delta\tau$, will be smaller for higher blade speeds. Generally a smaller increment is required for the Moonraker compared to the Darrieus because by definition the radius of curvature of the track is smaller for a Moonraker and the sharpest changes in conditions occur on the curved parts of the track (and in inverse proportion to the radius of curvature). Therefore calculation sizes tend to be larger for the Moonraker. To reduce the size of calculations, the simulation begins with a coarse time-step which is then reduced to a medium time-step for three or four revolutions, and then a fine time-step for a further three or four revolutions. This results in a low resolution wake in the far field, and a

higher resolution wake in the near field, which is consistent with the influence of each part of the wake on the conditions at the blade and the fact that only steady results are desired.

The final calculations in the simulation are the most intensive because of the larger wake and the larger number of time-steps per revolution. Therefore the number of revolutions at this fine resolution should be only enough to ensure convergence of the results, i.e. that the final two revolutions are the same within a small margin. For lower blade speeds the (older) low resolution wake was advected downstream more quickly (in a smaller number of blade revolutions), while for higher blade speeds more revolutions were required at a fine time-step before convergence was evident. Usually four revolutions were used, ensuring convergence at all blade speeds up to $\Lambda = 7$. Results presented throughout this thesis are the superposition of the last two revolutions so that the convergence can be seen - in the majority of plots the two sets of data are indistinguishable. For the highest speed, $\Lambda = 7$, small but acceptable differences are evident. These high blade speeds are the least relevant but the most computationally demanding. For blade speeds below $\Lambda = 5$ three final revolutions was sufficient.

A range of increments, $\Delta\Theta$, were tested, in combination with the scheme of reducing the time-step for the final revolutions. Final time-steps below $\Delta\Theta = 0.02$ (1/50 of a revolution) showed convergence. These results were for $g_{\mathrm{M}} = 0.193$ – for smaller values of g_{M} further tests would be required and it is expected that the increment required for convergence would reduce, thus increasing the calculation size. Ultimately a more sophisticated system is required where the blades do not necessarily move by equal increments at all points on the path, and vortices are not necessarily shed after every calculation. Such optimisation would make a useful future project.

3.6.3.2 Case A

Figure 3.13 shows a plot of the vortices in the wake after simulating 5 revolutions of a 3 bladed case A Moonraker. This shows that the wake develops in an ordered way and the behaviour of the code when simulating a Moonraker is reasonable. Further attention to the results is via the blade forces predicted by the code.

An example of the blade forces predicted for a Moonraker in case A is plotted in Figure 3.14, showing a plateau in both the tangential and normal forces while the blade is on the straight path. The magnitude of both forces is higher on the upstream pass ($0 < \Theta < 0.5$) where there is more energy available. This difference in conditions upstream and downstream is a key benefit to the vortex model; there is no generally applicable theory for tandem rows of energy extraction separated by arbitrary distance. The pattern of blade forces in Figure 3.14 is representative of the results for all blade speeds above stall. The full collection of results are plotted together in Figure 3.15 showing that the blade forces (both tangential and normal components) at higher blade speeds are of the same nature as Figure 3.14 and that as the blade speed increases, the magnitude of tangential force reduces and the magnitude of the normal force increases. Below a

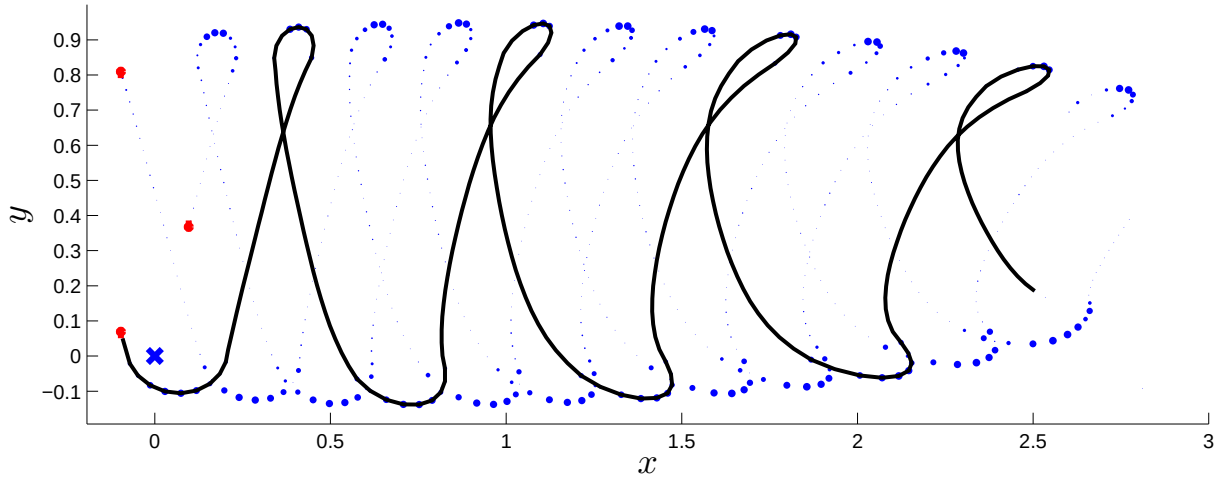

Figure 3.13: *A plot of the vortices in the wake of a 3 bladed case A Moonraker at* $\Lambda = 3$ *after 5 revolutions using* $\Delta\Theta = 1/64$. *Upstream flow is uniform in the* $x-$*direction. The size of the vortices represents their strength; the red circles indicate the quater chord point of the 3 blades and the short red lines from the quarter chord point represent the chord length. The blue 'X' marks the origin and the length scales on the axes are normalised by* W. *The black line joins all the vortices that have been shed by one of the blades, so that the structure of the wake can be seen. The wake flow is slower than the ambient flow, so that the edges of the wake move slightly faster.*

blade speed of about $\Lambda = 2.5$ the angle of attack is higher than the stall angle and the tangential force becomes much lower.

The average of the tangential blade force (plotted in Figure 3.14 for $\Lambda = 4.5$) over a revolution, $\overline{F_t^+}$, can be used to calculate the torque coefficient (3.15) and power coefficient (1.2) which are plotted in Figure 3.16 against blade speed ratio, Λ where results for a Darrieus turbine are included for comparison. In Figure 3.16 it is evident that at a blade speed between 2.0 and 2.5 the angle of attack drops below that of stall which leads to a significantly increased torque coefficient. The sharp increase in torque coefficient is higher for a Moonraker than for a Darrieus turbine because for the Darrieus some parts of the blade path experience stall while others do not; in contrast a small increase in Moonraker blade speed can suddenly bring the blade angle below stall for the majority of the blade's path. It is in this range of blade speed that the Moonraker is able to operate with higher peak efficiencies than the Darrieus. For both devices, as the blade speed increases further, the angle of attack reduces and hence the lift and therefore the torque coefficient reduces and the performance of each device becomes roughly the same.

Figure 3.16 also includes a plot of thrust coefficient (3.19) vs blade speed ratio, Λ, where it is evident that the extra power for the Moonraker is associated with an increase in thrust. The peak power coefficient of the Moonraker is 21% higher than for the Darrieus, while at their respective blade speeds for peak power, the ratio of power to thrust is similar for both devices: it is 2.6% higher for a Darrieus. In conclusion the vortex model predicts a significant increase in power coefficient, with a relatively small increase in thrust per unit power.

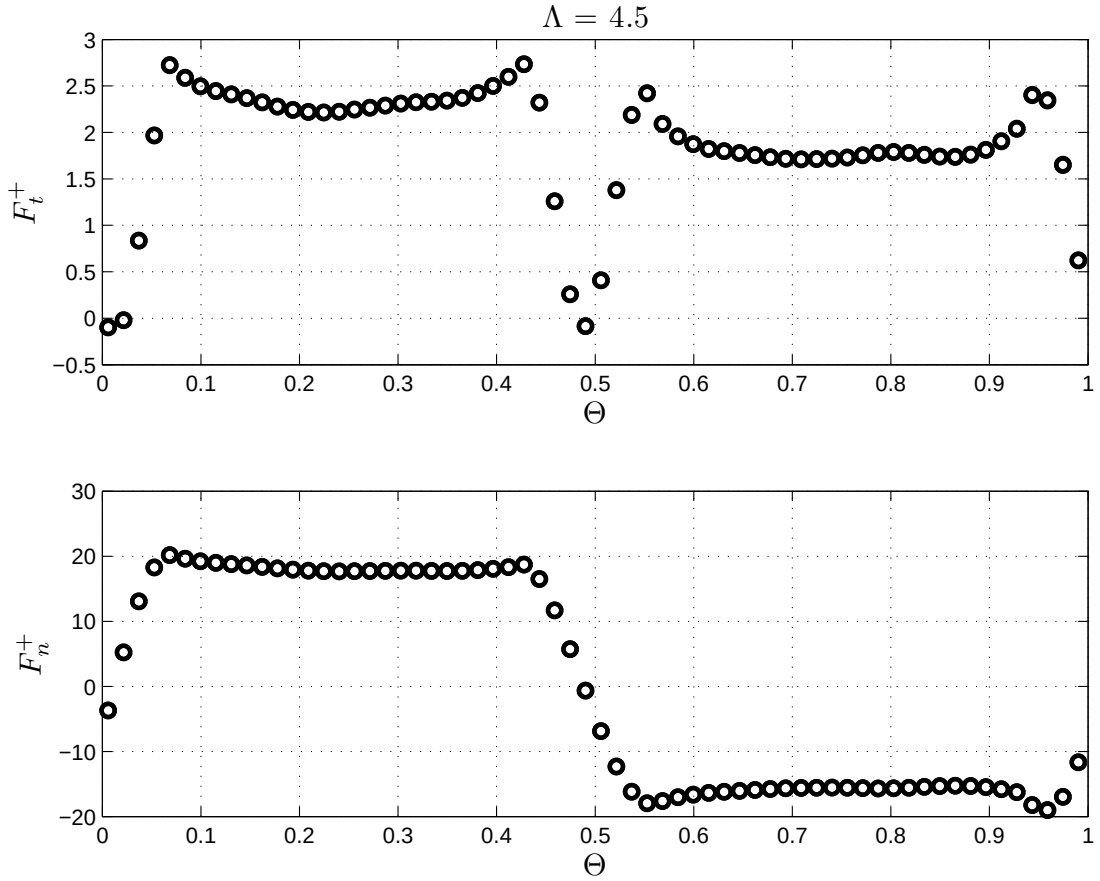

Figure 3.14: *Predictions by the vortex model for case A with 3 blades: an example of the forces on a blade during the final two revolutions (81 and 82) of a Moonraker after* $\tau = tU/W = 40$. *Incremental azimuth:* $\Delta\Theta = 1/64$ *for revolutions 79-82;* $\Delta\Theta = 1/32$ *for revs. 75-78;* $\Delta\Theta = 1/16$ *for revs. 1-74.*

High efficiencies are possible for case A (plotted in Figures 3.14-3.16) because of the low drag at high Reynolds numbers, the theoretically infinite blade aspect ratio, and the lack of practical losses such as track friction, chain meshing, drag on carriages, and other mechanical losses. These high efficiencies would not be possible on a practical device, but its simulation is useful: firstly to explore the potential of the Moonraker, and secondly to investigate the performance of the vortex model in extreme cases. The results for case A (in Figure 3.16) show a peak power coefficient of 0.65, which is 1.5% above the theoretical limit of 0.64 for tandem actuator surfaces. Chapter 5 deals in more detail with comparisons between actuator surfaces and the vortex model, showing that the vortex model consistently predicts higher thrust and power than linear momentum theory (from which the limit of 0.64 is derived), and discussing this issue further.

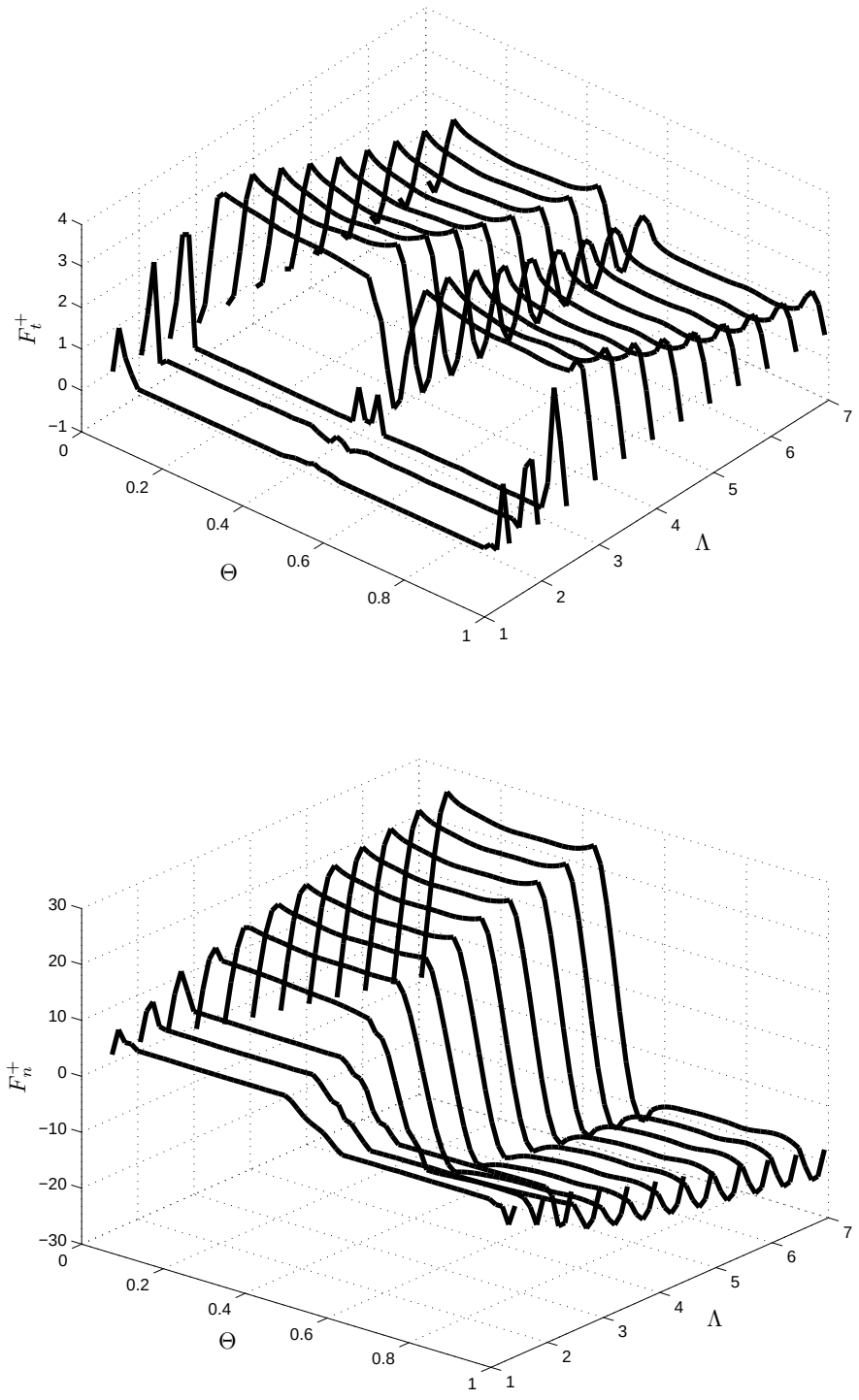

Figure 3.15: *Predictions by the vortex model for case A (parameters as Figure 3.14).*

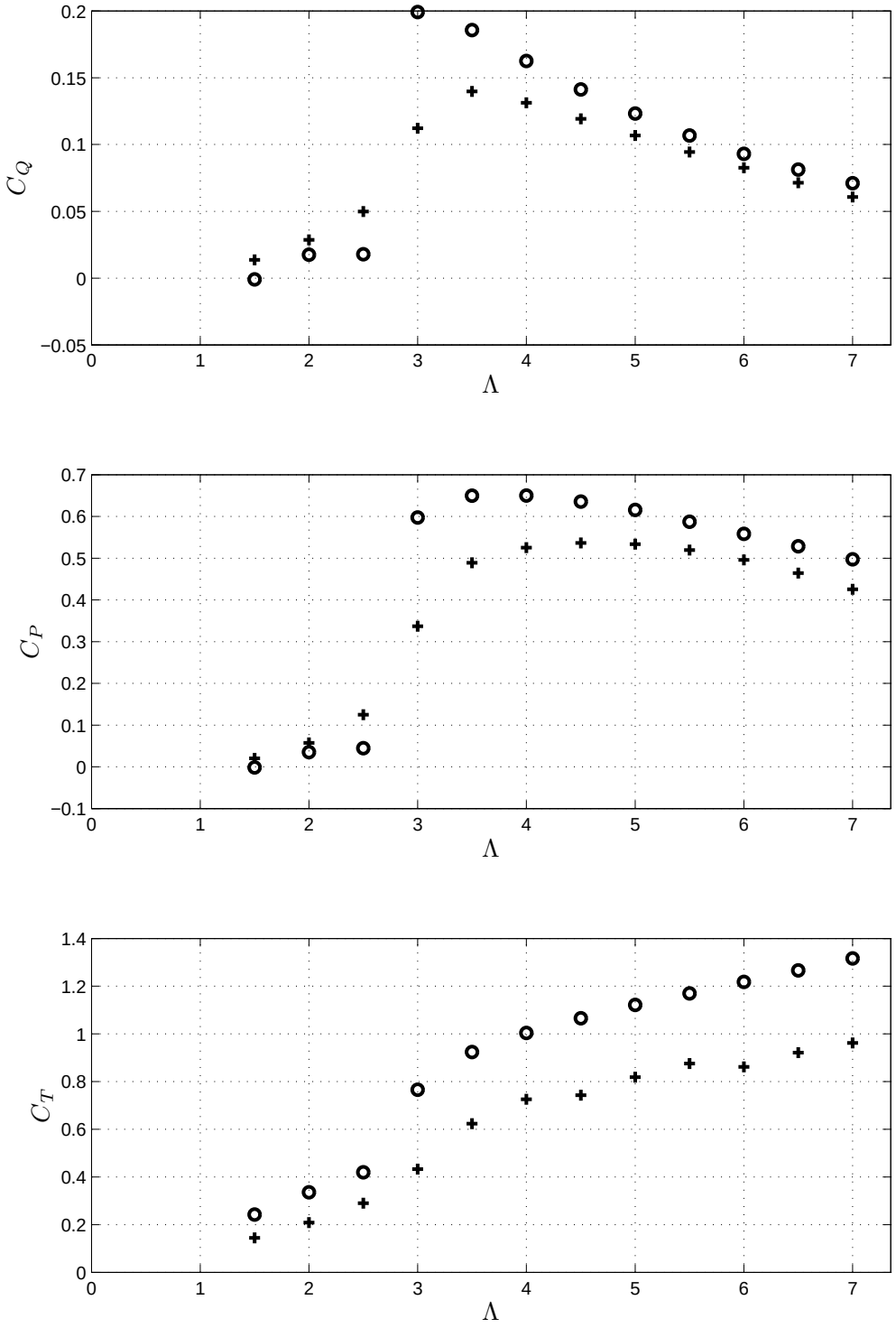

Figure 3.16: *Torque coefficient, C_Q, power coefficient, C_P and thrust coefficient, C_T vs blade speed ratio Λ predicted by the vortex model for a case A Moonraker ($\circ$) and equivalent Darrieus ($+$), with the same parameters as in Figure 3.14.*

3.6.3.3 Case B

The sole difference between case A and case B (see Table 3.3) is that in case A the blade aspect ratio is infinite, i.e. there is no induced drag, while in case B the blades have an aspect ratio of 20. This is a relatively high aspect ratio, probably near the limit of what is practically possible in terms of blade strength. Therefore case B serves to illustrate the effect of including induced drag in the vortex model and represents, at this early stage, the best estimate of the hydrodynamic performance of a Moonraker configuration which might possibly be built. Such an estimate is only a theoretical exercise until the model can be validated - validation is discussed in Chapter 4.

Figure 3.17 plots the tangential and normal blade forces from case B, for a typical blade speed, showing the same characteristic pattern as found in case A (for comparison, see Figure 3.14). For case B, which includes induced drag, the normal force, F_{n}^{+}, is only slightly reduced in magnitude - this is the loss of lift associated with the change in angle of attack due to the trailing vortices. A more substantial effect is seen in the tangential force, F_{t}^{+}, because it is so sensitive to the drag. Comparing Figure 3.17 to Figure 3.14, the finite blade correction reduces the magnitude of F_{t}^{+} on the upstream pass by about half; subsequently on the downstream pass more energy is available so the tangential force is higher in case B than for case A. On average the tangential force is less for case B - the net effect is a reduction in torque and thus power and this is evident in Figure 3.18 which plots the torque and power coefficients for both cases A and B. The reduction is greater for higher blade speeds and the peak power coefficient of 0.527 occurs at a slightly lower blade speed than it did in case A.

Finally, to explore the effect of solidity, Figure 3.19 shows case B with 3 blades ($\sigma = 0.075$) and 4 blades ($\sigma = 0.1$). The higher solidity case shows the torque and power curves shifted to the left on the $C_{\mathrm{P}} - \Lambda$ and $C_{\mathrm{Q}} - \Lambda$ graphs as expected. The blade speed below which stall occurs has not shifted as much, so that the peak power occurs at the stall point; the peak power is lower for the higher solidity.

The resolution of the calculations is high enough for convergence (i.e. $\Delta\Theta$ is low enough that it does not affect the results), however there is a requirement for higher resolution in the calculations in order to get a more accurate integral of the blade forces (average blade forces). The key areas for improvement are on the curved areas of the blade path. However, until a dynamic stall model is implemented, such improvements are of limited value, because the behaviour of the blades in that part of the path is highly dynamic. For now, at this early stage, the predictions are of a high enough quality to warrant experimental measurements for comparison.

Numerical results for case C are presented in Chapter 4, where they are compared to experimental measurements.

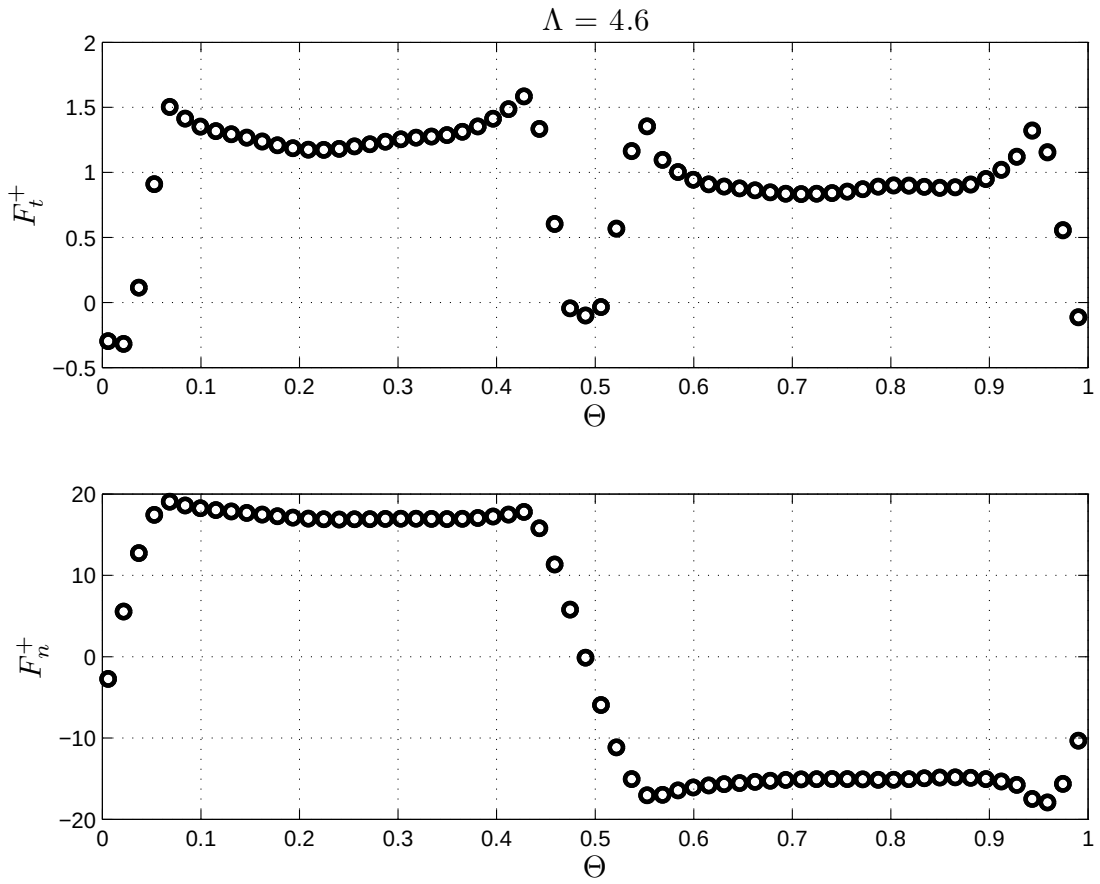

Figure 3.17: *Predictions by the vortex model: an example of the forces on a blade during the final two revolutions of a Moonraker after $\tau = tU/W = 40$ using the configuration of case B with 3 blades and the computational parameters given in Figure 3.14.*

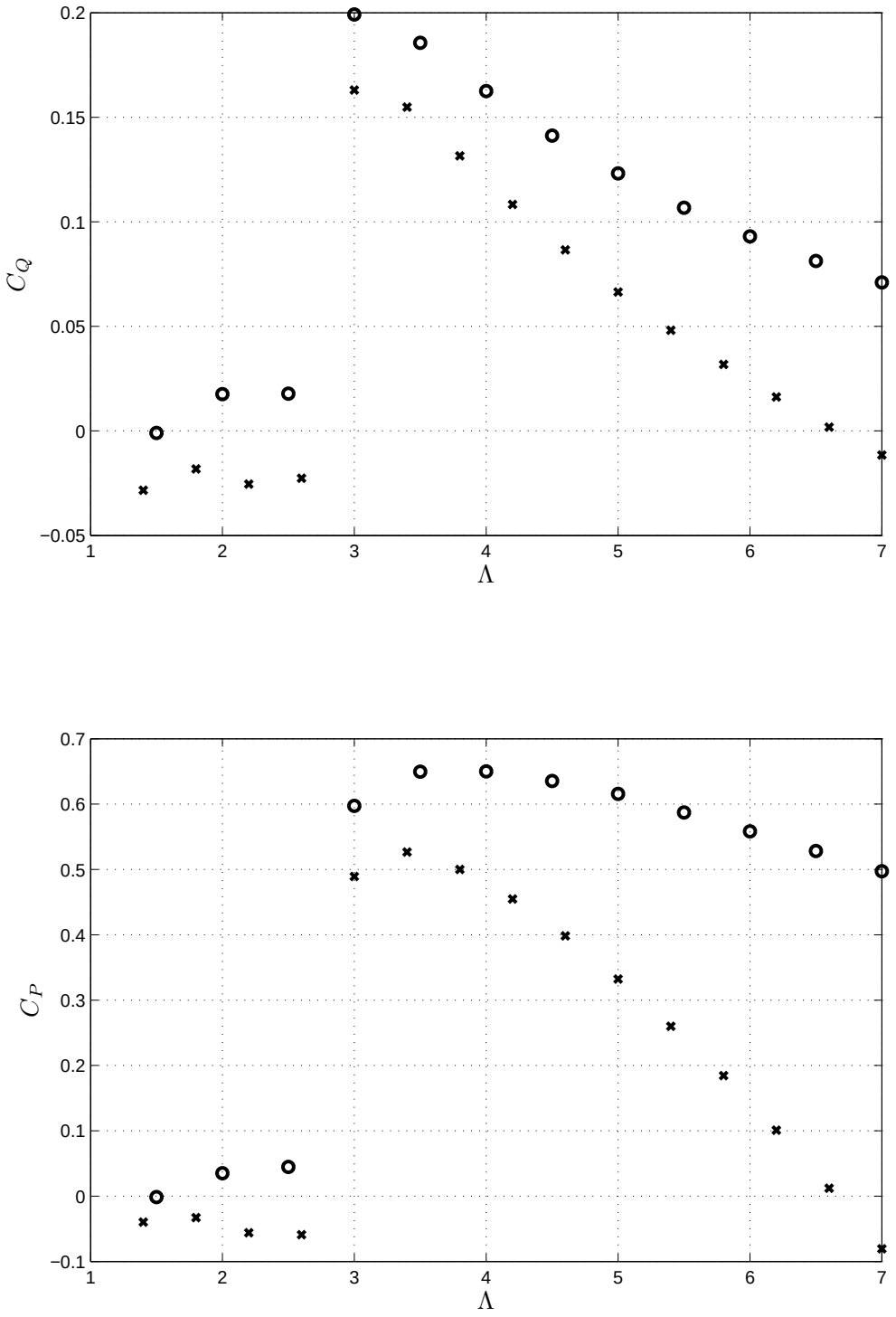

Figure 3.18: *Predictions by the vortex model for a Moonraker with case A, $AR = \infty$ ($\circ$) and case B, $AR = 20$ ($\times$): power coefficient, C_P and torque coefficient, C_Q vs blade speed ratio Λ. Computational parameters are as in Figure 3.14.*

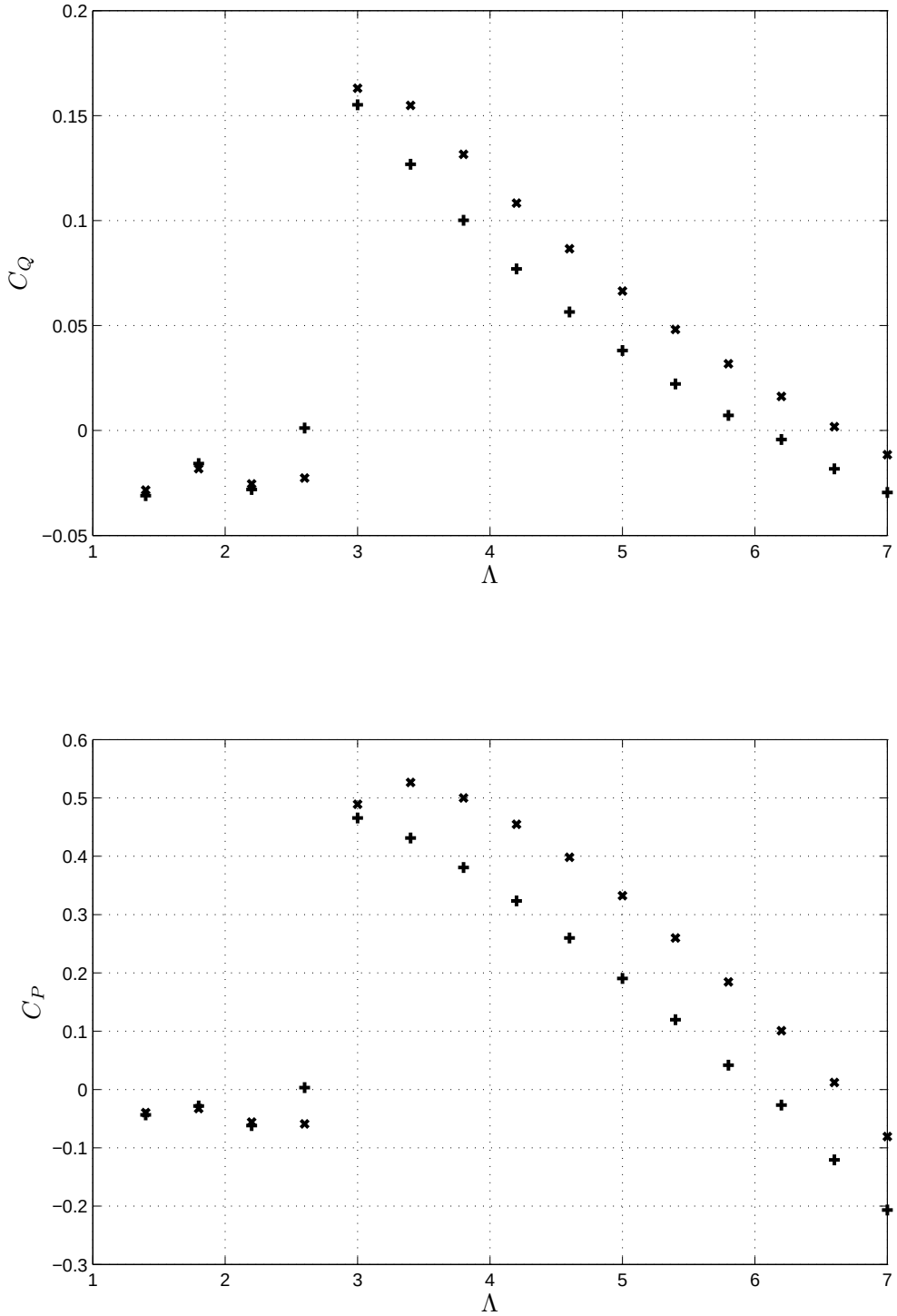

Figure 3.19: *Predictions by the vortex model for a Moonraker with case B, 3 blades (×) and case B, 4 blades (+). Computational parameters same as Figure 3.14.*

3.7 Summary and conclusions

This chapter presented a series of predictions of blade forces on cross-flow turbines. Initially the blade element momentum (BEM) model was introduced, which is the standard tool for analysis in the wind and tidal turbine industries and the BEM model was used to illustrate the effectiveness of a blade moving across the flow in generating a high power coefficient.

Following this the vortex model, originally developed by Strickland et al. (1981) at Sandia National Laboratories, was employed in this work and modified to accommodate the oval blade path of a Moonraker. The model was implemented in Matlab in two-dimensions, and a three-dimensional model was discussed here but not implemented due to time constraints. The vortex model was subjected to a series of tests: initially it was applied to a Darrieus turbine, showing close agreement with the original results of Strickland et al. (1981). Following this the vortex model was directly compared to the results of Gretton (2009) for a Darrieus turbine. Gretton (2009) used multiple streamtube BEM model based on the method of Read and Sharpe (1980), and a RANS model using a commercial solver (CFX). The vortex model and the multiple streamtube BEM model show very close agreement. Their comparison with the RANS model showed fair agreement at high blade speeds, and partial agreement at lower speeds but also significant disagreement which can be attributed to the lack of dynamic stall model in the BEM and vortex models. This highlights the importance of the dynamic stall model, which it is recommended should be implemented in any further work.

The vortex model was then used to simulate a Moonraker, with sets of simulations of a Moonraker at full scale being presented in this chapter, both with and without the correction for finite blade length. For the ideal case of infinite blades, simulations predicted a 21% increase in peak power coefficient for the Moonraker compared to a Darrieus turbine with equivalent configuration, while the thrust per unit power on the Moonraker at peak power is approximately 2.6% higher than that on the Darrieus when it reaches peak power. The effect of the finite blade corrections was to reduce the peak power coefficient, and to shift the power curve slightly to lower blade speeds.

In summary of the work in this chapter:

1. The BEM model shows that a single row of translating lifting blades is very efficient and approaches the Betz limit.

2. The BEM model cannot account for two rows of blades of arbitrary spacing and so it was not applied to the Moonraker.

3. The vortex model in two dimensions has been applied to the Darrieus turbine, showing close agreement with the original vortex model of Strickland et al. (1981), and the BEM model of Gretton (2009). Comparison with the RANS model of Gretton (2009) showed fair agreement at high blade speeds, but disagreement with the RANS model at low speeds due to the lack of dynamic stall model.

4. The vortex model in two dimensions was applied to the Moonraker, showing a 21% increase in peak power relative to an equivalent Darrieus turbine, and an increase in thrust to power ratio (at the speed at which peak power occurs on each device) of 2.6%.

The further work that arises from Chapter 3 is listed below, most of which is then presented later in the thesis as indicated:

1. Experimental measurements of blade forces on a Moonraker are required for comparison with the predictions of the vortex model (validation) - this is the subject of Chapter 4.
2. Given the discrepancy between the vortex model and linear momentum theory, a more direct comparison would be useful: a simplified vortex model of energy extraction could be used to investigate further the difference between the vortex model and linear momentum theory - this is the subject of Chapter 5.
3. The application of the BEM model in its current form to the Moonraker would make an interesting exercise and could be compared with the experiments presented later in this thesis.
4. In order to employ the BEM model to the Moonraker, a theory for actuator surfaces in close proximity is required necessary. The vortex model developed in Chapter 5 can be used for this, and this is addressed in Chapter 5.
5. There is an outstanding need to include a dynamic stall model in the vortex model. This is recommended for future work.
6. The vortex model could be extended to three dimensions, to accommodate a Moonraker in unbounded flow. This is recommended for future work.

Chapter 4

Experimental Moonraker device

4.1 Introduction

This chapter describes physical experiments with Moonraker devices at a laboratory scale, with the purpose of producing experimental measurements that can be compared to predictions from the previous chapter. Two lab-scale Moonrakers were built and tested, the first of which was mainly a vehicle for learning, and the second of which produced quantitative data and is therefore the main focus of this chapter.

The focus of this research is on the hydrodynamics of the Moonraker: the forces exerted on the blades by the water. The most economical way to carry out this research is in a laboratory, but it is important that the results are of use in developing the Moonraker for its intended use in the ocean on a much larger scale. Dynamic scaling of the hydrodynamics is therefore the first issue that is discussed in this chapter, beginning with the Reynolds number, Re, which is the ratio of inertial forces to viscous forces in a fluid. Froude scaling is also discussed, along with the relevant non-dimensional parameters that are specific to the Moonraker. It is shown that valuable measurements can be made at the laboratory scale, subject to certain limitations.

The discussion of scaling leads to a parametric specification of a lab-scale experimental device, which is given in this chapter and is followed by a summary of the design and development of such a device, which was built and tested in the water tanks at UCL and QinetiQ. A novel instrumentation system was developed that was sealed inside one of the blades and measured the two-axis loading on the blade (tangential and normal to the blade's motion). Measurements over a range of blade speed ratios $1 < \Lambda < 7$ were attempted, though in practice were limited to $\Lambda < 5$. The blade Reynolds number was maximised, with a target of ~150,000 but in practice this was limited to a range of 65,000–112,000. The experimental method and results are presented compared to predictions by the vortex model, followed by a summary and discussion of results.

4.2 Scaling and parameter selection

The bulk motion of the fluid through and around the Moonraker can be scaled using the Reynolds number $Re = Uh/\nu$ where U is the speed of the currents and h is the height of the device. A 20 m high device in a 2 m/s current will have $Re \approx 4{\times}10^7$. The flow is clearly inertially dominated and this is expected to continue down to a scale around $Re = 10^3$ (see Chapter 5), which can be achieved in a reasonably small laboratory. For example, the flume at UCL is 18 m long, 1.2 m wide, and up to 0.7 m deep; this can easily host a Moonraker approximately 0.2 m high and 0.9 m wide in currents on the order of 0.5 m/s. The bulk flow in the lab would then have $Re = 10^5$ which is clearly still inertially dominated and useful experimental measurements are therefore possible (see Chapter 5).

However, it is also important to consider the fluid flow on the scale of the blades, whose chords are an order of magnitude smaller than the device itself; this is the smallest scale of fluid motion in the system (other than turbulence, which is neglected here). It is the flow around the blades and the wake that they shed which originally causes the bulk momentum reduction of the fluid; from a fluid dynamic perspective it is this blade chord scale that is the essential driving mechanism of the whole system. Any experimental measurements of the interaction of the blades and the fluid must be taken at a scale where that interaction is principally the same as it is at the scale at which the Moonraker is intended to be used.

A large scale Moonraker (or any device) is likely to have a blade chord of about $c = 2$ m, and when moving at three times the fluid speed, i.e. about 6 m/s, has $Re_c \approx 10^7$ which is inertially dominated. However, for the small scale device mentioned above with a width of $W = 0.9$ m, if it is has a solidity of $\sigma = Nc/W \approx 0.1$ where N is the number of blades, then the blade chord will be $c = \sigma W/N$. Even with only 3 blades, this gives $c = 0.03$ m. Such a small blade moving at three times the fluid speed (i.e. at 1.5 m/s) has $Re_c = 4.5 \times 10^4$. This is inertially dominated and the behaviour of the blade (its lift and drag as a function of angle of attack) is still qualitatively the same: the lift increases approximately linearly with angle of attack until stall, at which point the lift drops off and the drag increases dramatically.

However, while the regime of behaviour is the same, at scales as small as $Re_c = 10^4$ the boundary layer on the blade is of considerable thickness: the drag will be higher, and the stall angle will be significantly lower. This is evident in the blade section data presented in Section 2.4.4. This has a drastic impact on the performance of the device because performance depends on, and is very sensitive to, the lift-to-drag ratio of the blade.

If the blade Reynolds number can be made to exceed $Re_c \sim 10^5$ then the behaviour of the blade will more closely resemble that of a full scale. For $Re_c > 10^6$ the behaviour is essentially unaffected by the scale of the device. These conclusions are made based on an inspection of experimental data, for example that which is presented Section 2.4.4 or alternatively see Abbott and Doenhoff (1959).

The Froude number is the ratio of the water velocity to the speed of propagation of a surface wave: $Fr = U/\sqrt{gz}$ where g is acceleration due to gravity and z is the water depth. Tidal

stream turbines sit in flows where $Fr < 0.2$, for example a 2.5 m/s current in 30 m water depth gives $Fr = 0.15$. As the rotors of tidal stream energy devices are below the water surface, the key effect of the free surface (assuming no waves) is to provide a boundary in relatively close proximity to the rotors, and this has been modeled by Whelan et al. (2009).

Although the free surface can deform and generate a hydrostatic pressure gradient, the deformation at low Froude numbers is relatively small so that the effect of the free surface is very similar to that of a rigid surface. This is verified by the model of Whelan et al. (2009), which shows that the effect of the free surface at low Froude numbers ($Fr < 0.2$) compares very closely with those for the limiting case $Fr \to 0$. The latter case is effectively assuming that the surface is rigid, and is identical to the simplified model presented earlier in equation (2.64). The problem of free-surface proximity is therefore considered here as a blockage problem - based on the blockage ratio B =device area/flow area, and this can be relatively easily held constant at a lab scale. The implication for experimental scaling is that if the Froude number is low, then it does not need to be identical when performing lab-scale experiments. Towing at 0.5 m/s in a 1 m channel depth gives $Fr = 0.16$.

The blockage ratio, B, is zero for the predictions in Chapter 3 so, for the sake of comparison, should be kept to a minimal value in the experiments.

In conclusion, assuming the Froude number is low ($Fr < 0.2$) the blade Reynolds number is the most important scaling parameter: the higher this is, the more closely lab measurements will represent full scale behaviour. If the blade Reynolds number is $Re \gtrsim 10^5$ then similar behaviour can be expected at a large scale.

4.2.1 Lessons learnt from the first prototype, PI

A small prototype device, known as PI, was built as suggested above, 0.9 m wide and 0.2 m high, to fit in the flume at UCL and is pictured in Figure 4.1. Blades with a symmetric profile, 12.7% thickness, and a 30 mm chord were employed. The blades were secured onto toothed belts; the pulleys were attached to shafts which were cantilevered from above the water, with the bearings above the water. A friction brake was included on one of the shafts (out of the picture in Figure 4.1), in order to measure shaft torque. The most fundamental problem with this device was the large frictional forces caused by the bearings and the toothed belt. Bearing friction was reduced by removing the seals and cleaning the grease out and this reduced the contribution of bearing friction down to 25% of the total friction. The remaining friction was due to the toothed belt: each rubber tooth is compressed slightly when it meshes with the pulley, and at operational speeds with four pulleys this amounted to about 1400 tooth meshes per minute. Approximate measurements showed that the torque required to overcome the friction was approximately double that produced by any reasonably efficient device operating with the same cross-section area and the same flow speed.

The problem of belt and bearing friction raises two important points when considering the hydrodynamics of a Moonraker. Firstly, frictional forces are proportionately much larger at a lab scale: they grow linearly with velocity, while hydrodynamic forces grow with the square of

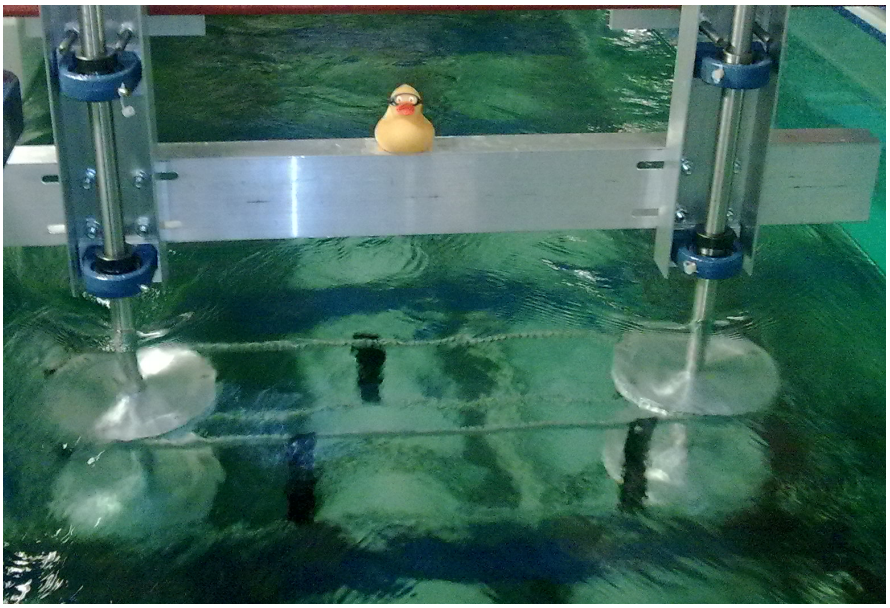

Figure 4.1: *Photo of the first prototype, PI (only 3 of the 5 blades are in view).*

velocity. The implication here is that it may be necessary to assist the device in overcoming the friction at lab scale.

The second implication is that, with such high friction, perhaps a belt system is not a practical solution for this type of device - after all, although lab scale friction is well known to cause problems, it is possible to generate positive shaft torque in the lab from axial-flow and cross-flow (Darrieus) turbines and this has been achieved in the same facilities at UCL. Perhaps such mechanical issues are the main short-coming of the Moonraker device? This second point is not a hydrodynamic issue and is beyond the scope of this thesis.

Following the experience with PI a second device, known as PII, was developed. The lessons learned from PI, including those mentioned above, informed some important characteristics of PII, which were incorporated from the outset when designing the device:

4.2.2 Key features of PII

1. Tracks

It is impractical to use a tensioned belt or chain to resist the high streamwise forces on a tidal device, and attempts to do so on a lab scale with PI were also unsuccessful. The tension required in the belt depends on the amount of deflection that is permitted. A first order estimate of the tension in the belt is illustrated in Figure 4.2a: given a deflection angle, θ, from equilibrium considerations the tension in the belt is larger than the thrust on the belt by a factor $1/\sin\theta$ which in practice will probably be on the order of 10. The fundamental engineering task of resisting the large thrust in an economic manner has therefore been made significantly more

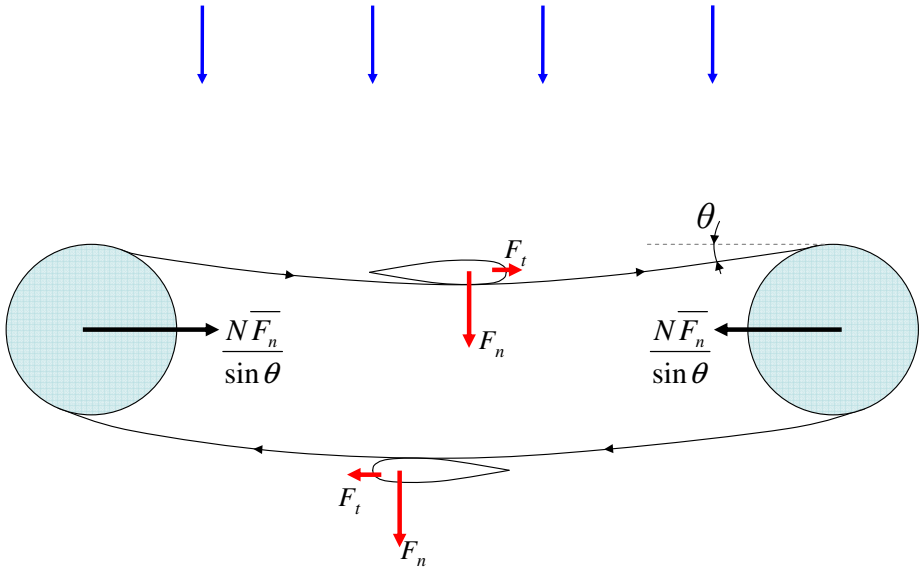

(a) *Diagram of a belt system: the thrust force is magnified by a factor* $1/\sin\theta$.

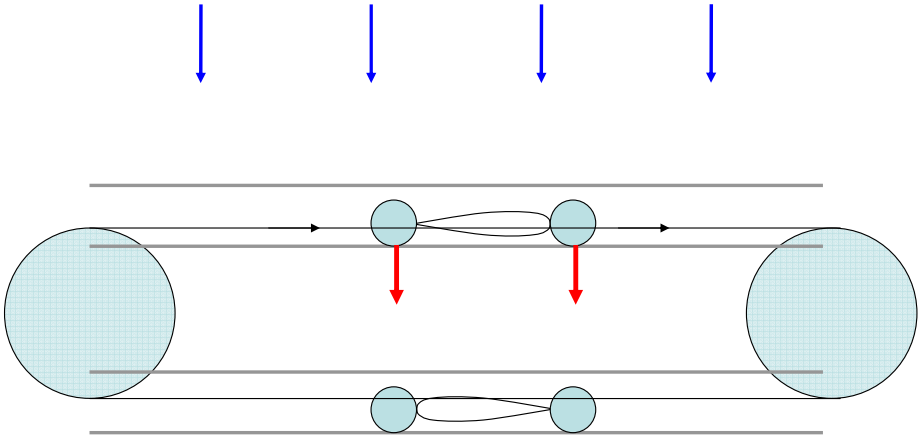

(b) *Diagram of a track system, which is the basis of PII and does not magnify the thrust force.*

Figure 4.2: *Evolution from a belt system to a combined belt and track system.*

difficult. Beyond these considerations, which could perhaps be overlooked when creating small scale prototypes, the following issues arise: firstly, the friction due to the required belt tension was extremely high even at such a small scale, and secondly it is not practical to measure the force on a blade when it is moving along such a flexible path.

The forces on the blades, which are almost entirely horizontal, can alternatively be resisted using tracks as illustrated in figure 4.2b: the blades run along a rigid track and pass streamwise forces (F_{n}, normal to the blade's motion) on to the track. The component of force tangential to the blade's movement (F_{t}) is passed on to a chain. This is the useful part of the force on the blade and, via the chain and sprocket, it contributes to the shaft torque.

2. Chains and sprockets

The top and bottom of each blade must be synchronised and therefore either a toothed belt or a chain must be used for power transmission. Given that the meshing of a toothed belt on PI caused massive friction, for PII a chain and sprocket system was trialled.

3. Motor system

The purpose of the experiment is to quantitatively assess hydrodynamic forces on the blades of a Moonraker. This can be achieved by assisting the motion of the blade using a motor system (motoring or generating accordingly) to overcome any friction between the blade and the motor shaft. The PI was motored in an *ad hoc* way with an electric drill, and this led to the suggestion for a dedicated motor system, which was incorporated in PII from the outset.

Most of the friction of the PII system came from the meshing of the chain and from the pulley system. Although it was hoped that a chain system would offer less friction than a toothed belt, it was still expected to have a high resistance hence including a motor system in the design for the PII. The strategy for PII was therefore to use a motor system to enforce the blade speed, and to make direct measurements of the blade loads (which required a new, larger device - see below and Section 4.4).

4. Blade force measurement

Measuring the shaft torque alone would not give sufficient data on the hydrodynamic forces on the blades. Given that the blades were to follow a prescribed path on the PII (because tracks were to be used), at a prescribed speed, measuring the fluid loading on the blade was possible and is discussed further in Section 4.4.

Most of the above points led to the design of a new prototype, rather than modifying the PI: to incorporate tracks required a new design; to incorporate a chain system required a new design; the PI was too small to incorporate blade force measurements (see Section 4.4). Additionally, by designing a new prototype, PII, a larger device was possible; the motivation for a larger device is discussed in the following section.

Parameter	Definition
W	Device width (m)
N	Total number of blades
c	Blade chord (m)
$\sigma = Nc/W$	Solidity

Table 4.1: *Key parameters on the PII, in addition to blade Reynolds number, Re_c.*

4.2.3 Parameter selection

The blade Reynolds number has been identified as the most important scaling parameter: it must be maximised. We now turn to the relative dimensions of the Moonraker and explain the selection of these parameters for PII, listed in Table 4.1.

The experimental device has the following requirements:

1. The number of blades is large ($N \gg 1$) , in order to approximate the large scale concept.
2. Blade Reynolds number is large ($Re = \Lambda U c/\nu > 10^5$), i.e. maximise blade chord (c) and/or flow speed (U).
3. Induced drag on the blades must be minimised - the height is much larger than blade chord ($h \gg c$).
4. The frontal projection must be like a 'letterbox' - i.e. width is larger than height ($W > h$).

Parameter selection for the PII begins with an assumption about the solidity, which predictions from BEM and vortex models in Chapter 3 suggest is likely to be in the region $0.05 < \sigma < 0.25$. We then follow the above points, in the order given, which leads to the requirement of a device which is either very large, or operates at very high speed. An exploration of this is illustrated in Table 4.2. Three chord sizes are considered and two flow speeds are considered; all six combinations in Table 4.2 have the same blade aspect ratio ($h = 8c$) and the same width to height ratio ($W = 4h$) and therefore have the same ratio $c/W = \frac{1}{32}$. Solidity is therefore $\sigma = N/32$ for all variants, i.e. one blade gives $\sigma = 0.03$ and eight blades give $\sigma = 0.25$.

There are practical limits to the thrust that can be resisted, firstly because of cost implications, and secondly because towing facilities have a limited thrust because they were originally designed to tow streamlined bodies. QinetiQ Haslar, which has the largest towing facility in Europe, has a thrust limit of 1500 N.

Clearly a device larger than PI is necessary; but there are practical limits to the size of a device: firstly it must fit in the water tank in which it is tested, and secondly it is desirable to keep the blockage, B, minimal. In the UCL towing tank, which is 2.5m wide and 1m deep, it is not possible to meet the above 4 criteria *and* to minimise blockage. Therefore the strategy with

Speed U (m/s)	Chord c (mm)	Blade speed ratio $\Lambda = V/U$	$Re = \Lambda U c/\nu$	Blade length (m) $h = 8c$	Device width (m) $W = 4h$	Thrust (N) ($C_T = 1$)
1	25	3	75,000	0.2	0.8	80
1	50	3	150,000	0.4	1.6	320
1	75	3	225,000	0.6	2.4	720
1.5	25	3	112,000	0.2	0.8	180
1.5	50	3	225,000	0.4	1.6	720
1.5	75	3	337,500	0.6	2.4	1620

Table 4.2: *Exploration of the parameters of the PII.*

the PII experiment was to develop a device that meets the 4 criteria above and will *fit into* the UCL tank. This would allow development and testing of the device in-house, and measurements in low blockage could then be made off-site in a larger tank.

A towing speed of 1 m/s was selected to limit the forces on the system and to increase the ratio W/S (see discussion below). A blade chord of 60 mm was chosen, which gives a typical blade Reynolds number of 180,000, a blade length of 0.48 m, and an overall device width of just under 2 m. The expected thrust is about 500 N.

4.2.4 Blade row spacing

The streamwise distance between each row of blades is $2R = g_M W$ or, in non-dimensional form: g_M, and this is illustrated in Figure 3.1a. Attempts to definitively determine the hydrodynamically optimum spacing, s, are described in Chapters 5, however this work is incomplete.

Hydrodynamics aside, there are still important practical implications of the blade spacing, g_M because the value of g_M and W determine the radius of the blade path. In the ocean devices can be very wide, in which case $g_M \to 0$ and the radius R can then be adjusted significantly without affecting g_M. However in the laboratory, where the width, W, is limited, g_M is finite and this will affect the blade path radius, R. In the limit $g_M \to 1$ the blade path is circular and the device is a Darrieus turbine: this should be avoided as it is not the purpose of the investigation, so the row spacing should be smaller than the device width. This implies a small turning radius, $R = g_M W/2$, for the blade, which in turn implies rapid acceleration of the blades as they change direction:

$$\text{centripetal acceleration} = r\omega^2 = \frac{2\Lambda^2 U^2}{g_M W}, \tag{4.1}$$

where the substitution $\Lambda = R\omega/U$ has been used and $R = g_M W/2$. The range of blade speed ratios of interest, Λ, will not change; so that centripetal acceleration depends only on the square of the tow speed, U^2, and inversely on the spacing, g_M. While we seek to minimise g_M, we must

Width, W	1.991 m
Total blade length	0.52 m
Effective blade length, h	0.46 m
Projected area, A	0.916 m^2
Row spacing, S	0.384 m
Geometric ratio, $g_M = S/W$	0.1928
Solidity $\sigma = Nc/W$	0.03 – 0.25
Rated speed, U	1 m/s
Rated power, P_{rated}	200 W_e
Design thrust	500 N

Table 4.3: *Nominal specification for PII.*

also limit the acceleration of the blades i.e. increase $g_M W$.

Some examples of blade acceleration will now be given so that a practical trade off can be made. We therefore look at the effect of g_M and tow speed, U, on the blade acceleration for the example case of $g_M = 1/5$.

On a 2m wide device this would give $g_M W = 0.4$ m. At 1 m/s towing speed this gives a centripetal acceleration of 45 m/s^2, 80 m/s^2, and 125 m/s^2 for blade speeds of $\Lambda = 3$, 4, and 5 respectively. At a blade speed ratio of 5, this is an acceleration of 12g which is very high and illustrates why a faster towing speed is not practical (given the constraints on the geometry): at 1.5 m/s this acceleration would be 27g. A slower towing speed is therefore preferable. The acceleration can be reduced by increasing R, which in a laboratory with limited width also means increasing the geometric ratio, g_M.

Although the accelerations are fairly high and should be reduced if possible, there are three reasons not to increase the radius, R. Firstly, the size of the wheels turning the blades would become large, heavy, and expensive, and the drop on rotational speed would increase the shaft size, weight, and cost, and increase the gearbox size, weight and cost. Secondly, the ratio $2R/h$, would exceed 1 and this would not be representative of a large scale device - if the blades are 20 m long, then rows of blades are unlikely to be spaced more than 20 m apart in the streamwise direction. Thirdly, the proportion of the blade's movement that is along a straight path would be reduced: this would not be significantly different from a Darrieus turbine and would not be representative of the Moonraker concept.

4.3 PII device design

Following the discussion in the previous section, the nominal specification for the PII was chosen and this is given in Table 4.3. This section presents a summary of the design of the device based on this specification; Figure 4.3 is a CAD rendering of the whole PII device.

4.3.1 Structural design

The first purpose of the structure is to provide a track, the second purpose is to resist the thrust imposed on the track, and the third purpose is to attach the shaft bearings to a

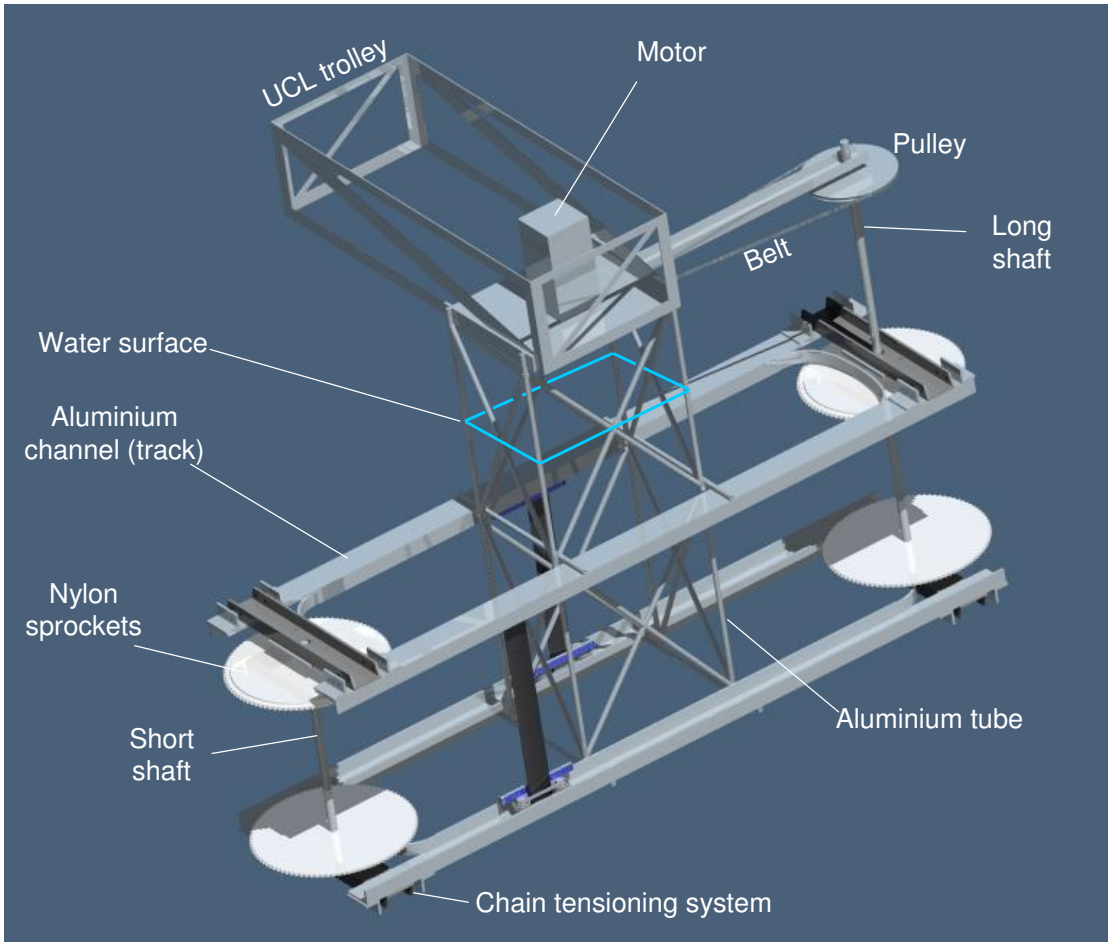

Figure 4.3: *CAD rendering of the PII device attached to the towing carriage at UCL. Two blades are shown, and the chain is not present except for short lengths attached to the blade.*

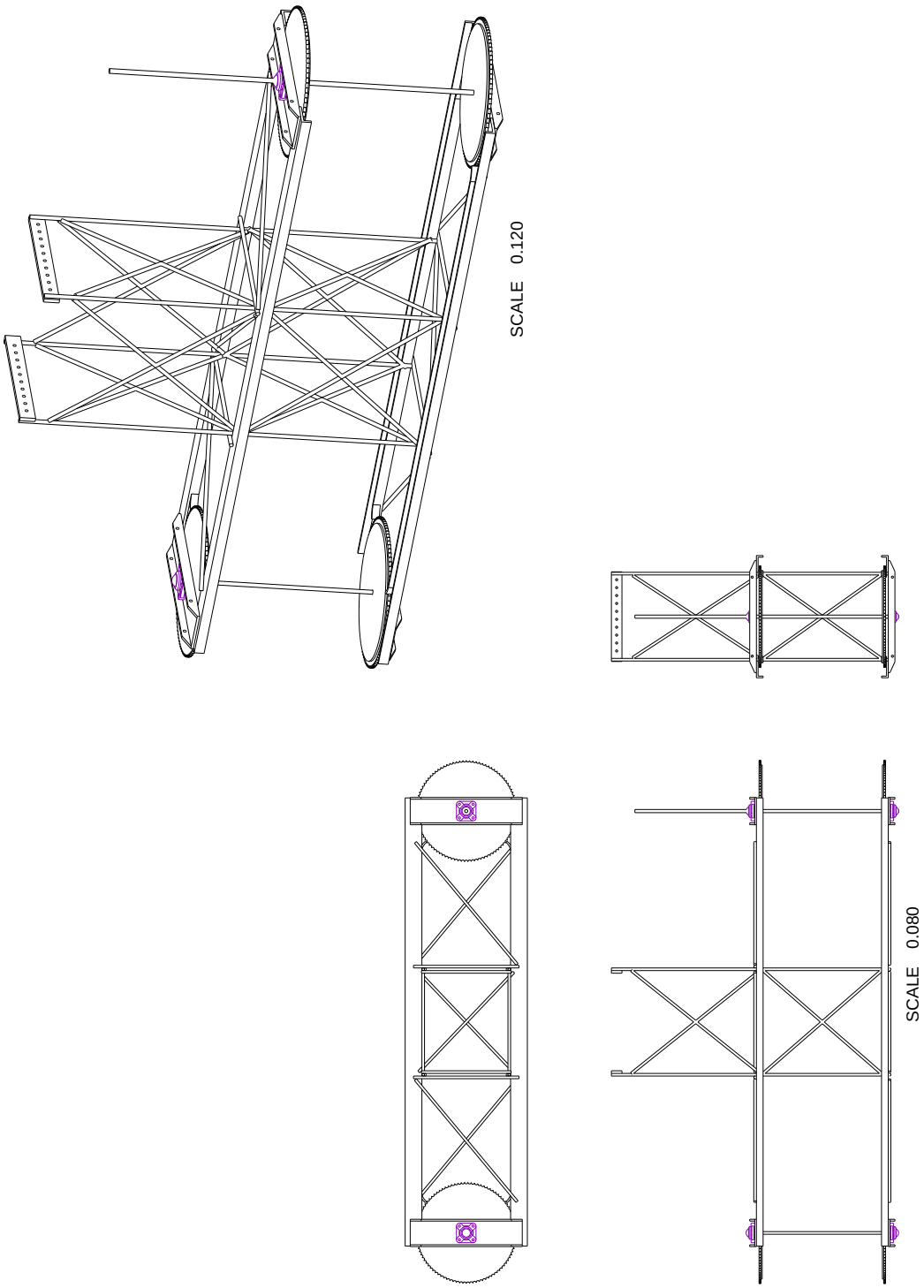

Figure 4.4: *Drawing of the aluminium PII structure. Bearings, sprockets, and shafts are included. The pulley and its supporting structure are not shown.*

'fixed' point (in this case, a towing trolley) so that the device can be secured and torque can be transferred.

Channel section was used for the tracks, providing good resistance to bending; aluminium was used for its light weight and good corrosion resistance. The use of channel sections minimised the frontal area of the blade carriages and was relatively cheap: all structural parts cost approximately £500 for the PII. An alternative option was to use an off-the-shelf stainless steel monorail - originally designed for food processing - however this would have cost £6000 for the tracks and carriages alone and was beyond the budget of the PII experiments.

The four aluminium channel sections (upstream, downstream, front and rear tracks) were attached to each other via a space-frame of hollow aluminium tube, creating a high second moment of area. The space frame then extended vertically to connect to the towing trolley. The width of the central space frame structure is based on the width of the UCL towing trolley (380 mm). The basic structural design was analysed using the finite element analysis package ANSYS. Thrust, weight, and lateral loads were applied in combination and in isolation, to find the largest deflection case. The diameter of the aluminium rod was chosen based on a maximum deflection of 1 mm, and avoiding buckling criteria by a factor of 2; a small diameter of the members was desired so that interference with the water flow would be minimised. This resulted in a requirement of 4 mm diameter rod. Although this is theoretically sound, a more conservative 12 mm tube with 3 mm wall thickness was used. This resulted in a much stiffer and stronger structure, with a marginally increased coverage of the frontal area. The interference with the flow was still minimal. The basic structural design is illustrated in Figure 4.4.

4.3.2 Transmission design

A chain and sprocket system was used to transmit torque to and from the blades. Each blade sits vertically and connects at each end to a chain; and each chain turns around a pair of sprockets, which rotate about a vertical axis. An ISO standard 08B chain was chosen, with a 12.71 mm (1/2") pitch. The chain, which can be identified by its bright blue colour in the photos, is a specialist *Renold Syno PC* chain (Renold product no. 1215360) with polymer inner links and nickel plated steel outer links. The chain was chosen because of its polymer links, and the three reasons for this are: lower weight, no corrosion, no lubricant required. The chain tensile strength is nominally 1600 N. The sprockets were chosen according to the requirement that $S = 0.4$ m. The closest standard sprocket size has a pitch circle diameter of 384 mm (95 teeth). Aluminium sprockets are not manufactured this large, and cast iron was deemed too heavy and would have corrosion problems. Therefore a sprocket was cut out of Nylon 6, which is approximately neutrally buoyant in fresh water but may have a limited lifetime. In retrospect a cast iron sprocket may have been useful: it would be cheaper, it could be coated to avoid corrosion, and it would add some much needed inertia to the system. However, the lightweight nature of the sprockets was very helpful when moving the PII into and out of tanks.

The sprockets were connected to the shaft via an aluminium keyed flange which was manufactured in house. The flange then connects via a key-way onto a stainless steel shaft. The

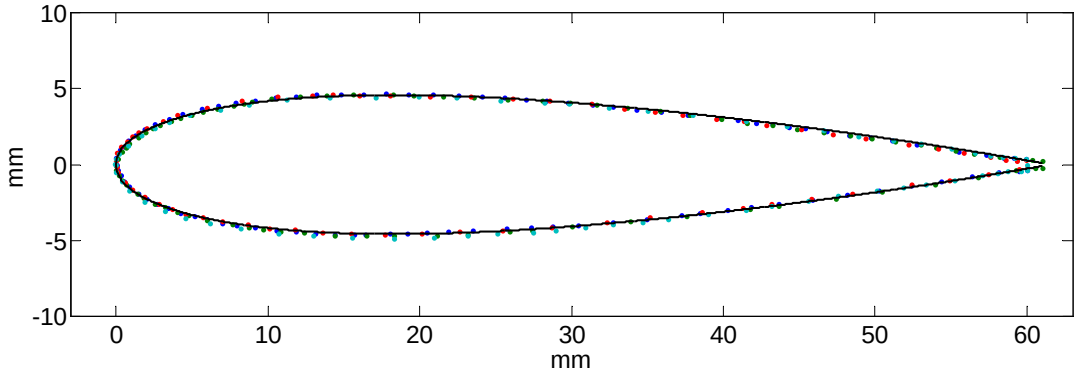

Figure 4.5: *PII blade profile: (•) Measured, (-) NACA 0015.*

shaft is slender and so its diameter was chosen based on a deflection criterion $\delta < 0.1\%$ where δ is the deflection per unit length, and also on torque requirements. The device has two shafts: one shaft is simply an idle wheel that provides a torsional connection between an upper and lower sprockets; the other shaft connects the remaining two sprockets and also protrudes above the water surface where it has a third connection, to a pulley. This shaft has three supports so is statically indeterminate and was designed using ANSYS.

The pulley transmits torque via a belt to the motor, which is situated centrally due to its weight of 8.1 kg. The pulley system has a ratio of 3.75:1 and no further torque reductions (e.g. gearbox) are used. The design torque requirement was based on overcoming a negative power of 125 W, which was derived from a conservative estimated minimum $C_{\mathrm{P}} = -0.25$ which is based on BEM and vortex model simulations in Chapter 3. At a blade speed ratio of $\Lambda = 1.5$ the torque requirement is 16 Nm – i.e. this is necessary to start the turbine. The torque rating dominated the shaft designs: 20 mm diameter stainless steel was used and the two shafts constitute 2% of the projected area of the turbine. This is an improvement compared to 5.6% for the PI, but with the penalty that underwater bearings are necessary. Polymer bearings with stainless steel balls were used; the bearing friction was not a problem due to the strategy of motoring where necessary.

4.3.3 Blades and carriages

Model helicopter blades with a 61 mm chord were used on PII. The blades are mass produced using carbon fibre epoxy composite with a foam inner. The blade manufacturer does not provide details on the blade profile geometry. To ascertain the profile shape, data was extracted using digital photographs, and this process was repeated independently 4 times. The results for one end of a blade are plotted in Figure 4.5, where a NACA0015 is plotted as a solid line. The

profile for the NACA 00 series is

$$y(x) = \frac{t}{0.2} c \left(0.2969 x^{\frac{1}{2}} - 0.1260 x - 0.3516 x^2 + 0.2843 x^3 - 0.1015 x^4 \right), \tag{4.2}$$

where c is the chord length, t is the thickness to chord ratio and x is the normalised position along the chord. Figure 4.5 shows that the blade profile has been extracted with satisfactory repeatability. The data agrees very well with the NACA0015 profile. The blade profile becomes thinner along the blade and drops to 13% thickness at the other end.

The blades were connected to the chain and track via carriages, which are illustrated in Figure 4.6. The carriage was designed to run freely within two tracks, so that it would push against the relevant track depending on the direction of fluid flow. The alternative would be to run the carriage along a central track. This was discarded based on the fact that twice as much frontal area would be required by the carriage due to the wheels on both sides being required to take a full load - a larger frontal area increases the drag proportionately. In retrospect this could have been overcome.

By neglecting the vertical force on the blade, only two wheels were necessary (to resist the streamwise loads on the blade). The bearings were chosen by minimizing the frontal area for a load requirement of 180 N per wheel. Bearings with polymer races were used directly as wheels - the races acted as tyres. The bearings are illustrated in Figure 4.6 and seen in the photograph in Figure 4.7b. Polymer sliders were attached to the underside of each blade (not shown in Figure 4.6) to resist the moderate weight in water of the blade, carriage and chain. The polymer sliders added friction to the system. The slider was close to the attachment of the chain to the blade, so that the moment exerted on the blade by the polymer was small and this is discussed more in Section 4.4.4.

The stability of the carriage in pitch (about an axis parallel to the blade) was considered: the carriage was designed to ensure that both wheels would be in contact with the track at all times. The total load on the blade, which is split between the two wheels, must exceed the product of the moment about the blade multiplied by the distance to each wheel. This was satisfied by more than a factor of ten and in practice the wheels stayed firmly attached to the tracks.

4.3.4 Electrical system

An AC synchronous machine with an internal resolver was used as the motor / generator and the specification is listed in Table 4.4. The combination of a pulley system with a ratio of 3.75:1 and a motor torque of 6.8 Nm gave a system torque of 25.5 Nm. The motor was powered and controlled by an *SEM* controller with full PID control.

The shaft speed was kept constant by the control system. The accuracy and stability of the system was determined by the PID system. The efficacy of the control system was limited by the large ratio of Moonraker inertia to motor inertia, however the shaft speed was kept constant to a satisfactory extent. To quantify the variability of the shaft speed the shaft position, which

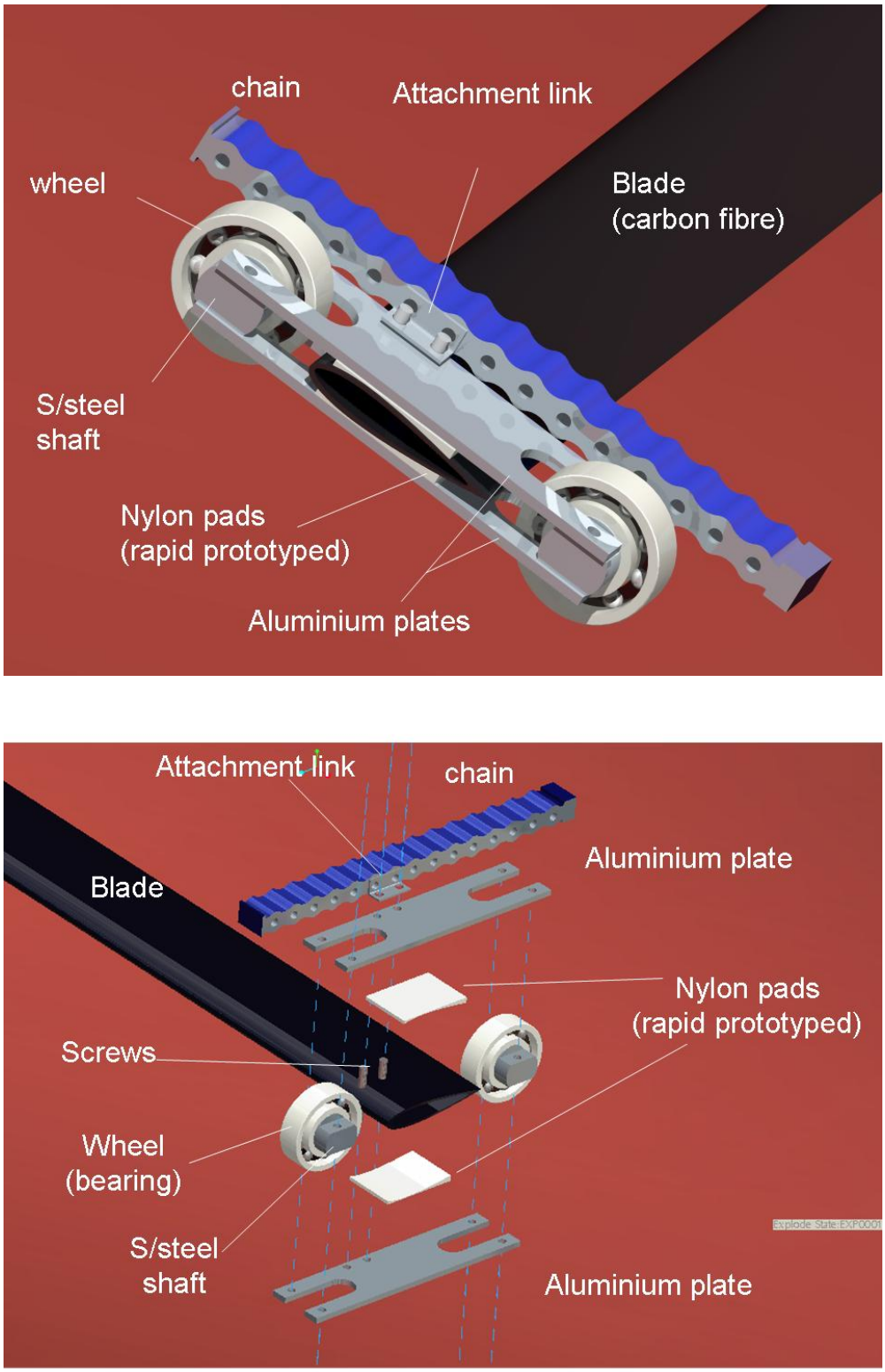

Figure 4.6: *The carriage connected the end of a blade to the track via two wheels, and also to the chain via a K2 attachment link.*

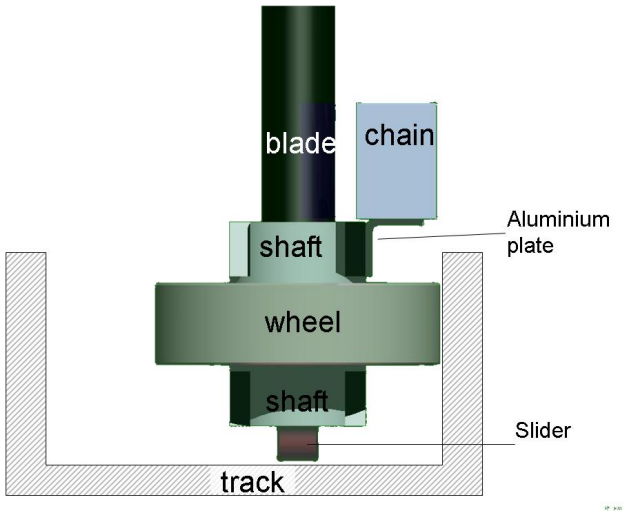

(a) *CAD sketch of the blade and carriage within the track.*

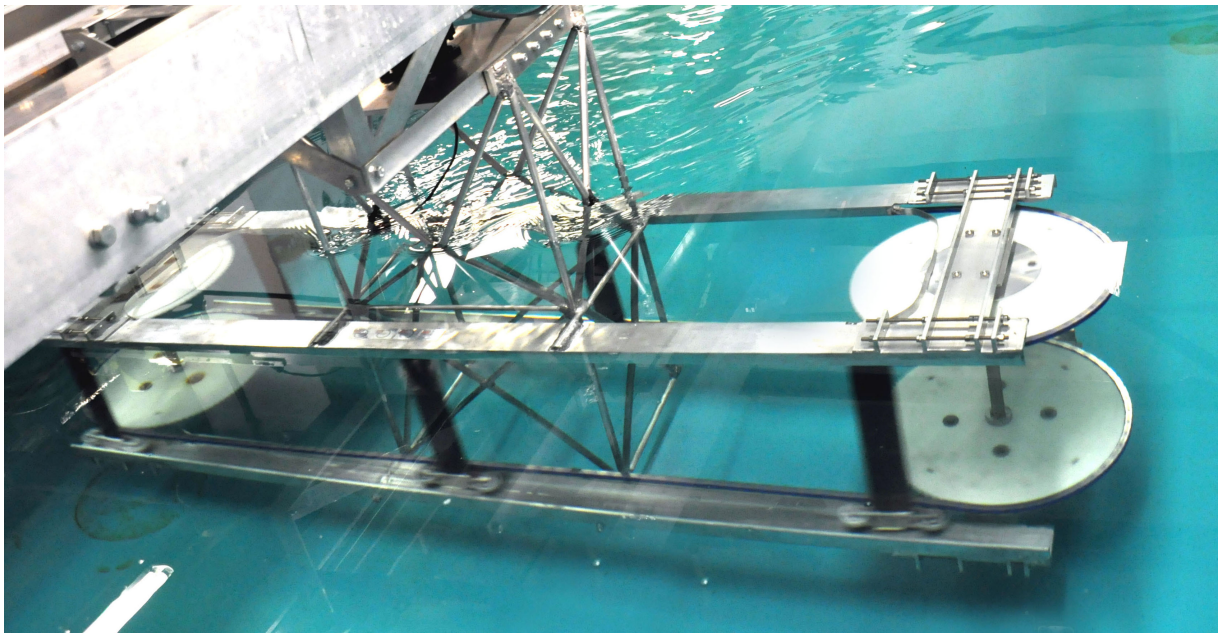

(b) *Photo from above showing blades moving along the track as the PII is towed through the UCL towing tank.*

Figure 4.7: *The blades fit within the two tracks created by the channel section.*

Torque	6.8 Nm
Peak torque	22 Nm
Rotational speed (max)	5400 rpm
Power @ 3000 rpm	1.8 kW
Weight	8.1 kg

Table 4.4: *Specification of the AC synchronous motor/generator*

could be output by the control system, was sampled at 125 Hz, differentiated, and filtered with a third order low pass Butterworth filter at successively lower cut-off frequencies. As the filtering frequency was reduced, the standard deviation of the signal also reduced. Reducing the cut-off frequency removes more noise but also removes actual physical shaft speed variations from the signal. Filtering at 10 Hz, which should be high enough not to filter out the shaft's speed variations, results in a standard deviation in motor shaft speed of less than 5% for all runs. For most runs this standard deviation was below 2%. In future, even more inertia should be added to the Moonraker, e.g. by using cast iron sprockets, so that chain oscillations and fluctuating blade forces have a smaller effect on the shaft speed. It was also possible to record the motor current which, via the motor constant, can be converted to an estimate of the shaft torque. However, the controller could only output one variable at any one time; for most experiments the shaft position was recorded, in order to synchronise blade force measurements; however some torque measurements were also made.

The motor/controller system was also able to act as a generator. A 300 W resistor was included with the system to account for potential shaft power generation in excess of the friction generated by the chain.

4.3.5 Operational experience

This section summarises the experience gained when operating the PII. The device was manufactured and assembled at UCL, where it was also tested in the towing tank which is 2.5 m wide, 1 m deep, and approximately 18 m long. The PII was also tested at QinetiQ Haslar in the ship towing tank which is 12 m wide, 5.4 m deep, and 270 m long. With an area of 0.916 m^2 the PII had a blockage ratio of 0.366 in the UCL tank, and 0.014 in the QinetiQ tank. The maximum Froude numbers were 0.15 and 0.1 at UCL and QinetiQ respectively.

At UCL the device was in the centre of the water column (upper track 250 mm from the free surface). At QinetiQ the device was near the top of the water column because there was not sufficient time to build a frame that allowed the motor shaft to be extended (the motor must remain out of the water). The water level was 75 mm lower than expected at QinetiQ and the water surface was therefore 175 mm from the upper track.

Generally the PII performed well and this is illustrated by the photo in Figure 4.8. In this photo the PII is being towed through the UCL towing tank (from right to left in the photo) and the blades are rotating. All blades that are on the tracks can be seen to adhere to the tracks and this was the case throughout the testing period. The structural and electrical aspects of

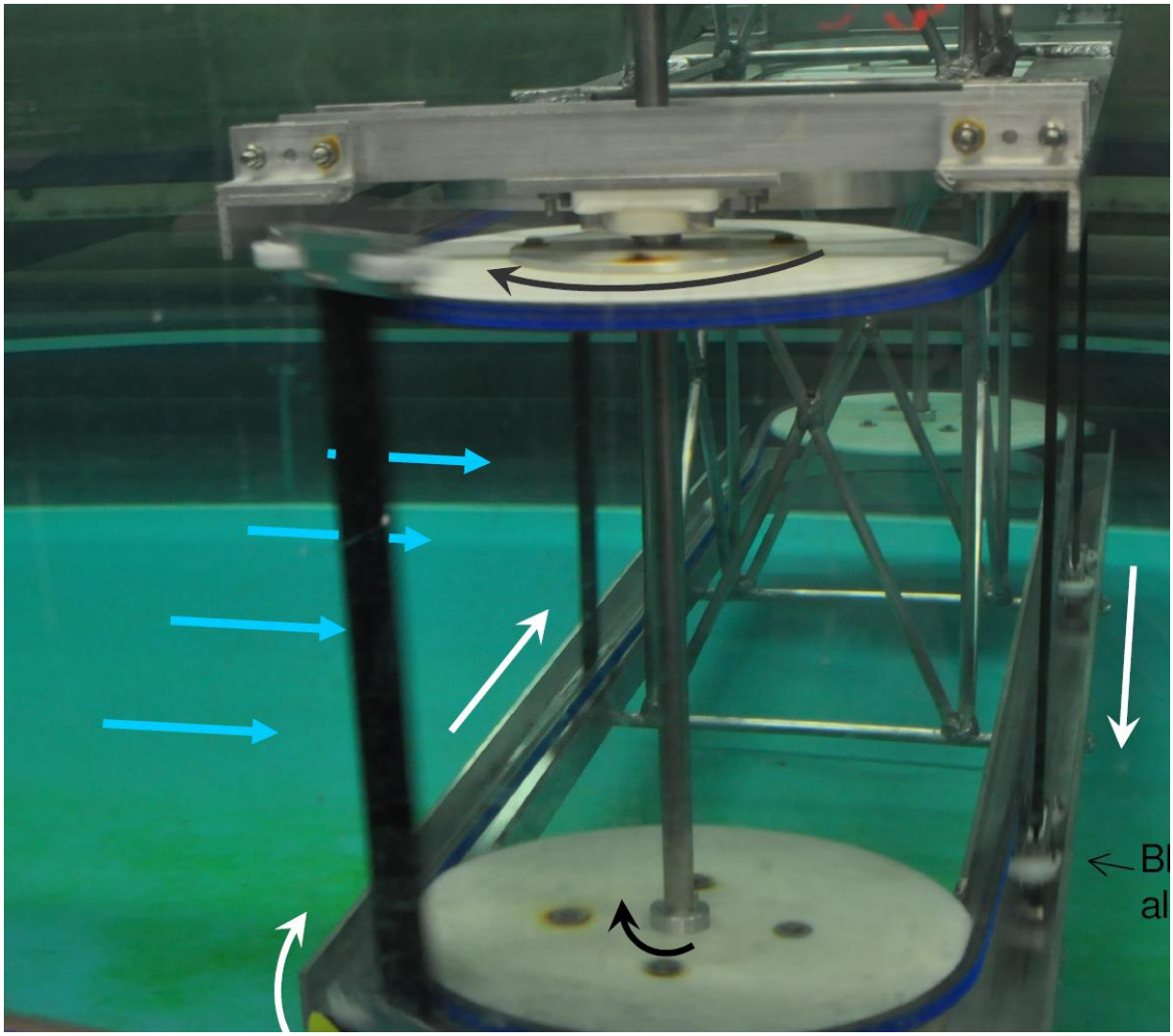

Figure 4.8: *Photo of the PII being towed through the UCL tank showing that all blades are adhering well to the tracks - on both the upstream and downstream passes. From the turbine's frame of reference, water is flowing from the left of the photo to the right, indicated by blue arrows. Six blades are attached and their motion is indicated by white arrows, and the motion of the sprockets is indicated by black arrows. When viewed from above rotation is clock-wise.*

the design performed their basic functions very well. The mechanical system was also sound, except for the transition of the blade carriages from the sprockets to the tracks and vice-verse, a discussion of which follows.

One minor problem, minor in the sense that it was easily improved, was that during each blade's travel around the sprocket the chain tension is released by the sprocket and the blade is able to pitch freely by at least 10 degrees. The inertial load on the blade was centred approximately at the half-chord point of the blade and the blade therefore pitched as it turned the corner (it is attached at the quarter chord point). The problem was solved by tying the carriage to the chain at a second point so that pitching was limited. This was successful but any future work should incorporate this consideration from the outset. The pitching also affected the orientation of the load cell in the instrumented blade, and this is discussed in Section 4.4.

One major problem did occurred at the four transition points: leaving the sprocket to join the track (upstream and downstream); and leaving the track to join the other sprocket (upstream and downstream). As seen in Figure 4.8, the downstream carriage was well placed to smoothly join the sprocket due to chain tension and a gradual parting from the sprocket. However, on the upstream side the blade was not perfectly aligned with the track when it rejoined on the upstream track; the blade was thrust back by the oncoming fluid. This created a large impact when the blade reached the track, and this was exacerbated at higher blade speeds.

This repeated impact put a practical limit on the rotational speed and the towing speed of the device. At QinetiQ one of the chain links snapped during operation, shown in Figure 4.9a, at a blade speed of 1.9 m/s and a towing speed of 0.7 m/s . The link that snapped was a polymer inner link (much weaker than the nickel plated steel outer links) and was connected directly to the carriage's attachment link (which is made from stainless steel). It is fairly safe to assume that the impact of the carriage rejoining the track caused this failure.

A slight improvement was found by creating a transition to the track that is smoother and more compliant. The broken PII and the improved transition are seen in Figure 4.9a and 4.9b respectively. Following this the PII was successfully taken to slightly higher blade speeds but the repeated impact still caused a practical limit at around 2 m/s. Although slightly higher blade speeds were achieved, the highest blade speed for which data was successfully recorded was 2 m/s (motor speed: 355 rpm); see Table 4.5 for details. This limited the blade speed ratio at which measurements could be made to about 5, 4, 3.33, and 2.85 at towing speeds of 0.4, 0.5, 0.6 and 0.7 m/s respectively. It also limited the blade Reynolds number to approximately 112,000.

Except for the problem with the upstream transition from sprocket to track, the PII system should be capable of operating at higher blade speeds: with the turbine in air, as opposed to water, the blades were tested at up to 5 m/s, and the structure also proved successful at resisting representative thrusts. The following section details measurements of the force on the blades as they rotate.

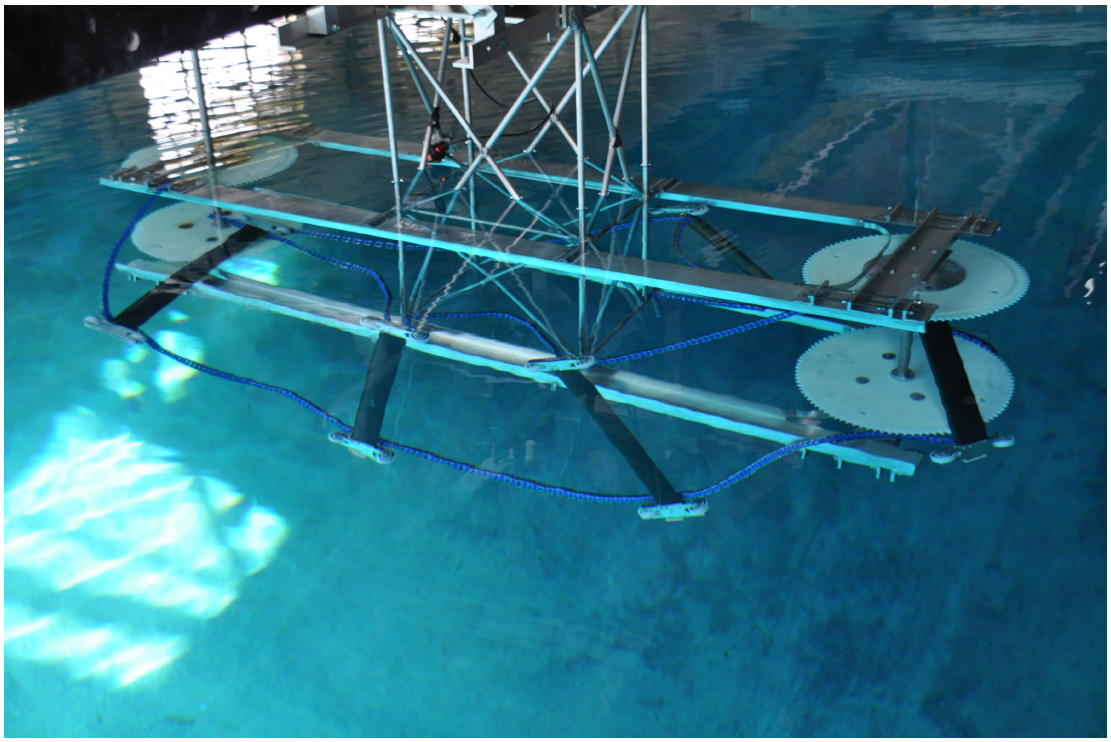

(a) *PII with a broken chain in the QinetiQ towing tank.*

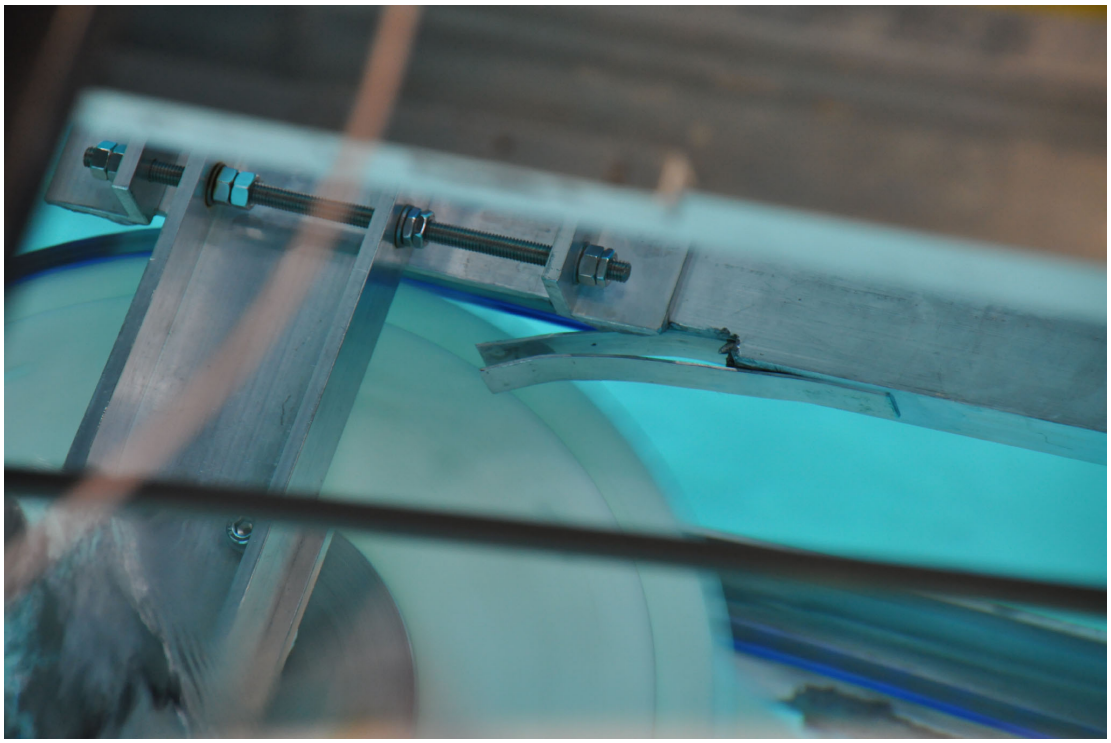

(b) *A smoother transition, with some compliance.*

Figure 4.9: *a) The large and repeated impact of the blade rejoining the upstream track caused the chain to snap. b) An* ad hoc *improvement was to glue on strips of aluminium that gave a smoother transition and were slightly compliant. The strips were a significant improvement.*

4.4 Blade force measurements

The strategy of the PII experiments was to directly measure the load on the blades and to use this as the primary quantitative outcome. A single blade was instrumented and is described in this section. The basic assumption is that all blades experience the same periodic forces over each rotation, so that only one blade needs to be instrumented.

It is also assumed that the vertical loads on the blade will be small and unchanging, and therefore only the two horizontal components of the load on the blade need to be measured. As the horizontal load is usually decomposed into the component tangential to the blade's motion, F_{t}, and the component normal to the blade's motion, F_{n}, a blade was developed that measured these two components.

Blade forces can be measured in a variety of ways, many of which have been developed by aeronautical researchers over the past 80 or so years. The simplest methods use a weight balancing system to measure steady loads, and this is often complemented by a traversing pitot-static tube in the wake to estimate the drag of the blade by calculating the momentum deficit.

More detailed measurements can be made by using static pressure taps on the surface of the blade itself, though this is easier in a wind tunnel than in water because the opening to atmospheric pressure must be above the water surface. Such a method was used by Graham (1982) to measure the instantaneous pressure distribution on a blade undergoing cycloidal motion (i.e. that of a Darrieus turbine) in water, with pressure taps in the blade linked via small tubes to the atmosphere above the water level.

A similar technique was used by McCroskey et al. (1982) who measured the unsteady forces on oscillating helicopter blade sections including the NACA0012. Blade forces were measured by placing 26 small pressure transducers around the chord of the blade. This allowed high frequency measurements of the pressure distribution around the chord, which was then integrated to give tangential and normal forces, and moments; skin friction was not measured.

The method of pressure tapping was not a practical option due to the size of the chord in the PII experiment: the chord used in McCroskey's (1982) experiments was 0.61 m - ten times the size of the blades on the PII; fitting the pressure transducers in a small blade, such as the 0.06 m chord on the PII, was not practical. Further, pressure transducers are prohibitively expensive (quotes for the same *Kulite* transducers were around £800 each). Even if the pressure tapping method could be employed, it is not well suited to the PII experiment firstly because it does not detect skin friction, and secondly because it is not well suited to resolve the forces tangential to the blade's motion. Further, such detailed information about the distribution of pressure along the chord, while potentially insightful, was not actually necessary for the PII experiment: net force was deemed sufficient at this stage.

For the PII the unsteady total blade loads were measured using a load cell following the technique used by Strickland et al. (1981), illustrated in Figure 4.10, when measuring the unsteady blade forces on a Darrieus turbine as it was towed through a water tank. In that experiment the blades were cantilevered from above, and the strain at the root of the cantilever was measured.

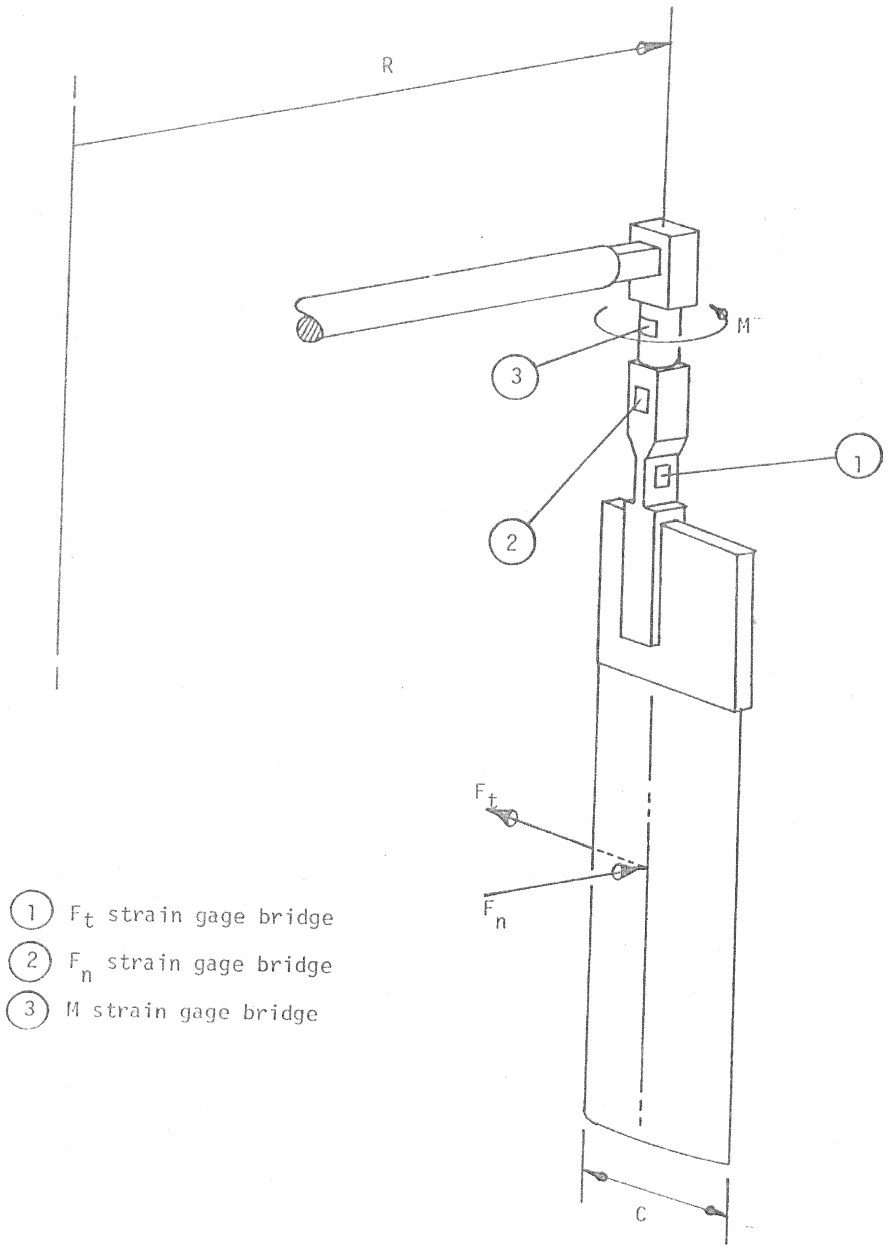

Figure 4.10: *Image from Strickland et al. (1981) showing their instrumented blade on a Darrieus turbine. The blade is cantilevered from above and strain gauges are attached at the root of the blade.*

The key assumption was that the blade was approximately uniformly loaded and therefore that the measured bending moment corresponded directly to the total load on the blade. That assumption was fair firstly because the blade was quite slender, and secondly because it stretched from the water surface to very near the base of the towing tank. For the PII experiments a similar approach was taken and it will now be described in detail.

4.4.1 Load cell concept

For the PII experiments the blades were aligned vertically and only the horizontal loads were measured. The moment about the blade was not measured as it would add relatively little value to the results, but would significantly increase the complexity of the system. Therefore a two-degree of freedom measurement system was required. It was not practical to mimic the cantilevered concept of Strickland et al. (1981) because the larger blade loads would cause excessively high deflections. Therefore a solution was required that could measure loads on a blade that is supported at both ends.

No commercial two-axis load cells could be found that fitted in the small space available. Further, the attachment of strain gauges directly to the carbon fibre blades was not attempted firstly because the blades were not homogeneous, secondly because the bending in the direction of the blade's motion would be extremely low, and thirdly because there is no practical position for the strain gauges when measuring that axis of bending. If only normal loads were to be measured, then strain gauges could potentially be attached directly to the blade. However, in this case tangential force measurements were also required hence it was necessary to develop a bespoke two-axis measurement system.

Two concepts were considered: firstly, the blade could be secured at each end by a cantilevered strut, whose bending could be measured; secondly, the blade could be split in the centre and rejoined with a beam whose bending could be measured. Both concepts are illustrated in Figure 4.11. The blades are illustrated in a horizontal position, so that they correspond to a beam in linear elastic beam theory. This frame of reference is maintained in figures throughout Section 4.4 (this section).

The cantilevered concept is illustrated in Figure 4.11a and consists of connecting the blade at each end via a stainless steel cantilever that is inserted into the carbon fibre blade. If the connection between the cantilever and the tracks is a 'simple' support, i.e. it does not resist any moments, then the bending at the root of the cantilever will be considerable. This bending moment can be measured via strain gauges.

The cantilever solution was developed in detail ready for manufacture but was judged to be a weaker solution than the split blade concept. In summary the cantilever solution is viable but has the following weaknesses:

- The strain gauge will cover a region of significant strain gradient
- The cantilever will be subject to vibrations as it is near the track

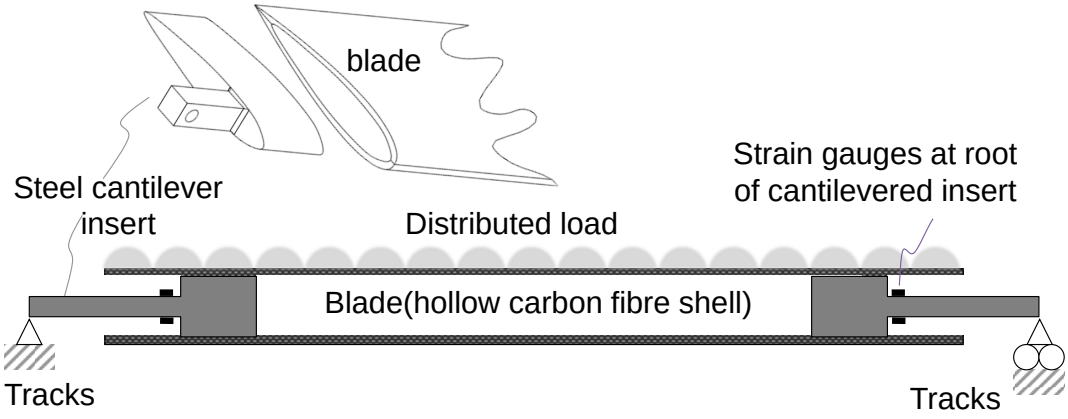

(a) *The blade is attached at each end using cantilevered beams.*

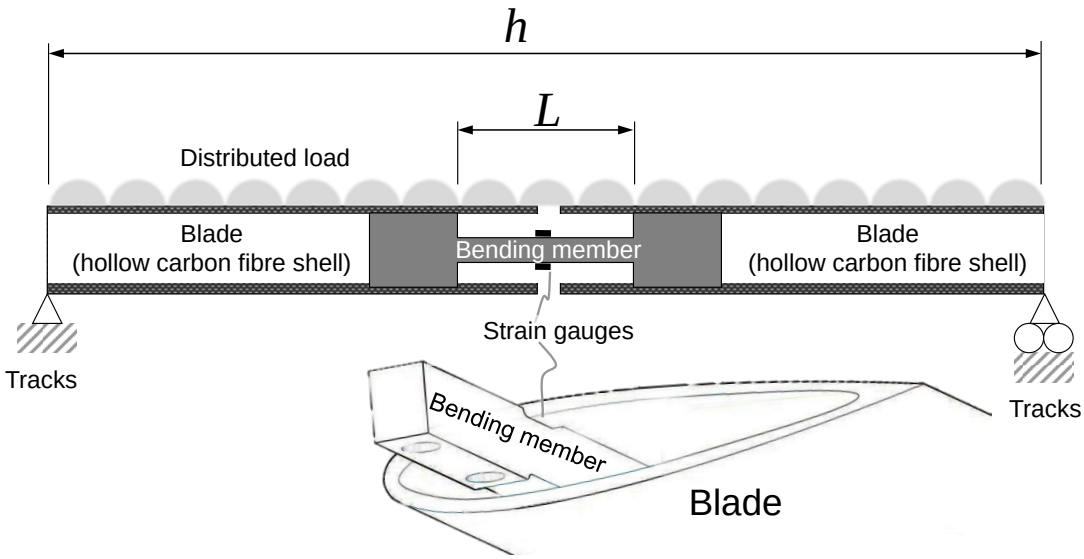

(b) *The blade is split in the centre and rejoined with a strain-gauged beam.*

Figure 4.11: *Cross section of a blade, illustrating two load cell concepts for measuring blade forces (blade sketched horizontally to correspond with beam theory).*

- Two load cells would be required to measure the total load

The split blade concept, first suggested by Nicolle (2010), is illustrated in Figure 4.11b. The blade is split in two and joined by a so-called 'bending member', which is inserted inside the blade so that the external shape of the blade is unaffected. The blade will have a bending moment, $M(z)$, distributed along its length in the $z-$direction, and the moment can be deduced by measuring the strain, ϵ, on the surface of the bending member:

$$M = EI\epsilon/y \tag{4.3}$$

where I is the appropriate second moment of area, y is the distance from the neutral bending axis to the surface and E is the elastic modulus of the bending member. By splitting the blade in half and rejoining it with a stainless steel bending member, the variables y, E, and I in (4.3) are accurately known. The bending moment can be used to estimate the load on the blade, but this is subject to four assumptions, which are discussed in the next section.

4.4.2 Assumptions to relate bending moment to blade load

The load on the blade can be deduced from the bending moment at the centre, according to the following assumptions:

1. The load distribution is known, e.g. uniform or elliptical.
2. The bending moment provided by the support of the blades is known.
3. The composite beam (blade and bending member) does not deflect significantly with respect to its total length.
4. The bending member is much shorter than the blade: $h \ll L$,

where L is the length of the bending member and h is the length of the blade. These four assumptions, when combined with simple beam theory, produce a relationship between the moment, M, on the bending member, and the load on the blade.

The first three assumptions are necessary in order to use beam theory to relate the load on the blade to the bending moment at the centre. For example a load f (N/m) distributed uniformly (assumption 1) along a simply supported blade (assumption 2) that does not deflect significantly (assumption 3) will cause a bending moment $M = fL^2/8$ half way along the blade.

The fourth assumption is only necessary if the the blade is not simply supported; in which case the rotational stiffness of the bending member must be much less than the rotational stiffness of the supports – and this is likely to be the case if $h \ll L$.

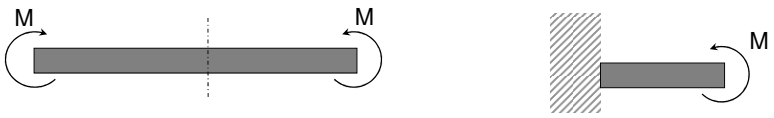

Figure 4.12: *Diagram of the bending member: left, the full beam is symmetrically loaded and will have zero slope in the centre; right, model of a half beam as a cantilever with a moment at the end.*

Figure 4.12 illustrates the bending member subjected to some moment, M, at each end. The bending member is loaded symmetrically and has zero slope in the centre, so each side can be modelled as a cantilever with a moment, M, applied at the free end and this is illustrated on the right of Figure 4.12. In that case the bending moment along the bending member is constant and therefore the strain is constant. Even if the bending member is relatively short, the strain gauges will still cover an area of theoretically constant strain so there is less constraint on the size of the strain gauges: this is a significant advantage over the cantilever concept. The bending member can therefore be designed for minimum deflection.

The first assumption, that the load distribution is known, is a hydrodynamic assumption. The blades of the PII have a uniform chord distribution and no twist. If the blades were infinitely long they would be uniformly loaded, but their finite length causes a non-uniform load distribution. This was discussed in Section 2.4.5 and the same lifting line model will be used here. The results of calculations in Section 2.4.5, using the panel method, included the load distribution, $f(z)$, along the blade, where z is the position along the span and are plotted in Figure 2.8. The blade is assumed to be simply supported (this is discussed in detail in the following section) and the symmetric loading produces equal reactions at each end of the blade

$$F_{\text{reaction}} = fL/2, \tag{4.4}$$

$$= F/2, \tag{4.5}$$

where $F = fL$. The shear force distribution is obtained by integrating the load distribution and the bending moment is obtained from the integral of the shear force:

$$Q_s(z) = \frac{F}{2} - \int_0^2 f(z)\,\mathrm{d}z, \tag{4.6}$$

$$M(z) = \int_0^z Q_s(z)\,\mathrm{d}z. \tag{4.7}$$

For an aspect ration of $AR = 8.33$ (matching the PII) the lift distribution was calculated and the maximum bending moment was:

$$\frac{M_{\max}}{Fh} = 0.1232, \tag{4.8}$$

and this compares closely with the value for a uniformly loaded beam, where $M_{\max}/Fh = 1/8 = 0.125$. The difference is on the order of 1%, which is not more than the uncertainty associated with the theoretical estimate. It will therefore be assumed that the blade is uniformly loaded and the total load is related to the measured bending moment, M, as:

$$F = 8M/h. \tag{4.9}$$

The drag also has an effect on the bending moment, especially in the direction tangential to the direction of motion. The distribution of drag along the span is due partly to the profile drag, and partly due to induced drag. The profile drag will be distributed in a similar way to the lift, and the induced drag distribution can be approximated from the panel method and for $AR = 8.33$ we have a moment at the blade centre due to induced drag of $0.082Fh$ which is 34% less than for a uniform load. This is because the induced drag is concentrated at the end of the blades. The conversion of moment measurement to total load estimate therefore depends on the relative magnitudes of the induced drag and the profile drag. Their actual ratio is difficult to predict with certainty. It is likely to be on the order of 1:1 below stall, and above stall the drag will be dominated by profile drag. Therefore the drag will be assumed to be uniform but it must be noted that a much higher uncertainty is associated with this assumption. Below stall the uncertainty in drag measurements will be on the order of half the total uncertainty in the estimate of the contribution of induced drag to the moment in the centre of the blade: ~17%.

The use of lifting line theory to relate bending moment to lift is subject to the following uncertainties:

1. The PII blades have a small non-lifting extension to the blade due to its carriage, extending the wing length by a further 12% and this has not been accounted for.

2. The tips of the PII blade are not totally free – they are surrounded by aluminium tracks, so the development of the tip vortices will not be as clean as is assumed by lifting line theory. However, according to Miley et al. (1982, V) the shape of the tips has a negligible effect on the lift and drag characteristics of the blade.

3. The vortex wake of the blade will not develop as assumed by lifting line theory: it will be advected at a different speed and, rather than extend in one plane to infinity it will take a zig-zag shape.

Further, the post-stall lift of a three-dimensional blade is not accurately predicted by measurements on a two-dimensional section (Miley et al., 1982, V).

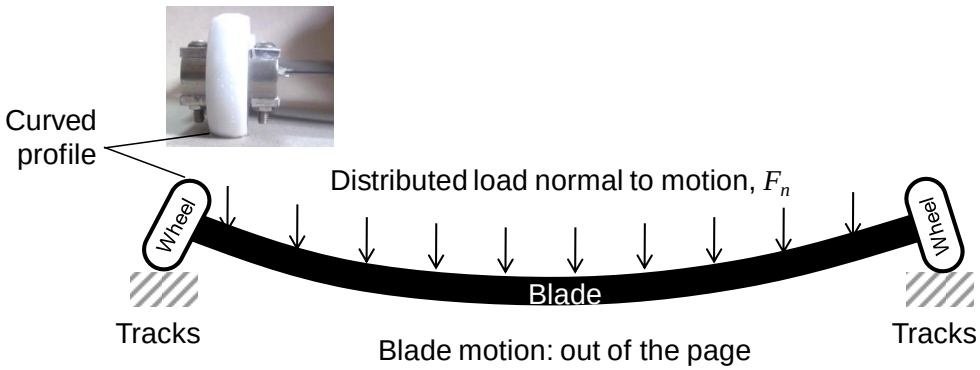

(a) *Cross-section of a blade in a plane normal to its motion, showing the support mechanism for normal loads,* F_n. *The wheels are curved so that they are 'simple' supports, not offering significant resistance to moments.*

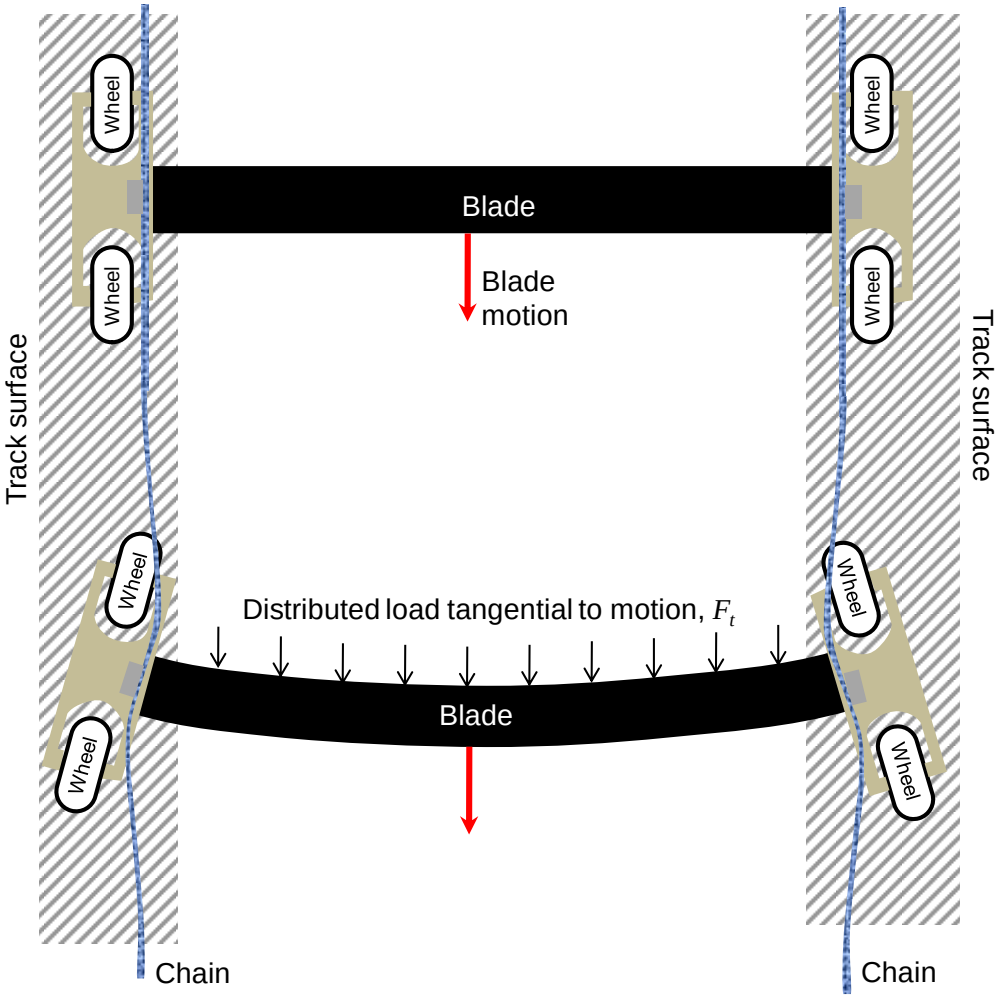

(b) *Cross-section of a blade in a plane parallel to its motion, showing the support mechanism for tangential loads,* F_t.

Figure 4.13: *Diagrams of the support mechanisms on the blade.*

The second assumption is that the moment provided by the blade supports is known. If the blade supports, i.e. the wheels on the tracks and the connection to the chain, do not resist moments then the blade is considered 'simply supported'; if the supports resist all moments so that the slope remains constant, then the blade is considered 'fixed'. In practice there is always some degree of moment provided by the support. The supports, and the bending member at the centre of the beam, are effectively rotational springs with a given stiffness (Nm/rad) and it is the ratio of these rotational stiffnesses that is important. If the bending member is much stiffer than the supports, then the beam is effectively simply supported. The blade on the PII was designed with supports that have a much lower rotational stiffness than both the bending member and the blade itself, so that the blade is effectively simply supported.

There are two axes of bending and each is supported independently. Figure 4.13a illustrates a blade cross-section in a plane perpendicular to the blade's motion; therefore a normal blade load, F_{n}, will be vertical in the figure. A photo of the wheels at the end of the blade is included, showing the curved cross section. As illustrated in Figure 4.13a this is a 'simple' support and negligible moments are resisted by the wheels. This was verified during the calibration of the instrumented blade (section 4.4.4): the wheels were removed and the blade supported on one sharp edge and one curved edge and the results were the same as when supported by the wheels.

Figure 4.13b illustrates a frontal view of a Moonraker, showing blades moving along their tracks and subject to tangential loads, F_{t}. The in-line motion of the blades is controlled by the chains. The support mechanisms in this plane include the chain, and also the wheels. When a load F_{t} is applied to the blade, the wheels will change direction slightly as illustrated in the lower part of Figure 4.13b . Given the enormous stiffness of the blade in this direction, and the relatively small loads ($F_{\mathrm{t}} < 50$ N), the change of angle will be so small as to not be visible. When the wheels change direction, although they will have some 'stiction' and some dynamic friction as the angle changes, they will not offer any static resistance to moments. It is assumed here that the wheels do not offer any resistance – force or bending moment – in the plane illustrated in Figure 4.13b. Therefore all resistance in this plane must come from the chains. The chain will alter its shape as the blade is loaded, as illustrated in the lower part of Figure 4.13b. The chain will provide a force to resist the load, F_{t}, and this is regulated by the motor controller. The chain will also provide a small moment which will depend upon the slope of the blade and the tension of the chain. We assume that both the chain tension and the blade slope are small, so that the bending moment provided by the chain is small in comparison to the bending resisted by the blade and its instrumented bending member at the center.

4.4.3 Implementation

Assuming that the load on the blade can be measured by using strain gauges, a signal corresponding to the strain in the bending member must then be recorded. A direct electrical connection between the blade and a computer, e.g. via a wire or slip ring, was not practical due

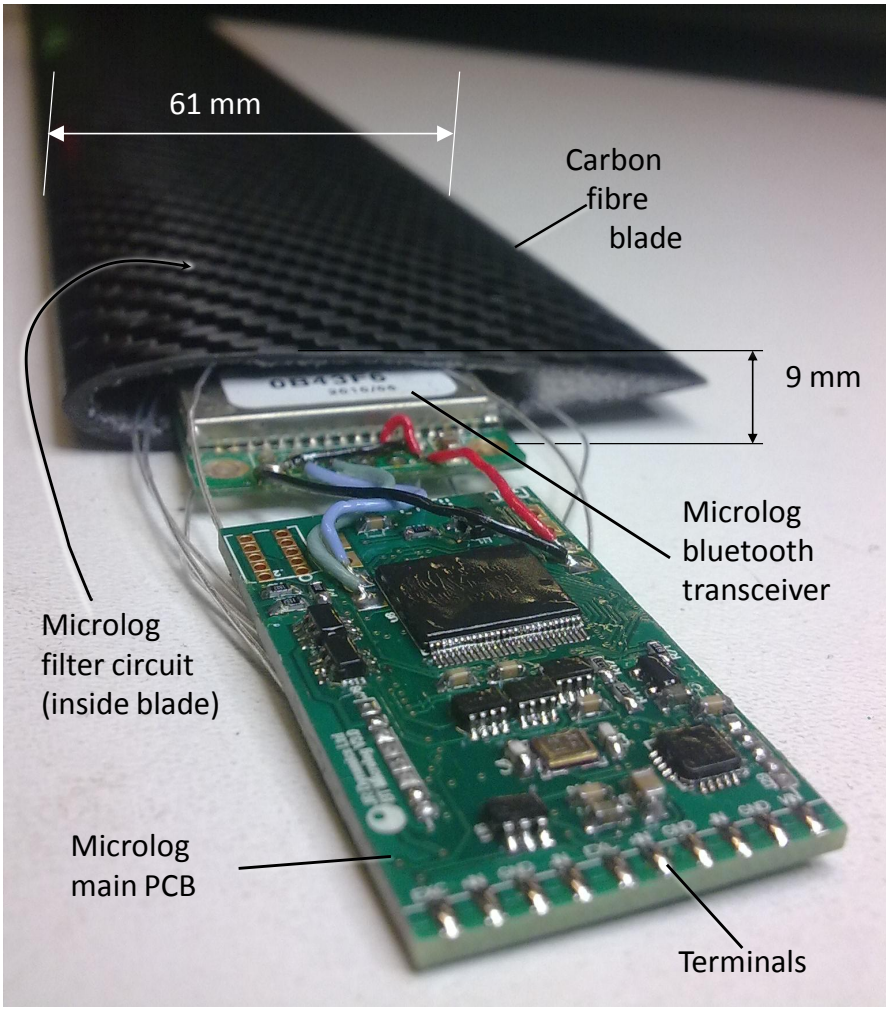

Figure 4.14: *The* Microlog, *half inserted into a blade, illustrating the close fit.*

to the oval path followed by the blade. The solution was either to wirelessly transmit the signal from the blade, or to record the signal on-board the blade and retrieve it later. Space in the blade was limited: the window of hollow space inside the blade is approximately 30 mm x 6 mm.

The *Microlog* product, from *Transmission Dynamics* (JRD Ltd), was purchased for this purpose. It is a two channel strain gauge bridge amplifier with a digital to analogue converter and data-logger. It is also very small. The Microlog consists of three PCBs: a main board with terminals, a Bluetooth transceiver, and a filtering circuit. When laid out in-line, these circuits fit inside the PII blades with about 0.5 mm space above and below and this is shown in Figure 4.14, which is a photo of the *Microlog* half-inserted into a blade. The *Microlog* communicates with a PC via Bluetooth. Data can be streamed live at up to 400 Hz (dual channel), however this was not possible firstly due to the high power requirements and secondly because the range of the Bluetooth connection in water was only a few centimeters. Therefore the *Microlog* was used to excite the bridges on the bending member, digitise their output, and record it on its internal memory (4GB); after the experiment, when the blade was stationary, a waterproof aerial was lowered into the water and the data was transferred via Bluetooth. The *Microlog* requires a DC power supply higher than 3.4 V so batteries from an *iPod nano* were used, providing 3.7 V with 440 mAh capacity – this is the largest capacity battery that fits inside the 6 mm window of the blade; two batteries were inserted into the blade.

The assembly of the instrumented blade is shown in Figures 4.15 and 4.16 and is briefly described here. The importance of the assembly method to the experiment is that firstly the outer shape of the blade should not be affected, secondly that the bending member should be properly aligned and its central section should not touch the walls of the blade, and thirdly that all bending should pass through the bending member, so that the beam is statically determinate.

Strain gauges were attached to the polished surface of the bending member using superglue (cyanoacrylate) and were then coated in two layers of *Plasti-dip*, a flexible rubber that renders the strain gauges and terminals waterproof. The three *Microlog* circuits were glued to a frame of stainless steel rods to give the assembly of PCBs a rigid form. This assembly was then coated twice in *Plasti-dip* which should keep all water away from the circuits. The assembly of PCBs was inserted into one half of the blade followed by half the bending member which was located using dowel pins. The blade was then sealed with epoxy resin for two reasons: it seals the PCBs inside the blade, forming a redundant shield from the water, and it provides a robust joint between the blade and the bending member, which would otherwise be joined only by the dowel pins and the thin carbon fibre skin which would be susceptible to tearing.

Figure 4.16a shows the blade at this point in construction: epoxy resin was only filled up to a point below the strain gauges. The remaining volume was filled with silicone sealant, offering double water protection for the strain gauges, but it was so flexible that it did not resist significant bending. The silicone was cast so that it protruded out of the top of half of the blade, beyond the strain gauges. The second half of the blade, which contained the batteries, was then filled with epoxy only up to the point at which the epoxy would not interfere with the strain gauges. The cast silicone ensured that when joining the two halves of the blade, no epoxy could

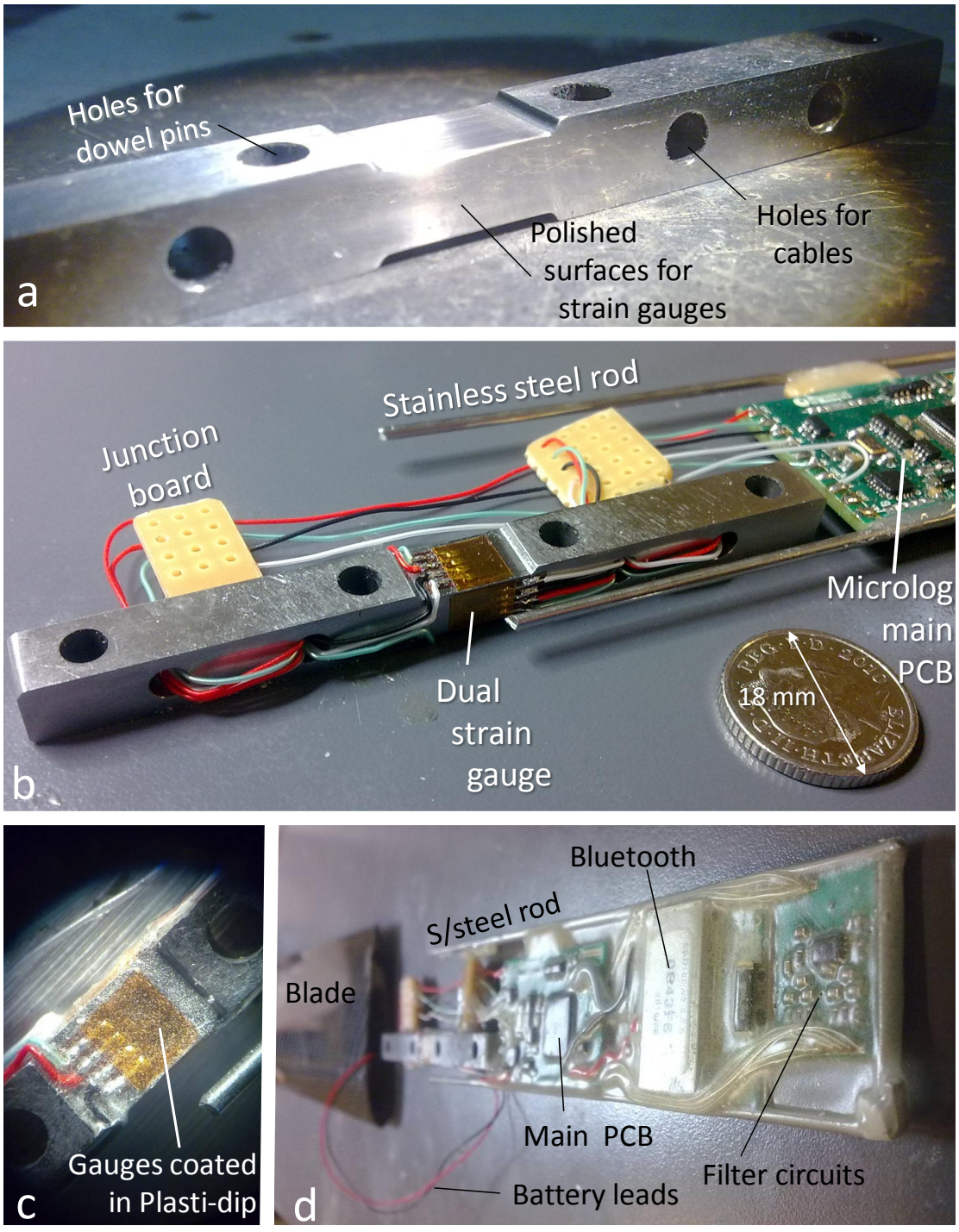

Figure 4.15: *Assembly of the bending member: a) beam after machining and polishing b) with strain gauges attached and connected to the* Microlog *via junction boards – a 5p coin is shown for scale, c) strain gauges coated in two layers of* Plasti-dip*, d)* Microlog *attached to stainless steel rods for rigidity, coated in two layers of* Plasti-dip*, connected to the bending member and batteries which are in the other half of the blade (pictured in the background).*

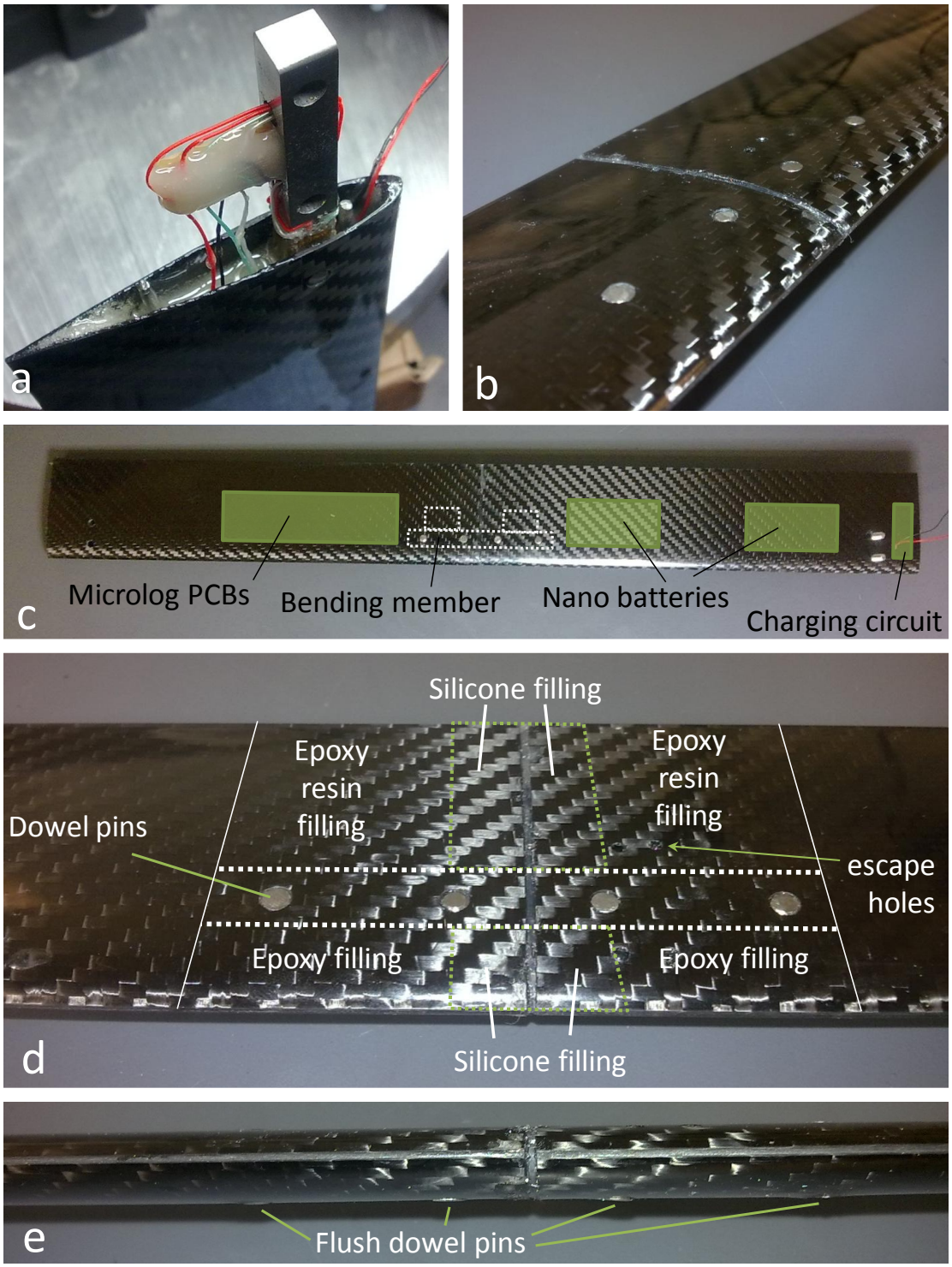

Figure 4.16: *Final assembly: a)* Microlog *has been inserted into half a blade, followed by half of the beam, which is sealed in with epoxy. b) the other half of the blade has been attached and the joint is complete. c) plan view of the finished blade, showing the location of the contents. d) Close up of the rejoined blade showing which areas were filled with epoxy for a strong joint, and silicone for the central section which must be flexible. e) view from the leading edge, aligned with the photo above, showing that the dowel pins, which were tightly fitted to the beam and blade, are flush against the surface.*

reach the strain gauges. Small holes, visible in Figures 4.16b and 4.16d, allowed excess epoxy to escape the blade. The result was a blade that was robustly assembled, but would be impossible to disassemble without destroying it.

4.4.4 Calibration

To convert the bridge voltage (V) to blade load (N) a known point load was applied to the centre of the blade while it was held in a horizontal plane on supports that provide negligible moments and the strain on the bending member was measured. An example of the results of this process is plotted in Figure 4.17. The blade was loaded and unloaded, showing that the process was reversible (there was no hysteresis). The gradient of a line of best fit is used in the experiments to convert the voltage to an equivalent load. Calibration used a point load rather than a distributed load because a point load can be applied more reliably. The bending from a point load is different than from a distributed load and the conversion between voltage and load must account for this: when the blade is simply supported then the bending due to a point load ($FL/4$) will be twice that due to the same load being uniformly distributed ($FL/8$).

The two axes of the instrumented blade are orthogonal so theoretically independent. Any cross-talk will be the result of misalignment of the strain gauges. To verify this, the blade would ideally be fully calibrated as a two-dimensional load cell: a matrix of loads $0 < F_\mathrm{n} < \max(F_\mathrm{n})$ and $0 < F_\mathrm{t} < \max(F_\mathrm{t})$ should then be applied, to check there is not significant cross-talk between the two axes. Due to time constraints this was not possible before the experiments, and due to damage sustained during the experiments no calibration tests were possible after the experiments. It is therefore assumed firstly that the axes are independent, and secondly that the calibration data taken before hand was valid throughout the experiment.

The load cell output was offset to zero based on the value given once the blade was attached to the PII and left standing on the track in static water. To verify that this offset value was appropriate, it was checked after every run and confirmed to be sufficiently similar (within a few percent). Further, measurements were made with the blade rotating around the PII while in static water; the mean value of the normal force was zero, and the value of the tangential force (while on the track) was slightly below zero with a magnitude similar to the value of $C_D = 0.02$ measured at zero angle of attack by Althaus (1980) (see Section 2.4.4 and Figure 2.5 for a discussion of this data). The measurement of tangential force while the blade was rotating in static water includes the effects of drag on the blade (as mentioned), and also includes the effects of the friction on the polymer pad under the blade (described in Section 4.3.5). It was not possible to remove the friction of the polymer pad – measuring its friction in air would not be the same as in water, while measuring its effect in water is not possible without knowing the drag of the blade. The effect of the friction on the polymer pad is to produce an artificial positive tangential force; given that the reading of tangential force was slightly below zero when the blade was spun in static water, this implies that the effect of the polymer friction was less than the drag on the blade at zero angle of attack and therefore is small.

In Figure 4.17b the upper region of the plot has been shaded grey and the results are evidently

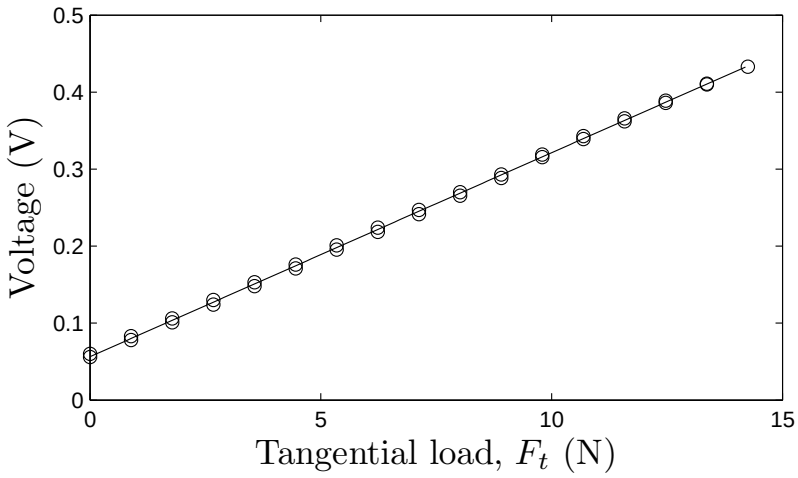

(a) *The axis F_t, loaded and unloaded, with a line of best fit. There is a minor difference between the loading and unloading, due to the difficulty in supporting the blade consistently during calibration. There is an offset of 0.06 V due to the self-weight of the blade.*

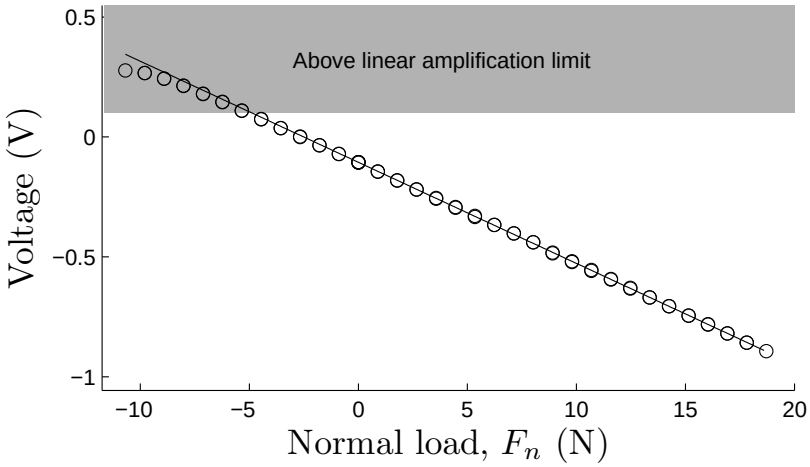

(b) *The F_n axis, loaded and unloaded. See text for discussion of non-linearities and offsets.*

Figure 4.17: *Calibration of the two axes of the instrumented blade.*

non-linear. The bridge output requires offsetting due to the slight imbalances in the resistances of the strain gauges, however for the normal force there was stray resistance in the circuit so that the necessary voltage offset was very high. The supply voltage to the bridge was 3.27V, so that a range of ± 1.635 V is possible, but the result of the offset an asymmetric range: in this case the maximum voltage that produced a linear output was approximately 0.1 V, while the minimum voltage was below -2 V. Results are therefore distorted; above 0.1 V the load cell is non-linear, and above an asymptotic value of approximately 0.25 V the results are clipped. This effect of distortion and clipping is referred to hereafter simply as clipping and explains the flat top to the wave forms seen in Section 4.6. It would have been possible to find a non-linear line of best fit to account for some of the distortion at high ranges, and this could be done as future work. In this work the linear relationship between voltage and load was used and results above the linear range should be discarded. In Figure 4.17b the blade has been loaded both ways, and the load due to the weight of the blade has been removed from both sets of readings so that a continuous plot is possible.

4.4.5 Post-processing

Post-processing of blade force measurements was performed in Matlab. Blade measurements were split into sets corresponding to a fixed towing speed and a fixed blade speed. Transient periods were cropped – these tended to be small because the increment in towing speed was small. The cropped samples typically contained between 10 and 20 periods of blade rotation, depending on blade speed and towing speed (worst case: 57 s towing and a period of $\sim$4 s gave 14 rotations, minus cropping).

A typical set of blade force measurements is shown in Figure 4.18. The force signature is highly periodic: cycle to cycle variations are limited to high frequency vibrations. Given the repeatability of the force signature from one period to another, the information can be compacted by finding a signature that best represents all the cycles. The fundamental frequency of the force signature, ω (rad/s), is found by dividing the length of the signal by the number of periods and multiplying by 2π. The simplest approximation to the force signature is a sine wave of frequency ω:

$$F_{\text{approx}} = a_0 + A_1 \sin(\omega + \phi_1) \tag{4.10}$$

where a_0 is a mean value of the original force signature, F:

$$a_0 = \frac{1}{t}\int_0^t F \mathrm{d}t, \tag{4.11}$$

and $t/2\pi$ is an integer multiple of the fundamental frequency, ω . The magnitude A_1 and phase ϕ_1 can alternatively be represented by Fourier coefficients a_1 and b_1:

$$A_1 = \sqrt{a_1^2 + b_1^2}, \tag{4.12}$$

$$\phi_1 = \arctan\left(b_1/a_1\right), \tag{4.13}$$

$$F_{\text{approx}} = a_0 + a_1 \sin\omega + b_1 \cos\omega \tag{4.14}$$

Fourier coefficients can be found for any harmonic, $k\omega$ where k is an integer, by the convolution of a sine wave (or cosine wave) of the same frequency with the original wave form, F:

$$a_k = \frac{1}{t}\int_0^t F.\sin\left(k\omega t\right)\mathrm{d}t, \tag{4.15}$$

$$b_k = \frac{1}{t}\int_0^t F.\cos\left(k\omega t\right)\mathrm{d}t. \tag{4.16}$$

Using Fourier coefficients for higher harmonics as well as the fundamental frequency, the force signature can be approximated more closely:

$$F_{\text{approx}} = a_0 + \sum_{k=1}^{n} a_k \sin\left(k\omega\right) + \sum_{k=1}^{n} b_k \cos\left(k\omega\right). \tag{4.17}$$

The number of harmonics only needs to be on the order of $n = 20$ to replicate the salient features of the force signature.

Figure 4.18 shows a typical blade force sample, from both axes simultaneously (F_{t}^{+} and F_{n}^{+}), where the towing speed was $U = 0.5$ m/s and blade speed $v = 1.1$ m/s, giving $\Lambda = 2.20$ and $Re_c \simeq 66,000$. On the left of each plot is the raw blade data, sampled at 125 Hz. This whole sample was used to generate a Fourier averaged signal (4.17) using the first 25 harmonics. On the right of Figure 4.18 the Fourier averaged signal (in black) is compared to an arbitrary period from the measured data (in grey). This plot, which is typical, shows firstly that the Fourier averaging acts as a low pass filter (6.85 Hz in this case), and secondly that the cycle to cycle variation in the measured data is minimal. The Fourier averaged signal is therefore representative of the entire measured sample and hereafter only the Fourier averaged blade forces will be presented. All of the Fourier averaged signals are presented in Appendix A.2.

4.5 Experimental procedure

Experiments were carried out over two days at the ship towing tank at QinetiQ. During each run, the PII device was towed through static water and the blades were rotated at a constant speed. The towing speed was constant for 40 m (20 device widths; 80 device heights) and was then increased to a higher speed, which was maintained for a further 40 m. The tank had enough space for four sections of 40 metres, allowing towing speeds of 0.4, 0.5, 0.6, and 0.7 m/s. During some runs, towing speeds were restricted to 0.6 m/s due to the problems of blade impact as

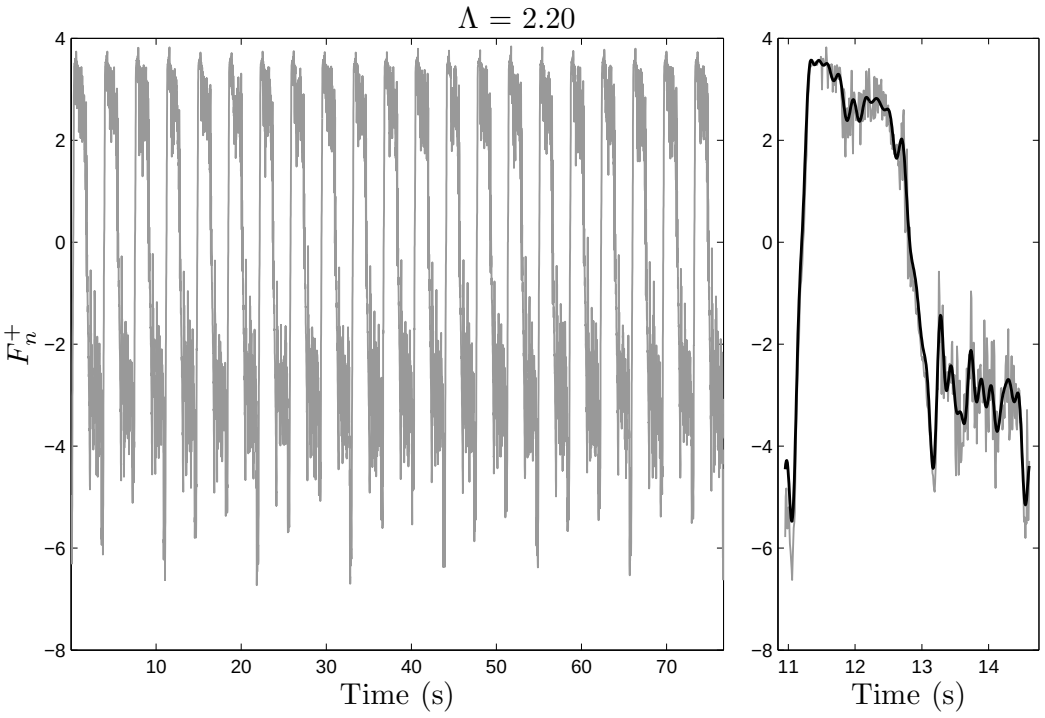

(a) *Non-dimensional normal force, F_{n}^+, assuming a uniform load. The signal is clipped at 3.5.*

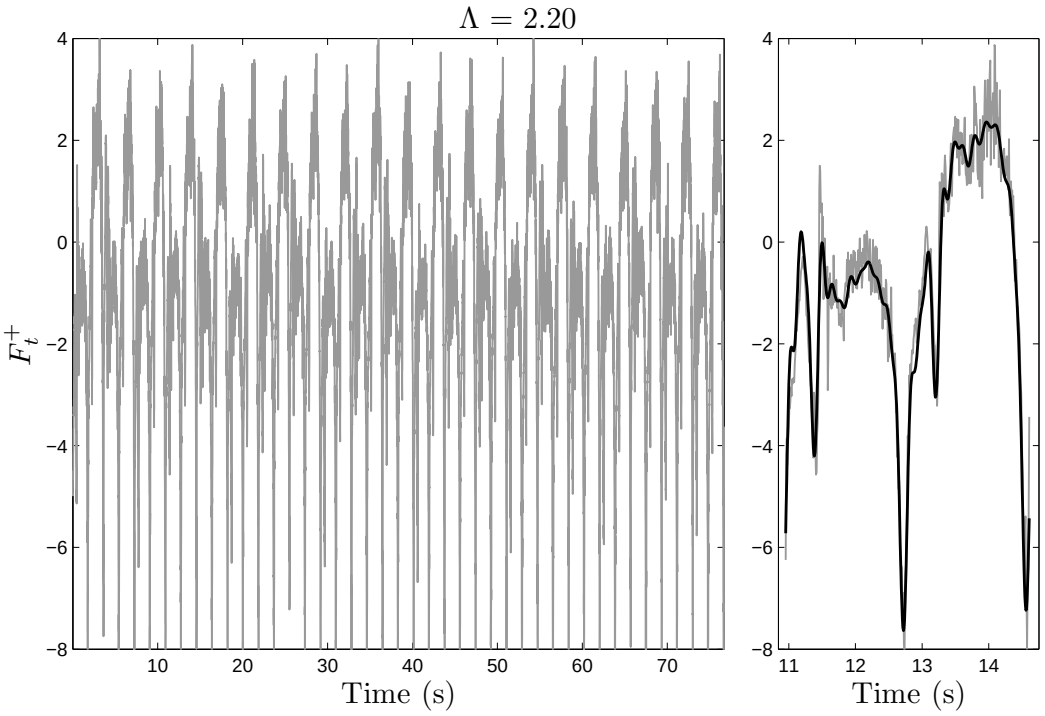

(b) *Non-dimensional tangential force, F_{n}^+, assuming a uniform load.*

Figure 4.18: *A typical sample of measured forces, in grey. On the right of both plots the fourth period, arbitrarily chosen, is plotted in grey along with the Fourier averaged approximation in black. The approximation is based on the whole sample, i.e. in (4.15) and (4.16) $t = 77$ s, and uses $n = 25$ harmonics (up to 6.85 Hz). Towing speed was 0.5 m/s, $\Lambda = 2.2$, and three blades were present, $N = 3$.*

N	v (m/s)	Re_c (10^3)	U (m/s) 0.4	0.5	0.6	0.7	F_t	F_n	Q	Θ
6	1.08	65	$\Lambda = 2.70$	2.15[a]	1.80	1.54	✗	✓	✗	✓
6	1.44	87	$\Lambda = 3.61$	2.89	2.41[e]	2.06*	✓	✓	✗	✓
3	0.73	44	$\Lambda = 1.82$[b]	1.46	1.22	1.04	✓	✓	✗	✓
3	1.10	66	$\Lambda = 2.75$	2.20[c]	1.83	1.57	✓	✓	✗	✓
3	1.45	87	$\Lambda = 3.64$[d]	2.91	2.42	2.08*	✓	✓	✓	✗
3	1.80	108	$\Lambda = 4.49$	3.60	3.00	✗	✗	✓	✓	✗
3	1.99	112	$\Lambda = 4.97$	3.96	3.31	✗	✗	✓	✗	✓
1	1.55	93	$\Lambda =$✗	3.10	✗	✗	✗	✓	✗	✓

* Forward run only, no reverse run due to mechanical problems.
a: Forward speeds quoted; for reverse run: v =1.10 m/s; $\Lambda = 2.20$.
b: Forward speeds quoted; for reverse run: v =0.75 m/s; $\Lambda = 1.86$.
c: Forward speeds quoted; for reverse run: v =1.12 m/s; $\Lambda = 2.25$.
d: Forward speeds quoted; for reverse run: v =1.48 m/s; $\Lambda = 3.69$.
e: Reverse speeds quoted; for forward run: v =1.49 m/s; $\Lambda = 2.48$.

Table 4.5: *Summary of the experimental program at QinetiQ, where N is the number of blades, v (m/s) is blade speed, U (m/s) is towing speed, $\Lambda = v/U$ is the blade speed ratio and $Re_c \approx \frac{U\Lambda c}{\nu}$ is the estimated blade Reynolds number. Ticks and crosses indicate whether data was recorded. All runs were repeated in forward and reverse except where stated; blade speeds when towing in reverse were equal within 1% except where stated.*

discussed in Section 4.3.5. Every run was repeated in the reverse direction. Between runs the wake from the previous run flowed over the PII device; the currents were tested by holding a pole in the water and waiting until its drag became negligible – this was typically about one minute. The delay between runs was always more than one minute.

4.5.1 Synchronisation

Despite careful attempts to synchronise blade force data with blade position (via the motor shaft encoder) there was significant drift in the data and the synchronisation was unsuccessful. This is mainly because of the uncertainty in the pulley ratio, which is small but has a large cumulative effect – a typical run would constitute thousands of motor shaft rotations, so that a 0.1% error in the pulley ratio leads to a >100% error in blade position by the end of the experiment. Additionally, there will have been some unknown amount of slippage in the pulley. Therefore the blade position was deduced from the periodic nature of the blade force signature. The accuracy of the phase of the force data is likely to be approximately 5% of a revolution.

4.5.2 Torque measurement

The motor controller could only output one variable to the data-logger at one time: usually blade position was chosen (although this was in fact ultimately of no use) but for a small number of runs the motor torque was recorded. Motor torque can be derived from the motor current via the motor torque constant, which is derived theoretically and is subject to an uncertainty

of ±10%. The uncertainty can be reduced through physical measurements on the actual motor used, for example using a friction brake, but this was not carried out due to time constraints.

The torque measurements on the PII were also of limited ultimate value because the friction in the system is unknown. Tests were carried out to measure the torque required to rotate the system at given rotational speeds when the PII was in stationary water and this gives a reasonable estimate of the losses in the motor, the friction in the pulley, the work done in meshing the chain with the sprockets, and the friction of the sliding pads on the underside of the blades. This could then be subtracted from torque measurements taken when the PII was towed (and the blades are rotated at the same speed), which should give an indication of the torque caused by hydrodynamic forces. However when the PII is towed the blades are forced onto the tracks, along which they roll and experience friction. This could be accounted for by determining the effective friction coefficient of the blade carriages, and then making an assumption about the length of track over which the blade experiences these frictional losses and an assumption about the normal force on the blades. Additionally the drag of the carriages on the blades is not known; again this could be estimated. However the uncertainties associated with these estimates of friction and drag would be very high so it was not carried out.

4.5.3 Programme

A summary of the experimental programme is in Table 4.5. Tests were completed with six blades and three blades, and one run was completed with one blade. The blade speed is derived from the frequency of rotation in the blade data. Blade force measurements were always taken, but due to a suspected loose connection in the blade, the measurements were not always successful. Only runs with successful measurements are included in Table 4.5, and ticks and crosses indicate which data was successfully recorded. Torque (Q) and blade position (Θ) could be recorded, but not simultaneously and neither were ultimately useful anyway.

4.6 Results and discussion

This section presents results from the PII experiments and compares them to predictions using the two-dimensional vortex model, described in Chapter 3, with the same parameters as the experimental PII (listed in Table 4.5). The two-dimensional vortex model is referred to as the 'vortex model' or simply the 'model' for brevity hereafter in this chapter. Blade forces predicted by the model *without* the correction for finite blade length are presented here because agreement was generally better; however average results for the corrected vortex model are included, for the sake of comparison.

4.6.1 Blade forces – normal force

An example of results for the normal force on a blade over one revolution is plotted in Figure 4.19. Two independent experiments (in opposite towing directions) are compared to results from the vortex model. The grey regions are the curved part of the blade path, where the experimental measurements are invalid due to the unknown support conditions on the blades

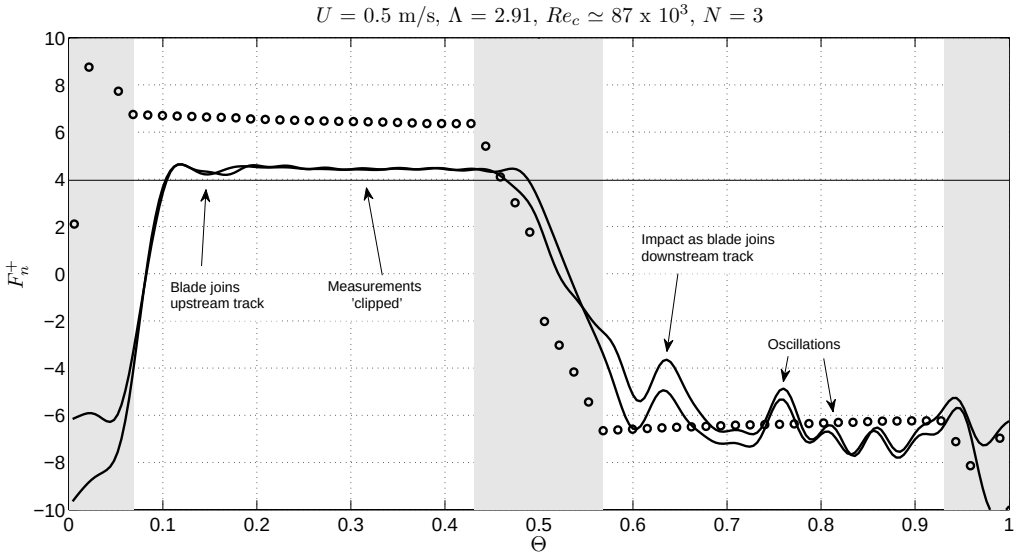

Figure 4.19: *The normal force on a blade over one revolution for 3 blades towed at 0.5 m/s and rotating at a blade speed ratio of* $\Lambda = 2.91$. ($\circ$) *vortex model* without *finite blade correction,* ($-$) *Fourier averaged experimental measurements from the PII. The thin horizontal line shows, approximately, the point above which results are clipped due to stray resistance in the load cell.*

although in practice the support conditions are approximately simply supported; the vortex model is inaccurate in and near the grey region due to the lack of dynamic stall model. There are 26 sets of results from the experiments (16 of which were also successfully repeated) and the results in Figure 4.19 are representative of the majority – full results are in Appendix A.2. These results show relatively good agreement between the model and experiments and will be discussed first, followed by an example of results showing less agreement; finally a summary of the results is given, indicating the regimes in which the results agree and disagree. Results for the normal force, from both model and experiments, are broadly similar for the three bladed and six bladed PII so are discussed together here.

The normal force is seen in Figure 4.19 to reverse as the blade switches from the upstream half to the downstream half. A positive value of F_{n}^+ corresponds to a force towards the centre of the device and is experienced on the upstream track ($0 < \Theta < 0.5$); and vice-verse for the downstream track ($0.5 < \Theta < 1$).

The two experimental results in Figure 4.19 show good repeatability and this is typical of all the results; there are three exceptions to this (out of 16): in those three cases the force signatures are the same shape as each other but differ in magnitude on the downstream pass by up to 10%.

The experimental results in Figure 4.19 are in phase with the numerical results within 5% for all results; half of the results are in phase within 1% although no pattern has been detected regarding which results are more in phase than others; as stated in Section 4.5, direct synchron-

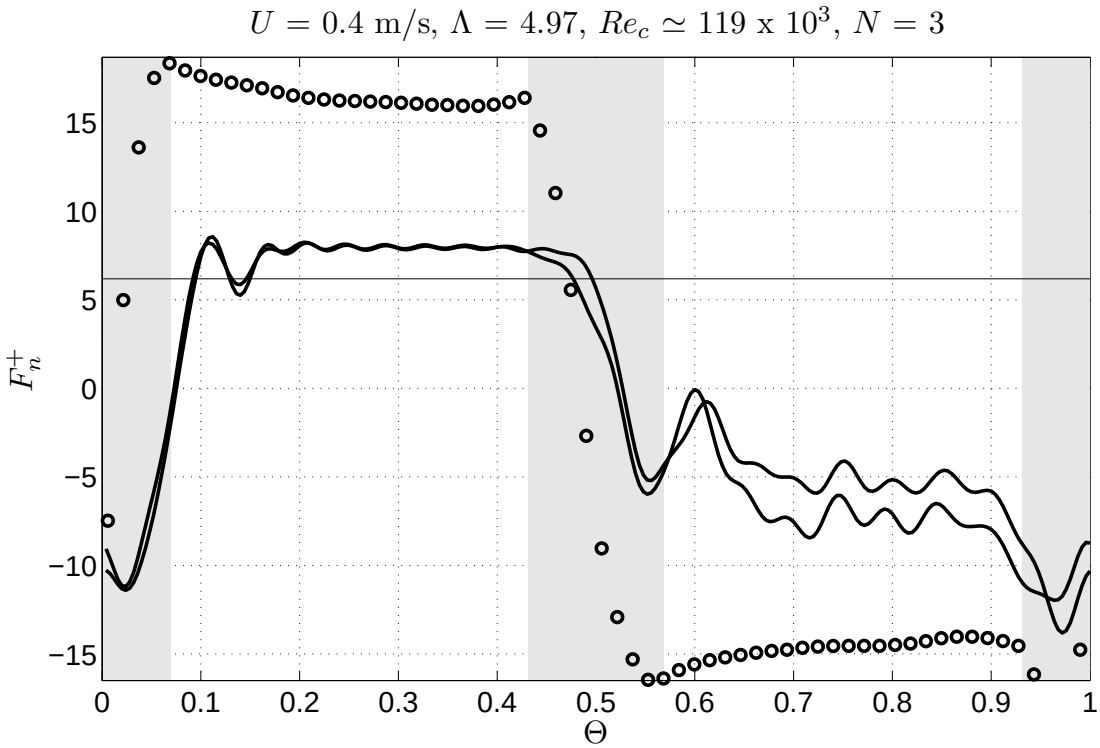

Figure 4.20: *Normal force, F_n^+ over one revolution: an example of disagreement between the numerical and experimental results at a higher blade speed.*(∘) *uncorrected vortex model,*(−) *Fourier averaged measurements from the PII.*

isation efforts failed and an alternative method was used based on finding the peaks in blade forces and this is only reliable to within 5%.

The experimental results in Figure 4.19 are distorted and effectively 'clipped' on the upstream pass due the non-linear relationship between voltage (V) and load (N) as discussed in Section 4.4.4; a horizontal line has been added to the plot, which corresponds to the magnitude identified in Section 4.4.4, above which the load cell is nonlinear (see also Figure 4.17). The horizontal line is approximate because it does not account for the individual offset for each experiment and this should be improved in the future. This clipping explains why the experimental measurements do not exceed a certain value on the upstream pass, and hence unfortunately no conclusions can be made about the agreement between the measurements and the predictions on the upstream pass.

There is a distinct undulation in the force signal as the blade rejoins the track and this has been annotated in Figure 4.19. This undulation is present in every measurement. As described in Section 4.3.5, during the experiments the impact of the blade on the track was considerable and that is evident in the force measurements. This undulation is not present in the numerical

results because in those simulations the blade follows a perfectly smooth path.

In Figure 4.19 further oscillations in the experimental measurements are annotated as the blade runs along the track, and these are not predicted by the vortex model which predicts a smooth, almost constant force. Using the Fourier coefficients from which the averaged signal was constructed, a frequency analysis did not show any dominant frequencies. There is also no pattern to the magnitude of these oscillations with blade speed ratio or Reynolds number. These oscillations were either due to the flexibility of the mechanical system of chains and blades, or some kind of hydrodynamic instability that was not predicted by the vortex model. One possible explanation is that the turbulence caused by the structure of the PII (which was not present in the vortex model) causes these oscillations. To corroborate this, an additional result is plotted in Figure 4.21 for a slow towing speed; this is one of the very few results that is not 'clipped'. The slow tow speeds means that the forces are within the linear range of the load cell. The results in Figure 4.21 show an undulation where the blade joins the upstream track, followed by a blade force which is remarkably smooth and showing excellent agreement with the vortex model. On the downstream side the repeated measurements are either side of the vortex model, showing good agreement on average. This one result is insufficient to conclude that good agreement would have been seen if measurements on the upstream pass were not clipped. However the smooth nature of the force on the upstream pass corroborates the suggestion that turbulence generated by the structure causes the oscillations in the normal force on the blade during its downstream pass.

The extent of agreement between experimental and numerical data seen in Figure 4.19 is representative of the majority of experimental results. However, there are five exceptions (out of 26) where there is not close agreement: the three highest and the two lowest blade speed ratios (and all occurring with three blades, not six). An example of results which disagree is given in Figure 4.20. Further, Figure 4.22 illustrates the cases where disagreement occurred. At blade speeds above stall, the numerical model predicts higher normal forces on the blade than were found experimentally.

In summary there is encouraging agreement between numerical predictions and experiments measurementsat low blade speeds, with disagreement arising at and above blade speeds where the blade is expected to come out of stall. The distortion or 'clipping' of the data on the upstream pass means that comparisons can only be made for the downstream path.

4.6.2 Blade forces – tangential force

The results for tangential forces are distinctly different for the three bladed and six bladed PII and are therefore discussed separately here. For the six bladed PII there are eight sets of results, five of which were also successfully repeated. Figure 4.23a shows a typical measurement of F_t^+ for six blades at low blade speeds, showing good repeatability. Again the part of the plot corresponding to the curved path is filled grey: in this region the blade moves around the sprocket and its support conditions change, rendering the data invalid. The impact of the blade on the track is seen once again as a distinct undulation at the beginning of the upstream pass;

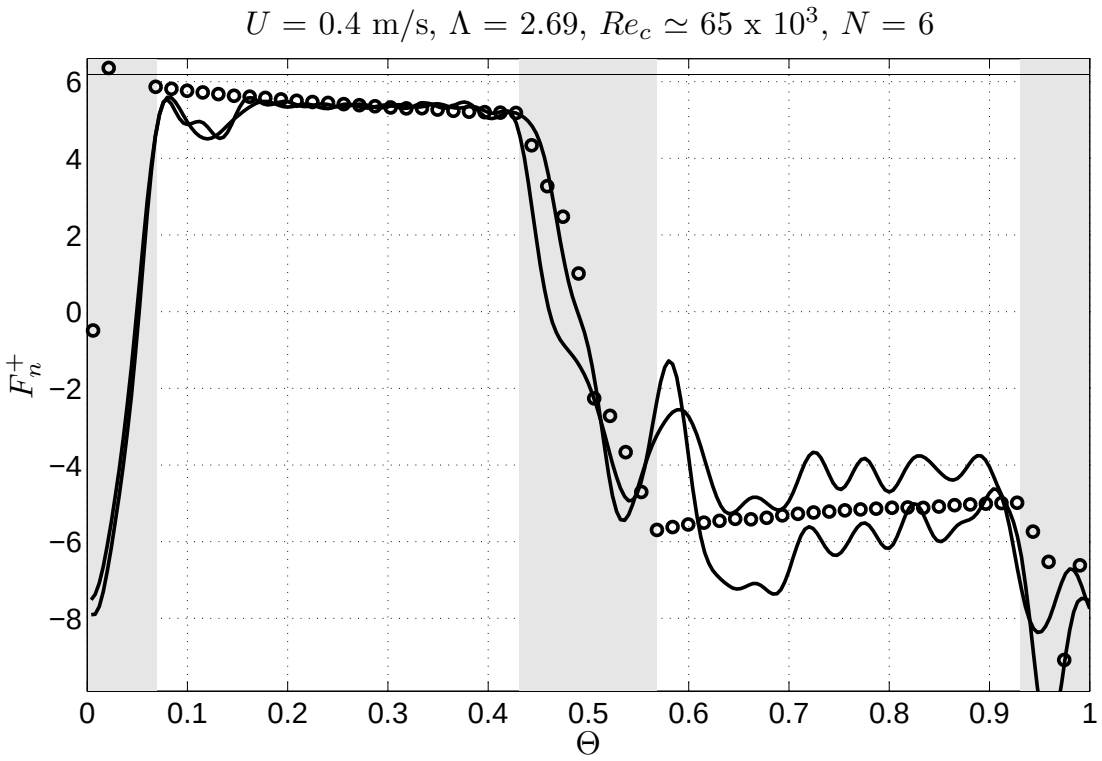

Figure 4.21: *One of the few results that is not clipped on the upstream pass. (○) uncorrected vortex model, (-) Fourier averaged measurements from PII.*

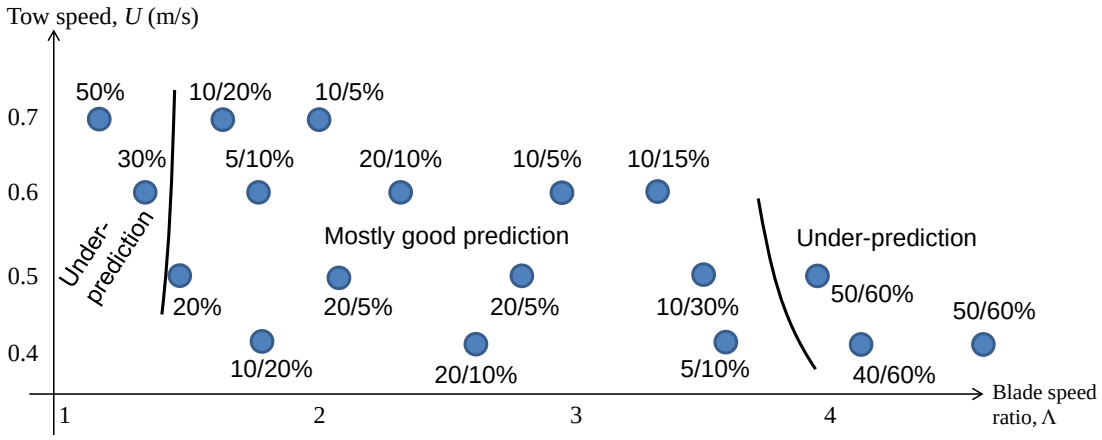

Figure 4.22: *A summary of the agreement between numerical prediction and experimental measurements of the normal force on the blade, F_n^+, for experiments with three blades (18 results in total, 11 of which include repeats). The percentage indicates the approximate difference between the predicted and measured values on the downstream pass (measurements for the upstream pass are clipped so can't be compared). The first number is for the corrected vortex model, and the second number is for the uncorrected vortex model; for example, 20/10% means the difference between experiment and corrected vortex model was 20%, while for the uncorrected vortex model it was 10%. If only one percentage is given then it applies to both corrected and uncorrected vortex models*

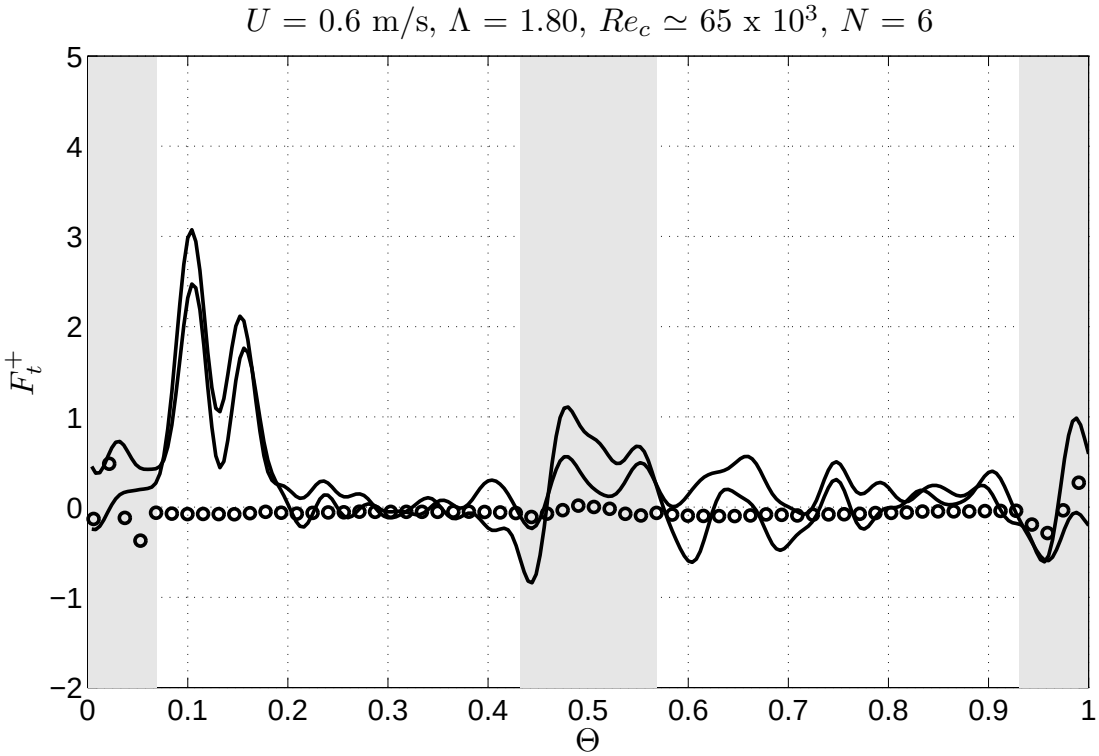

(a) *A typical measurement of* F_t^+ *with six blades at low blade speed.*

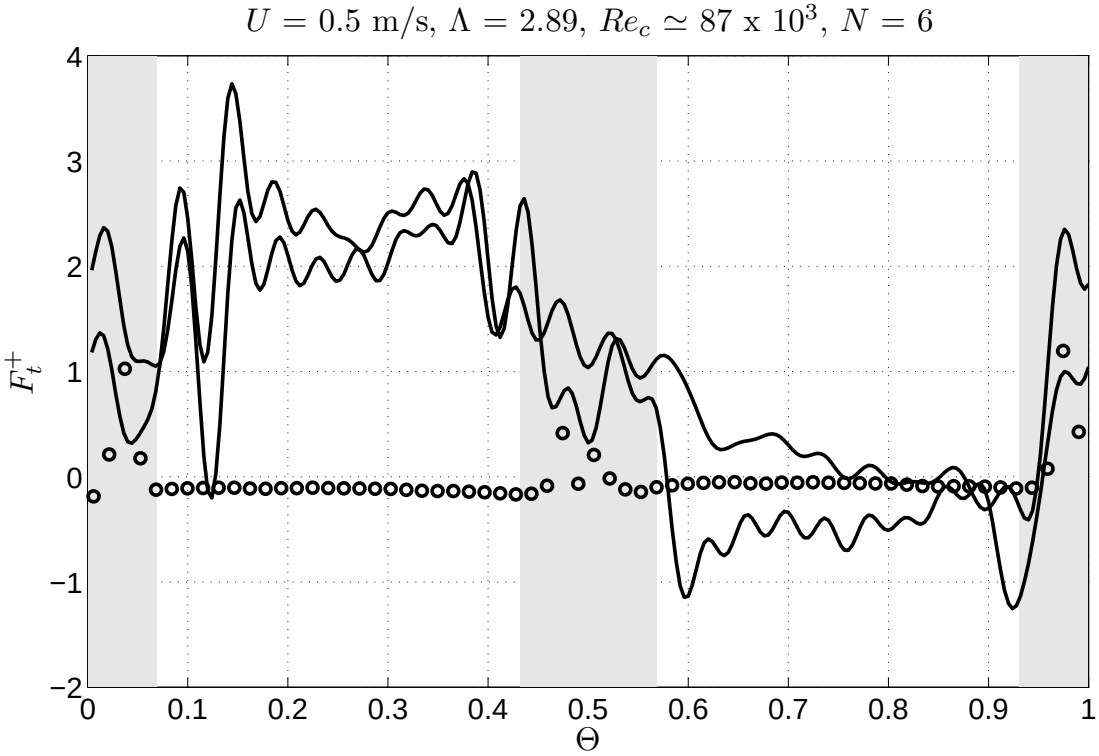

(b) *Example of positive tangential force.*

Figure 4.23: *Two examples of the tangential force,* F_t^+*, over one revolution on the PII with six blades.* (○) *vortex model (*without *finite blade correction),* (—) *Fourier averaged measurements from the PII.*

this is followed by a brief spell of positive tangential force before returning to approximately zero for the remainder of the revolution. The undulations in the tangential force could be a mechanical oscillation[1] or it could be a hydrodynamic instability, i.e. the delayed onset of stall; or more probably some combination of the two effects. The delayed onset of stall happens because the blade has a low angle of attack during the curved part of the path (below stall) and when it returns to the straight path and the angle of attack increases above that of stall there is a delay before the boundary layer separates. The vortex model does not predict the impact of the blade on the track nor does it predict the delayed onset of stall because it lacks a dynamic stall model; however the model does correctly predict that the tangential force will be approximately zero for the majority of the up- and down-stream passes.

Figure 4.23b shows another measurement of tangential force on the six bladed PII, this time for a higher blade speed. The clear pattern in Figure 4.23b is that the tangential force is positive all along the upstream pass, and then approximately zero on the downstream half (see Appendix A.2 for more results). This is typical of measurements on the six bladed PII at higher blade speeds and is evidence of significant positive torque generation by the Moonraker.

The vortex model predicts positive torques which are similar to experimental measurements on average, but agreement is not good in the sense that the model predicts very similar forces both upstream and downstream, while experimental measurements show distinctly higher forces upstream, and approximately zero force downstream. This will become more clear in the following section where the average forces are discussed.

Generally the repeatability of the tangential forces, in an absolute sense, was equal or better than was found for the normal force measurements. However the tangential forces are an order of magnitude smaller than the normal forces, so that the repeatability is expected to be worse in a relative sense. For low blade speeds, such as Figure 4.23a, the repeatability of the tangential forces is in fact very good, even in a relative sense. At higher blade speeds, such as Figure 4.23b, the repeatability of the tangential forces, in a relative sense, is worse than for the normal forces and this is true in particular on the downstream pass; nevertheless the results are still reasonably repeatable.

The measurements of tangential force on the three bladed PII will now be discussed: there were 12 sets of measurements, five of which were successfully repeated. The forces of the three bladed PII, seen in Figure 4.24, are characterised by a plateau on the upstream and downstream tracks, each beginning with a large undulation as the blade joins the track; large negative values are seen on the curved path (in the grey region).

The magnitude of the tangential force on the upstream side was approximately zero and this is also predicted by the vortex model; no significant positive tangential forces were measured on the upstream pass with three blades – higher blade speeds would have been required to achieve this, but were not possible.

On the downstream pass the tangential force is distinctly higher – this is the case in all

[1] The instrumented blade had failed by the end of the experiments so an analysis of its harmonic response was not readily possible.

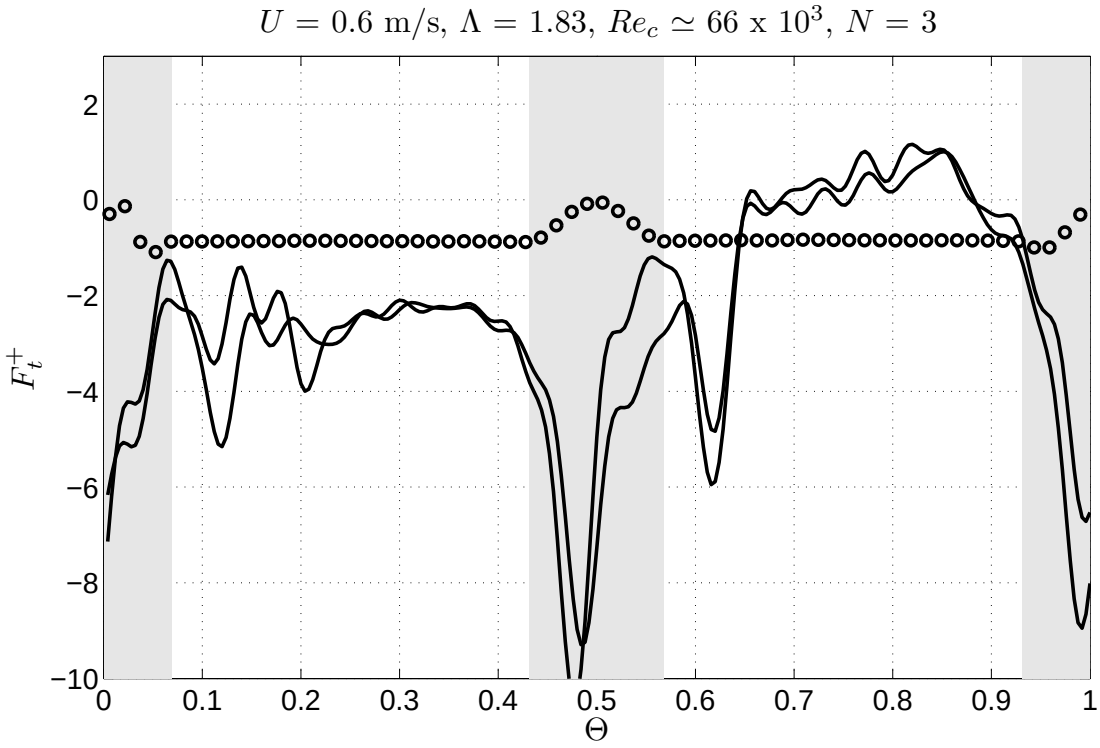

Figure 4.24: *An example of the tangential force, F_t^+, over one revolution on the PII with three blades. (∘) vortex model (without finite blade correction), (−) Fourier averaged measurements from the PII.*

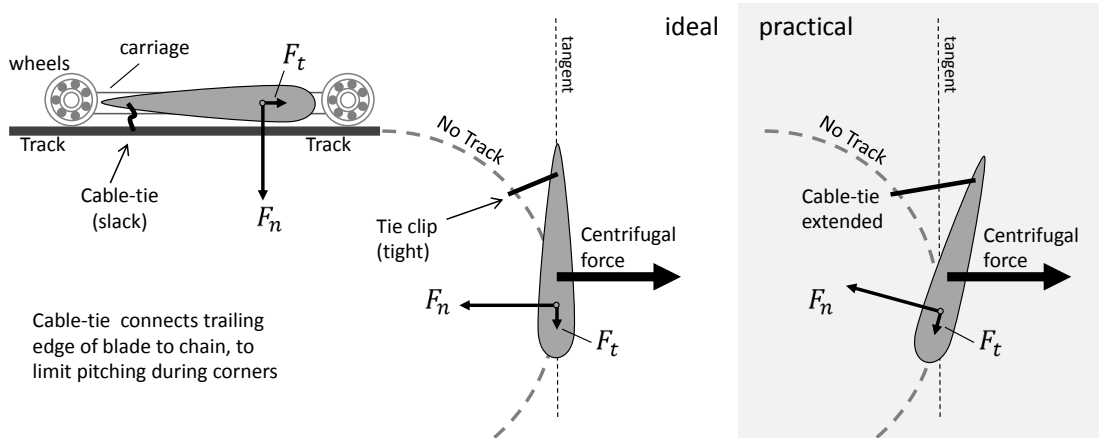

Figure 4.25: *While the blade was on the track, its pitch angle was ensured by two wheels. On the curved path the blade was free to pitch due to centrifugal forces and an* ad hoc *solution was to use a cable-tie to limit the pitching. The solution was temporarily successful but over time the cable-tie stretched and became less effective.*

measurement with three blades. This distinct pattern of a higher force on the downstream pass is not predicted by the vortex model. One possible explanation is that the structure on the PII (which is not simulated in the vortex model) created slower flow and hence a lower angle of attack and a higher lift-to-drag coefficient such that the tangential force increased. Alternatively it may be the two-dimensional limitation of the vortex model which results in a lack of predicting the higher force on the downstream pass. Velocity measurements, or a three-dimensional model, would provide insight into this problem.

The tangential force in Figure 4.24 shows large negative values in the grey areas, corresponding to the curved path. This was not the case for six bladed experiments and this can be explained as follows. On the curved path there is no track and the blade was free to pitch, as illustrated in Figure 4.25. The centrifugal force acts through the centre of mass of the blade section, which is attached to the chain at the quarter chord point. The chain is slack when meshed onto the sprocket. To remedy this a 'cable-tie' was used as illustrated in Figure 4.25 and this successfully limited the pitching. However, the clip stretched over time, in particular during maintenance after six bladed experiments and before three bladed experiments; this allowed some pitching, as illustrated on the right hand side in Figure 4.25, which led to a negative tangential force measurement. Given the small magnitude of the hydrodynamic contribution to the tangential force, the centrifugal force was able to dominate and this explains the large negative values in some readings (this effect grew monotonically over time). It was not possible to correct for the centrifugal force because the length of the tie clip, and therefore the pitch angle of the blade, was not known. Also attempts to 'dynamically calibrate' the blade using readings from rotations in still water to cancel out these effects were also unsuccessful because the hydrodynamic forces affect the pitching (both in static water and towing water, but with

slightly different effects).

4.6.3 Torque derived from blade forces

The tangential blade forces can be integrated to obtain a torque coefficient:

$$\overline{F_{\mathrm{t}}^{+}} = \int_0^1 F_{\mathrm{t}}^{+} \mathrm{d}\Theta, \tag{4.18}$$

$$C_Q = \overline{F_{\mathrm{t}}^{+}}\sigma. \tag{4.19}$$

where $\sigma = Nc/W$ is the solidity. Such measurements from the PII are at best an approximation: the force measurements are not valid during the curved parts of the blade path so it is not possible to accurately calculate the mean tangential blade force (4.18) for the whole cycle.

The measurements from the PII fall into two categories. For six blades, the tangential forces measured during the curved part of the path are small in magnitude so that they do not drastically affect the average (4.18), resulting in reasonable estimates for C_Q. In contrast, for three blades the tangential forces measured on the curved path have very large negative values and these dominate the average values.

For six blades the averages are plotted in Figure 4.26. In Figure 4.26 it is evident that the effect of the finite blade correction in the vortex model is to reduce the torque and power such that they are always negative. Meanwhile the model without corrections predicts negative torque at low speeds and positive above a blade speed ratio of 3. The experimental results show a similar pattern to that predicted by the model: the torque and power are low, and then rise up after a particular blade speed and maintain high levels of torque and power. However, the experimental measurements show that the rise in torque and power happens at a much lower blade speed than predicted by the vortex model. The experimental measurements are probably higher than is realistic because the measurements of F_{t}^{+} in the grey regions, which are invalid, were always positive while at least a short period of negative tangential force would be expected. Nevertheless there is a clear picture from the experiments that the rise in torque and power happens at a lower blade speed than was predicted.

The model has three main short comings: a lack of dynamic stall model, the reliance on empirical blade data, and the lack of three-dimensional considerations. Further, the experiment is not the same as the model: the effect of the structure is not accounted for by the model, and this additional thrust may increase the effective solidity of the device, moving the C_Q- and $C_P - \Lambda$ curves to the left.

For three blades the averages are plotted in Figure 4.27. Once again the effect of the finite blade correction in the vortex model is seen to reduce the torque and power significantly – so that it is never positive at this scale. The experimental results for torque and power are very negative because of the disproportionate effect of the measured blade force on the curved part of the path, which is in fact just the effect of centrifugal force. There is a general pattern in the measurements showing higher (less negative) torque and power with higher absolute towing

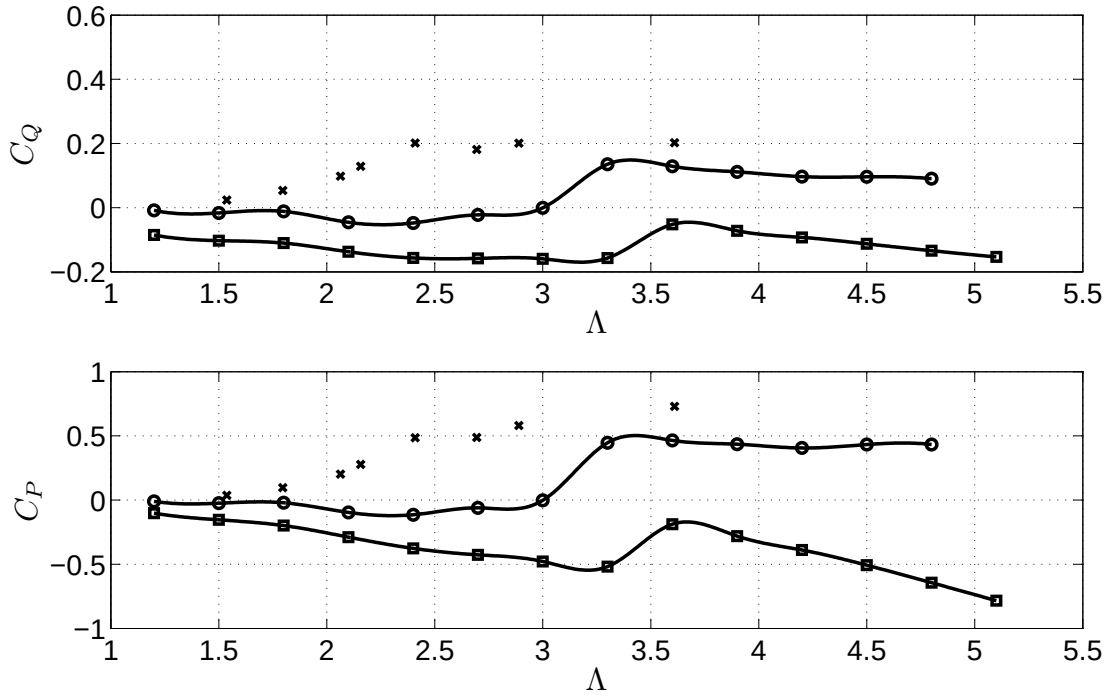

Figure 4.26: *Six bladed PII: average torque, C_Q, and power, C_P, from the tangential force, F_t^+, using (4.19). Vortex model:* –○– without *finite blade corrections,* –□– with *finite blade corrections;* × *Measurements from PII with 6 blades.*

speed, and also a general pattern of torque and power rising with blade speed ratio. The measured net torque and power increase with towing speed, but this is likely to be because the hydrodynamic forces become higher relative to centrifugal forces (which remain essentially the same) so is not necessarily a hydrodynamic (e.g. Reynolds number) effect.

The predictions by the vortex model in Figures 4.26 and 4.27 show a much lower power coefficient when the blades are corrected for three dimensional effects; the power coefficient is always negative. This is due to the inconsistency of the correction factor described in Section 2.4.6.

4.7 Summary and conclusions

4.7.1 Experimental programme: PII

The prototype Moonraker, PII, was successfully operated at UCL and QinetiQ and the instrumented blade has been used to record blade loading over a range of conditions including blade speed, towing speed, and number of blades. Mechanical issues at high blade speeds limited blade speeds to 2 m/s or blade speed ratios of $\Lambda < 5$. Due to the large friction in the system, and the disproportionately high effect of friction at lab-scale, the device required a motor to rotate the blades at all times.

A blade on the PII was instrumented with a two-component load cell and a series of blade

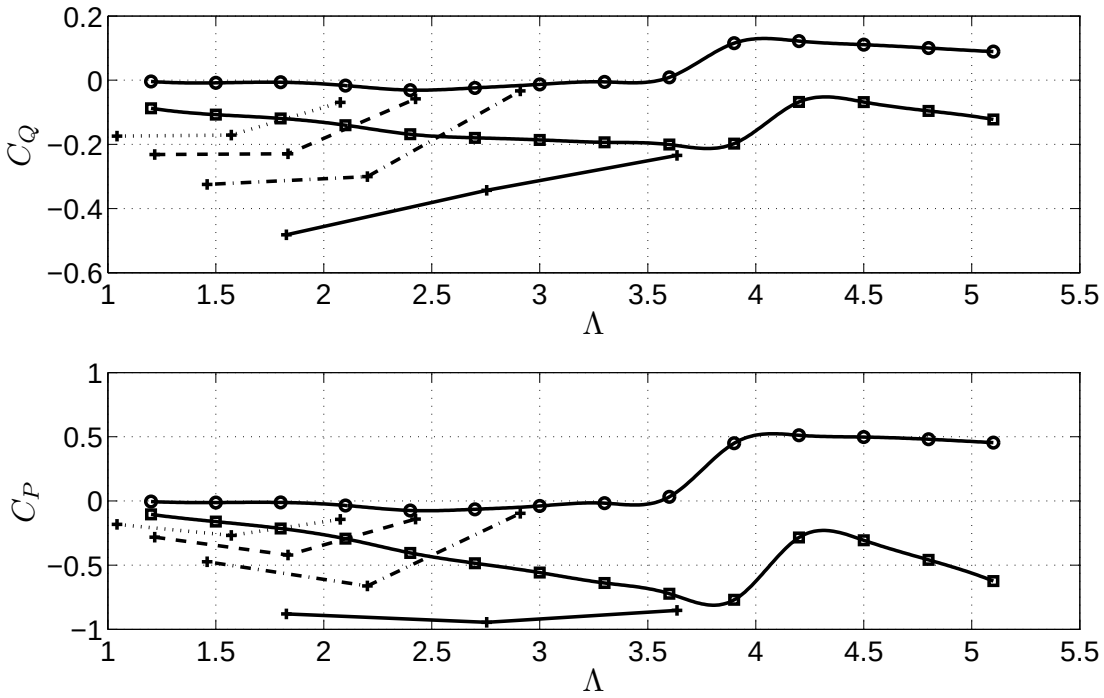

Figure 4.27: *Three bladed PII: C_Q, and power, C_P, from the tangential blade force, F_t^+, using (4.19). Where repeated measurements are available, the mean of the two has been used. Vortex model:* —○— without *finite blade corrections,* —□— with *finite blade corrections, PII measurements:* —+— *$U = 0.4$ m/s,* $-\cdot-+-\cdot-$ *0.5 m/s,*$--+--$*, 0.6 m/s,* $\cdot\cdot+\cdot\cdot$ *0.7 m/s.*

force measurements were made. The repeatability of the blade loading measurements when performed independently and in opposite directions is very good.

Blade force measurements, both normal and tangential to the blade's motion, show clear undulations as the blade joins the track (upstream and downstream) and this is due to the mechanical design of the PII. It is recommended that future designs aimed at making blade loading measurements use a continuous monorail track to avoid this problem.

The blade force measurements are not valid on the circular parts of the blade's path due to unknown support conditions although in reality they are probably approximately simply supported; in practice the real problem with the circular path is that the blade was allowed to pitch and the centrifugal force pollutes the measurements of tangential force which is an order of magnitude smaller. For measurements with six blades the *ad hoc* 'cable-tie' system did a reasonable job of correcting this problem, so that the average torque measurements derived from blade forces are artificially positive for the circular path but nevertheless provide useful measurements. For three blades the 'cable-tie' had stretched and the results on the circular path are extremely negative which makes the average torque measurements unrealistically low.

For three blades rotational speeds were not high enough to achieve high torques, but for six blades, where solidity is higher, the necessary speed to achieve high torques was possible. This supports the predictions that higher solidity moves the torque and power curves to lower blade speeds. Regarding the magnitude of the power coefficient, measurements have been presented over a range of blade speeds with good repeatability and showing a smooth power curve ($C_P - \Lambda$), and the measurements showed power coefficients above 0.5. This is encouraging in terms of the types of power coefficient of which the Moonraker may be capable, however the uncertainty associated with the experimental results is fairly high so the measurements made here are not definitive. The main cause of the uncertainty is the fact that the power coefficient is derived from the average tangential force, which is not valid during the curved parts of the blade's path. The next biggest cause of uncertainty is from the variability of the measurements, which is less than 5% for low blade speeds, but for high blade speeds is approximately 10% on the upstream path and higher on the downstream path (due to the approximately zero mean on the downstream path, it is difficult to quantify this variability, but it is an order of magnitude higher than for the upstream pass).

The measurements of normal force were distorted and effectively 'clipped' due to some stray resistance in the instrumented blade. This problem could have been addressed by performing experiments with the blades rotating in the opposite direction and combining signals, however there was not time for this type of alteration during the two days of testing at QinetiQ.

4.7.2 Comparison of experimental and numerical results

There is encouraging agreement between the numerical model and experimental measurements of the force normal to the blade's motion. However, at higher blade speeds, where the blade was predicted not to stall, the agreement was not good.

Measurements of tangential forces show distinctly different magnitudes on the upstream and

downstream passes, while the model showed forces of similar magnitude on the upstream and downstream pass; in this sense the model does not agree with the experiment. The averages of tangential force have been used to compare the torque and power coefficients and there is qualitative agreement for six blades in that both model and experiment predict low torque and power up to a certain blade speed ratio, above which the torque and power increase dramatically. However, experiments suggest that this rise in torque and power occurs at a lower blade speed than was predicted.

While the measurements are subject to some uncertainty, they are repeatable and so are deemed to be fairly reliable. The reason for the disagreement between predictions and experiments is therefore probably due to shortcomings of the model which can be summarised as follows:

1. The numerical model is heavily reliant on empirical blade section data, and data for NACA0012 was used instead of for a blade tapered from NACA0015 at one end to NACA0013 at the other end.
2. The numerical model lacks a dynamic stall model.
3. The numerical model is two-dimensional in the $x-y$ plane yet it is clear that there will be dynamically significant motions in the $z-$direction.
4. The model does not account for the effect of the structure of the PII.

4.7.3 Further work

There is a discrepancy between the predictions and experiment and this has highlighted the need to further develop the models presented in Chapter 3. In particular a dynamic stall model could improve the predictions, and also either a BEM model with considerations of double actuator discs in close proximity, or a three-dimensional vortex model, could improve predictions. The issue of double actuator discs in close proximity is addressed in Chapter 5.

If the present experiments were repeated then improvements could be made. Firstly stray resistance in the load cell on the circuit for the normal load could be ameliorated or, alternatively, if the blades were reversed and rotated in opposite directions then a composite of each data set could be used. Additionally measurements of the velocity field would permit further comparisons with the predictions. Velocity measurements with the PII were attempted with an acoustic Doppler velocimeter but were unsuccessful due to the lack of reflective particles in the water at QinetiQ. A minor issue which would be relatively easily fixed would be in the results processing: the horizontal line on the plots for normal force, which corresponds to the limit of the linear voltage-loading relationship in the load cell, could in future be corrected for the individual offset values in each experiment. Additionally, a non-linear relationship between load and voltage could be used, which would remove the clipping effect on some of the results.

Given the problems with empirical blade data at low Reynolds number, a comparison of experimental measurements with predictions is likely to be more fruitful at a higher Reynolds number. To allow the PII to reach its potential blade Reynolds number of 180,000 the mechanics of the track system would need improvement. Some improvement can be achieved by implementing, in a more permanent way, the smoother transition applied in an *ad hoc* way at QinetiQ, described briefly in Section 4.3.5 and seen in Figure 4.9. Alternatively, a continuous mono-rail system is suggested. The continuous rail would remove the problem of the blade rejoining the track twice per revolution and would ensure a much smoother blade path and controlled blade pitching, so that useful results could be obtained over the whole revolution. Such a design would suffer from higher drag on the blade carriage, but if the centre of this drag coincides with the connection point of the blade, then it will not affect the bending moment measured in the centre of the blade. To achieve a more significant increase in Reynolds number would require a larger device, for example one that could be placed in a river.

Chapter 5

Vortex model of actuator surfaces

5.1 Introduction

This chapter addresses issues raised in the conclusions of Chapters 3 and 4. Chapter 3 showed that the vortex model predicted power output in excess of the limits derived from linear momentum theory and concluded that this should be investigated further. In this chapter the vortex model is simplified to that of a uniformly loaded actuator surface normal to a planar flow; this avoids the complexities of hydrofoils so that the vortex model itself can be tested. Following a thorough test of the vortex model of an actuator surface, this chapter uses the model to investigate double actuator surfaces in close proximity, which Chapters 3 and 4 concluded would be useful if it led to a theory that would enable the BEM method to be applied to the Moonraker.

This chapter is primarily concerned with developing the vortex model for a single actuator surface and testing the model for convergence and for its agreement with theory and experiments, including some new theory and experiments which are presented herein. The use of the vortex model to investigate double actuator surfaces is briefly demonstrated at the end of this chapter. The remainder of this introduction focuses on the need to test the vortex model and outlines the work in this chapter.

In Chapter 3 the vortex model was used to simulate extreme cases, such as high Reynolds number and infinitely long blades, which in practice it would be difficult to create physically due to the limitations of typical laboratories. Those cases showed very high performance, sometimes predicting a power coefficient above the Betz limit of 59.3%, and above the higher limit of 64% for double actuator surfaces (see Section 2.6 or Newman, 1983). These aforementioned 'limits' are derived from linear momentum theory which becomes less accurate as the loading increases; van Kuik (1991) found that linear momentum theory consistently under-predicts the velocity at and thrust on an actuator surface.

The flow induced by an actuator surface is characterised by the pair of vortex sheets em-

anating from its edges and the approach here is to model these vortex sheets with the same point vortex method used in Chapter 3. The point vortex method is reviewed in more detail Section 5.2. The vortex model applied to an actuator surface in planar flow is presented in Section 5.3 and a convergence study is presented including some visualisations of the vortex system.

In Section 5.4 results for the quasi-steady velocity at the surface and quasi-steady drag on the surface are compared to linear momentum theory (Section 2.6), semi-empirical models, and published experimental results. Results show agreement for light loads, then as the loading increases the linear theory and the vortex model show growing discrepancies; published results are too scattered to make conclusions, although it can be noted the vortex model predicts drag at the high end of the range of experimental results.

Following this the unsteady loading is given more attention, in particular the transient response of an impulsively started actuator surface in steady, uniform, planar flow. Section 5.5.1 presents an asymptotic model for an impulsively started actuator surface in planar flow in the limit of a lightly loaded surface. Section 5.5.2 compares results from the vortex model to the asymptotic theory, showing excellent agreement in the limit of light loading ($\kappa \to 0$). For heavier loads, given the scatter of published data and discrepancies with linear theories, new experimental data is required. Section 5.5.3 presents new experimental measurements of the drag on a mesh as it is towed through water. The mesh was towed at a constant speed following rapid acceleration from rest, and results show fair agreement with the vortex model during the transient stage, and good agreement with the final (steady) drag values. Finally Section 5.6 uses the vortex model to simulate some cases of double actuator surfaces. The emphasis in this chapter is on an actuator surface in planar flow; three dimensional cases are not considered.

5.2 Review of point vortex models

The point vortex method is applicable to a general vorticity field but this review is restricted to the use of point vortices to represent vortex sheets in two-dimensions. A vortex sheet is an infinitely thin shear layer and is therefore a streamline across which there is a discontinuity in tangential velocity.

The advantages of the point vortex method are its simplicity and its physical relevance, and also in its correctness when considering a fluid of infinite extent. The disadvantages lie in the inherent instability of a vortex sheet, the errors introduced by computer round-off, and the increase of computational cost with the square of the number of point vortices. This review identifies the origin and development of the technique including its main problems and the established solutions or adaptations that have been tested. Implemented of the method is detailed in Section 5.3.2, with the appropriate modifications for studying an actuator surface.

The earliest known example of the point vortex method is by Rosenhead (1931), who studied an infinite, straight vortex sheet with a small periodic initial disturbance. Rosenhead discretised one period of the vortex sheet (according to equation (5.6), given later), replacing the continuous

sheet with a finite number of point vortices. The point vortices represent small segments of the vortex sheet, and each vortex takes the same position and circulation as the centroid of that segment's vorticity. The vortex sheet was given an initial sinusoidal disturbance and each vortex was advected (according to (5.7), given later) for a number of time steps, Δt, using an Euler integration method. Rosenhead found that the sheets curled up in a familiar Kelvin-Helmholtz type pattern. Westwater (1936) made similar calculations to Rosenhead but applied to a finite vortex sheet representing the wake of an elliptically loaded wing. He found that the ends rolled up into a spiral.

Birkhoff and Fisher (1959) criticised the conclusions drawn by Rosenhead's work on an infinite vortex sheet. They show that repeating Rosenhead's calculations but with higher resolution leads to irregular motion including self-crossing of the vortex sheet which is not physically possible. Hama and Burke (1960) also tested Rosenhead's method with more vortices and reached the same conclusion. Further criticism came when Westwater's results, for a finite vortex sheet, were repeated at higher resolution by Takami (1964) and Moore (1971), both of whom found that chaotic motion was generated.

Between around 1970 and 1980 the problem of chaotic motion was approached by many researchers and a number of review papers were published (Clements and Maull (1975), Saffman and Baker (1979), Leonard (1980)). Moore (1981) outlined the four main problems with the point vortex method:

1. The velocity is singular at the vortex sheet.
2. The ends of a finite sheet cannot be accurately represented.
3. Vortices in very close proximity lead to accuracy problems, for example in a tightly wound spiral or when fluid separates from a body.
4. A vortex sheet is inherently unstable except when rapidly stretching; the problem is ill-posed.

The first problem, that of the singular velocity on the vortex sheet, was solved by van der Vooren (1965). That solution is not necessary in the present work, which uses a linear approximation of the vortex sheet, i.e. it is replaced purely by point vortices, whose self-induced velocity is assumed to be zero and the singularity problem is avoided altogether. To address the second problem Moore (1974) introduced an adaptation which is reviewed below. The third problem is exemplified by a tightly wound spiral vortex sheet or when fluid separates from a body. This is simply a warning that care needs to be taken in these particular situations.

The fourth problem, that of instabilities, is a result of the inviscid assumption – even a very small viscosity would dampen small disturbances and steep curvature in a shear layer, but in an inviscid fluid a vortex sheet is inherently unstable to any perturbation, however small. Numerical integration of the governing equation introduces small errors due to round-off or

truncation and this introduces very small perturbations (depending on the machine precision). This tends to ruin calculations because a disturbance in a vortex sheet grows at a rate inversely proportional to its wavelength (Krasny 1986). As a result, if vortices are closer together, i.e. for higher resolution calculations, instabilities grow at a greater rate. This is why instabilities were not detected in early, lower resolution calculations and it explains why as the number of vortices increases the discretised system will not converge to the original continuous system; the problem is ill-posed.

The rapid growth of short-waves, whatever their source, ruins most practical calculations. Increasing machine precision will reduce but not remove the problem (Krasny 1986). Three adaptations, each designed to cope with the instabilities, have been considered when implementing the point vortex method to simulate an unsteady actuator surfaces and they are reviewed below: roll-up approximation, rediscretisation, and vortex cores.

5.2.1 Adaptations of the vortex method

5.2.1.1 Roll-up approximation

Moore (1974) addressed the problem of a vortex sheet behind an elliptically loaded wing with particular attention paid to spiral roll-up at the tip, which is the source of chaotic motion in a finite vortex sheet. The roll up of a free-ended vortex sheet is particularly relevant for the actuator surface case. The passage below is from Moore (1974) and explains why the discretised tip roll-up causes an instability to grow over the entire vortex sheet. In the passage, $\tau = Ut/a$ where a is half the length of the initially straight vortex sheet which is elliptically loaded with a vorticity, Ω along its length, x: $\Omega(x) = 2Ux(a^2 - x^2)^{-\frac{1}{2}}$ where U is its initial downward speed, and the polar equation refers to polar coordinates (r, θ).

> "If the distance between turns [in the spiral] is much less than the typical arc distance between the constituent vortices then there will be instants when vortices on neighbouring turns will come very close together. This will lead to a spuriously large interaction between this pair which might disrupt the orderly evolution of the system.
>
> ... [A] possible explanation of the failure of the discrete representation [of a vortex sheet] arises out of an examination of Kaden's results [Kaden, 1931]. When $\tau \ll 1$ the spirals at the ends of the vortex sheet evolve independently and Kaden showed analytically that the vortex sheet at either tip has the form of a spiral whose polar equation is $r \propto (\tau/\theta)^{\frac{2}{3}}$. Thus any attempt to replace the sheet by a finite number of point vortices will cease to be adequate sufficiently near the centre of the spiral, since the spiral has an infinite number of turns. This is obvious and Westwater pointed out that no detail of the inner portion of the spiral could be found by his

> method. What is less obvious is that the failure of the discretization is not local. There is no reason to assume that the vortices representing the inner spiral portion of the sheet maintain their correct positions on the vortex sheet but, even if they did, the vortices in the outer part of the sheet would not experience the true velocity field induced by the inner spiral. This velocity field varies smoothly with time and is almost axisymmetric, whereas the velocity field due to these inner point vortices is irregularly fluctuating and is non-axisymmetric. Thus the outer vortices, which one might have hoped would represent correctly the outer part of the sheet, respond by themselves starting to move irregularly. Thus chaotic motion spreads to ruin the calculation, the long-range nature of the coupling between individual vortices facilitating the process."

Moore proposed replacing vortices located in the inner spiral with a single point vortex, with an equal centroid of vorticity to the vortices that it replaces. This will produce a stable and axisymmetric velocity field in the outer spiral. The technique consists of gradually amalgamating vortices at the end of the sheet as they become too tightly wound. The condition for a vortex to be amalgamated is based on the number of vortices per turn, where a minimum of four is suggested. Once there are fewer than four vortices per turn, an appropriate number of vortices are amalgamated into the central vortex so that the condition of four vortices per turn is met. The errors introduced by the amalgamation process were shown to be satisfactorily small, and the technique successfully suppressed chaotic motion in the tip region.

In the present work Moore's technique was applied to the sheet rolling up behind an actuator surface to see if it had any benefit. The use of the technique offered no clear benefit in terms of stability or any other measure so it was not implemented. The reason for the failure of the technique is not clear. The vortex sheet behind an actuator surface is different from that behind a wing, in particular because it is continuously growing.

5.2.1.2 Re-discretisation

To illustrate the ill-posed nature of the point vortex problem, Moore (1971) used increased precision and a fourth-order Runge-Kutta integration technique to simulate a pair of orbiting vortices, for which there exists an analytical solution. After 40 revolutions the fractional error was about 10^{-9} in the coordinates, i.e. no chaos was present. The same technique was applied to Westwater's vortex sheet and chaotic motion was found, matching the results of Takami (1964). Further, reversing the calculation returned the vortices to their starting point. Moore therefore suggests that the cause of the chaos lies with the discretisation, not the integration.

To address the problem of discretisation researchers have implemented various methods of adjusting vortices between time steps, in an attempt to suppress growing instabilities. This can be done with simple smoothing or full rediscretisation. Smoothing, or filtering, refers to an adjustment of vortex positions. Rediscretisation means introducing a replacement set of vortex

strengths and positions i.e. the vortex strengths may change and the number of vortices may also change.

The first known attempt at smoothing is provided by Longuet-Higgins & Cokelet (1976) who calculated the evolution of steep surface waves on water and found growing instabilities at the surface of discontinuity. To remedy the problem, which is analogous to the instability in vortex sheets, their smoothing method applies a filter to the wave form represented by the discrete points, at each time-step, removing small-wavelengths. The new (filtered) position of each vortex was determined using a weighted average of the position of surrounding vortices, and this was an effective technique for suppressing the growth of instabilities. Moore (1981) tested this method on a circular vortex sheet with 60 vortices and found that it delayed chaotic motion, but that such motion still set in after about one and a quarter revolutions. In summary filtering can improve some calculations but does not remove the underlying problem and also has unknown effects on the accuracy.

Krasny (1986) studied an infinite vortex sheet with an initial periodic disturbance – the same problem addressed by Rosenhead (1931). Krasny used a spectral filtering method which is similar in principle to the linear smoothing of Longuet-Higgins & Cokelet (1976). The method is based on a discrete Fourier transform of the wave where, at a given time, frequencies that could not have grown naturally (i.e. are sourced by finite-precision) are removed and the inverse transform provides the revised positions of the vortices. This careful method minimises accuracy losses, but is only applicable to periodic waves. In summary, filtering methods can aid some calculations of discretised vortex sheets, but none is particularly suited to the actuator surface problem.

A method of fully rediscretising the vortex sheet between time steps was introduced by Fink & Soh (1978). They derived the discretisation of the vortex sheet including higher order terms, showing that if a point vortex is at the centre of its segment then the discretised vortex sheet is an accurate approximation to the continuous vortex sheet to second order, so that errors are $O\left(\Delta s^3\right)$ which can be made arbitrarily small (where Δs is the segment length). However, should the vortex move away from the centre of its segment due to non-uniform stretching, a new error is introduced of the form $\gamma \ln \frac{\Delta s_{1/2}}{\Delta s_{-1/2}}$ where $\Delta s_{\pm\frac{1}{2}}$ are the distances between the point vortex and each edge of the segment it represents. This error term can be large regardless of how small the segment size is, hence convergence cannot be found as the number of vortices increases. Rather than account for the higher-order terms, Fink & Soh (1978) rediscretised the vortex sheet between time steps: a new set of point vortices is introduced to replace the old set, each placed at the centre of their respective segments, removing the logarithmic error term. As with the initial discretisation, the vorticity is assumed to be varying linearly along the vortex sheet. Fink & Soh (1978) used this technique on the vortex sheet behind an elliptically loaded wing, including the use of Moore's technique for amalgamating the spiral vortices. They found very smooth results, even when introducing a sinusoidal perturbation to the sheet at the location that most commonly exhibits instabilities (given that tip instabilities have been suppressed).

A similar rediscretising technique was used by Sarpkaya (1979) who simulated the growth and

advection of vortex sheets in the wake behind a cylinder. Sarpkaya rediscretised the vortices so that they were equi-spaced, and found that the irregular growth of the vortex sheets was suppressed.

Baker (1980) criticised Fink & Soh's (1978) technique because it did not account for the curvature of the vortex sheet; Baker claimed that, without the amalgamating method at the tip, Fink & Soh's (1978) vortex sheet would not be stable. Baker suggested that a vortex sheet without ends, e.g. that shed by a ring wing, is a better test for the method, but found that even that test case was not stable – the sheet crossed itself. Moore (1981) also investigated the technique of Fink & Soh (1978) and concluded that, although it does introduce inaccuracies, it does remove the most unstable modes of growth in the sheet and is therefore an effective stabiliser. Note, however, that it relies on the method of Moore (1974) to stabilise the spiral at the free ends of the vortex sheet.

Fink & Soh's (1978) method of rediscretisation introduces unknown errors and the strategy behind rediscretisation for general scenarios is also not clear. Because of the uncertain errors and the reliance on Moore's amalgamation method (which was not effective for an actuator surface) Fink & Soh's (1978) method was not implemented in the present work.

5.2.1.3 Desingularised Vortex cores

A two-dimensional point vortex is a concentration of vorticity such that, in an inviscid fluid, the circulation around that point is

$$\Gamma = \int_A \boldsymbol{\Omega}\left(\boldsymbol{x}\right) \mathrm{d}A = \oint_C \boldsymbol{u} \cdot \mathrm{d}\boldsymbol{x}$$

where $\boldsymbol{\Omega}$, the vorticity, is a two-dimensional delta function and C is any closed loop around the point vortex. The velocity induced by a point vortex is axi-symmetric:

$$\boldsymbol{u}\left(\boldsymbol{r}\right) = \frac{\Gamma}{2\pi r} \times \hat{\boldsymbol{e}}_r \tag{5.1}$$

where $\boldsymbol{r}$ is a vector from the vortex centre to the location of the induced velocity. The velocity is singular at the vortex, and is very large near to the vortex. The velocity gradient across the point vortex is infinite. Even as the Reynolds number tends to infinity, the effect of viscosity will still be finite at these infinite gradients. The effect of viscosity in a point vortex is to diffuse the vorticity so that the size of the rotational vortex core becomes finite. Numerous methods have been developed that desingularise the core of each vortex and such techniques can improve the stability of calculations but the accuracy must be carefully monitored. The general method consists of using vortex 'blobs', which have a mollified core:

$$\lim_{r \to 0} \boldsymbol{u}\left(\boldsymbol{r}\right) \quad \rightarrow \quad 0 \tag{5.2}$$

$$\lim_{r \to \infty} \boldsymbol{u}\left(\boldsymbol{r}\right) \quad \rightarrow \quad \frac{\Gamma}{2\pi r} \times \hat{\boldsymbol{e}}_r \tag{5.3}$$

The actual velocity profile used, and the radius at which the velocity profile returns to that of a point vortex varies between different models but generally corresponds to a Reynolds number type scale. Krasny (1987) introduced the desingularisation parameter, δ, so that the velocity induced by a point vortex is

$$\boldsymbol{u}(\boldsymbol{r}) = \frac{r}{r^2+\delta^2}\frac{\Gamma}{2\pi} \times \hat{\boldsymbol{e}}_r \tag{5.4}$$

This method is generalised and justified in Cottet and Koumoutsakos (2000). Krasny applied the desingularisation parameter to the case of a vortex sheet behind an elliptically loaded wing (Krasny, 1987) and to a flat plate normal to uniform flow (Krasny 1991) and achieved very smooth results, showing convergence as $\delta \to 0$.

The power of the desingularising technique in stabilising point vortex calculations, which are otherwise practically useless for large times and high resolution, is clear (Krasny 1987). Varying the value of δ will lead to different results because it is effectively introducing a Reynolds number to each vortex. As δ decreases, solutions will converge to the inviscid case.

To be physically consistent the vortex core, which is now presumed viscous, should diffuse in time, i.e. $\delta = \delta(t)$. This introduces problems because as the core of a vortex grows it will be subject to non-uniform deformation, e.g. a straining flow field, and the vorticity field of each vortex will cease to be axisymmetric. Each vortex would thus need to be discretised into smaller parts which is undesirable; either this would lead to a traditional finite-difference grid based numerical method, or it would imply splitting the vortex into smaller vortices whose cores are presumably too small to experience significant straining; however this latter method has been shown to be incorrect (Greengard 1985).

Various techniques have been developed, e.g. Chorin (1973), to account for the physical processes implied by a viscous core, i.e. random walk due to vorticity diffusion, and the annihilation of opposite vorticity in close proximity. Most of these methods require experimentally derived constants or assumptions in order to tune the calculations. For example, Jaroch and Graham (1988) used the discrete vortex method to simulate a flat plate normal to the flow and the circulation of their vortices decayed exponentially in time; the rate of decay was varied until the length of the recirculation bubble downstream of the flat plate agreed with experiments.

To reach a more general conclusion about the effectiveness of the vortex method, in this work empirical tuning of the simulation was avoided. In the present work the limiting case of infinite Reynolds number is assumed, so that viscosity is only effective in regions of infinite velocity gradient, i.e. the vortex core. The vortex core is mollified using the desingularisation parameter, which is constant in time. The effect of the desingularising parameter, δ, is investigated and tested for convergence.

5.2.2 Time integration methods, improved efficiency and parallel processing

The Euler integration method is the simplest to implement but introduces growing errors. Higher-order schemes such as the fourth order Runge-Kutta (RK4) method improve accuracy but require extra computation for a given time-step size. The RK4 method is commonly used in point vortex calculations such as those of Moore (1971; 1974; 1981) and Krasny (1986; 1987; 1991); however some researchers claim that the Euler method produces more 'realistic' results (e.g. Inoue, 1989). Given a lack of clear choice this work used both the Euler and RK4 methods and compared their performance.

The calculations required for a system of n point vortices is $O\left(n^2\right)$. In the case of an actuator surface, where $n \propto t$, the total calculations for a simulation of time, t, is $O\left(t^3\right)$. This problem can be addressed by using the fast multi-pole method. This method treats clumps of vortices as a single vortex when calculating their effect at a location that is far away with respect to the diameter of the clump. However, such computational complexity was avoided during this work as calculations tended to be completed in a conveniently short time.

The point vortex method is well suited to parallel processing as, within each time-step, calculations are independent. No parallel processing has been carried out during this work, would make a useful improvement in the future if larger scale calculations were desired.

5.3 Numerical model

5.3.1 Formulation

The velocity induced by a two-dimensional vorticity field is given by the Biot-Savart integral (see, for example, Leonard 1980):

$$\boldsymbol{u}\left(\boldsymbol{x},t\right) = \frac{\mathrm{d}\boldsymbol{x}}{\mathrm{d}t} = -\frac{1}{2\pi}\int \frac{\left(\boldsymbol{x}-\boldsymbol{x}'\right)\times\Omega\left(\boldsymbol{x}',t\right)\hat{\boldsymbol{z}}}{\left|\boldsymbol{x}-\boldsymbol{x}'\right|^2}\mathrm{d}\boldsymbol{x}' \tag{5.5}$$

In two-dimensional flow the vorticity field, $\Omega\left(\boldsymbol{x},t\right)$, is scalar and can be discretised as (see, for example, Leonard 1980):

$$\boldsymbol{\Omega}\left(\boldsymbol{x},t\right) = \sum_{i=1}^{n}\Gamma_i\delta\left(\boldsymbol{x}-\boldsymbol{x}_i\left(t\right)\right) \tag{5.6}$$

where $\boldsymbol{x}_i$ are the locations of n point vortices with respective circulation Γ_i. Combining (5.5) and (5.6) we have a system of $2n$ nonlinear ODEs:

$$\frac{\mathrm{d}\boldsymbol{x}_i}{\mathrm{d}t} = -\sum_{j=1,\,(i\neq j)}^{n}\frac{\Gamma_j\left(\boldsymbol{x}_i-\boldsymbol{x}_j\right)\times\hat{\boldsymbol{z}}}{2\pi\left|\boldsymbol{x}_i-\boldsymbol{x}_j\right|^2}, \tag{5.7}$$

where a point vortex has no self induced velocity. In the limit $n\to\infty$, (5.7) tends to (5.5);

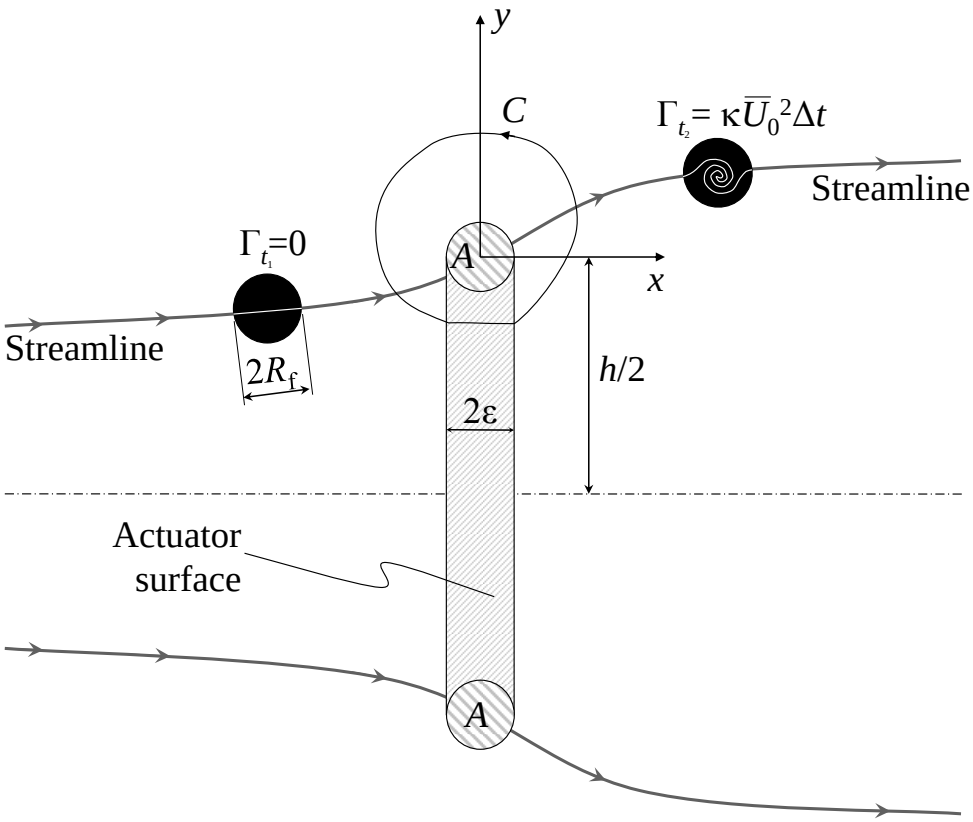

Figure 5.1: *An 'actuator surface' in planar flow with uniform pressure jump, Δp. A particle is illustrated which passes through the surface edge and gains circulation.*

the issue of convergence and how this problem is not 'well posed' was discussed in the previous section. The point-vortex method consists of determining the strength, Γ_i, and location, $\boldsymbol{x}_i$ of the n vortices, i.e. solving for $\boldsymbol{x}_i(t)$ and is therefore a Lagrangian method. In the present section a discretisation scheme appropriate to an actuator surface is derived and then reviews methods of calculating the solution. Equation (5.7) is often modified in order to stabilise the calculation and this is discussed in Section 5.3.2.

The actuator surface generates a force field, $\boldsymbol{F}$ (Nm^{-3}) and, as stated in Section 2.6.1, this leads to the generation of vorticity wherever the term $\nabla \times \boldsymbol{F}$ is non-zero; equation (2.44) showed that this will only be the case at the surface edge. In other words a uniformly loaded actuator surface only generates vorticity at its edges; to study this we define the origin at the edge of the actuator surface, as in Figure (5.1). Starting with the upper edge, we analyse this infinitesimal area A, which we define by:

$$A = \pi \epsilon^2. \tag{5.8}$$

Stokes's theorem can be applied to a closed contour, C, enclosing the edge area A:

$$\int_A \nabla \times \boldsymbol{F} \cdot \mathrm{d}A = \oint \boldsymbol{F} \cdot \mathrm{d}C = \frac{1}{2}\kappa\rho U_s^2(t). \tag{5.9}$$

Substituting (2.47) into (5.9):

$$\rho \int_A \frac{\mathrm{D}\Omega}{\mathrm{D}t}\mathrm{d}A = \rho\frac{\mathrm{d}\Gamma}{\mathrm{d}t} = \frac{1}{2}\kappa\rho U_s(t)^2\frac{\delta(\epsilon)}{\pi\epsilon}. \tag{5.10}$$

This derivation is the same as van Kuik (1991; 2003) except that $\Delta p = \frac{1}{2}\kappa\rho U_s^2(t)$, so that the surface behaviour is coupled to the flow field it induces.

Equation (5.10) says that a material group of fluid particles passing through the surface edge will gain circulation. For planar flow, the edge of the surface is a 2-D delta-function and so is an infinitesimal area, meaning that circulation is generated at a point. Figure (5.1) illustrates this: a particle of radius R_f travelling at speed U will contain the surface edge for a finite time:

$$\Delta t = 2R_f/U. \tag{5.11}$$

The particle will gain circulation during that time, such that when it leaves the surface edge:

$$\Delta\Gamma = \frac{\mathrm{d}\Gamma}{\mathrm{d}t}\Delta t = \mp\frac{1}{2}\kappa U_s^2(t)\Delta t \tag{5.12}$$

where the negative sign applies to the upper edge, and positive to the lower edge. The problem is approached numerically by the injection of point vortices at the surface edges after regular time steps, Δt. The circulation of the point vortices generated at time t_1 will remain constant after creation:

$$\Gamma_{t=t_1} = \frac{1}{2}\kappa U_s^2(t_1)\Delta t \tag{5.13}$$

As time progresses multiple vortices are shed and advected according to the total velocity field, which is determined by an appropriate integration method. The total velocity at any point in the flow field is the sum of the contributions from all n vortices, plus the external ambient flow:

$$\frac{\mathrm{d}\boldsymbol{x}_i}{\mathrm{d}t} = -\sum_{j=1,\,(i\neq j)}^{n} \frac{\Gamma_j(\boldsymbol{x}_i - \boldsymbol{x}_j)\times\hat{\boldsymbol{z}}}{2\pi|\boldsymbol{x}_i - \boldsymbol{x}_j|^2} + \boldsymbol{u}_E(\boldsymbol{x},t), \tag{5.14}$$

In the limit $n \to \infty$ (5.14) is the velocity induced by a continuous vortex sheet, as in (5.5).

5.3.2 Implementation

Vortices are advected by the local velocity according to (5.14) and an appropriate time integration method is employed. Three methods were employed in this work; the first was the Euler method:

$$\boldsymbol{x}_i\left(t+\Delta t\right)=\boldsymbol{x}_i\left(t\right)+\Delta t\frac{\mathrm{d}}{\mathrm{d}t}\boldsymbol{x}_i\left(t\right). \tag{5.15}$$

The second was the Euler method but with sub-time steps of $\frac{\Delta t}{2}$:

$$\boldsymbol{x}_i\left(t+\Delta t\right)=\boldsymbol{x}_i\left(t\right)+\frac{\Delta t}{2}\frac{\mathrm{d}}{\mathrm{d}t}\boldsymbol{x}_i\left(t\right)+\frac{\Delta t}{2}\frac{\mathrm{d}}{\mathrm{d}t}\boldsymbol{x}_i\left(t+\frac{\Delta t}{2}\right). \tag{5.16}$$

The third method employed was the fourth order Runge-Kutta (RK4) method:

$$\begin{aligned}
\boldsymbol{k}_1 &= \frac{\mathrm{d}\boldsymbol{x}_i}{\mathrm{d}t}\left(t,\boldsymbol{x}\right),\\
\boldsymbol{k}_2 &= \frac{\mathrm{d}\boldsymbol{x}_i}{\mathrm{d}t}\left(t+\frac{\Delta t}{2},\,\boldsymbol{x}+\frac{\Delta t}{2}\boldsymbol{k}_1\right),\\
\boldsymbol{k}_3 &= \frac{\mathrm{d}\mathbf{x}_i}{\mathrm{d}t}\left(t+\frac{\Delta t}{2},\,\boldsymbol{x}+\frac{\Delta t}{2}\boldsymbol{k}_2\right),\\
\boldsymbol{k}_4 &= \frac{\mathrm{d}\mathbf{x}_i}{\mathrm{d}t}\left(t,\,\boldsymbol{x}+\Delta t\boldsymbol{k}_1\right).
\end{aligned}$$

The updated position is determined by a weighted average of the intermediate velocities:

$$\boldsymbol{x}_i\left(t+\Delta t\right) = \boldsymbol{x}_i\left(t\right)+\frac{\Delta t}{6}\left(\boldsymbol{k}_1+2\boldsymbol{k}_2+2\boldsymbol{k}_3+\boldsymbol{k}_4\right). \tag{5.17}$$

After each time-step a new vortex is shed at the surface edge according to (5.13). A point vortex simulation of an actuator surface according to this analysis was written in Fortran. Distances are normalised with the surface height, h, velocities with U_∞, and times with an advective time scale h/U_∞. The quantitative diagnosis of a simulation is made through the normal velocity at the surface, $U_s\left(t\right)$ for given pressure drop coefficient, κ. The thrust and power coefficients can then be determined as per (2.48) and (2.49) respectively. A qualitative comparison can also be made through the shape of the vortex sheets (the vortex locations) and the distribution of vorticity along the sheets (vortex strengths).

5.3.3 Verification and convergence study

The purpose of this section is to find the range of computational parameters over which the results of the simulations are invariant - within 1% at all times. All verification work is for the case of impulsively started planar flow and a single actuator surface with a pressure drop coefficient $\kappa=2$. Systematic simulations consisted of all 60 permutations of the following variables:

- $\delta = 0.01,\ 0.03,\ 0.05\,, 0.071.$
- $\Delta\tau = 0.005,\ 0.01,\ 0.02,\ 0.04,\ 0.08.$
- Integration method: Euler, Euler with a sub-time-step, fourth order Runge-Kutta (RK4).

The effect of these parameters on the code could then be assessed to verify that its performance is self-consistent, invariant to non-physical parameters, and physically realistic. The measure for comparison between different simulations is the normal velocity at the surface:

$$u_s(t) = U_s(t)/U_\infty, \tag{5.18}$$

$$u_s(t) = \frac{1}{h}\left[\int_{-h/2}^{h/2} (\boldsymbol{u}\cdot\hat{\boldsymbol{x}})^2 \,\mathrm{d}\boldsymbol{x}\right]^{\frac{1}{2}}, \tag{5.19}$$

this average is possible because the vortices have been desingularised and it is used because it is a closer approximation to a turbine than using the velocity at the centreline (u_0).

The results invariably show that the normal velocity at the surface, $u_s(t)$, decreases monotonically in time towards an asymptotic value. It tends to reach the asymptotic value by $\tau \sim 60$, at which point it oscillates by less than 0.1% with no dominant frequency. For a given value of κ the values of $U_s(t)$ from simulations with different input parameters were compared; the maximum difference between simulations at any time was ∼1%.

Generally any inadequacy of the simulations is expected to increase with higher values of κ, as the system becomes more non-linear and more unstable. It is therefore important to verify the code for a value of κ at which the code is expected to perform further duties. The value $\kappa = 2$ represents an optimally configured tidal turbine. Other simulations were also performed and these will be discussed in the following section.

For all simulations, at $\tau = 50$ the normal velocity at the surface is still decreasing but at a relatively slow rate: $\frac{\mathrm{d}}{\mathrm{d}\tau}u_s(50) \sim 6\times10^{-5}$. Quantitative comparisons will be made at this time. Evidence of convergence as the computational parameters reduce will now be presented and discussed.

The computational cost is $O\left(\Delta\tau^3\right)$ hence the computational time for $\Delta\tau = 0.08$ is 4096 times that of $\Delta\tau = 0.005$. The integration method also affects the computational cost: compared to standard Euler integration and for equal $\Delta\tau$, the use of a sub-time-step doubles the computational cost, the RK4 method costs four times more.

5.3.3.1 Convergence and quantitative comparison

Figure 5.2a shows the normal velocity at the actuator surface at time $\tau = 50$ for simulations with the three different integration methods and five different time steps, using the same desingularisation parameter, $\delta = 0.071$. Convergence of the value $u_s(50)$ can be seen as $\Delta\tau \to 0$ and the different integration methods show a maximum difference in u_s, at any time, of less than about 0.15%. For time steps smaller than $\Delta\tau = 0.02$, the difference in $u_s(50)$ are less than 0.01%. This result is representative of the systematic set of 60 simulations that were run to verify the performance of the code.

Figure 5.2b shows another collection of values $u_s(50)$ for one integration method (Euler) but

with varying values of δ. For each value of δ, convergence of the value of $u_s(50)$ can be seen as $\Delta\tau \to 0$. Further, convergence can also be seen as $\delta \to 0$. These tests were repeated for all permutations of parameters and the same pattern of convergence was found. The plots in Figure (5.2) show that the difference in $u_s(50)$ when using extreme values $\delta = 0.071$ and $\delta = 0.01$ is less than 1%. The difference between $u_s(50)$ when using extreme time steps of $\Delta\tau = 0.08$ and $\Delta\tau = 0.005$ is also less than 1%. The value of $u_s(\tau)$ is quite steady; by interpreting the results using a 10-timestep average for $u_s(\tau)$ the difference is negligible.

In summary the results show convergence of $u_s(\tau)$ with time-step and desingularisation parameter, as well as invariance with time integration method. This gives confidence in the current implementation of the vortex method as a measure of $u_s(\tau)$ within about 1% when using $\Delta\tau < 0.05$ and $\delta < 0.05$.

5.3.3.2 Visualisation and qualitative comparison

Figure 5.3 shows the evolution of vortices during the time period $0 < \tau < 10$ for a representative simulation: $\kappa = 2$, $\Delta\tau = 0.02$, $\delta = 0.05$ using RK4 integration. The vortex sheets are initially independent due to their physical separation and small total circulation. Their initial growth consists of advection downstream at the external flow speed, and local rolling up of the tip into a spiral. This behaviour shows features also found in the vortex sheet shed from a bluff body with sharp edges in impulsively started flow, as described by Pullin and Perry (1980). As the spirals grow they have an increasing effect on each other and by $\tau = 5$ their interaction is strong: they form a vortex dipole system and force each other in the upstream direction. The wake length is now growing at a rate significantly less than 1. By $\tau \sim 10$ the section of the vortex sheets not entrained in the spirals have overtaken the dipole system and meet each other on or near the $x-$axis.

For larger times, $\tau > 10$ (shown in Figure 5.4), the vortex sheets are arranged in close proximity and instabilities arise. This scenario of opposing vortex sheets approaching each other is similar to the meeting of boundary layers behind a cylinder in impulsively started flow; small, unstable waves form in the vortex sheets, causing them to break down into coherent vortex pairs. An ordered vortex street does not form, possibly because of the fluid in the wake splitting the vortex sheets ('bleed air' - Castro 1971). The instabilities also travel upstream along the vortex sheets as short waves but their growth is inhibited due to the desingularising parameter, δ.

Generally excellent agreement was found between vortex positions from different integration methods until $\tau \sim 10$ and Figure 5.5 is an example of this: an enlarged view of a simulation at $\tau = 8$ comparing the results of Euler and RK4 integration. The RK4 vortices have been joined by straight lines, and the results from Euler integration are represent by circles. Figure 5.5 shows that at $\tau = 8$ small differences are appearing at the strained areas of the vortex sheet and also at the spiral, which is unresolved. The spiral is self-similar, with infinite turns, so it is not possible to resolve (see section 5.2 or Moore 1974, Pullin 1978, van Kuik 2003, van Kuik 2004a).

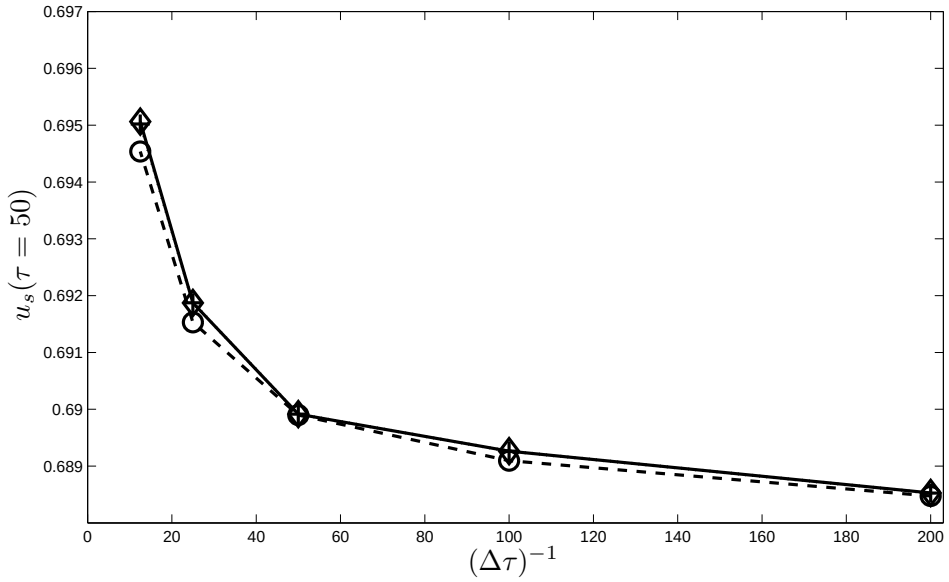

(a) $\delta = 0.071$ *with different methods of time integration:* ○- *Euler integration,* ◇- *Euler integration with sub-time-step,* +- *RK4 integration.*

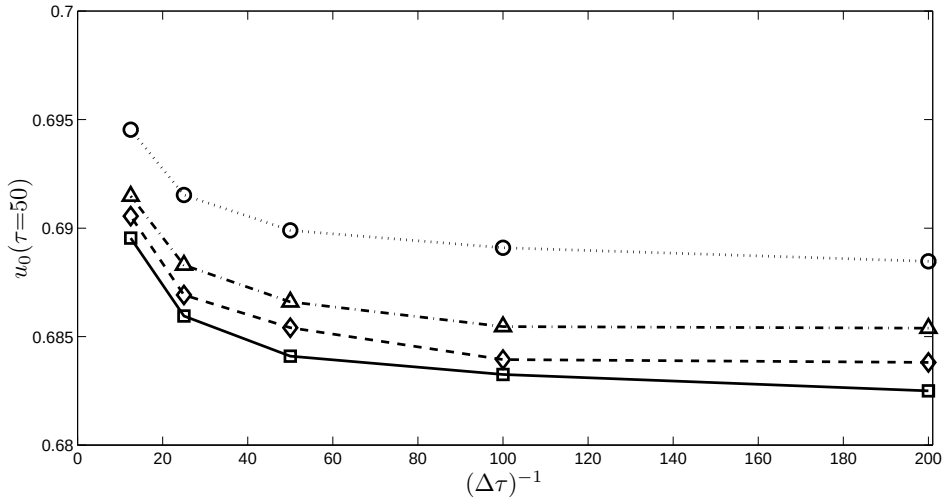

(b) *Euler integration with varying values for desingularising parameter,* δ*:* ○- $\delta = 0.071$*;* △- $\delta = 0.05$*;* ◇- $\delta = 0.03$*;* □ − $\delta = 0.01$.

Figure 5.2: *Convergence of the normal velocity at the surface,* u_s *at* $\tau = 50$ *with reducing time-step,* $\Delta\tau$ *for (a) different integration methods, and (b) desingularisation values,* δ.

Figure 5.6 shows how the system evolves for larger time ($\tau > 10$) for both Euler and RK4 time integration. The small differences arising from use of different time integration methods are allowed to grow so that the vortices now take distinctly different positions in different simulations. However, the general behaviour of the system, i.e. the time-averaged locations of vortices, is the same. As previously discussed, measures of the normal velocity at the surface, u_s, show excellent agreement between simulations.

Figures 5.4 and 5.6 use the same time-step and pressure drop coefficient ($\kappa = 2$, $\Delta\tau = 0.02$) but different desingularisation parameters: $\delta = 0.03$ and $\delta = 0.05$ respectively. There are two clear effects of increasing δ: firstly, the tip roll-up is inhibited: the spiral is less concentrated. This is consistent with the results of Krasny (1991) for the wake behind a flat plate normal to uniform flow. The second effect of the larger desingularisation parameter is that the break down of the vortex sheets is more inhibited. Comparison of Figures 5.4 and 5.6 shows that a larger δ reduces the upstream distance that the instabilities can travel - the smooth part of the vortex sheets are about three times longer in Figure 5.6. The dipole formed from the tip roll-up process is therefore still evident in Figure 5.6, although it has started to mingle with the rest of the wake. Longer time simulations show that the dipole will still eventually break down.

5.3.3.3 Verification summary

The point vortex method has been applied to the actuator surface problem and its performance has been verified as self-consistent, invariant to non-physical parameters within less than 1% (for $\Delta\tau < 0.05$, $\delta < 0.05$), and physically realistic. Euler integration is the least computationally expensive. The conclusion from this section is that the vortex simulation of an actuator surface is performing well, and that it should now be validated through comparison with analytical and experimental results. In future, following the suggestion of van Kuik (2008), the vortex model could be further verified by investigating the conservation mass and momentum in a control volume encompassing the actuator surface.

5.4 Steady flow

In this section the case of a uniformly loaded actuator surface in steady flow is used to compare the vortex model with published data. The comparison is made either with the velocity at the centre of the actuator surface, u_s, or with the thrust coefficient, C_T, which for the vortex model is derived from the velocity at the centre of the surface using equation (2.48): $C_T = \kappa u_s^2$. In order to compare the vortex model with results for steady flow, the results are used for $\tau = 100$, at which point $u_s(\tau)$ is essentially steady: between $\tau = 70$ and $\tau = 100$ the value of u_s is no longer decreasing monotonically, it varies with predominantly low frequencies (none of which are individually dominant) and the maximum difference over that time period is 0.05%.

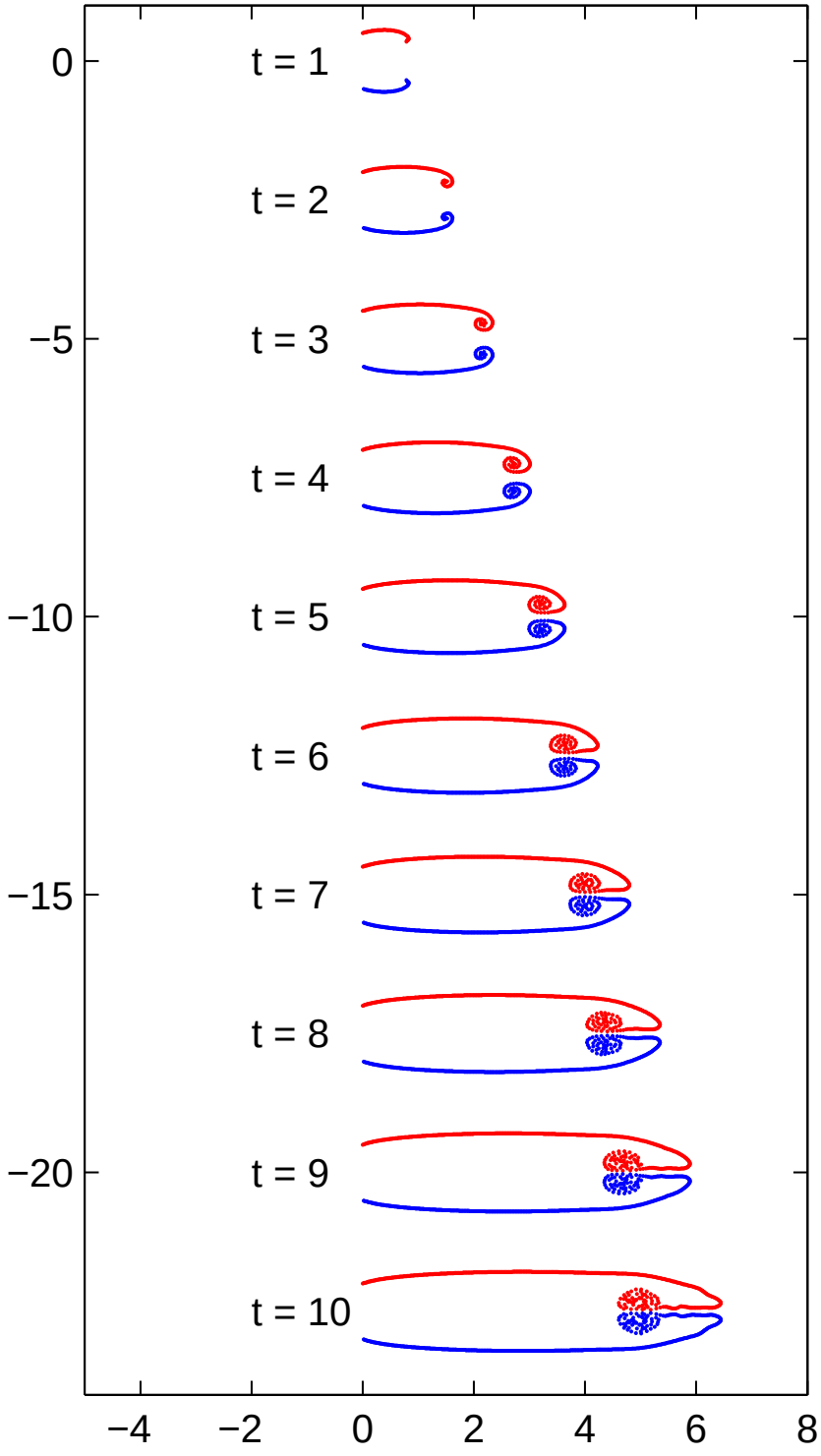

Figure 5.3: *Plots of vortex positions at regular time increments for* $\kappa = 2$, $\Delta\tau = 0.02$, $\delta = 0.05$, *RK4 integration.*

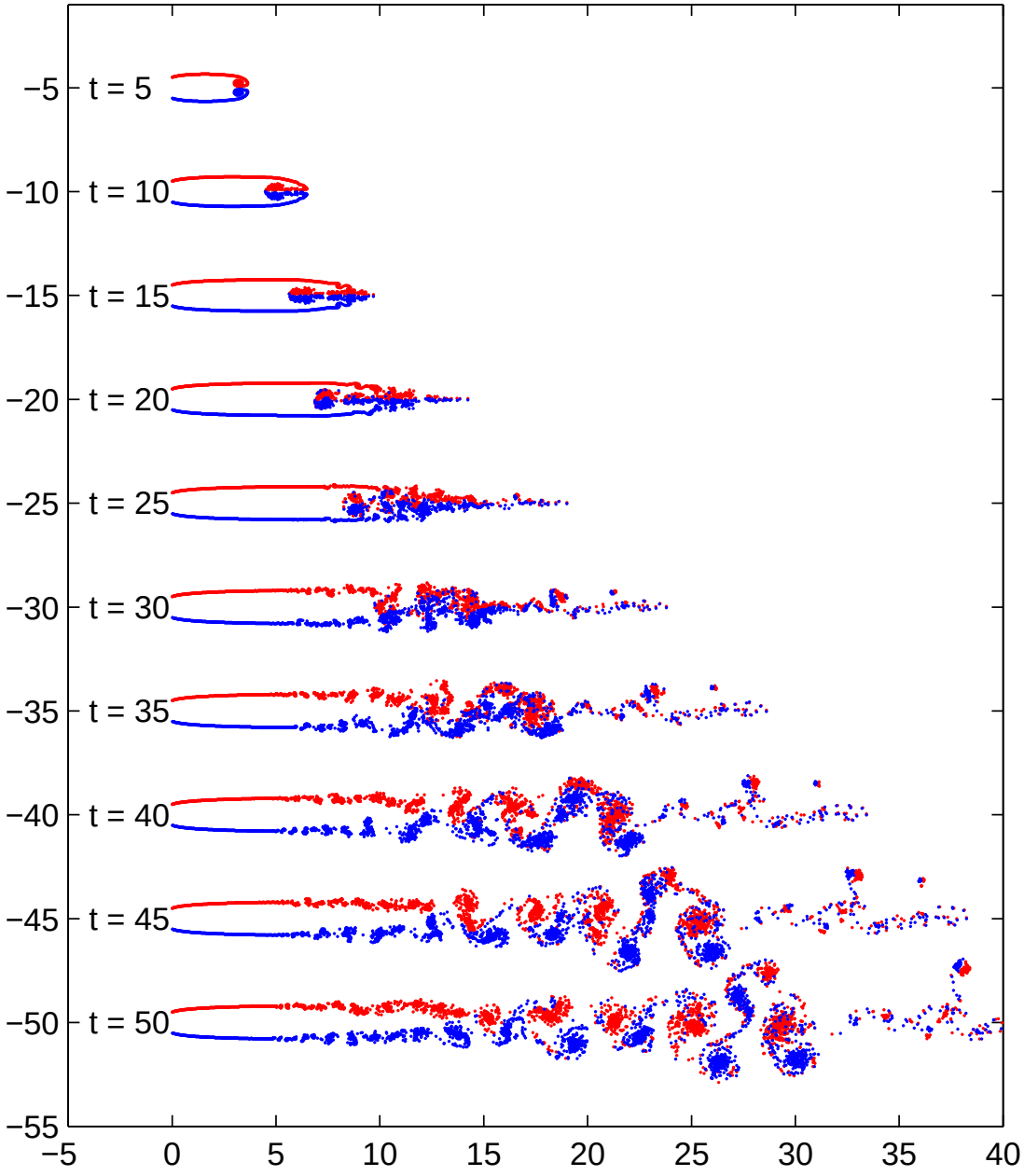

Figure 5.4: *Plots of vortex positions at regular time increments for* $\kappa = 2$, $\Delta\tau = 0.02$, $\delta = 0.03$.

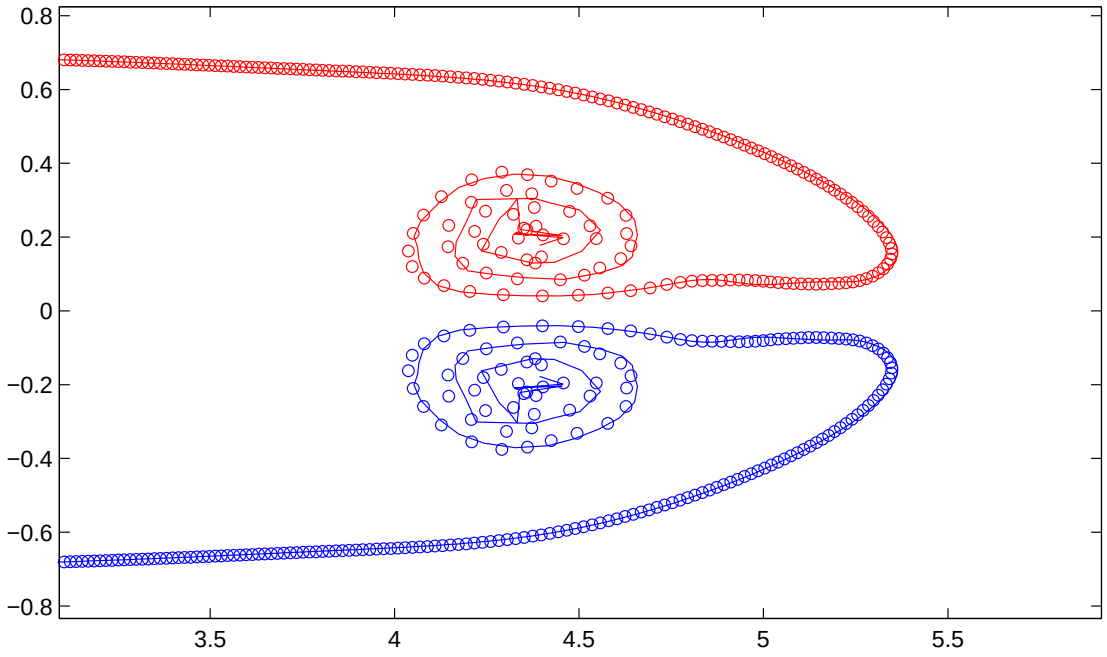

Figure 5.5: *Plots of vortex positions at $\tau = 8$ for $\kappa = 2$, $\Delta\tau = 0.02$, $\delta = 0.05$, comparing integration methods. (o) Euler (-) RK4.*

5.4.1 Vortex model results compared to theory

The solution from linear momentum theory, presented and reviewed in Section 2.6.2:

$$u_s\left(\infty\right) = \frac{1}{1+\kappa/4} \tag{5.20}$$

can be compared with values from the point vortex method after large time. Figure 5.7 compares (5.20) with the results from the point vortex model.

The comparisons in Figure 5.7 show close agreement for low values of κ. As κ increases there is a growing discrepancy between the results of theory and the vortex model: for $\kappa =$ 2, 3, and 3.5 the error is 2.6%, 4.7% and 6.7% respectively.

For high values of κ the linear theory breaks down; when $\kappa > 4$ it predicts net flow backwards through the momentum sink ($u_s < 0$), which is not possible, it also predicts that for $\kappa > 4$ the thrust will decrease (with an increase in κ) from its peak of $C_T = 1$ when in practice we would expect it to rise continually with κ, tending towards the high Reynolds number drag of a flat plate of large aspect ratio: $C_T = 2$. As κ approaches values close to 4 the linear momentum theory becomes less valid and under predicts the velocity at the actuator surface (van Kuik, 1991). For intermediate values, say $1 < \kappa < 3$, the small difference between the vortex model and linear momentum theory may be due to the finite length of the wake in the vortex model.

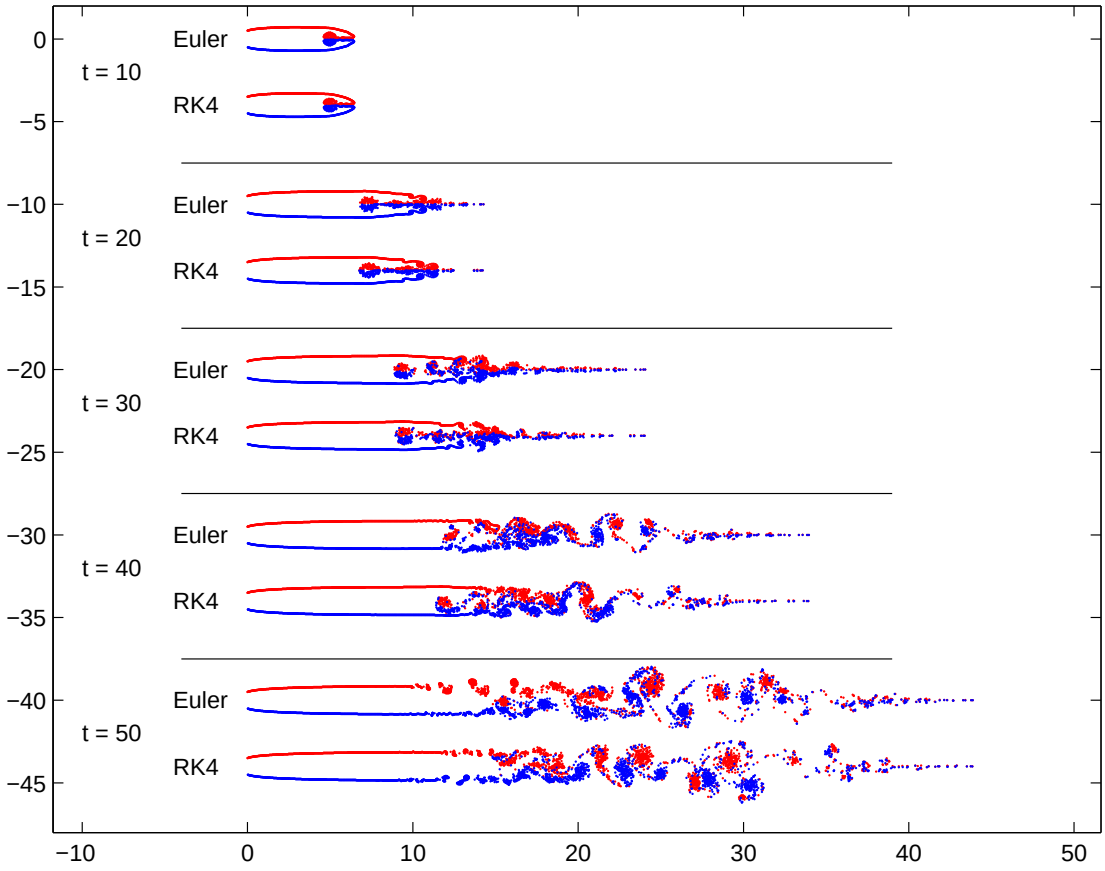

Figure 5.6: *Plots of vortex positions at regular time increments for* $\kappa = 2$, $\Delta\tau = 0.02$, $\delta = 0.05$, *comparing RK4 and Euler integration .*

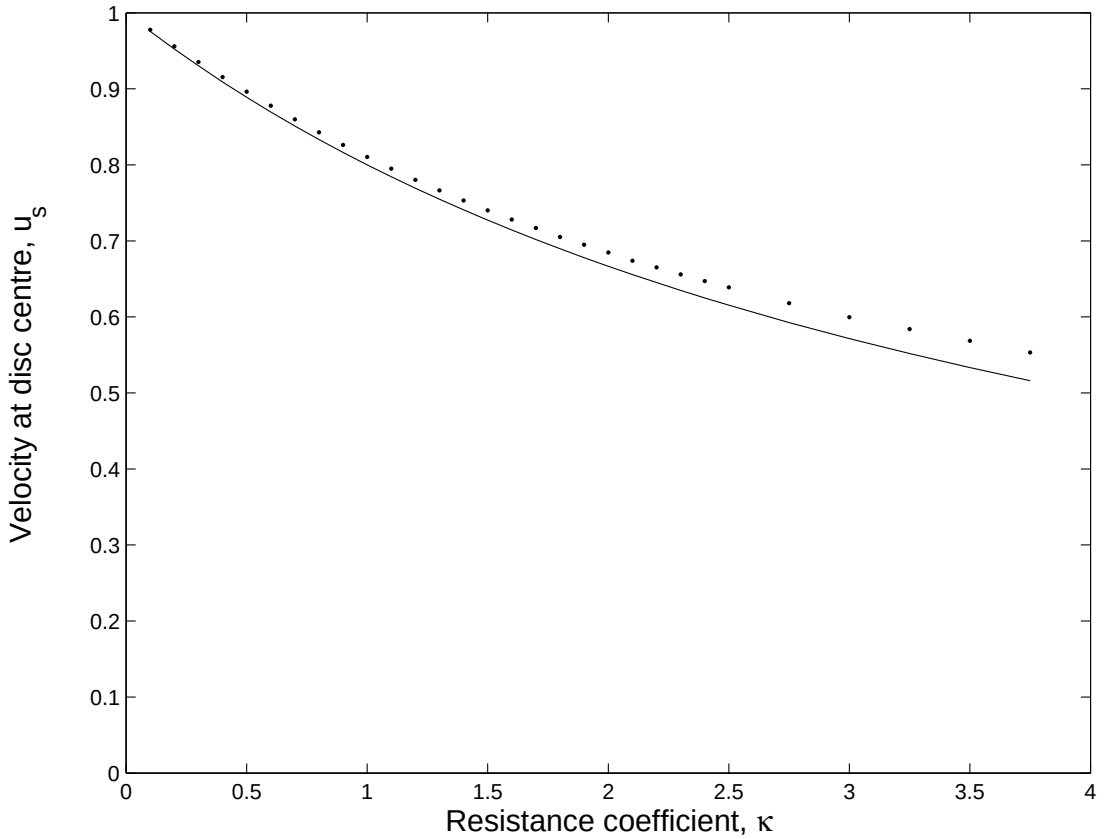

Figure 5.7: *Comparison of the steady state velocity at an actuator surface, u_s, predicted by linear momentum theory and the vortex model. (–) Linear momentum theory (5.20), (•) vortex model at $\tau = 100$.*

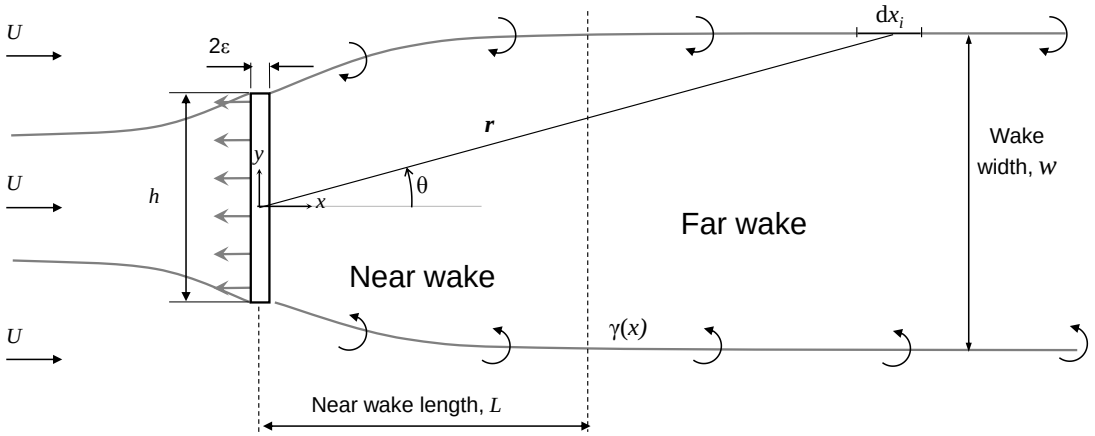

Figure 5.8: *Illustration of near and far field components of the wake.*

5.4.2 Correction for finite wake length

Simulations for steady flow were run until apparently steady results were obtained at $\tau = 100$. However the wake length is still finite and this section focuses on the derivation of an estimated correction for the finite nature of the wake. In order to do so the 'missing wake', from some point downstream to infinity downstream, is analysed and its contribution to the velocity at the surface is approximated.

5.4.2.1 Velocity at the surface due to the far wake (u_{0i})

The wake of the actuator surface in planar flow is defined by the vortex sheets at its edges. The shape and strength of the vortex sheets is sufficient to describe the wake. For the present analysis the wake will be divided into the 'near wake' and the 'far wake', which meet at a distance downstream, L, as illustrated in Figure 5.8.

The present analysis is restricted to the far wake, which is assumed to have a constant width, w. The origin is at the centre of the actuator surface. A small segment of one of the vortex sheets, $\mathrm{d}x_i$, located at a distance x downstream and $w/2$ from the $x-$axis, will induce a velocity at the origin with magnitude:

$$|\boldsymbol{U}_{0i}| = \frac{|\gamma(x)|\,\mathrm{d}x_i}{2\pi\,|\boldsymbol{r}|}, \tag{5.21}$$

where $\boldsymbol{r}$ is the vector position of the segment (when the origin is at the centre of the surface). In the far wake γ is constant and the horizontal component of the velocity induced at the surface is:

$$U_{0i} = \frac{\gamma \mathrm{d}x_i}{2\pi r}\sin\theta. \tag{5.22}$$

where $r = |\boldsymbol{r}| = \sqrt{x^2 + (w/2)^2}$. Using $\sin\theta = w/2r$ and this becomes:

$$U_{0i} = \frac{w\,|\gamma|}{4\pi} \frac{\mathrm{d}x_i}{\left(x^2 + (w/2)^2\right)}. \tag{5.23}$$

The total velocity induced by the far wake at the origin is then:

$$U_{0i} = -\frac{w\,|\gamma|}{2\pi} \int_L^\infty \frac{\mathrm{d}x}{\left(x^2 + (w/2)^2\right)}. \tag{5.24}$$

This accounts for the effect of both vortex sheets, and is equal to the total induced velocity because the lateral component $(\boldsymbol{u} \cdot \hat{\boldsymbol{y}})$ will be zero due to symmetry. Hereafter $\gamma = |\gamma|$ is used. The integral (5.24) gives:

$$U_{0i} = -\frac{\gamma}{\pi} \left(\frac{\pi}{2} - \arctan \frac{2L}{w} \right). \tag{5.25}$$

If γ and w can be determined, then U_{0i} can be determined as a function of L.

5.4.2.2 Determining γ and w

If a uniform transverse velocity profile is assumed within the wake, the circulation per unit width, γ, in the far wake is described by the wake velocity, U_w:

$$\gamma = U_\infty - U_w. \tag{5.26}$$

The wake speed can be estimated to first order from momentum theory:

$$U_w = U_\infty - 2\,(1 - U_s) = 2U_s - U_\infty, \tag{5.27}$$

hence from Taylor's result (2.59):

$$u_w = 2 \left(\frac{1}{1 + \kappa/4} \right) - 1, \tag{5.28}$$

where $u_w = U_w/U_\infty$. Combining (5.26) and (5.28):

$$\frac{\gamma}{U_\infty} = -\frac{2\kappa}{4 + \kappa}. \tag{5.29}$$

The wake width, w, can be determined from conservation of mass:

$$h u_s = w u_w, \tag{5.30}$$

$$w = h u_s / u_w, \tag{5.31}$$

Using (5.27) and (2.59) gives:

$$\frac{w}{h} = \frac{1}{1-\kappa/4} \tag{5.32}$$

5.4.2.3 General correction factor

The effect of the far wake can now be expressed as:

$$u_{0i} = -\frac{2\kappa}{\pi\left(4+\kappa\right)}\left(\frac{\pi}{2} - \arctan\left[\frac{2L}{h}\left(1-\frac{\kappa}{4}\right)\right]\right). \tag{5.33}$$

where $u_{0i} = U_{0i}/U_\infty$. In the limit $L/h \to 0$, (5.33) recovers the result of linear momentum theory (2.59):

$$u_s = \lim_{L/h\to 0}\left(1+u_{0i}\right) = 1 - \frac{\kappa}{4+\kappa} = \frac{1}{1+\kappa/4}. \tag{5.34}$$

5.4.2.4 Estimated correction when wake length is unknown

Equation (5.33) is an expression of the difference:

$$u_{0i}\left(L/h\right) = u_s\left(\infty\right) - u_s\left(\tau\right). \tag{5.35}$$

With an expression for u_{0i} as a function of wake length, L/h, the final stage of the correction is to estimate the value of L/h as a function of time, τ. In other words, how long is the wake after a finite time, τ? For small values of κ, we can approximate:

$$\lim_{\kappa\to 0} L/h \to \tau, \tag{5.36}$$

hence

$$\lim_{\kappa\to 0} u_{0i} \to -\frac{2\kappa}{\pi\left(4+\kappa\right)}\left(\frac{\pi}{2} - \arctan\left(2\tau\right)\right). \tag{5.37}$$

For values of τ larger than about 10, we can estimate

$$\lim_{\kappa\to 0} u_{0i} \to -\frac{2\kappa}{\pi\left(4+\kappa\right)\tau}, \qquad \text{where } \tau \gtrsim 10. \tag{5.38}$$

For finite κ the wake length will be significantly shorter: $L/h < \tau$. In this case L/h can be taken from from the numerical simulations, however it is difficult to judge the 'length' of the wake in the simulations – some vortex particles have been advected far downstream, but generally they are quite unevenly spread and there is no clear 'end' to the wake. Alternatively the wake length can be estimated by assuming that it grows at a rate approximately equal to the final wake speed (5.28). Then we have:

$$L/h \approx u_w\tau = \left[2\left(\frac{1}{1+\kappa/4}\right) - 1\right]\tau. \tag{5.39}$$

Combining (5.39) and (5.33) we have:

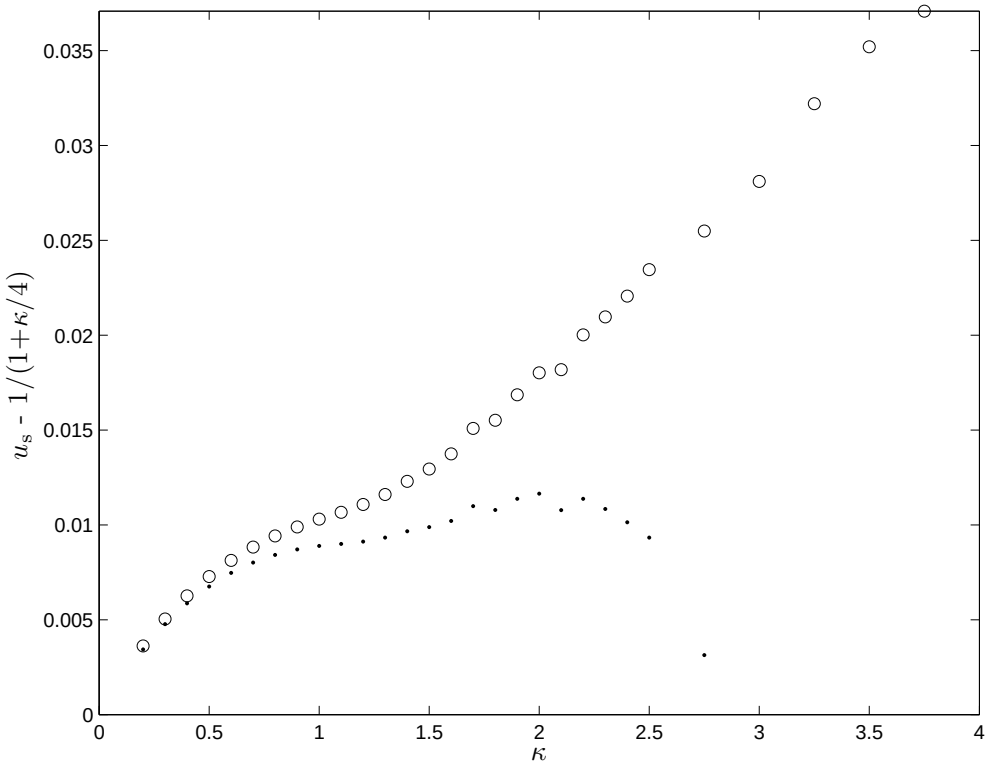

Figure 5.9: *The velocity at an actuator surface predicted by the vortex model, with the value from linear momentum theory subtracted. (○) vortex model, (·) vortex model corrected using (5.40).*

$$u_{0i} = -\frac{2\kappa}{\pi\left(4+\kappa\right)}\left(\frac{\pi}{2} - \arctan\left[\frac{1-\kappa/4}{1+\kappa/4}2\tau\right]\right), \tag{5.40}$$

which is the correction for velocity at the actuator surface after finite time, τ, due to the 'missing wake' in a simulation of finite time. This result is plotted in Figure 5.9 where the velocity at the actuator surface from the vortex model is plotted, with the value from linear momentum theory subtracted. Additionally results are plotted for the vortex model, corrected with $u = u_s + u_{0i}$ using (5.40). As κ increases the correction starts to account for the majority of the difference between the vortex model and momentum theory until $\kappa > 2.3$ where the correction accounts for more than the difference. For higher values of κ the correction becomes unrealistically large, and in the limit $\kappa = 4$ the correction is equal and opposite to the total velocity at the actuator surface ($u_{0i}\left(\kappa = 4\right) = 0.5$). This is because the correction itself breaks down for high values of κ due to its reliance on linear momentum theory to estimate the wake width and wake length. In summary, the correction helps explore the effect of finite wake length, but due to its own reliance on linear momentum theory, it will not be applied to results outside of this section.

5.4.3 Vortex model results compared to published data

Published experimental data, which is reviewed in Section 2.6, can be compared to results

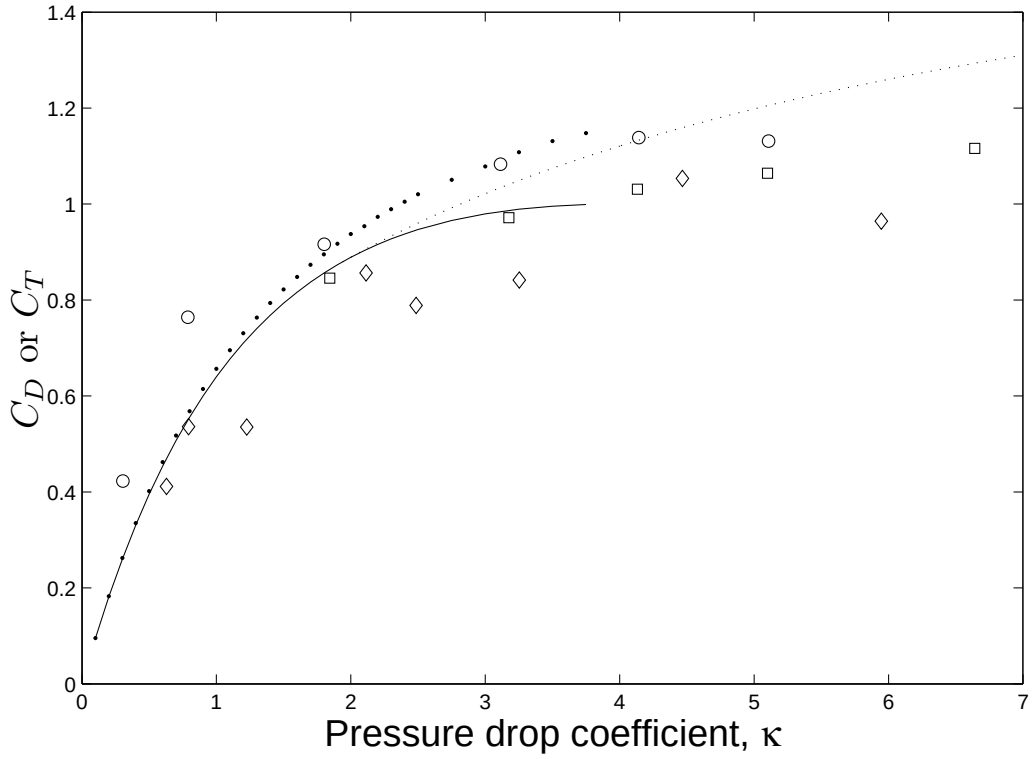

Figure 5.10: *Variation of the steady thrust on an actuator surface or gauze, $C_{\rm D}$ or $C_{\rm T}$ vs pressure drop coefficient, κ: comparison of experimental, theoretical, and numerical results. (–) Linear momentum theory (2.61), (···) Burton semi-empirical (5.41), (•) Vortex method, (○) Castro (1971) (wake traverse), (□) Castro (1971) (drag balance), (◇) Taylor & Davies.*

from the vortex model. Further, some semi-empirical models are available. The most commonly used semi-empirical relationships for wind turbines are those by Burton et al. (2001):

$$C_{\rm T} = 1.816 - 1.39036/(1 + \kappa/4), \tag{5.41}$$

and Wilson and Lissaman (1974):

$$C_{\rm T} = 1.6 - 1.05/(1 + \kappa/4). \tag{5.42}$$

Figure 5.10 compares the thrust of an actuator surface in steady flow: the vortex method is compared with theoretical, semi-empirical, and experimental.

The results shown in Figure 5.10 are quite scattered, this is partly due to the uncertainty in thrust measurement, and also due to uncertainty in estimations for κ. However some observations can still be made:

- The thrust is proportional to u_s^2, so any differences in velocity measurement/prediction will lead to larger differences in values of thrust
- The semi-empirical relationship shows similar behaviour to the vortex results but with approximately 5% lower thrust
- The results of Taylor & Davies (1944) are highly scattered so difficult to interpret. They generally give a lower thrust than the other results.
- The measurements of Castro (1971) show significant variation between the different methods of measurement. Their difference and also their uncertainties make it difficult to draw a useful conclusion.
- The point vortex method is clearly picking up the key physical effects.
- The vortex method is predicting thrust values at the higher end of the envelope given by published results.

van Kuik (1991) examined the discrepancy between theory and experiment for actuator surfaces and suggested that linear momentum theory tends to under predict the velocity at the surface by a few percent. This is consistent with the results of the vortex method.

van Kuik (1991) compiled results from the rotor experiments of other researchers, and also performed his own experiments. All three sets of results may be useful for comparison with the vortex results however they too are scattered and do not help validate the vortex model. Koo and James (1973) and Lee and Greenberg (1984) performed experiments with uniformly loaded energy sources, i.e. $\kappa < 0$. Comparison of the vortex method with these cases may be insightful and this is something that could be pursued in the future.

In summary, a comparison of the thrust of an actuator surface in steady flow has been made, comparing the vortex model with published data (theoretical, semi-empirical, and experimental measurements). The published data shows considerable scatter; the comparison shows that the vortex is predicting behaviour that is consistent with all available data and within the range of thrust values given by published data. However, the vortex model predicts thrust values that are at the top end of this envelope. It appears that the vortex model is providing a reasonable estimation but that it may be over-predicting thrust values. Given the lack of clarity, and the lack of attention to unsteady flow, further investigations were carried out and are described in the following section.

5.5 Impulsively started flow

To further investigate the vortex model of an actuator surface, this section focuses on the transient response of a uniformly loaded actuator surface in impulsively started flow. Theoretical

solutions to the case of a lightly loaded actuator surface are presented and then compared to results from the vortex model. Following this a new experiment is described where meshes were towed through static water and drag measurements were recorded. The results of the vortex model are then compared to the experimental measurements.

5.5.1 Asymptotic solutions for a weakly loaded actuator surface

This section provides asymptotic solutions for an impulsively started weakly loaded actuator surface in planar flow, in order to provide a test case for the point vortex method. The velocity at the centre of the surface is denoted U_0:

$$U_0 = (\boldsymbol{U} \cdot \boldsymbol{x})|_{\boldsymbol{x}=0}\,, \tag{5.43}$$

where $\boldsymbol{x} = (x, y, z)$ and in this section the normal velocity at the surface is measured at the centre of the surface:

$$U_\mathrm{s} = U_0. \tag{5.44}$$

This is used because the velocity becomes infinite at the vortex sheet so an average velocity is not practical.

In the limit $\kappa \to 0$, the vortex sheets generated are weak and we can analyse how an impulsively started actuator surface reaches a steady state. For a uniform incident flow, $\boldsymbol{u}_\mathrm{E} = U\hat{\boldsymbol{x}}$ and assuming uniform conditions all over the surface, the vortex sheet strength at the actuator surface can be found from (2.47) and (2.44):

$$\gamma = \frac{1}{2}\kappa U_\mathrm{s}\,(t)\,, \tag{5.45}$$

where γ is the circulation per unit length along the vortex sheet and U_s is the normal velocity at the surface (which is here assumed to be uniform over the surface and this is appropriate when the loading, κ, is weak or the time is small). For the weak actuator surface we neglect the small self-induced velocity of the vortex sheets and assume that, as they grow, they are advected only by the external flow. Then the velocity induced at the centre of the surface, $U_0\,(t)$, is:

$$U_0\,(t) = U - \frac{1}{2\pi}\int_0^L \frac{\gamma h}{L^2 + h^2/4}\mathrm{d}x. \tag{5.46}$$

where h is the height of the actuator surface and L is the length of the vortex surfaces which, if their self-induced velocity is neglected, is $L = Ut$. The assumption that the velocity is uniform all over the surface means that we use $U_s = U_0$.

5.5.1.1 First order unsteady solution

This sub-sub-section is based on Eames (2008). For short time ($2Ut/h \ll 1$), $\gamma \to \frac{1}{2}\kappa U$ giving a constant vortex sheet strength and a simplified normal velocity:

$$U_0(t) = U - \frac{\kappa U^2}{4\pi} h \int_0^t \frac{\mathrm{d}t}{(Ut)^2 + h^2/4} \tag{5.47}$$

Integrating yields an expression for the normal velocity at the surface for all time:

$$U_0(t) = U - \frac{\kappa U^2}{2\pi} \arctan\left(\frac{2Ut}{h}\right), \tag{5.48}$$

and a steady solution:

$$\lim_{t\to\infty} U_0 = U(1 - \frac{1}{4}\kappa U) \tag{5.49}$$

The comparison between prediction and calculation is between $k^{-1}\frac{\mathrm{dU_0}}{\mathrm{d}t}$ which is found by differentiating (5.47):

$$\kappa^{-1}\frac{\mathrm{d}U_0(t)}{\mathrm{d}t} = -\frac{hU^2}{4\pi\left[(Ut)^2 + h^2/4\right]}, \tag{5.50}$$

for small time:

$$\lim_{t\to 0} \kappa^{-1}\frac{\mathrm{d}U_0(t)}{\mathrm{d}t} \to -\frac{U^2}{\pi h}, \tag{5.51}$$

or

$$\lim_{t\to 0} \frac{\pi h}{U^2}\left(\frac{\mathrm{d}U_0(t)}{\mathrm{d}t}\right) \to -\kappa. \tag{5.52}$$

5.5.1.2 Second order unsteady solution

This sub-sub-section is based on Eames (2008). A second order prediction of $\kappa^{-1}\mathrm{d}U_\mathrm{s}/\mathrm{d}t$ accounts for the variation of γ along the vortex sheet: $\gamma(t) = \frac{1}{2}\kappa U_0(t)$. Combining this with (5.46):

$$\frac{2}{\kappa}\frac{\mathrm{d}\gamma}{\mathrm{d}t} = U - \frac{\kappa}{2\pi}\arctan\left(\frac{2Ut}{h}\right), \tag{5.53}$$

or

$$\gamma = \gamma_0 \exp\left(-\frac{\kappa}{2\pi}\arctan\left(\frac{2Ut}{h}\right)\right). \tag{5.54}$$

where $\gamma_0 = \frac{1}{2}\kappa U$. Using (5.54) in (5.46) gives

$$\kappa^{-1}\frac{\mathrm{d}U_s}{\mathrm{d}t} = -\frac{U^2 h \exp\left(-\frac{\kappa}{2\pi}\arctan\left(\frac{2Ut}{h}\right)\right)}{2\pi\left((Ut)^2 + h^2/4\right)} \tag{5.55}$$

where $\gamma_0 = \frac{1}{2}\kappa U$ is a constant. For small time:

$$\lim_{t\to 0} \kappa^{-1}\frac{\mathrm{d}U_\mathrm{s}}{\mathrm{d}t} \to -\frac{U^2}{\pi h} \tag{5.56}$$

Hole diameter	Hole separation	Estimated κ	Open area / total area Θ
4 mm	5 mm	1.97	58 %
5 mm	6 mm	1.52	63%
12 mm	13 mm	1.0	73%

Table 5.1: *Data for the three meshes used, where the approximation* $\kappa = \frac{1}{\Theta^2} - 1$ *(Taylor and Davies, 1944) has been used.*

which matches the first order solution (5.52).

This model could be used to investigate double actuator surfaces, however it is only valid in the limit $\kappa \to 0$. Alternatively, the vortex sheets could be discretised and their evolution could be calculated. This method, known as the point vortex method, could represent higher values of κ.

5.5.2 Results and comparison with asymptotic theory

The results of the vortex model are compared here to the solutions derived in Section 5.5.1. Comparison is made through $\kappa^{-1}\frac{\mathrm{d}u_s}{\mathrm{d}t}$ and this is illustrated in Figure 5.11 for $\kappa = 0.01$, 0.1, and 1. Agreement is excellent in the first case, very good in the second case, and the third case shows significant discrepancies. The asymptotic solution is only valid for $\kappa \ll 1$ so agreement is not expected in the latter case. These results validate the unsteady point vortex method, over all time, for small values of κ.

5.5.3 Towing experiment

In this section a series of new experiments is presented that provide a more detailed comparison of the vortex model with physical measurements. Strips of steel mesh were towed through water and drag was measured. This allows a more comprehensive validation of the vortex model in both unsteady and steady flow. Results showed good agreement - mostly within the repeatability of the experimental measurements.

5.5.3.1 Mesh characteristics

It was not practical to create a totally permeable drag such as that investigated by the vortex model. Following the work by Taylor and Davies (1944) and Whelan et al. (2009), steel meshes with circular holes in a hexagonal formation were used. These meshes are exactly the same as used by Whelan et al. (2009) (supplied by F. H. Brundle) and so the approximate values of κ obtained by those investigators were assumed to be reliable and are listed in Table 5.1.

The meshes are mild steel and are 1 mm thick and 1.14 m long. Mesh heights of 5 cm and 20 cm were used, giving a width to height ratio of 22.8 and 5.7 respectively. A larger ratio is desirable in order that the flow is more approximately planar, however the results of Whelan et al. (2009) showed no difference between measurements with circular meshes and measurements with rectangular meshes.

There are some advantages, in the present experiment, to using a larger mesh (with a lower width-height ratio) and these will be discussed. The towing tank has a width of 2.5 m and a

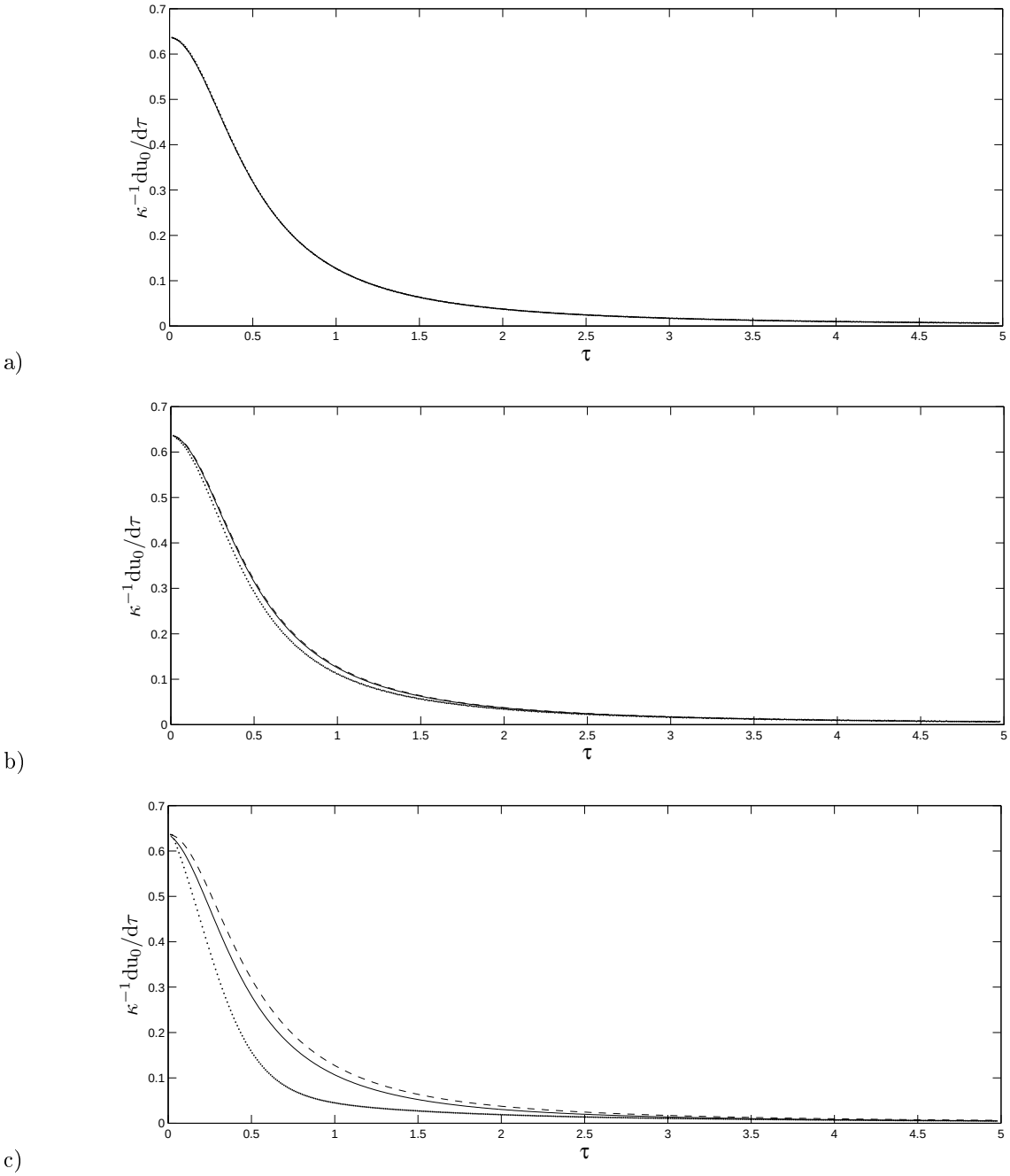

Figure 5.11: *Comparison between the asymptotic unsteady solutions of Section 5.5.1 and the point vortex method. a)*$\kappa = 0.01$*, b)* $\kappa = 0.1$*, c)* $\kappa = 1$*. (–) first order (5.50), (- -) second order (5.55), (·) point vortex.*

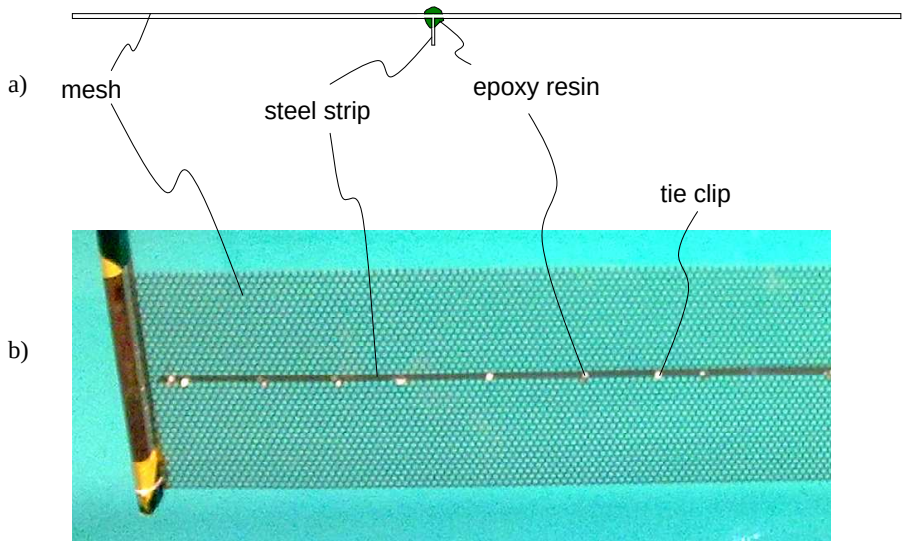

Figure 5.12: *a) Sketch of a cross section of the reinforced mesh b) photograph of the reinforced 20 cm mesh in the water, taken upstream of the mesh from a view point above the centre, so that the steel strip can be seen running along the rear (downstream) face of the mesh.*

water depth of 1 m.

5.5.3.2 Drag measurement system

The meshes are thin and as a result they bend easily under the force of the water. Experiments with the 5 cm high mesh showed deflection of about 5 cm at 0.4 m/s, and up to 10 cm at 0.7 m/s. This deflection, while just about tolerable over a width of 1.14 m, is undesirable. The 20 cm mesh was reinforced with a thin strip of steel, giving a 'T' section to the mesh as sketched in Figure 5.12. The strip adds stiffness to the mesh and following this no significant bending was experienced. The strip is attached along a part of the mesh that has no open area, so that it does not affect the open area. The strip was attached using epoxy resin and some cable-ties. These attachments interfere very slightly with the open area: it is estimated that approximately an additional 0.5% of the frontal area is covered by epoxy (this would be approximately 2% on the 5 cm mesh). The steel used to make the 'T' section protrudes back 10 mm in the streamwise direction and is positioned at the centre of the mesh, perpendicular to the mesh. This should have a negligible effect on the fluid flow.

The mechanical system of holding the mesh in place and measuring the drag is illustrated in Figure 5.13. The mesh was held at each end by hollow aluminium struts of square 12.71 mm

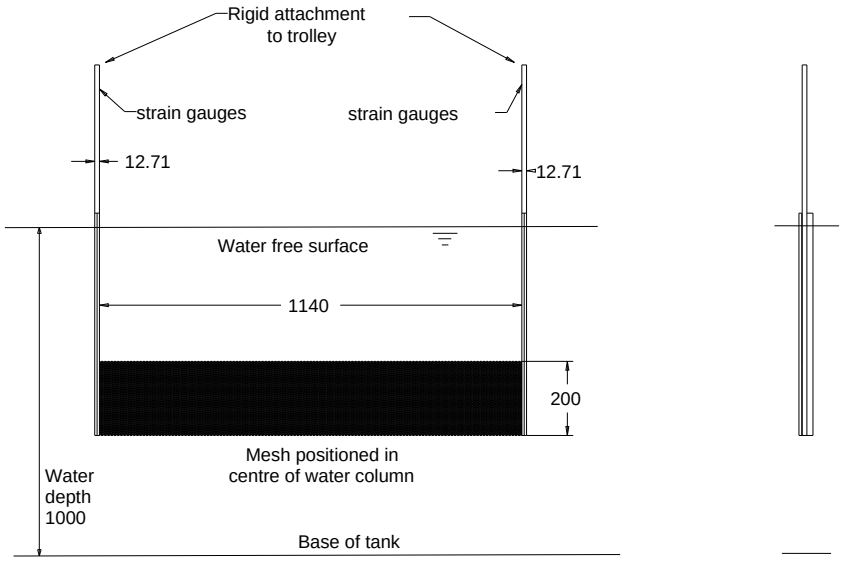

a)

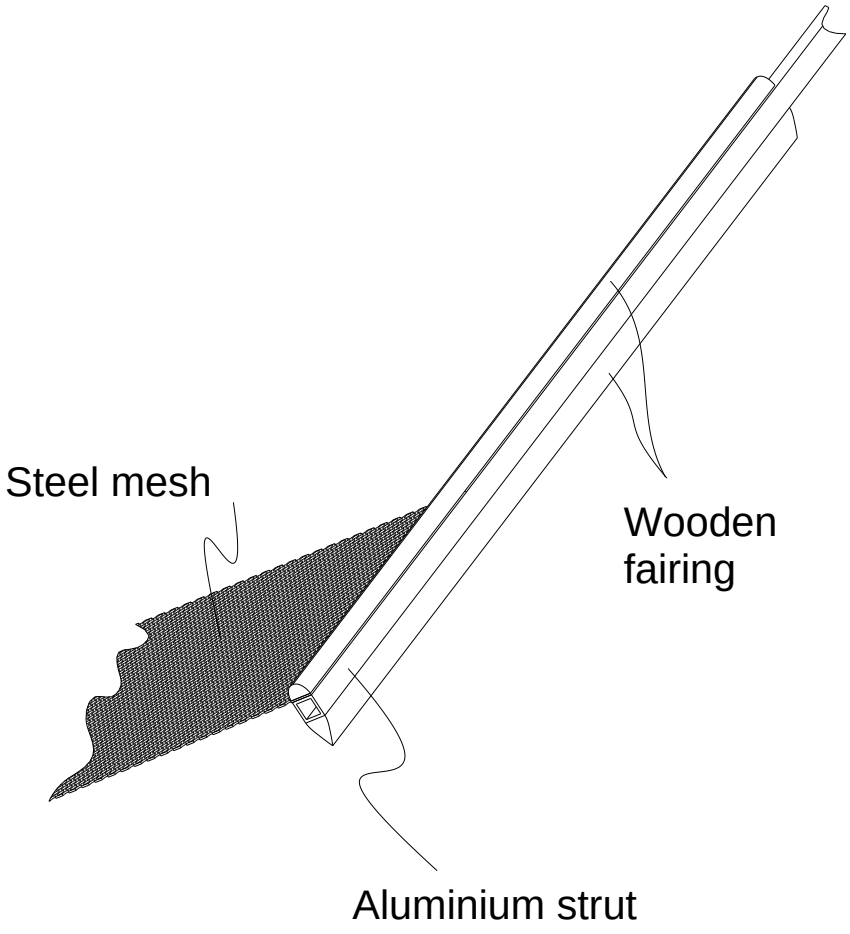

b)

Figure 5.13: *Sketch of the drag measurement system with a 20 cm mesh. a) front and side projection (dimensions in mm), b) close up of the a strut and part of a mesh.*

(1/2") cross-section with 1.59 mm (1/16") wall thickness. The part of the mesh that is covered by the struts is not included in the nominal 1.14m mesh width. The struts were streamlined using wooden fairings shaped like a symmetric aerofoil and with 12.71 mm width. The mesh was screwed to the struts, and the wooden fairings were taped to the struts. The struts were cantilevered: they were rigidly attached above the free water surface, and their free end protruded down into the water.

A system of strain gauges was fitted to the up- and down-stream sides of the aluminium strut, near the attachment point. Dual gauges were attached to each side, and connected in a full Wheatstone bridge configuration. The strain gauges were attached to the surface using superglue (cyanoacrylate) and their wires were soldered to pads which allowed electrical connection to lead wires without transmitting any tension. *Omega* strain gauges with resistance of 1000 Ω were used; the larger resistance value minimised the effect of lead wire resistance. A full Wheatstone bridge was used on both struts and screened cable was used between the gauges and the processing electronics, to reduce noise.

To excite the bridge and read its output a *Microlog V3* from *Transmission Dynamics (JRD Ltd)* was used. This provided a bridge excitation of 3.27 V and read the bridge output via analogue filters and a 16 bit analogue to digital converter. The reason for using the *Microlog* is that the experiments presented in this chapter were carried out before those described in Chapter 4, so the *Microlog* was readily available. The *Microlog* was discussed in more detail in Chapter 4

5.5.3.3 Calibration of the cantilevers

To calibrate the drag measuring system, known loads were applied to the cantilevers and the bridge output voltage was measured. To represent the effect of a loaded mesh, point loads were applied to the cantilevers at the mesh centre. This produces the same strain at the root of the cantilever that a symmetrically distributed load on a mesh would cause. Weights were used to apply a load to the cantilever. Attempts were made to apply a horizontal load to the cantilever while it was held vertically, by using a pulley to redirect the load from the weights. However, the 'stiction' force on the pulley made the applied load unreliable and this system was discarded in favour of hanging weights on the cantilever while it was orientated horizontally. This resulted in an offset in the voltage measurement, due to the self weight of the cantilever. Figure 5.14 shows the results of the calibration. The loading and unloading produced the same results within less than 0.5%.

5.5.3.4 Natural frequency of the cantilever system

The cantilevered struts were chosen so that under typical loads the strain could be reliably measured. A result of this is a system with significant flexibility. The natural frequency of the strut system (combined struts and fairings) was found by displacing the end of the beam and allowing it to oscillate freely. The bridge output voltage was sampled at 400 Hz and this was repeated in air and in still water. The results for water are plotted in Figure 5.15a showing a very clean signal. The small pulses, evident towards the end of the sample, are

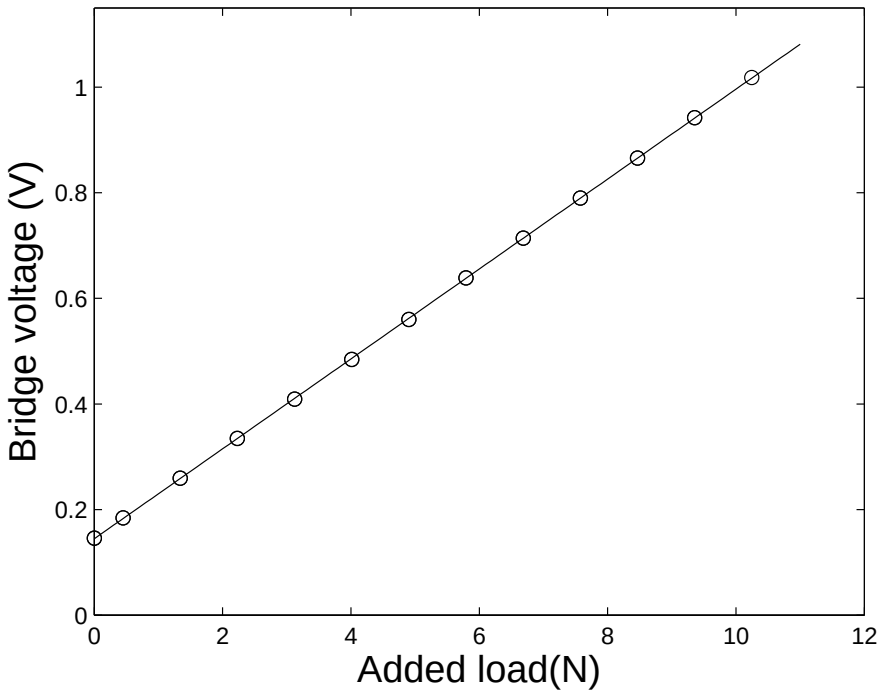

Figure 5.14: *Calibration of the cantilever system (loaded and unloaded): ∘ measured, – fitted. The offset (0.159V) is due to the self-weight of the cantilever. The gradient of the fitted line is 0.0852 V/N. Both cantilevers produced the same results.*

due to use of the *Microlog* in streaming Bluetooth mode. Streaming the signal via Bluetooth is convenient but involves drawing current in high intensity pulses, which affect the bridge excitation voltage and there fore the signal. Streaming was therefore not used for any further experimental measurements. Figure 5.15b shows a Fourier transform of these results, and also of those in air. The natural frequency of the system in air is estimated at 12.5 Hz, and in water the system is damped and the natural frequency drops to approximately 9.8 Hz.

5.5.3.5 Drag of the support struts

To determine the drag of the struts, the cantilever system without an attached mesh was dragged through still water. The average drag force over a period between 10 and 30 seconds was measured. The bridge output was converted to an equivalent force at the mesh centre-point, so that the effect of the struts on mesh drag measurements could be quantified. This amounted to a drag coefficient equivalent of 0.062 on a 5 cm high mesh, or 0.0156 on a 20 cm mesh; these values can then be subtracted from drag measurements with a mesh attached.

Strut drag measurements were made at speeds of 0.4, 0.5, 0.6, and 0.7 m/s, with each measurement repeated. The drag coefficient stayed constant across the range of speeds, which is to be expected as the flow is inertially dominated. The standard deviation of all the measurements was 3.1%. The cause of the variation is suspected to be the vibrations of the towing trolley and the variations are acceptable because the drag coefficient of the meshes is two orders of magnitude larger than that of the struts. A 3% error in strut drag measurements will result in a 0.05% error in mesh drag for a 20 cm mesh or 0.2 % error for a 5 cm mesh.

5.5.3.6 Towing speed measurement

The towing trolley is pulled by a steel cable on a pulley system which is driven by a servo motor. The speed and acceleration of the trolley are determined by a digital control system. The accuracy of this system was tested by using a laser on-board the trolley to detect static objects as it passed them. A set of 4 wooden struts with rectangular cross sections was placed next to the trolley's path and when the trolley passed each wooden strut a distinct step was recorded. A set of four struts produced eight 'edges', which gives a combination of 28 distance measurements during one trolley pass. The four shortest measurements were discarded, as these carried the highest uncertainty. By using two lasers, and making four passes, a total of 192 distance measurements could be made, and this was repeated for a range of trolley speeds between 0.1 m/s and 2.5 m/s. The width of the struts was measured with calipers, the limiting factor being the uniformity of the strut width (37.7 mm $\pm$0.1 mm). The gap between the struts was determined using hardened steel measuring blocks (250 mm $\pm$0.05 mm). The laser measurements were sampled at up to 10 kHz. For lower towing speeds slightly lower frequencies were used (minimum 1 kHz). The result was 192 measurements of trolley speed at each towing speed, from which a mean and standard deviation could be obtained. The standard deviation increases with trolley speed due to the limited sampling speed of the laser. For the speeds used in this thesis, the standard deviation is less than 0.1%. The result was that the trolley speed was consistently higher than the input speed by 1.96% $\pm$ 0.1%; the trolley speeds were corrected

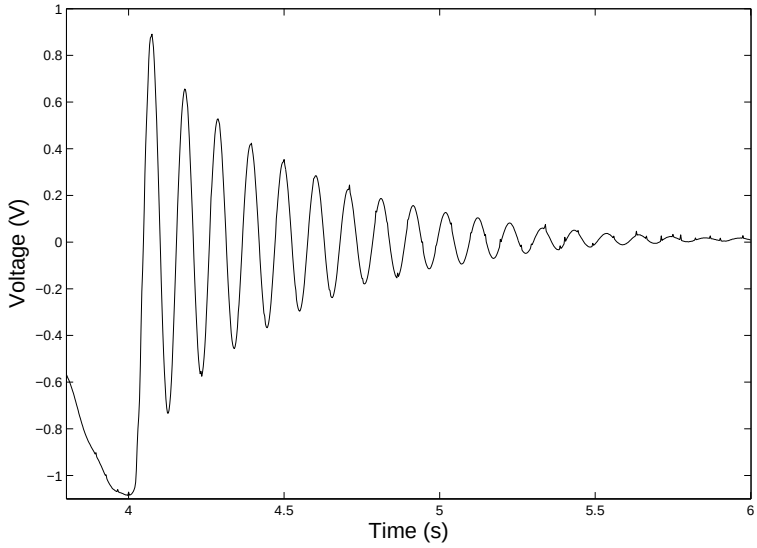

a)

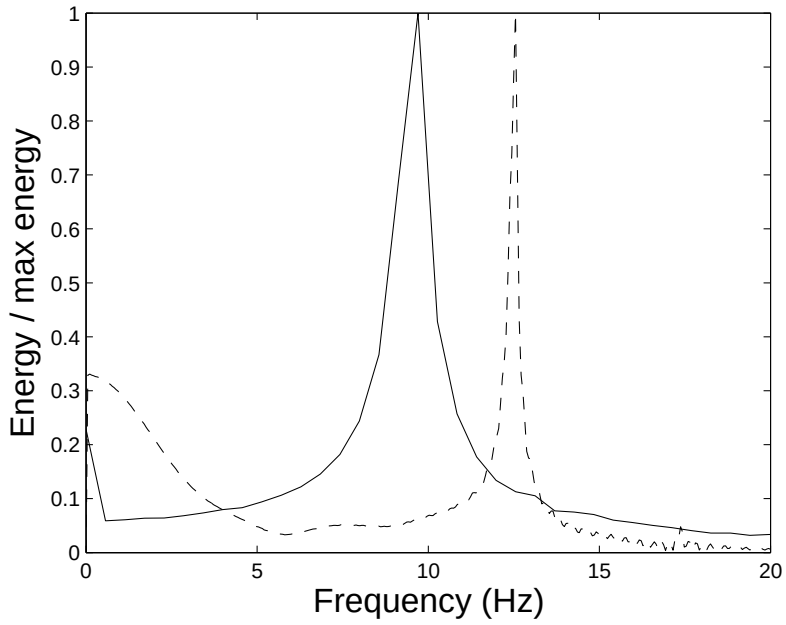

b)

Figure 5.15: *Natural frequency of the cantilever system: a) free oscillations in water after a forced displacement, sampled at 400 Hz b) Fourier transforms of the oscillations in water (–) and air (- -).*

Tow speed, U (m/s)	Time to reach full speed, t (s)	τ_{5cm}	τ_{20cm}
0.3	0.1	0.6	0.15
0.4	0.133	1.1	0.27
0.5	0.167	1.7	0.4
0.6	0.2	2.4	0.6
0.7	0.233	3.3	0.82

Table 5.2: *Time taken for the towing trolley to reach full speed for 5 cm and 20 cm meshes, where* $\tau = tU/h$.

C_D	τ
2	0
1.5	0.24
1.2	0.93
1	5.7

Table 5.3: *Decay of the drag coefficient for* $\kappa = 2$*, predicted by the vortex model.*

accordingly.

5.5.4 Results and comparison with towing experiment

This section presents results for rapid acceleration (3 m/s^2) up to a speed which was thereafter held constant. The meshes were towed at between 0.3 m/s and 0.7 m/s. The time taken to reach full speed is given in Table 5.2 where $\tau = tU/h$.

The significance of the time taken to accelerate to full speed becomes evident when compared to predictions from the vortex model. Taking the case of $\kappa \sim 2$, which represents an optimum tidal turbine, the vortex model predicts that the drag coefficient decays from its peak of 2 at a rate given in Table 5.3. This suggests that for an experiment to capture the decaying drag coefficient, it must be moving at full speed when $\tau < 1$, and preferably when $\tau < 0.1$. Experiments were initially conducted with the 5 cm mesh however, as Table 5.2 shows, such a small mesh is inadequate to capture most of the decay in drag; further, these experiments suffered from significant oscillations in the region of the the natural frequency of the system.

Experiments with the 20 cm mesh yielded more useful results for two main reasons:

1. The time, τ, to accelerate to full speed is less: more of the decay can be captured (see Tables 5.2 & 5.3).

2. The natural frequency is higher (shorter period in terms of τ) so could be filtered out without ruining the measurements.

Results of the experiments with the 20 cm mesh are plotted in Figures 5.16 and 5.17. Figure 5.16a shows an example result with the unfiltered sample at 400 Hz in grey. The electrical noise in the system was very low, so all of the fluctuations are assumed to be physical vibrations.

Most of the energy of the vibrations is at the lower frequencies, with a noticeable peak at the natural frequency around 9.8 Hz. The sample was then filtered using a third-order Butterworth low-pass filter at 8 Hz, to remove small vibrations and the natural oscillations of the system. Figure 5.16a shows this with a solid black line. Figure 5.16b shows three filtered data sets, all repeating the same experimental setup. These results show very good repeatability for the first part of the data during the decaying drag force. Beyond that time the signals vary and this is presumably because of differences in trolley motions.

Figure 5.17 compares the results from four different towing speeds with predictions of the vortex model. The drag coefficient is plotted in Figure 5.17a, showing very good agreement between experimental results and the vortex model. The magnitude is in close agreement. The vortex model predicts a slightly slower decay than shown by the experimental results. By subtracting the theoretical drag coefficient (2.61) from the measured drag coefficient, as shown in Figure 5.17b, a clearer comparison can be made. Both the experiments and the vortex model show higher values of drag coefficient than the theoretical prediction (2.61), and this is consistent with van Kuik (1991). There is considerable variability between different towing speeds and it appears that the drag coefficient is consistently higher for higher towing speeds. This is unexpected at such high Reynolds numbers. However, each measurement is the combination of three, and all three components vary quite considerably as shown in Figure 5.16b, so the one farthest from the average dominates the average. More repeats should be run to investigate this further. In conclusion, the impulsively started experiments showed good agreement with the vortex model.

5.6 Application to double actuator surfaces

The studies presented in this chapter show convergence and agreement with experiments with a low enough uncertainty – broadly speaking within a few percent in terms of drag – that its use to model double actuator surfaces can be expected to yield some insight. This section presents the results of an initial study of double actuator surfaces using the vortex model. The model is used in the same way as presented earlier in this chapter in order to achieve quasi-steady results. Figure 5.18 shows the thrust coefficients C_{T_1} and C_{T_2} against a varying surface spacing, s, for $\kappa_1 = 0.25$ and $\kappa_2 = 1$; the larger values represent C_{T_2}. For the limiting case $s \to 0$ a solid line represents (2.69) and (2.70). For the 'medium' spacing the dashed lines represent (2.73) and (2.74). The results from the vortex method for the upstream actuator surface in the two special cases of $s \to 0$ and $s \approx 10$ show close agreement. For the downstream surface results for the special cases ($s \to 0$ and $s \approx 10$) show good agreement but with a slightly higher prediction from the vortex model.

In Figure 5.18 the small-medium range $0 < s < 10$, which is the region of interest, indicates how the thrust on each actuator surface changes with different spacing. For small, increasing

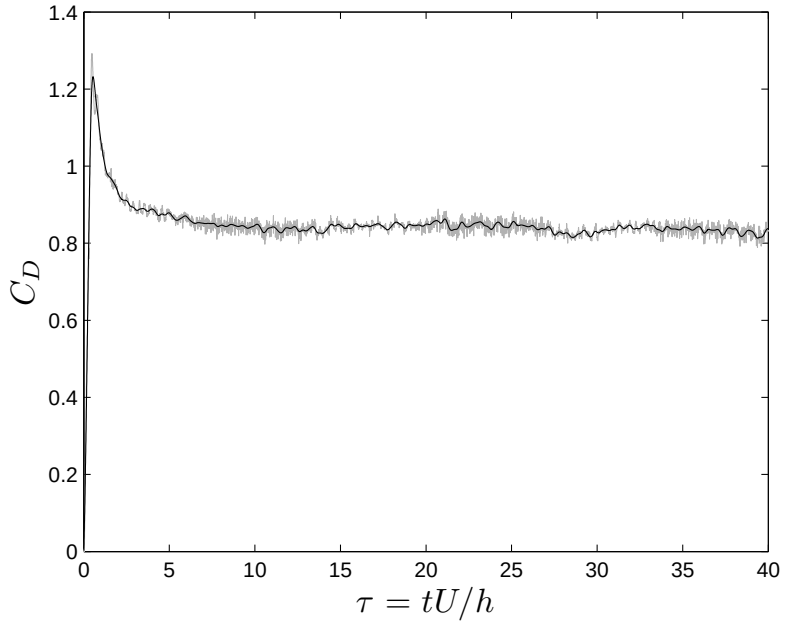

(a) *An example of measured drag coefficient, C_D, vs non-dimensional time, $\tau = tU/h$ for $U = 0.3$ m/s, $h = 0.2$ m. The grey line is the unfiltered signal sampled at 400 Hz, the black line is filtered at 8 Hz using a third order Butterworth low-pass filter. This removes the natural oscillations of the cantilever, but does not remove trolley vibrations.*

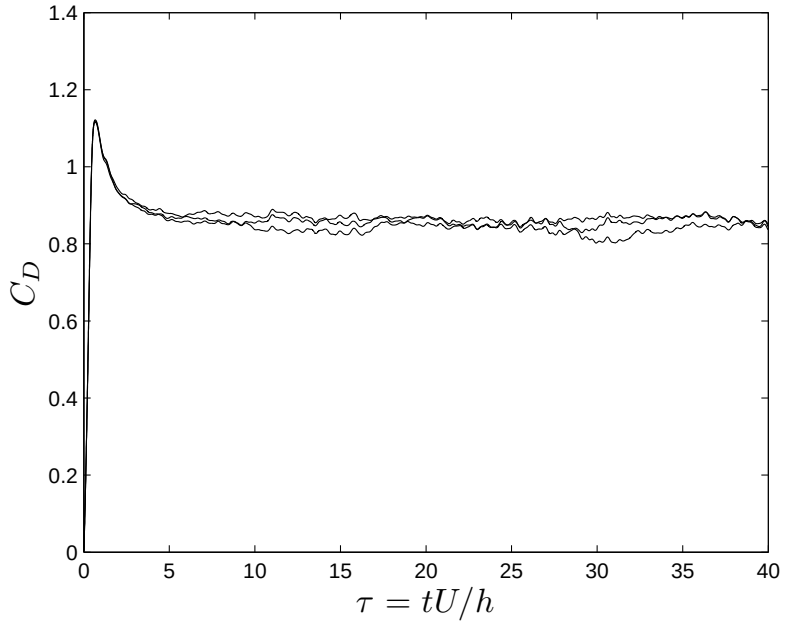

(b) *Three repeated runs at $U = 0.35$ m/s, after filtering. This is representative of all the data that was taken.*

Figure 5.16: *Measurements of the drag on a mesh towed at constant speed.*

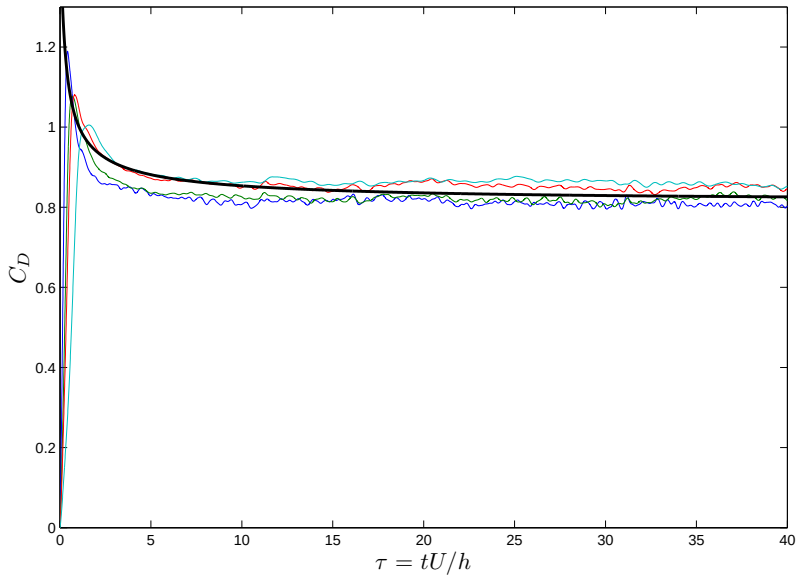

(a) *Comparison of drag coefficient.*

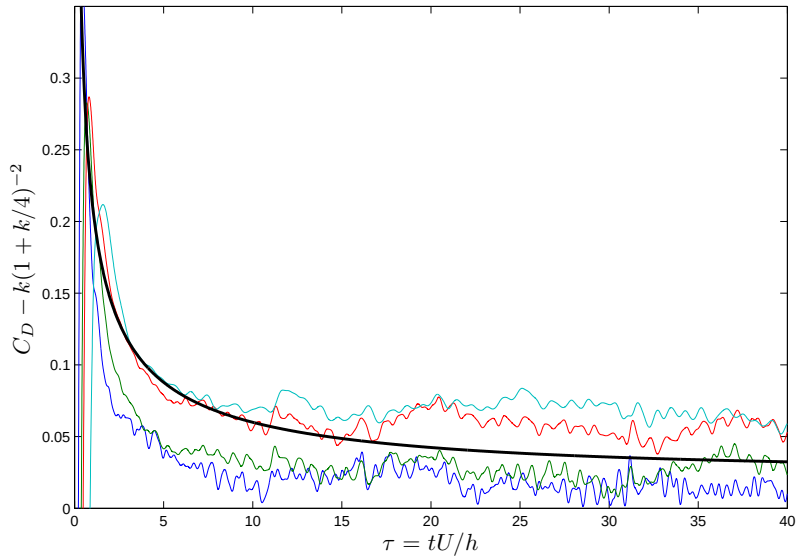

(b) *Comparison of drag coefficient with theoretical drag (2.61) subtracted.*

Figure 5.17: *Comparison predicted and measured drag on a 20cm mesh, where experimental results are the average from three repeat runs. 0.3 m/s (blue), 0.35 m/s (green), 0.4 m/s (red) and 0.5 m/s (cyan). The results from the vortex model, in thick black, use* $\kappa = 1.5$.

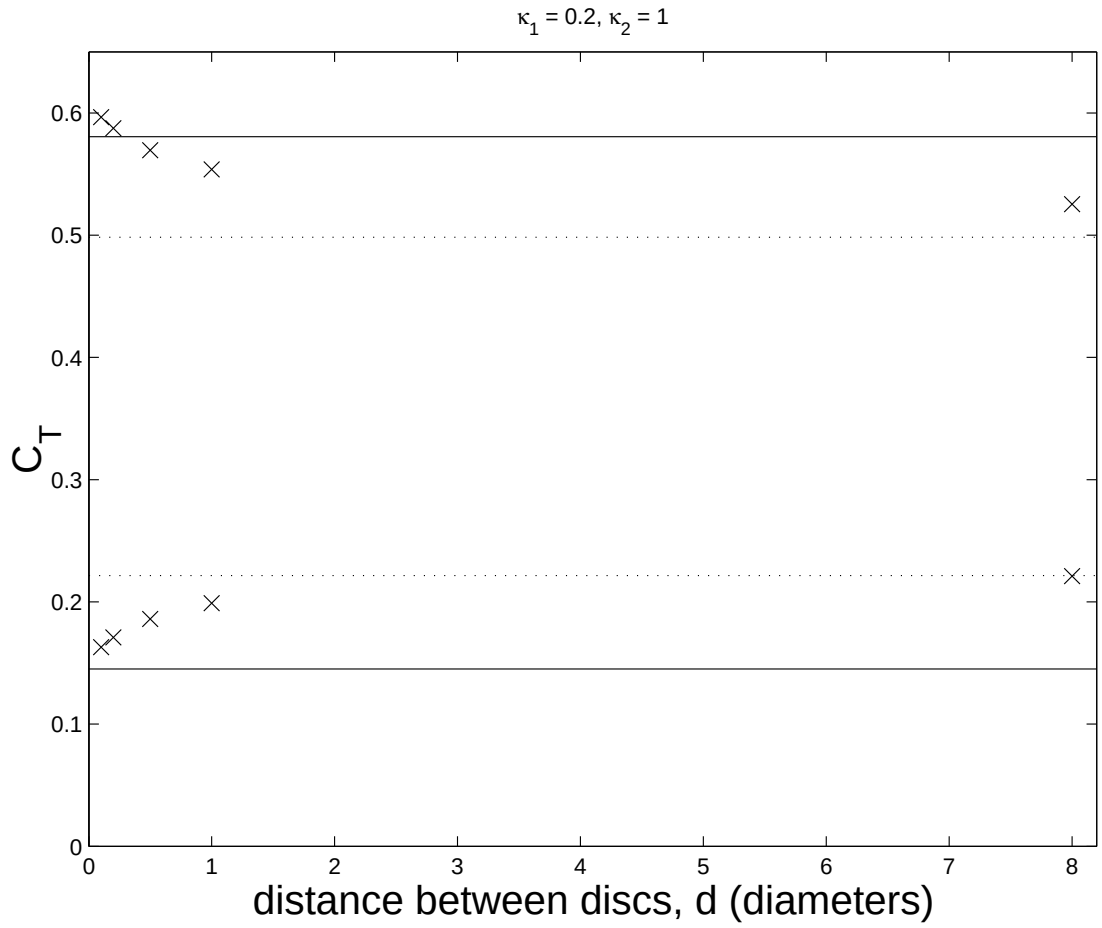

Figure 5.18: *Initial investigation into the thrusts on double actuator surfaces of varying spacing, s. The solid lines represent the theoretical case $s \to 0$, dashed lines represent the theoretical case of 'medium' spacing. The crosses are results from the vortex model. The lower half of the graph represents the upstream actuator surface; the upper portion of the graph represents the downstream actuator surface.*

spacing, the change is initially steep but becomes shallower, apparently approaching the medium solution asymptotically. The discrepancy between theoretical and computational results for the downstream surface is the same discrepancy found when using the point vortex method seen for single actuator surfaces; this has been investigated by using smaller values of κ_2, showing that the vortex and 'medium' solutions converge as $\kappa_1 \to 0$ and $\kappa_2 \to 0$. The results indicate that there is a smooth change in conditions between $s = 0$ and $s \to 10$. An extension of this work is recommended as future work, to investigate the dynamics of double actuator surfaces.

5.7 Effects of ambient turbulence

Ambient turbulence is expected to be significant in most tidal streams (see, for example, McCann et al., 2008) and this will have an important effect on wake mixing and wake recovery.

The effect of ambient turbulence is to increase the rate of lateral diffusion of streamwise momentum so that the wake velocity recovers more quickly. Experimental and theoretical results to show this effect are presented by Jonsson et al. (2011), where the same meshes as described in Section 5.5.3 were placed in the constant current flume at UCL and the centreline velocity was measured using an acoustic Doppler velocimeter; thrust measurements were unsuccessful. The theoretical model for wake mixing draws from the work by Eames et al. (2011a) and Eames et al. (2011b) on the growth of wakes of cylinders and spheres. The same effects are seen in the experimental and numerical work presented by Harrison (2011).

The point vortex model does not predict the wake recovery. Generally the effects of turbulence are not accounted for in two-dimensional vortex models because it is a three-dimensional effect which relies on vortex stretching. Jaroch and Graham (1988) make this general point about vortex models in their conclusions.

Fung et al. (1992) describe a kinematic model of turbulence which could be superposed with the velocity field in the vortex model and this could potentially augment the vortex model to predict the effects of ambient turbulence and this would make interesting research in the future. However, an analysis of the effects of ambient turbulence on wake mixing is beyond the scope of this thesis.

5.8 Conclusions

5.8.1 Summary

The vortex method has been tested for the general case of energy extraction from a uniform planar flow using the actuator surface approximation. The point vortex method has been reviewed and its practical problems, strengths, and weaknesses have been discussed. A numerical model of an actuator surface was presented, using discrete vortices to simulate the vortex sheets in the wake. The vortex cores were mollified using Krasny's desingularisation parameter, which was constant throughout each simulation.

Convergence of the results against numerical parameters was shown, with the steady velocity at the actuator surface as the key quantitative measure. Results showed good convergence as the time-step was reduced, so that the time-step used for the calculations here is considered small enough to yield results with less than 1% uncertainty.

Three time-integration techniques were used: Euler-integration, Euler-integration with sub-time-steps, and the fourth order Runge-Kutta method. As time progressed in the simulations the different time integration methods showed very close agreement until the wake became unstable, at which point the position of the vortices became different but their strength and mean distribution remained very similar. The velocities at the actuator surface, for the different time integration methods, showed very little difference; convergence of the results with decreasing time-step was essentially the same for different integration techniques. Hence the Euler-method was used thereafter due to its simplicity.

The effect of the desingularisation parameter, δ, was not insignificant. For all values of δ

that were tested the mean velocity at the actuator surface converged with decreasing time-step; but smaller values of δ generally led to smaller steady velocities at the surface. However the effect was still small, for example: by reducing δ from 0.05 to 0.03 the convergence of the mean velocity at the surface with decreasing time-step was the same except that it was smaller by about 0.2%.

The convergence of steady velocity at the actuator surface with decreasing time-step and decreasing desingularisation parameter is considered acceptable, and that the uncertainty in the steady velocity at the actuator surface is less than 1%.

The numerical model was then used to simulate actuator surfaces in planar flow with a range of resistance coefficients, κ. The initial test of these results was through the steady thrust (or drag) coefficient, which is derived from the steady velocity at the actuator surface. The results show behaviour that is within the range of scatter of published experimental data, though it is at the high end of that envelope. The behaviour is qualitatively the same as predicted by linear momentum theory and semi-empirical models; quantitatively the drag predicted by the vortex model is higher than predicted by linear momentum, with the difference increasing with κ: for $\kappa = 2$, 3, and 3.5 the error in steady velocity is 2.6%, 4.7% and 6.7% respectively. This difference is to be expected because the linear theory breaks down as κ increases. A theoretical correction for the difference was suggested, yielding useful insight but it, too, broke down for higher values of κ because it relied on linear momentum theory. The correction was therefore not employed. Agreement between the vortex method and semi-empirical methods for steady drag is better: the difference is approximately 5% but does not grow with κ.

The vortex method in unsteady planar flow was also investigated with a focus on the case of an impulsively started actuator surface. A theoretical solution for the asymptotic case of an impulsively started, weakly loaded actuator surface was presented for use in validation. For low values of κ the numerical results could be compared to the asymptotic model developed here, and in the limit $\kappa \to 0$ agreement is excellent.

For steady state, given the breakdown of theory and the scatter of published data for heavy loading on an actuator surface more experiments were deemed necessary; further, there is lack of experimental data on an impulsively started actuator surface. Hence, new experiments were carried out: a mesh was towed through static water and drag measurements were recorded. The experimental results are approximately equivalent to an impulsively started actuator surface and showed, across a range of towing speeds, repeatability within approximately 5% in terms of drag measurements. Good qualitative agreement was found between measurements and the vortex model insofar as the drag is initially high and decays monotonically towards a steady value. The instantaneous drag at start-up cannot be compared because the experiments took a finite time to accelerate; however there is good quantitative agreement between the initial peak in the measured drag, and that predicted by the vortex model. The rates of decay seen in the experimental and numerical data are different: the numerical model predicts a slower decay, with the drag coefficient differing by up to 5% at times. There is good agreement with the steady value of drag: the vortex model predicts a value which is in the center of the range

of results obtained experimentally.

The comparison of the vortex model with theory and experiment in both steady and unsteady cases showed agreement within the uncertainty of experimental measurements and so this gives confidence in vortex model as a model of energy extraction. Following this the vortex model was used to simulate double actuator surfaces with different separations. The results showed good agreement in the limits of coincident and largely spaced surfaces, where thrust measurements were slightly higher than theoretically predicted which is to be expected due to the breakdown of linear momentum theory at heavier loads. The results for double actuator discs showed a smooth recovery from the 'coincident' case to the large spacing, with the majority of the recovery evident within one surface height downstream, as suggested by Newman (1983).

5.8.2 Further work

To further verify the vortex model of an actuator surface, the results could be processed to investigate the conservation of mass and momentum in a control volume which encompasses the actuator surface, as suggested by van Kuik (2008). To further validate the model, velocity measurements could be made in the vicinity of a mesh and these could be compared to the results of the vortex model. Further, the results of those experiments, and of the model, could be processed to compare predictions and measurements of the Reynolds stresses, as was done by Jaroch and Graham (1988). The experiments presented in this chapter only include measurements from one mesh ($\kappa = 1.5$), and further measurements with other meshes would provide more insight into the agreement between the vortex model and measurements. Additionally, more repeat measurements could be made to investigate further the apparent relationship in the data presented here between flow speed and drag on the mesh to establish whether this is a Reynolds number related effect.

Nevertheless, the vortex model has been established here with reasonable confidence as a useful model of energy extraction and has been shown to be capable of simulating multiple actuator surfaces including one simulation of double actuator surfaces where the separation of the surfaces was varied systematically. It is recommended that this method is used to perform a comprehensive investigation of actuator surfaces in close proximity and that a theory should be developed to understand this. Experiments to validate this theory, in a similar method to those presented in this chapter, are recommended. Experiments in a flume should be carried out with caution, because the ambient turbulence will encourage wake mixing which will in turn affect the conditions at the downstream mesh in a way not predicted by the vortex model. Following validation, a theory for actuator surfaces in close proximity could be applied in the blade element momentum (BEM) method so that it can be used to predict Moonraker performance in a much more efficient manner than the vortex model. Further, the theory may be helpful for other rotor designs with two rows of blades, for example contra-rotating propellers.

Chapter 6

Conclusions

This chapter begins by summarising the achievements of the research presented in this thesis. These achievements are split into three sections, following the same structure as the thesis: modeling of Moonraker blade forces, experimental measurements on a lab-scale prototype Moonraker (PII), and further research into the vortex model and its application to actuator surfaces. Following this a summary of recommendations for further work is presented, drawing from the respective conclusions of the foregoing chapters of this thesis. Finally, some closing remarks are made.

6.1 Research achievements

6.1.1 Modeling of Moonraker blade forces

6.1.1.1 Blade Element Momentum (BEM) model

The blade element momentum (BEM) method has been used to show that a cascade of lifting blades moving perpendicular to the oncoming flow can be very efficient, justifying the design of the Moonraker as having translating lifting blades.

6.1.1.2 Moonraker definitions

The geometry of the oval blade path of the Moonraker has been formalised, with the introduction of the geometric ratio g_M.

6.1.1.3 Two-dimensional vortex model

A two-dimensional vortex model of cross-flow devices has been implemented in Matlab following the method of Strickland et al. (1981), showing close agreement with the results of Strickland et al. (1981).

6.1.1.4 Comparison of BEM, vortex, and RANS models

The two-dimensional vortex model was compared to the BEM and RANS models developed by Gretton (2009). All three models were applied to exactly the same device (a Darrieus turbine) yielding insight into the relative merits of each model. The comparison between the three models showed that the vortex model and BEM model produce very similar results, probably because of their reliance on empirical blade data. The benefit of the vortex model is its greater flexiblity which, in the present research, makes it possible to simulate a Moonraker. There was significant disagreement at low blade speeds between the RANS model and the BEM and vortex models. This is because the BEM and vortex models lacked dynamic stall models. At high blade speeds the results showed fair agreement between all models.

6.1.1.5 Simulation of a Moonraker

The vortex model was used to simulate a series of Moonraker configurations. In the case studied the Moonraker was predicted to achieve a 21% higher power coefficient than an equivalent Darrieus turbine, while the ratio of thrust-to-power at peak power only slightly increased (2.6% in the case studied here). The power coefficients predicted for the Moonraker were competitive with conventional axial-flow rotors.

6.1.2 Lab-scale Moonraker experiments

6.1.2.1 Prototype development

A lab-scale experimental Moonraker device, PII, has been designed and built. The device was designed to maximise the blade Reynolds number, while also keeping the number of blades, the blade span-to-chord ratio, and the ratio of device width-to-height as high as possible. The PII is 2 m wide, 0.5 m high, with a turning radius of 0.192 m at each end, and up to six blades of 61 mm chord connected to chains and running between tracks on the straight parts of the blade path.

The PII device was tested in the towing tanks at UCL and at QinetiQ, where the ratio of device frontal area to channel cross sectional area (blockage ratio) was 0.366 and 0.014 respectively. The tests at QinetiQ were therefore comparable to the 'unbounded' vortex model.

6.1.2.2 Prototype testing

The PII device was tested at towing speeds of 0.7 m/s, 0.6 m/s, 0.5 m/s, and 0.4 m/s at QinetiQ. This generated blade Reynolds numbers in the range 65,000-112,000, and blade speed ratios in the range $1 < \Lambda < 5$. Tests were carried out with six blades, three blades, and one blade.

6.1.2.3 Blade load instrumentation system

A novel instrumentation system which measures the two axis bending at the centre of a NACA0015 blade with 61 mm chord has been developed and tested. The system sits entirely within the blade and works underwater. Data is stored on internal memory and can later be retrieved wirelessly.

6.1.2.4 Blade loading measurements

A series of blade loading measurements were recorded on the PII at QinetiQ. The samples, taken at 125 Hz, show very periodic results.

6.1.2.5 Blade loading results processing

Results were processed in Matlab and a series of Fourier averaged loading signals was produced for each combination of blade speed ratio, towing speed, and number of blades. Measurements taken from independent experiments in opposite directions showed very good repeatability. The Fourier averaged signals are effectively a 'master' signal that is representative of any period of rotation on the PII device once conditions are quasi-steady. Therefore the Fourier averaged experimental results can be compared to predictions.

6.1.2.6 Comparison between prediction and mesaurements - normal force

Some good agreement has been shown between predictions and measurements of the force normal to the blade's motion, but at higher blade speeds, where the vortex model predicted that the blade would not stall, there was less agreement. At these higher blade speeds the vortex model predicted a lower normal force than was measured. Measurements of the normal force were effectively clipped on the upstream pass due to stray resistance in the load cell so that, with the exception of very few results, comparisons between measurements and predictions of the normal force could only be made on the downstream pass (tangential force measurements did not suffer from this problem).

6.1.2.7 Comparison between prediction and mesaurements - tangential force

Comparisons of predictions and measurements of the loading tangential to the blade's motion showed some encouraging agreement when the averages were taken, with both predictions and measurements showing an increase in torque as the blade speed increases; however, experiments showed that this increase in torque occurred at a lower blade speed than was predicted. Comparisons of the measured and predicted tangential loading over a revolution showed less agreement: the experimental results showed distinctly different loading magnitudes on the up- and down-stream passes, while the predicted differences were only slight. Further, the absence of dynamic stall considerations was evident in the model, which did not predict the transient forces on the blade as it joined the straight part of the blade path.

6.1.2.8 Derivation of power coefficient from blade load measurements

Power coefficients of $C_P \approx 0.5$ were derived from the blade force measurements, which suggests that the Moonraker is capable of high power coefficients; these measurements are subject to some uncertainty because the force measurements were not valid over the curved parts of the blade path, but given the repeatability of the measurements they are considered to be fairly reliable.

6.1.2.9 Analysis of disagreement between predictions and measurements

The disagreement between the predictions and measurements were mostly attributed to shortcomings in the predictions. Two important causes of disagreement are likely to be the vortex model's lack of dynamic stall considerations and its limitation to two-dimensions, hence an upgrade of the predictions to include these features is recommended. The presence of the structure in the experiment was not simulated in the model, and this could be a cause of the difference between predictions and measurements (a three-dimensional model would also suffer from this problem). Additionally the reliance of the vortex model on empirical blade section data at low Reynolds number could be an important cause of the discrepancy between prediction and measurement, and this is a weakness in the model that is not easily overcome without increasing the Reynolds number of the experiments.

6.1.3 Vortex model of actuator surfaces

A two-dimensional vortex model has been formulated for an actuator surface and implemented in Fortran and subjected to a series of systematic tests yielding the following results:

- For any small desingularisation parameter ($\delta < 0.05$) the results showed agreement within less than 1%.
- All results showed convergence as the time-step decreases.
- Convergence of the results is almost identical when using three different integration methods: Euler, Euler with sub-timestep, and RK4.

6.1.3.1 Validation against published data

The quasi-steady velocity at the actuator surface predicted by the vortex model shows close agreement with linear momentum theory for weakly loaded surfaces ($\kappa \to 0$), and comparable behaviour for heavier loads but with some disagreement; the vortex model predicts higher velocities than linear momentum theory: for $\kappa = 2$, 3, and 3.5 the error in steady velocity is 2.6%, 4.7% and 6.7% respectively. This is consistent with van Kuik's (1991) finding that linear momentum theory under-predicts the velocity at the actuator surface.

The results of the vortex model have been compared to published experimental results and are within the scatter of those results but at the higher end of that envelope, which is encouraging in terms of the validity of the vortex model.

6.1.3.2 Validation against new theory and experiments

To test the vortex method further, the transient performance of an impulsively started actuator surface was investigated. Comparisons to a new asymptotic theory for lightly loaded surfaces showed good agreement in the limit of light loads ($\kappa \to 0$).

New experiments were carried out to test performance of the vortex model at higher values of κ. A steel mesh was towed through static water and the drag was measured. The mesh was accelerated rapidly and then towed at constant speed.

The comparison of the drag predicted by the vortex method with experimental measurements showed good agreement in terms of the initial high drag, the nature of the decay, and the final quasi-steady value. The decay predicted by the vortex method was slightly slower than was measured, with the predicted and measured thrusts differing by up to 5% during the transient period. The vortex model's prediction of the steady drag on an actuator surface was equal to the mean of the measured results, which varied by 5%.

6.1.3.3 Application to double actuator surfaces

The vortex model was applied to double actuator surfaces across a range of separations. The extension of this work is recommended, in order to develop a theory that can be implemented in a BEM model for the Moonraker or other device with two rows of blades.

6.2 Opportunities for further work

Critical discussions were included in the body of this thesis and, for Chapters 3, 4 and 5 were summarised at the end of each chapter. Opportunities to address these issues in the future are listed here:

- Measurements of the lift and drag on the blades used on the PII.
- Use of the multiple streamtube BEM on the Moonraker, using current models for single/double actuator surfaces.
- Investigation of double actuator surfaces using the vortex model developed here, and experiments on pairs of meshes, with an aim to develop a theory for double actuator surfaces for a range of streamwise separation.
- Implementation of a dynamic stall model in the vortex and BEM models of the Moonraker.
- Development of a three-dimensional vortex model of a Moonraker.

- Improvements to the computational efficiency of the vortex models.
- Measurement of blade section characteristics on the blades used on the PII.
- Use of a monorail on the PII to improve measurements of blade loading, increase maximum Reynolds number.
- Measurements of the velocity field in the vicinity of the PII or other experimental Moonraker device.
- Further verification of the vortex model of an actuator surface by calculating the loss of mass and momentum in a control volume encompassing the actuator surface.
- Further validation of the vortex model: velocity measurements around a mesh and comparison with the vortex model, including the Reynolds stress in the wake.
- Further validation of the vortex model: experimental measurements on different meshes.

6.3 Closing remarks

The purpose of this research was to quantitatively establish the hydrodynamic performance of the Moonraker device. Progress towards this goal has been made through the use of BEM and vortex models. The BEM model will be of further utility if a theory for double actuator surfaces in close proximity can be developed, and good progress has been made toward this goal by using the vortex model to investigate double actuator surfaces. Additionally important steps forward have been made in the development of lab-scale prototype Moonraker devices. The successes and lessons learned from the engineering of these small prototypes has been detailed in this thesis and should provide a useful springboard for future researchers. Additionally a novel instrumentation system for measuring blade loads has been developed, and this should be of use both in future research on the Moonraker and for a wide range of other research activities where a wireless, water-proof, small scale, streamlined, two-axis load cell is often required.

The results of the predictions from the vortex model and their comparison with the experimental results provide helpful insight into the performance of a Moonraker device. In particular the experimentally measured results, which are repeatible, show high power coefficients and are therefore encouraging for the prospects of the Moonraker concept.

In addition to the hydrodynamics aspects considered in this thesis, there remains much to do concerning the practical realisation of a working Moonraker device both at lab-scale and full-scale. The generation of positive shaft torque at a lab scale is an important milestone which should be the next priority; and the mechanical and structural design of a full-scale Moonraker are also essential before a business case can be made for such a device. All of this is vital if the potential of the Moonraker, as revealed through hydrodynamic analysis, is ever to be demonstrated. The work presented here has pointed to its ultimate potential.

References

Abbott, I. and Doenhoff, A. *Theory of wing sections: including a summary of airfoil data.* Dover books on physics and chemistry. Dover Publications, 1959. ISBN 9780486605869.

Althaus, D. Profilpolaren fur den modellflug, 1980.

Baker, G. R. A test of the method of fink & soh for following vortex-sheet motion. *Journal of Fluid Mechanics Digital Archive*, 100(01):209–220, 1980.

Batchelor, G. *An introduction to fluid dynamics.* Cambridge University Press, 1967.

BERR. *UK Renewables Atlas.* formerly UK Department for Business, Enterprise and Regulatory Refrom (BERR), now Department for Business, Innovation and Skills (BIS), 2008.

Betz, A. Das maximum der theoretisch moglichen ausnutzung des windes durch windmotoren. *Zeitschrift fur das gesamte Turbinenwesen*, 26:307–309, 1920.

Birkhoff, G. and Fisher, J. Do vortex sheets roll up? *Rendiconti del Circolo Matematico di Palermo*, 8(1):77–90, January 1959. ISSN 0009-725X (Print) 1973-4409 (Online).

Black & Veatch. *Tidal Stream - Phase II UK Tidal Stream Energy Resource Assessment.* 2005a.

Black & Veatch. *Tidal Stream Energy Resource and Technology Summary report.* 2005b.

Burton, T., Sharpe, D., Jenkins, N., and Bossanyi, E. *Wind Energy Handbook.* John Wiley & Sons, 2001.

Calcagno, G., Salvatore, F., Greco, L., Moroso, A., and H., E. Experimental and numerical investigation of a very promising technology for marine current exploitation: the kobold turbine. In *The Sixteenth International Offshore and Polar Engineering Conference (ISOPE)*, 2006.

Carbon Trust. *Variability of Wave and Tidal Stream Energy Resources.* 2005.

Carr, L. W. Progress in analysis and prediction of dynamic stall. *Journal of Aircraft*, 25:6–17, 1988.

Castro, I. P. Wake characteristics of two-dimensional perforated plates normal to an air-stream. *Journal of Fluid Mechanics*, 46(03):599–609, 1971.

Chorin, A. J. Numerical study of slightly viscous flow. *Journal of Fluid Mechanics Digital Archive*, 57(04):785–796, 1973.

Clements, R. R. and Maull, D. J. The representation of sheets of vorticity by discrete vortices. *Progress in Aerospace Sciences*, 16:129–146, 1975.

Conway, J. T. Analytical solutions for the actuator disk with variable radial distribution of load. *Journal of Fluid Mechanics Digital Archive*, 297(-1):327–355, 1995.

Cottet, G.-H. and Koumoutsakos, P. D. *Vortex Methods; theory and practice.* 2000. ISBN 9780521061704.

Crighton, D. G. The kutta condition in unsteady flow. *Annual Review of Fluid Mechanics*, 17 (1):411–445, 1985.

Critzos, C., Heyson, H., Boswinkle, R., and for Aeronautics, U. S. N. A. C. *Aerodynamic characteristics of NACA 0012 airfoil section at angles of attack from 0 to 180 degrees.* Technical note. National Advisory Committee for Aeronautics, 1955.

Cumberbatch, E. Two-dimensional flow past a mesh. *The Quarterly Journal of Mechanics and Applied Mathematics*, 35(3):335–344, 1982.

Darrieus, G. J. M. Turbine having its rotating shaft transvrse to the flow of the current, 1926. US Patent 1,835,018.

Draper, S., Houlsby, G., Oldfield, M., and Borthwick, A. Modelling tidal energy extraction in a depth-averaged coastal domain. In *Proceedings of the 8th European Wave and Tidal Energy Conference (EWTEC)*, 2009.

Eames, I., Jonsson, C., and Johnson, P. B. The growth of a cylinder wake in turbulent flow. *Journal of Turbulence*, 12:N39, 2011a.

Eames, I. (personal communication), 2008.

Eames, I., Johnson, P. B., Roig, V., and Risso, F. Effect of turbulence on the downstream velocity deficit of a rigid sphere. *Physics of fluids*, 23(9), 2011b.

Edinburgh Designs Ltd. Variable pitch foil vertical axis tidal turbine. Technical Report T/06/00234/00/REP URN 06/929, UK Department of Trade and Industry (DTI), 2006.

Fink, P. T. and Soh, W. K. A new approach to roll-up calculations of vortex sheets. *Proceedings of the Royal Society of London. Series A, Mathematical and Physical Sciences*, 362(1709): 195–209, 1978. ISSN 00804630.

Fraenkel, P. Development and testing of Marine Current Turbine's SeaGen 1.2MW tidal stream turbine. In *Proceedings of the 3rd International Conference on Ocean Energy (ICOE)*, October 2010.

Froude, R. E. On the part played in propulsion by differences of fluid pressure. *Transactions of the (Royal) Institution of Naval Architects.*, 30:390–405, 1889.

Fung, J. C. H., Hunt, J. C. R., Malkik, N. A., and Perkins, R. J. Kinematic simulation of homogeneous turbulence by unsteady random fourier modes. *Journal of Fluid Mechanics*, 236:281–318, 1992.

Garrett, C. and Cummins, P. The efficiency of a turbine in a tidal channel. *Journal of Fluid Mechanics*, 588(-1):243–251, 2007.

Gipe, P. *Wind energy comes of age / Paul Gipe*. Wiley, New York :, 1995. ISBN 047110924.

Gormont, R. E. A mathematical model of unsteady aerodynamics and radial flowfor application to helicopter rotor. Technical Report TR-72-67, USAAMRDL, 1973.

Graham, G. *Measurement of instantaneous pressure distributions and blade forces on an airfoil undergoing cycloidal motion*. Texas Tech University, 1982.

Graham, J. M. R. The lift on an aerofoil in starting flow. *Journal of Fluid Mechanics*, 133: 413–425, 1983.

Greengard, C. The core spreading vortex method approximates the wrong equation. *Journal of Computational Physics*, 61(2):345 – 348, 1985. ISSN 0021-9991.

Gretton, G. I. and Bruce, T. Aspects of mathematical modelling of a prototype scale vertical-axis turbine. In *Proceedings of the 7th European Wave and Tidal Energy Conference (EWTEC)*, 2007.

Gretton, G. I. *Hydrodynamic analysis of a vertical axis tidal current turbine*. PhD thesis, University of Edinburgh, 2009.

Hama, F. R. and Burke, E. R. On the rolling up of a vortex sheet. Technical Report BN-220, University of Maryland, 1960.

Harrison, M. E., Batten, W. M. J., Myers, L. E., and Bahaj, A. S. A comparison between cfd simulations and experiments for predicting the far wake of horizontal axis tidal turbines. In *Proceedings of the 8th European Wave and Tidal Energy Conference (EWTEC)*, 2009.

Harrison, M. E. *The accuracy of the actuator disc-RANS approach for modelling performance and wake characteristics of a horizontal axis tidal stream turbine*. PhD thesis, University of Southampton, 2011.

Howells, I. and Waechter, R. Plane irrotational flow against a porous plate. *Quarterly Journal of Mechanics and Applied Mathematics*, 48(pt 1):135–156, 1995.

Huang, Z. and Keffer, J. F. Development of structure within the turbulent wake of a porous body. part 1. the initial formation region. *Journal of Fluid Mechanics Digital Archive*, 329 (-1):103–115, 1996.

Inoue, O. Schemes and parameters in 2d vortex simulation. *Journal of the Physical Society of Japan*, 58(8):2767–2778, 1989.

Jacobs, E. and Sherman, A. *Airfoil section characteristics as affected by variations of the Reynolds number*. Report (United States. National Aeronautics and Space Administration). National Advisory Committee for Aeronautics, 1937.

Jaroch, M. P. G. and Graham, J. M. R. An evaluation of the discrete vortex method as a model for the flow past a flat-plate normal to the flow with a long wake splitter plate. *Journal de Mecanique theorique et appliquee*, 7(2):105–134, 1988.

Johnson, P. B., Gretton, G., and McCombes, T. Numerical modelling of cross-flow turbines: a direct comparison of four prediction techniques. In *Proceedings of the 3rd International Conference on Ocean Energy (ICOE)*, October 2010.

Jonsson, C., Johnson, P. B., and Eames, I. Energy extractors in turbulent flow: Wake decay and implications for farm layout. In *Proceedings of the 9th European Wave and Tidal Energy Conference (EWTEC)*, 2011.

Kaden, H. Aufwicklung einer unstabilen unstetigkeitsflilche. *Ing. Archiv*, 2(140), 1931. English trans. R.A.E. Library Trans. no. 403.

Karamcheti, K. *Principles of ideal-fluid aerodynamics*. R. E. Krieger Pub. Co., 1980. ISBN 9780898741131.

Katz, J. and Plotkin, A. *Low Speed Aerodynamics*. Cambridge University Press, 2 edition, 2001. ISBN 0-521-66219-2.

Koo, J.-K. and James, D. F. Fluid flow around and through a screen. *Journal of Fluid Mechanics Digital Archive*, 60(03):513–538, 1973.

Krasny, R. A study of singularity formation in a vortex sheet by the point-vortex approximation. *Journal of Fluid Mechanics Digital Archive*, 167(-1):65–93, 1986.

Krasny, R. Computation of vortex sheet roll-up in the trefftz plane. *Journal of Fluid Mechanics Digital Archive*, 184(-1):123–155, 1987.

Krasny, R. Vortex sheet computations: Roll-up, wakes, separation. In Anderson, C. R. and Greengard, C., editors, *Lectures in Applied Mathematics: Vortex Dynamics and Vortex Methods*, volume 28, 1991.

Kuchemann, D. and Weber, J. *Aerodynamics of propulsion / Dietrich Kuchemann, Johanna Weber*. McGraw-Hill, New York :, 1953.

Lanchester, F. W. A contribution to the theory of propulsion and the screw propeller. *Transactions of the (Royal) Institution of Naval Architects*, 57:98–116, 1915.

Le Chuiton, F. Actuator disc modelling for helicopter rotors. *Aerospace Science and Technology*, 8(4):285 – 297, 2004. ISSN 1270-9638.

Lee, J. H. W. and Greenberg, M. Line momentum source in shallow inviscid fluid. *Journal of Fluid Mechanics*, 145(AUG):287–304, 1984. ISSN 0022-1120.

Leonard, A. Vortex methods for flow simulation. *Journal of Computational Physics*, 37(3):289 – 335, 1980. ISSN 0021-9991.

Lighthill, M. J., S. *An Informal Introduction to Theoretical Fluid Mechanics*. IMA Monograph series; 2], isbn = 0-19-853631-3,. Oxford University Press, 1986.

Loftin, L. and Smith, H. *Aerodynamic characteristics of 15 NACA airfoil sections at seven Reynolds numbers*. Technical note // National Advisory Committee for Aeronautics. National Advisory Committee for Aeronautics, 1949.

Longuet-Higgins, M. S. and Cokelet, E. D. The deformation of steep surface waves on water. i. a numerical method of computation. *Proceedings of the Royal Society of London. Series A, Mathematical and Physical Sciences*, 350(1660):1–26, 1976. ISSN 00804630.

MacKay, D. J. C. *Sustainable energy : without the hot air / David JC MacKay*. UIT, Cambridge, England :, 2009. ISBN 9781906860011 9780954452933.

Madsen, H. The actuator cylinder: a flow model for vertical axis wind turbines. Technical report, Aalborg University Center, Institute of Industrial Construction and Energy Technology, Aalborg, Denmark., 1982.

McCann, G., Thomson, M., and Hitchcock, S. Implications of site specific conditions on the prediction of loading and power performance of a tidal stream device. In *Proceedings of the 2nd International Conference on Ocean Energy (ICOE)*, October 2008.

McCroskey, W. J. Unsteady airfoils. *Annual Review of Fluid Mechanics*, 14(1):285–311, 1982.

McCroskey, W. J., Mcalister, K. W., Carr, L. W., and Pucci, S. L. An experimental study of dynamic stall on advanced airfoil sections. volume 1: Summary of the experiment. *Nasa Technical Memorandum*, 2(TM 84245), 1982.

Mikkelsen, R., Sorensen, J. N., Oye, S., and Troldborg, N. Analysis of power enhancement for a row of wind turbines using the actuator line technique. In *Journal of Physics: Conference Series. Special Topic Conference 'The Science of making Torque from Wind'*, number 75, 2007.

Miley, S., of Aerospace Engineering, T. A. . M. U. D., and Program, R. I. R. F. P. W. S. *A catalog of low Reynolds number airfoil data for wind turbine applications.* Number v. 1982, pt. 1 in RFP-. National Technical Information Service, U.S. Dept. of Commerce, 1982.

Moore, D. W. The discrete vortex approximation of a vortex sheet. Technical Report Rep. AFOSR-1084-69, California Inst. of Tech., 1971.

Moore, D. W. On the point vortex method. *SIAM Journal on Scientific and Statistical Computing*, 2(1):65–84, 1981.

Moore, D. Numerical study of roll-up of a finite vortex sheet. *Journal of Fluid Mechanics*, 63 (APR3):225–235, 1974. ISSN 0022-1120.

Newman, B. Actuator-disc theory for vertical-axis wind turbines. *J. Wind Engineering and Industrial Aerodynamics*, 15(3):347–355, 1983.

Nicolle, A. (personal communication), 2010.

Oates, G. *Aircraft propulsion systems technology and design.* AIAA education series. American Institute of Aeronautics and Astronautics, 1989. ISBN 9780930403249.

O'Neill, F. Source models of flow through and around screens and gauzes. *Ocean Engineering*, 33(14-15):1884– – 1895, 2006. ISSN 0029-8018.

Paraschivoiu, I. Double-multiple streamtube model for darrieus wind turbines. In *Second DOE-NASA wind turbines dynamics workshop, NASA CP-2186, Cleveland, OH*, February 1981.

Pawsey, N. C. K. *Development and evaluation of passive variable-pitch vertical-axis wind turbines.* PhD thesis, The University of New South Wales, Sydney, Australia, 2002.

Ponta, F., Seminara, J., and Otero, A. On the aerodynamics of variable-geometry oval-trajectory darrieus wind turbines. *Renewable Energy*, 32(1):35 – 56, 2007. ISSN 0960-1481.

Pope, A. and Harper, J. *Low-speed wind tunnel testing.* Wiley, 1966.

Prandtl, L. Uber flussigkeits bewegung bei sehr kleiner reibung. In *Verhaldlg III Int. Math. Kong. (Heidelberg: Teubner)*, 1904. Also available in translation as: Motion of fluids with very little viscosity. NACA TM 452 (March 1928).

Prandtl, L. Induced drag of multiplanes. Technical Report TN 182, 1924.

Pullin, D. I. The large-scale structure of unsteady self-similar rolled-up vortex sheets. *Journal of Fluid Mechanics Digital Archive*, 88(03):401–430, 1978.

Pullin, D. I. and Perry, A. E. Some flow visualization experiments on the starting vortex. *Journal of Fluid Mechanics Digital Archive*, 97(02):239–255, 1980.

Rankine, W. J. M. On the mechanical principles of the action of propellers. *Transactions of the (Royal) Institution of Naval Architects.*, 6:13–30, 1865.

Read, S. and Sharpe, D. An extended multiple streamtube theory for vertical axis wind turbines. In *2nd BWEA Workshop, Cranfield, U.K.*, pages 65–72, April 1980.

Rethore, P.-E., Sorensen, N. N., Bechmann, A., and Zhale, F. Study of the atmospheric wake turbulence of a cfd actuator disc model. In *Proceedings of the European Wind Energy COnference (EWEC)*, 2009.

Rosenhead, L. The formation of vortices from a surface of discontinuity. *Proceedings of the Royal Society of London. Series A, Containing Papers of a Mathematical and Physical Character*, 134(823):170–192, 1931. ISSN 09501207.

Saffman, P. G. and Baker, G. R. Vortex interactions. *Annual Review of Fluid Mechanics*, 11 (1):95–121, 1979.

Salter, S. and Taylor, J. R. M. Vertical-axis tidal-current generators and the pentland firth. *Proceedings of the Institution of Mechanical Engineers, Part A: Journal of Power and Energy*, 221(2):181–199, 2007.

Salter, S. H. Correcting the under-estimate of the tidal-stream resource of the pentland firth. In *Proceedings of the 8th European Wave and Tidal Energy Conference (EWTEC)*, 2009.

Sheldahl, R. E. and Klimas, P. C. Aerodynamic characteristics of seven symmetrical airfoil sections through 180-degree angle of attack for use in aerodynamic analysis of vertical axis wind turbines. Technical Report SAND80-2114, Sandia National Laboratories, 1980.

Smith, E. H. *Mechanical Engineer's Reference Book (12th Edition)*. Elsevier, 1998.

Sorensen, J. N., Shen, W. Z., and Munduate, X. Analysis of wake states by a full-field actuator disc model. *Wind Energy*, 1(2), 1998.

Sorensen, J. N. and Kock, C. W. A model for unsteady rotor aerodynamics. *Journal of Wind Engineering and Industrial Aerodynamics*, 58(3):259 – 275, 1995. ISSN 0167-6105.

South, P. and Rangi, R. The Performance and Economics of the Vertical-Axis Wind Turbine Developed at the National Research Council, Ottawa, Canada. In *the 1973 Annual Meeting of the Pacific Northwest Region of the American Society of Agricultural Engineers, Calgary, Alberta*, 10-12 October 1973.

Strickland, J. H. Darrieus turbine: a performance prediction model using multiple streamtubes. Technical Report SAND-75-0431, Sandia Labs., Albuquerque, N.Mex. (USA), 1975.

Strickland, J. H., Smith, T., and Sun, K. A vortex model of the darrieus turbine: An analytical and experimental study. Technical Report SAND81-7017, Texas Tech University, 1981.

Takami, H. A numerical experiment with discrete vortex approximation with reference to the rolling up of a vortex sheet. Technical Report SUDAER 202., Dept. of Aeron. & Astron., Stanford University, 1964.

Taylor, G. I. Air resistance of a flat plate of very porous material. *Aeronautical Research Council. Reports and memoranda*, (no. 2236), 1944.

Taylor, G. I. and Davies, R. M. The aerodynamics of porous sheets. *Aeronautical Research Council. Reports and memoranda*, (no. 2237), 1944.

Templin, R. J. Aerodynamic performance theory for the NRC vertical-axis wind turbine. *NASA STI/Recon Technical Report N*, 76:16618–+, June 1974.

The Engineering Business Ltd. Stingray tidal stream energy device - phase 3. Technical Report T/06/00230/00/REP URN 05/864, UK Department of Trade and Industry (DTI), 2005.

Theodorsen, T. General theory of aerodynamic instability and the mechanism of flutter. Technical Report NACA Rep. 496, 1935.

van der Vooren, A. I. A numerical investigation of the rolling up of vortex sheets. Technical Report Rep. TW-21, Mathematical Institute, Univ. of Groningen. (note: re-published in Proc. R. Soc. Lond. A 1980 373, 67-91), 1965.

van Kuik, G. A. M. *On the limitations of Froude's actuator disc concept*. PhD thesis, Technische Universiteit Eindhoven, 1991.

van Kuik, G. A. M. The edge singularity of an actuator disc with a constant normal load. In *22nd AIAA/ASMA Wind Energy Symposium*, number AIAA-2003-0356, January 2003.

van Kuik, G. A. M. (personal communication), 2008.

van Kuik, G. The flow induced by prandtlś self-similar vortex sheet spirals at infinite distance from the spiral kernel. *European Journal of Mechanics B/Fluids*, 23:607–616, 2004a.

van Kuik, G. The generation of vorticity by actuator disc force fields, with an exact solution of wu's equation. In *Special Topic Conference 'The Science of making Torque from Wind'*, April 2004b.

van Kuik, G. A steady solution for prandtlś self-similar vortex sheet spirals. *European Journal of Mechanics - B/Fluids*, 28(2):296 – 298, 2009. ISSN 0997-7546.

Westwater, F. L. Rolling up of the surface of discontinuity behind an erofoil of finite span. Technical Report 1962, Aeronautical Research Committee Reports and Memoranda, 1936.

Whelan, J. I., Graham, J. M. R., and Peir, J. A free-surface and blockage correction for tidal turbines. *Journal of Fluid Mechanics*, 624(-1):281–291, 2009.

Wilson, R. E. and Lissaman, P. B. S. Applied aerodynamics of wind power machines. Technical report, Oregan State University, 1974.

Appendix A

Appendices

A.1 Blade section data

The data for NACA0012 from Sheldahl and Klimas (1980) and Althaus (1980) is listed below; additionally the hybrid data created from the two is below. Note that data from Althaus (1980) is also available in Miley et al. (1982).

NACA0012, Sheldahl and Klimas (1980) data

Lift coefficient, C_L

α (^{o})	Re: 10000	20000	40000	80000	160000	360000	700000	1000000	2000000	5000000
0	0	0	0	0	0	0	0	0	0	0
1	0.083	0.1057	0.11	0.11	0.11	0.11	0.11	0.11	0.11	0.11
2	0.1534	0.2072	0.22	0.22	0.22	0.22	0.22	0.22	0.22	0.22
3	0.2009	0.3032	0.3376	0.33	0.33	0.33	0.33	0.33	0.33	0.33
4	0.2003	0.3929	0.4464	0.44	0.44	0.44	0.44	0.44	0.44	0.44
5	0.0328	0.4781	0.5276	0.55	0.55	0.55	0.55	0.55	0.55	0.55
6	-0.1413	-0.0298	0.6115	0.6384	0.66	0.66	0.66	0.66	0.66	0.66
7	-0.1142	-0.1089	-0.0212	0.7227	0.746	0.77	0.77	0.77	0.77	0.77
8	-0.0703	-0.0699	-0.0615	0.693	0.8247	0.8542	0.88	0.88	0.88	0.88
9	-0.0215	-0.0198	-0.016	-0.001	0.8527	0.9352	0.9598	0.9661	0.99	0.99
10	0.0311	0.032	0.0344	0.0413	0.1325	0.9811	1.0343	1.0512	1.0727	1.1
11	0.0848	0.0856	0.0869	0.0911	0.1095	0.9132	1.0749	1.1097	1.1539	1.1842
12	0.1387	0.1894	0.1406	0.143	0.1533	0.4832	1.039	1.1212	1.2072	1.2673
13	0.1928	0.1934	0.1945	0.1966	0.203	0.2759	0.8737	1.0487	1.2169	1.3242
14	0.2468	0.2474	0.2484	0.2504	0.2546	0.2893	0.6284	0.8846	1.1614	1.3423
15	0.3008	0.3014	0.3024	0.3043	0.3082	0.3306	0.4907	0.7108	1.0478	1.3093
16	0.3548	0.3554	0.3563	0.3582	0.362	0.3792	0.4696	0.606	0.9221	1.2195
17	0.4079	0.4089	0.4107	0.4139	0.42	0.4455	0.5195	0.5906	0.7826	1.0365
18	0.4606	0.462	0.4644	0.4689	0.4768	0.5047	0.5584	0.603	0.7163	0.9054
19	0.5121	0.5147	0.5178	0.5232	0.5322	0.5591	0.6032	0.6334	0.7091	0.8412
20	0.5838	0.5663	0.5708	0.577	0.587	0.612	0.6474	0.6716	0.7269	0.8233
21	0.6161	0.6184	0.6232	0.6305	0.6414	0.6643	0.6949	0.7162	0.7595	0.8327
22	0.6687	0.6709	0.6755	0.6839	0.6956	0.7179	0.7446	0.7613	0.7981	0.8563
23	0.7216	0.7238	0.7283	0.7373	0.7497	0.7715	0.7948	0.8097	0.8429	0.8903
24	0.7744	0.7765	0.7809	0.7902	0.8043	0.8246	0.8462	0.8589	0.8882	0.9295
25	0.8276	0.8297	0.834	0.8432	0.8572	0.878	0.8984	0.9093	0.9352	0.9718
26	0.881	0.8831	0.8873	0.8963	0.9109	0.9313	0.9506	0.9618	0.9842	1.0193
27	0.9345	0.9365	0.8409	0.9496	0.923	0.9412	0.9583	0.9683	0.9882	1.068
30	0.915	0.915	0.915	0.915	0.9593	0.9709	0.9814	0.9878	1.002	0.915
35	1.02	1.02	1.02	1.02	1.02	1.02	1.02	1.02	1.02	1.02
40	1.075	1.075	1.075	1.075	1.075	1.075	1.075	1.075	1.075	1.075
45	1.085	1.085	1.085	1.085	1.085	1.085	1.085	1.085	1.085	1.085
50	1.04	1.04	1.04	1.04	1.04	1.04	1.04	1.04	1.04	1.04
55	0.965	0.965	0.965	0.965	0.965	0.965	0.965	0.965	0.965	0.965
60	0.875	0.875	0.875	0.875	0.875	0.875	0.875	0.875	0.875	0.875
65	0.765	0.765	0.765	0.765	0.765	0.765	0.765	0.765	0.765	0.765
70	0.65	0.65	0.65	0.65	0.65	0.65	0.65	0.65	0.65	0.65
75	0.515	0.515	0.515	0.515	0.515	0.515	0.515	0.515	0.515	0.515
80	0.37	0.37	0.37	0.37	0.37	0.37	0.37	0.37	0.37	0.37
85	0.22	0.22	0.22	0.22	0.22	0.22	0.22	0.22	0.22	0.22
90	0.07	0.07	0.07	0.07	0.07	0.07	0.07	0.07	0.07	0.07
95	-0.07	-0.07	-0.07	-0.07	-0.07	-0.07	-0.07	-0.07	-0.07	-0.07
100	-0.22	-0.22	-0.22	-0.22	-0.22	-0.22	-0.22	-0.22	-0.22	-0.22
105	-0.37	-0.37	-0.37	-0.37	-0.37	-0.37	-0.37	-0.37	-0.37	-0.37
110	-0.51	-0.51	-0.51	-0.51	-0.51	-0.51	-0.51	-0.51	-0.51	-0.51
115	-0.625	-0.625	-0.625	-0.625	-0.625	-0.625	-0.625	-0.625	-0.625	-0.625
120	-0.735	-0.735	-0.735	-0.735	-0.735	-0.735	-0.735	-0.735	-0.735	-0.735
125	-0.84	-0.84	-0.84	-0.84	-0.84	-0.84	-0.84	-0.84	-0.84	-0.84
130	-0.91	-0.91	-0.91	-0.91	-0.91	-0.91	-0.91	-0.91	-0.91	-0.91
135	-0.945	-0.945	-0.945	-0.945	-0.945	-0.945	-0.945	-0.945	-0.945	-0.945
140	-0.945	-0.945	-0.945	-0.945	-0.945	-0.945	-0.945	-0.945	-0.945	-0.945
145	-0.91	-0.91	-0.91	-0.91	-0.91	-0.91	-0.91	-0.91	-0.91	-0.91
150	-0.85	-0.85	-0.85	-0.85	-0.85	-0.85	-0.85	-0.85	-0.85	-0.85
155	-0.74	-0.74	-0.74	-0.74	-0.74	-0.74	-0.74	-0.74	-0.74	-0.74
160	-0.66	-0.66	-0.66	-0.66	-0.66	-0.66	-0.66	-0.66	-0.66	-0.66
165	-0.675	-0.675	-0.675	-0.675	-0.675	-0.675	-0.675	-0.675	-0.675	-0.675
170	-0.85	-0.85	-0.85	-0.85	-0.85	-0.85	-0.85	-0.85	-0.85	-0.85
175	-0.69	-0.69	-0.69	-0.69	-0.69	-0.69	-0.69	-0.69	-0.69	-0.69
180	0	0	0	0	0	0	0	0	0	0

Drag coefficient, C_D

α (^{o})	Re: 10000	20000	40000	80000	160000	360000	700000	1000000	2000000	5000000
0	0.0337	0.0245	0.0175	0.0133	0.0103	0.0079	0.0067	0.0065	0.0064	0.0064
1	0.0338	0.0247	0.0177	0.0134	0.0104	0.008	0.0068	0.0066	0.0064	0.0064
2	0.0343	0.0251	0.0181	0.0138	0.0108	0.0084	0.007	0.0068	0.0066	0.0066
3	0.0351	0.0259	0.0189	0.0145	0.0114	0.0089	0.0075	0.0071	0.0069	0.0068
4	0.0359	0.027	0.0199	0.0155	0.0124	0.0098	0.0083	0.0078	0.0073	0.0072
5	0.0351	0.0282	0.0218	0.017	0.014	0.0113	0.0097	0.0091	0.0081	0.0076
6	0.046	0.046	0.0232	0.0189	0.0152	0.0125	0.0108	0.0101	0.009	0.0081
7	0.058	0.058	0.058	0.0204	0.017	0.0135	0.0118	0.011	0.0097	0.0086
8	0.072	0.072	0.072	0.0222	0.0185	0.0153	0.0128	0.0119	0.0105	0.0092
9	0.086	0.086	0.086	0.06	0.0203	0.0167	0.0144	0.0134	0.0113	0.0098
10	0.101	0.101	0.101	0.06	0.0188	0.0184	0.0159	0.0147	0.0128	0.0106
11	0.117	0.117	0.117	0.117	0.076	0.0204	0.0175	0.0162	0.014	0.0118
12	0.134	0.134	0.134	0.134	0.134	0.0217	0.0195	0.018	0.0155	0.013
13	0.152	0.152	0.152	0.152	0.152	0.0222	0.0216	0.02	0.0172	0.0143
14	0.171	0.171	0.171	0.171	0.171	0.106	0.0236	0.0222	0.0191	0.0159
15	0.19	0.191	0.19	0.19	0.19	0.19	0.117	0.0245	0.0213	0.0177
16	0.21	0.21	0.21	0.21	0.21	0.21	0.21	0.128	0.0237	0.0198
17	0.231	0.23	0.231	0.231	0.231	0.231	0.23	0.231	0.138	0.0229
18	0.252	0.252	0.252	0.252	0.252	0.252	0.252	0.252	0.252	0.148
19	0.274	0.274	0.274	0.274	0.274	0.274	0.274	0.274	0.274	0.274
20	0.297	0.297	0.297	0.297	0.297	0.297	0.297	0.297	0.297	0.297
21	0.32	0.32	0.32	0.32	0.32	0.32	0.32	0.32	0.32	0.32
22	0.344	0.344	0.344	0.344	0.344	0.344	0.344	0.344	0.344	0.344
23	0.369	0.369	0.369	0.369	0.369	0.369	0.369	0.369	0.369	0.369
24	0.394	0.394	0.394	0.394	0.394	0.394	0.394	0.394	0.394	0.394
25	0.42	0.42	0.42	0.42	0.42	0.42	0.42	0.42	0.42	0.42
26	0.446	0.446	0.445	0.446	0.446	0.446	0.446	0.446	0.446	0.446
27	0.473	0.473	0.473	0.473	0.473	0.473	0.473	0.473	0.473	0.473
30	0.57	0.57	0.57	0.57	0.57	0.57	0.57	0.57	0.57	0.57
35	0.745	0.745	0.745	0.745	0.745	0.745	0.745	0.745	0.745	0.745
40	0.92	0.92	0.92	0.92	0.92	0.92	0.92	0.92	0.92	0.92
45	1.075	1.075	1.075	1.075	1.075	1.075	1.075	1.075	1.075	1.075
50	1.215	1.215	1.215	1.215	1.215	1.215	1.215	1.215	1.215	1.215
55	1.345	1.345	1.345	1.345	1.345	1.345	1.345	1.345	1.345	1.345
60	1.47	1.47	1.47	1.47	1.47	1.47	1.47	1.47	1.47	1.47
65	1.575	1.575	1.575	1.575	1.575	1.575	1.575	1.575	1.575	1.575
70	1.665	1.665	1.665	1.665	1.665	1.665	1.665	1.665	1.665	1.665
75	1.735	1.735	1.735	1.735	1.735	1.735	1.735	1.735	1.735	1.735
80	1.78	1.78	1.78	1.78	1.78	1.78	1.78	1.78	1.78	1.78
85	1.8	1.8	1.8	1.8	1.8	1.8	1.8	1.8	1.8	1.8
90	1.8	1.8	1.8	1.8	1.8	1.8	1.8	1.8	1.8	0
95	1.78	1.78	1.78	1.78	1.78	1.78	1.78	1.78	1.78	1.78
100	1.75	1.75	1.75	1.75	1.75	1.75	1.75	1.75	1.75	1.75
105	1.7	1.7	1.7	1.7	1.7	1.7	1.7	1.7	1.7	1.7
110	1.635	1.635	1.635	1.635	1.635	1.635	1.635	1.635	1.635	1.635
115	1.555	1.555	1.555	1.555	1.555	1.555	1.555	1.555	1.555	1.555
120	1.465	1.465	1.465	1.465	1.465	1.465	1.465	1.465	1.465	1.465
125	1.35	1.35	1.35	1.35	1.35	1.35	1.35	1.35	1.35	1.35
130	1.225	1.225	1.225	1.225	1.225	1.225	1.225	1.225	1.225	1.225
135	1.085	1.085	1.085	1.085	1.085	1.085	1.085	1.085	1.085	1.085
140	0.925	0.925	0.925	0.925	0.925	0.925	0.925	0.925	0.925	0.925
145	0.755	0.755	0.755	0.755	0.755	0.755	0.755	0.755	0.755	0.755
150	0.575	0.575	0.575	0.575	0.575	0.575	0.575	0.575	0.575	0.575
155	0.42	0.42	0.42	0.42	0.42	0.42	0.42	0.42	0.42	0.42
160	0.32	0.32	0.32	0.32	0.32	0.32	0.32	0.32	0.32	0.32
165	0.23	0.23	0.23	0.23	0.23	0.23	0.23	0.23	0.23	0.23
170	0.14	0.14	0.14	0.14	0.14	0.14	0.14	0.14	0.14	0.14
175	0.055	0.055	0.055	0.055	0.055	0.055	0.055	0.055	0.055	0.055
180	0.025	0.025	0.025	0.025	0.025	0.025	0.025	0.025	0.025	0.025

NACA0012, Althaus (1980) data, also available in Miley et al. (1982)

	Lift coefficient, C_L					Drag coefficient, C_D			
α (^{o})	Re: 40000	60000	80000	150000	α (^{o})	Re: 40000	60000	80000	150000
-8	-0.71	-0.75	-0.74	-0.77	-8	0.0444	-	-	0.0221
-7	-0.65	-0.67	-0.67	-0.69	-7	0.0362	0.0271	0.0267	0.0185
-6	-0.56	-0.57	-0.59	-0.61	-6	0.0332	0.0216	0.0222	0.0173
-5	-0.46	-0.47	-0.5	-0.53	-5	0.0293	0.0206	0.0196	0.0162
-4	-0.34	-0.37	-0.41	-0.44	-4	0.0262	0.0206	0.0184	0.0145
-3	-0.21	-0.27	-0.32	-0.35	-3	0.0236	0.0207	0.0181	0.013
-2	-0.07	-0.17	-0.22	-0.24	-2	0.0212	0.0208	0.0179	0.012
-1	0.02	-0.07	-0.1	-0.11	-1	0.0211	0.021	0.0177	0.0113
0	0.09	0.04	0.02	0.02	0	0.0226	0.0212	0.0176	0.0109
1	0.15	0.14	0.13	0.17	1	0.0242	0.0214	0.0176	0.011
2	0.23	0.24	0.25	0.3	2	0.026	0.0216	0.0178	0.0116
3	0.32	0.33	0.35	0.42	3	0.0279	0.022	0.0182	0.0126
4	0.41	0.41	0.45	0.51	4	0.0303	0.0224	0.0189	0.014
5	0.5	0.49	0.53	0.59	5	0.0329	0.0225	0.0199	0.0157
6	0.59	0.57	0.6	0.66	6	0.0367	0.0229	0.0217	0.0177
7	0.66	0.65	0.66	0.72	7	0.0474	0.0276	0.0254	0.0201
8	0.71	0.73	0.73	0.78	8	0.0612	0.0357	0.0305	0.0226
9	0.73	0.78	0.79	0.83	9	0.0727	0.0398	0.0343	0.0248
10	0.66	0.79	0.82	0.88	10	-	0.0403	0.0366	0.0267
11	0.63	0.66	0.73	0.9	11	-	-	-	-
12	-	0.64	0.66	0.72	12	-	-	-	-
13	-	0.62	0.64	0.68	13	-	-	-	-
14	-	0.62	0.64	0.66	14	-	-	-	-
15	-	0.63	0.65	0.66	15	-	-	-	-
16	-	0.64	0.66	-	16	-	-	-	-

NACA0012, Hybrid data

		Lift coefficient, C_L							
α (^{o})	Re: 40000	60000	80000	150000	360000	700000	1000000	2000000	5000000
0	0.09	0.04	0.02	0.02	0	0	0	0	0
1	0.15	0.14	0.13	0.17	0.11	0.11	0.11	0.11	0.11
2	0.23	0.24	0.25	0.3	0.22	0.22	0.22	0.22	0.22
3	0.32	0.33	0.35	0.42	0.33	0.33	0.33	0.33	0.33
4	0.41	0.41	0.45	0.51	0.44	0.44	0.44	0.44	0.44
5	0.5	0.49	0.53	0.59	0.55	0.55	0.55	0.55	0.55
6	0.59	0.57	0.6	0.66	0.66	0.66	0.66	0.66	0.66
7	0.66	0.65	0.66	0.72	0.77	0.77	0.77	0.77	0.77
8	0.71	0.73	0.73	0.78	0.8542	0.88	0.88	0.88	0.88
9	0.73	0.78	0.79	0.83	0.9352	0.9598	0.9661	0.99	0.99
10	0.66	0.79	0.82	0.88	0.9811	1.0343	1.0512	1.0727	1.1
11	0.63	0.66	0.73	0.9	0.9132	1.0749	1.1097	1.1539	1.1842
12	0.63	0.64	0.66	0.72	0.4832	1.039	1.1212	1.2072	1.2673
13	0.63	0.62	0.64	0.68	0.2759	0.8737	1.0487	1.2169	1.3242
14	0.63	0.62	0.64	0.66	0.2893	0.6284	0.8846	1.1614	1.3423
15	0.63	0.63	0.65	0.66	0.3306	0.4907	0.7108	1.0478	1.3093
16	0.63	0.64	0.66	0.66	0.3792	0.4696	0.606	0.9221	1.2195
17	0.63	0.64	0.66	0.66	0.4455	0.5195	0.5906	0.7826	1.0365
18	0.63	0.64	0.66	0.66	0.5047	0.5584	0.603	0.7163	0.9054
19	0.63	0.64	0.66	0.66	0.5591	0.6032	0.6334	0.7091	0.8412
20	0.63	0.64	0.66	0.66	0.612	0.6474	0.6716	0.7269	0.8233
21	0.63	0.64	0.66	0.66	0.6643	0.6949	0.7162	0.7595	0.8327
22	0.6709	0.6755	0.6839	0.6956	0.7179	0.7446	0.7613	0.7981	0.8563
23	0.7238	0.7283	0.7373	0.7497	0.7715	0.7948	0.8097	0.8429	0.8903
24	0.7765	0.7809	0.7902	0.8043	0.8246	0.8462	0.8589	0.8882	0.9295
25	0.8297	0.834	0.8432	0.8572	0.878	0.8984	0.9093	0.9352	0.9718
26	0.8831	0.8873	0.8963	0.9109	0.9313	0.9506	0.9618	0.9842	1.0193
27	0.9365	0.8409	0.9496	0.923	0.9412	0.9583	0.9683	0.9882	1.068
30	0.915	0.915	0.915	0.9593	0.9709	0.9814	0.9878	1.002	0.915
35	1.02	1.02	1.02	1.02	1.02	1.02	1.02	1.02	1.02
40	1.075	1.075	1.075	1.075	1.075	1.075	1.075	1.075	1.075
45	1.085	1.085	1.085	1.085	1.085	1.085	1.085	1.085	1.085
50	1.04	1.04	1.04	1.04	1.04	1.04	1.04	1.04	1.04
55	0.965	0.965	0.965	0.965	0.965	0.965	0.965	0.965	0.965
60	0.875	0.875	0.875	0.875	0.875	0.875	0.875	0.875	0.875
65	0.765	0.765	0.765	0.765	0.765	0.765	0.765	0.765	0.765
70	0.65	0.65	0.65	0.65	0.65	0.65	0.65	0.65	0.65
75	0.515	0.515	0.515	0.515	0.515	0.515	0.515	0.515	0.515
80	0.37	0.37	0.37	0.37	0.37	0.37	0.37	0.37	0.37
85	0.22	0.22	0.22	0.22	0.22	0.22	0.22	0.22	0.22
90	0.07	0.07	0.07	0.07	0.07	0.07	0.07	0.07	0.07
95	-0.07	-0.07	-0.07	-0.07	-0.07	-0.07	-0.07	-0.07	-0.07
100	-0.22	-0.22	-0.22	-0.22	-0.22	-0.22	-0.22	-0.22	-0.22
105	-0.37	-0.37	-0.37	-0.37	-0.37	-0.37	-0.37	-0.37	-0.37
110	-0.51	-0.51	-0.51	-0.51	-0.51	-0.51	-0.51	-0.51	-0.51
115	-0.625	-0.625	-0.625	-0.625	-0.625	-0.625	-0.625	-0.625	-0.625
120	-0.735	-0.735	-0.735	-0.735	-0.735	-0.735	-0.735	-0.735	-0.735
125	-0.84	-0.84	-0.84	-0.84	-0.84	-0.84	-0.84	-0.84	-0.84
130	-0.91	-0.91	-0.91	-0.91	-0.91	-0.91	-0.91	-0.91	-0.91
135	-0.945	-0.945	-0.945	-0.945	-0.945	-0.945	-0.945	-0.945	-0.945
140	-0.945	-0.945	-0.945	-0.945	-0.945	-0.945	-0.945	-0.945	-0.945
145	-0.91	-0.91	-0.91	-0.91	-0.91	-0.91	-0.91	-0.91	-0.91
150	-0.85	-0.85	-0.85	-0.85	-0.85	-0.85	-0.85	-0.85	-0.85
155	-0.74	-0.74	-0.74	-0.74	-0.74	-0.74	-0.74	-0.74	-0.74
160	-0.66	-0.66	-0.66	-0.66	-0.66	-0.66	-0.66	-0.66	-0.66
165	-0.675	-0.675	-0.675	-0.675	-0.675	-0.675	-0.675	-0.675	-0.675
170	-0.85	-0.85	-0.85	-0.85	-0.85	-0.85	-0.85	-0.85	-0.85
175	-0.69	-0.69	-0.69	-0.69	-0.69	-0.69	-0.69	-0.69	-0.69
180	0	0	0	0	0	0	0	0	0

	Drag coefficient, C_D								
α (°)	Re: 40000	60000	80000	150000	360000	700000	1000000	2000000	5000000
0	0.0226	0.0212	0.0176	0.0109	0.0079	0.0067	0.0065	0.0064	0.0064
1	0.0242	0.0214	0.0176	0.011	0.008	0.0068	0.0066	0.0064	0.0064
2	0.026	0.0216	0.0178	0.0116	0.0084	0.007	0.0068	0.0066	0.0066
3	0.0279	0.022	0.0182	0.0126	0.0089	0.0075	0.0071	0.0069	0.0068
4	0.0303	0.0224	0.0189	0.014	0.0098	0.0083	0.0078	0.0073	0.0072
5	0.0329	0.0225	0.0199	0.0157	0.0113	0.0097	0.0091	0.0081	0.0076
6	0.0367	0.0229	0.0217	0.0177	0.0125	0.0108	0.0101	0.009	0.0081
7	0.0474	0.0276	0.0254	0.0201	0.0135	0.0118	0.011	0.0097	0.0086
8	0.0612	0.0357	0.0305	0.0226	0.0153	0.0128	0.0119	0.0105	0.0092
9	0.0727	0.0398	0.0343	0.0248	0.0167	0.0144	0.0134	0.0113	0.0098
10	0.101	0.0403	0.0366	0.0267	0.0184	0.0159	0.0147	0.0128	0.0106
11	0.117	0.117	0.117	0.076	0.0204	0.0175	0.0162	0.014	0.0118
12	0.134	0.134	0.134	0.134	0.0217	0.0195	0.018	0.0155	0.013
13	0.152	0.152	0.152	0.152	0.0222	0.0216	0.02	0.0172	0.0143
14	0.171	0.171	0.171	0.171	0.106	0.0236	0.0222	0.0191	0.0159
15	0.191	0.19	0.19	0.19	0.19	0.117	0.0245	0.0213	0.0177
16	0.21	0.21	0.21	0.21	0.21	0.21	0.128	0.0237	0.0198
17	0.23	0.231	0.231	0.231	0.231	0.23	0.231	0.138	0.0229
18	0.252	0.252	0.252	0.252	0.252	0.252	0.252	0.252	0.148
19	0.274	0.274	0.274	0.274	0.274	0.274	0.274	0.274	0.274
20	0.297	0.297	0.297	0.297	0.297	0.297	0.297	0.297	0.297
21	0.32	0.32	0.32	0.32	0.32	0.32	0.32	0.32	0.32
22	0.344	0.344	0.344	0.344	0.344	0.344	0.344	0.344	0.344
23	0.369	0.369	0.369	0.369	0.369	0.369	0.369	0.369	0.369
24	0.394	0.394	0.394	0.394	0.394	0.394	0.394	0.394	0.394
25	0.42	0.42	0.42	0.42	0.42	0.42	0.42	0.42	0.42
26	0.446	0.445	0.446	0.446	0.446	0.446	0.446	0.446	0.446
27	0.473	0.473	0.473	0.473	0.473	0.473	0.473	0.473	0.473
30	0.57	0.57	0.57	0.57	0.57	0.57	0.57	0.57	0.57
35	0.745	0.745	0.745	0.745	0.745	0.745	0.745	0.745	0.745
40	0.92	0.92	0.92	0.92	0.92	0.92	0.92	0.92	0.92
45	1.075	1.075	1.075	1.075	1.075	1.075	1.075	1.075	1.075
50	1.215	1.215	1.215	1.215	1.215	1.215	1.215	1.215	1.215
55	1.345	1.345	1.345	1.345	1.345	1.345	1.345	1.345	1.345
60	1.47	1.47	1.47	1.47	1.47	1.47	1.47	1.47	1.47
65	1.575	1.575	1.575	1.575	1.575	1.575	1.575	1.575	1.575
70	1.665	1.665	1.665	1.665	1.665	1.665	1.665	1.665	1.665
75	1.735	1.735	1.735	1.735	1.735	1.735	1.735	1.735	1.735
80	1.78	1.78	1.78	1.78	1.78	1.78	1.78	1.78	1.78
85	1.8	1.8	1.8	1.8	1.8	1.8	1.8	1.8	1.8
90	1.8	1.8	1.8	1.8	1.8	1.8	1.8	1.8	0
95	1.78	1.78	1.78	1.78	1.78	1.78	1.78	1.78	1.78
100	1.75	1.75	1.75	1.75	1.75	1.75	1.75	1.75	1.75
105	1.7	1.7	1.7	1.7	1.7	1.7	1.7	1.7	1.7
110	1.635	1.635	1.635	1.635	1.635	1.635	1.635	1.635	1.635
115	1.555	1.555	1.555	1.555	1.555	1.555	1.555	1.555	1.555
120	1.465	1.465	1.465	1.465	1.465	1.465	1.465	1.465	1.465
125	1.35	1.35	1.35	1.35	1.35	1.35	1.35	1.35	1.35
130	1.225	1.225	1.225	1.225	1.225	1.225	1.225	1.225	1.225
135	1.085	1.085	1.085	1.085	1.085	1.085	1.085	1.085	1.085
140	0.925	0.925	0.925	0.925	0.925	0.925	0.925	0.925	0.925
145	0.755	0.755	0.755	0.755	0.755	0.755	0.755	0.755	0.755
150	0.575	0.575	0.575	0.575	0.575	0.575	0.575	0.575	0.575
155	0.42	0.42	0.42	0.42	0.42	0.42	0.42	0.42	0.42
160	0.32	0.32	0.32	0.32	0.32	0.32	0.32	0.32	0.32
165	0.23	0.23	0.23	0.23	0.23	0.23	0.23	0.23	0.23
170	0.14	0.14	0.14	0.14	0.14	0.14	0.14	0.14	0.14
175	0.055	0.055	0.055	0.055	0.055	0.055	0.055	0.055	0.055
180	0.025	0.025	0.025	0.025	0.025	0.025	0.025	0.025	0.025

A.2 PII blade forces

Where measurements are missing the data was faulty; no data available for a single bladed PII. Lines represent Fourier averaged experimental data; circles represent results from the vortex model (*without* corrections for finite blade length) for the last two revolutions (i.e. convergence is evident).

A.2.1 Six blades

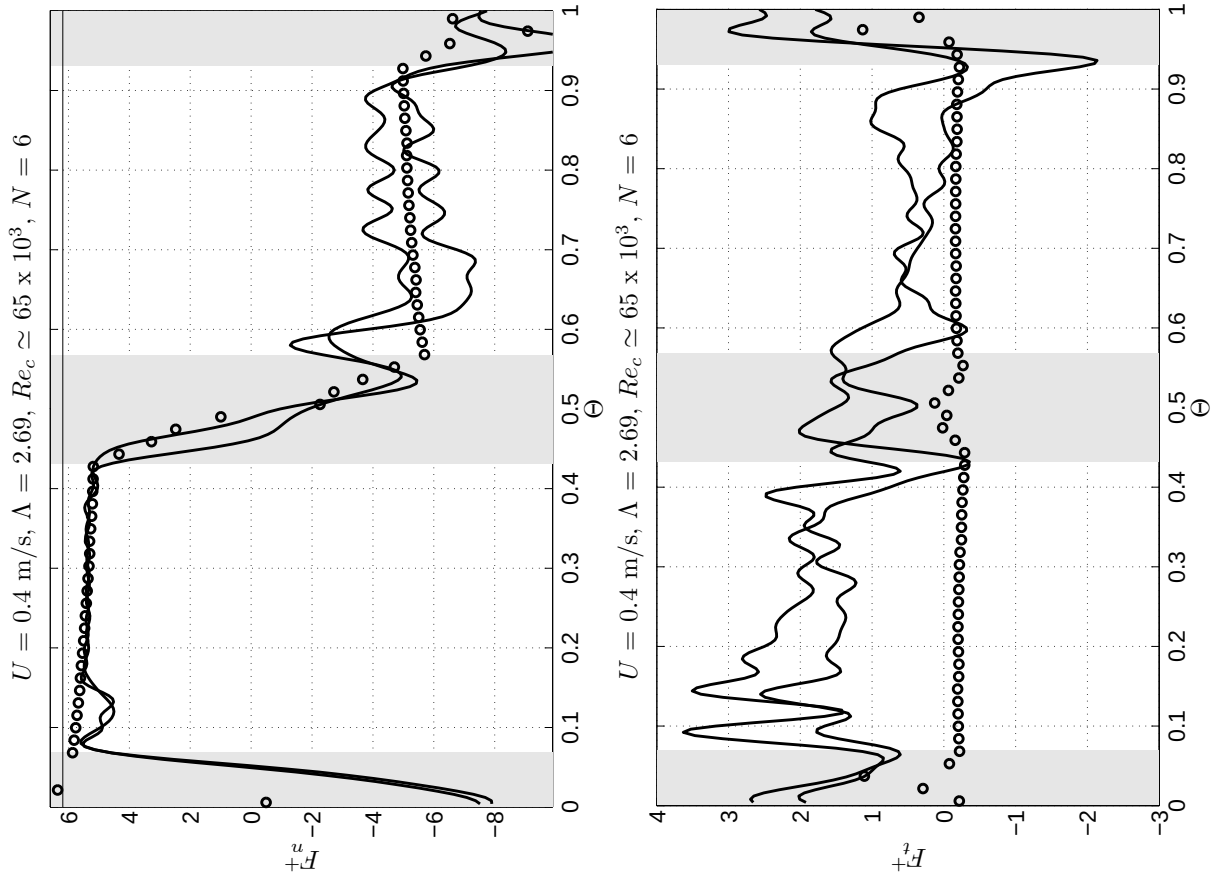

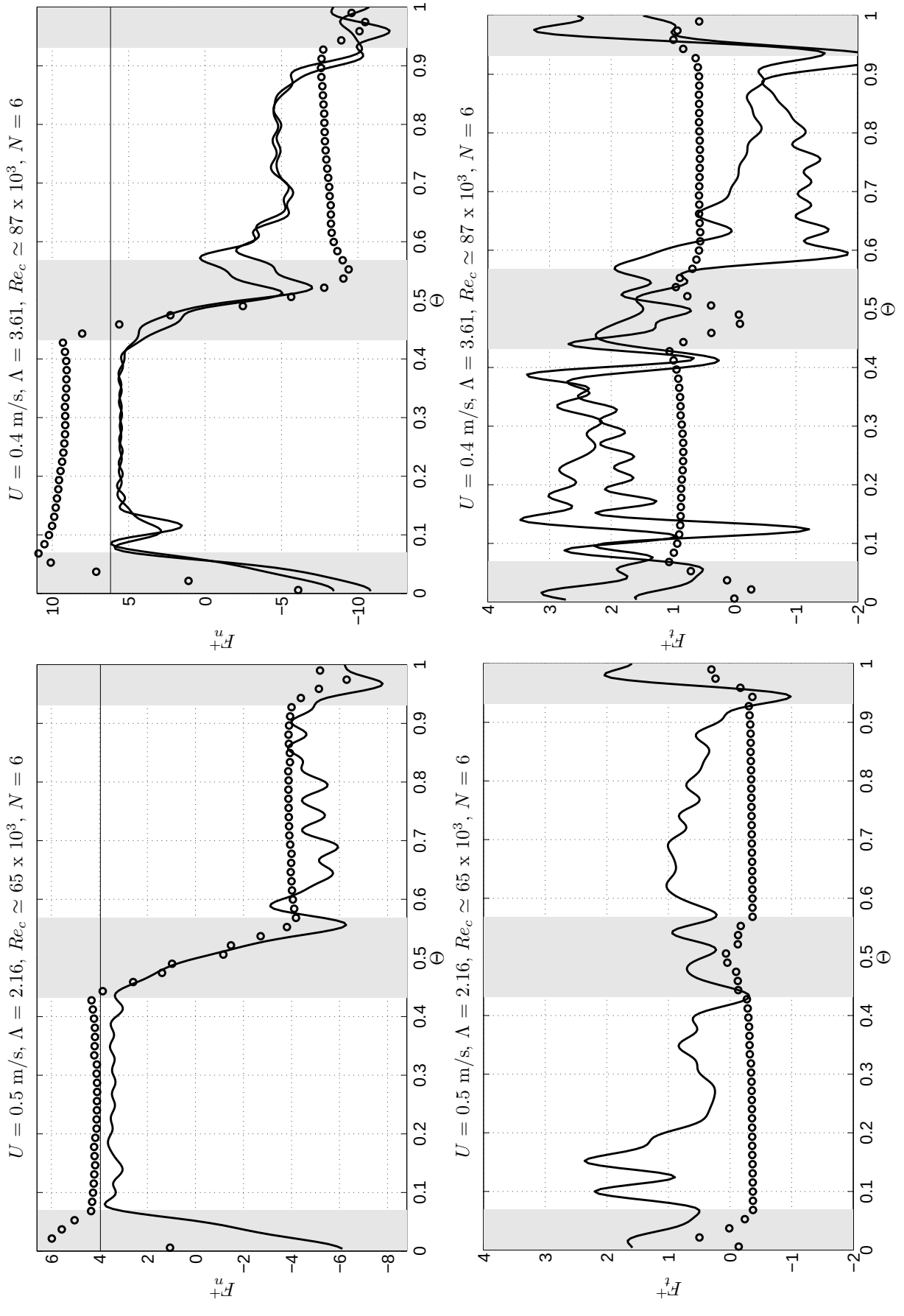
$U = 0.4$ m/s, $\Lambda = 3.61$, $Re_c \simeq 87$ x 10^3, $N = 6$
$U = 0.5$ m/s, $\Lambda = 2.16$, $Re_c \simeq 65$ x 10^3, $N = 6$
F_n^+
F_t^+
Θ

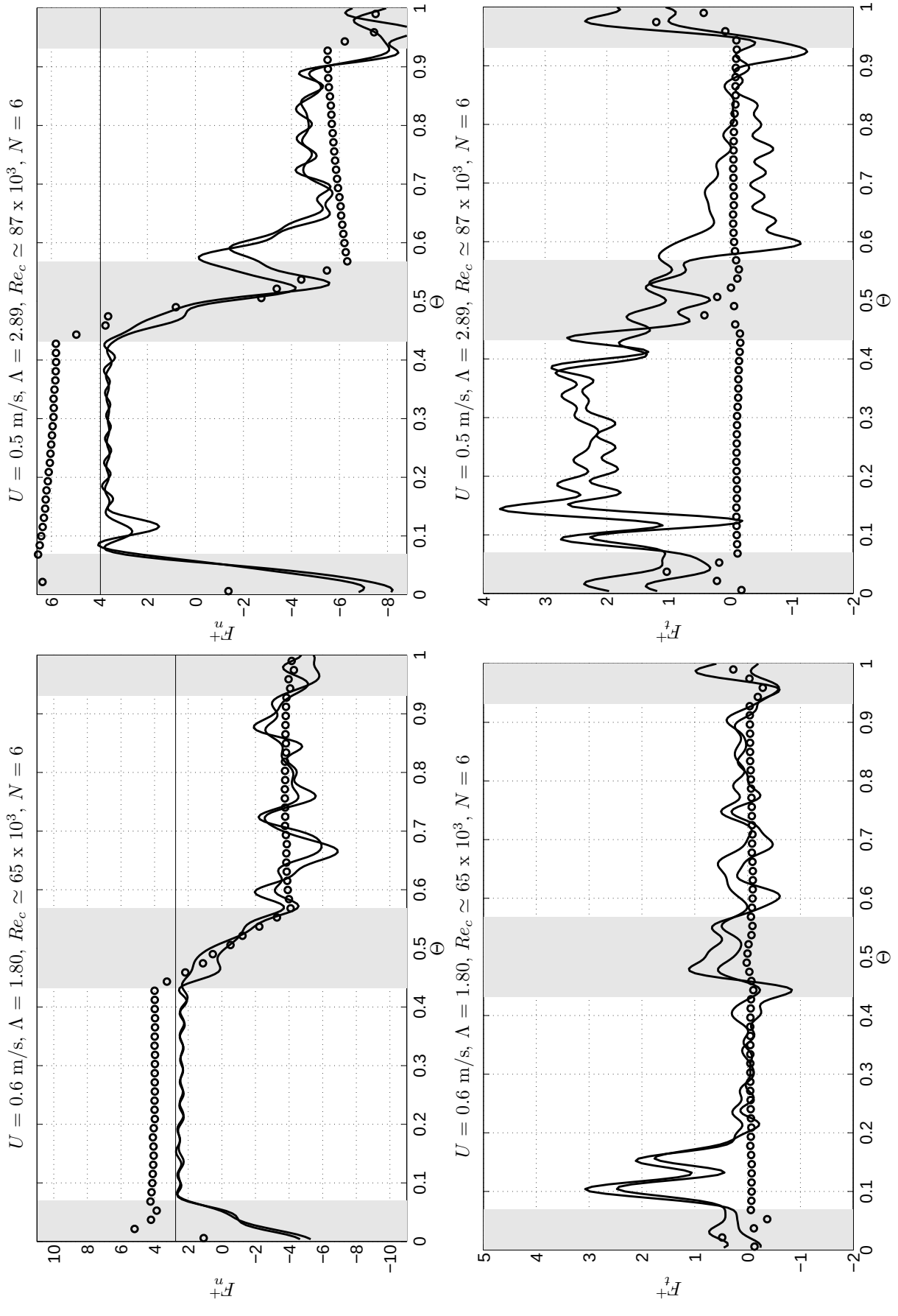
$U = 0.5$ m/s, $\Lambda = 2.89$, $Re_c \simeq 87$ x 10^3, $N = 6$
F_n^+
Θ
$U = 0.5$ m/s, $\Lambda = 2.89$, $Re_c \simeq 87$ x 10^3, $N = 6$
F_t^+
Θ
$U = 0.6$ m/s, $\Lambda = 1.80$, $Re_c \simeq 65$ x 10^3, $N = 6$
F_n^+
Θ
$U = 0.6$ m/s, $\Lambda = 1.80$, $Re_c \simeq 65$ x 10^3, $N = 6$
F_t^+
Θ

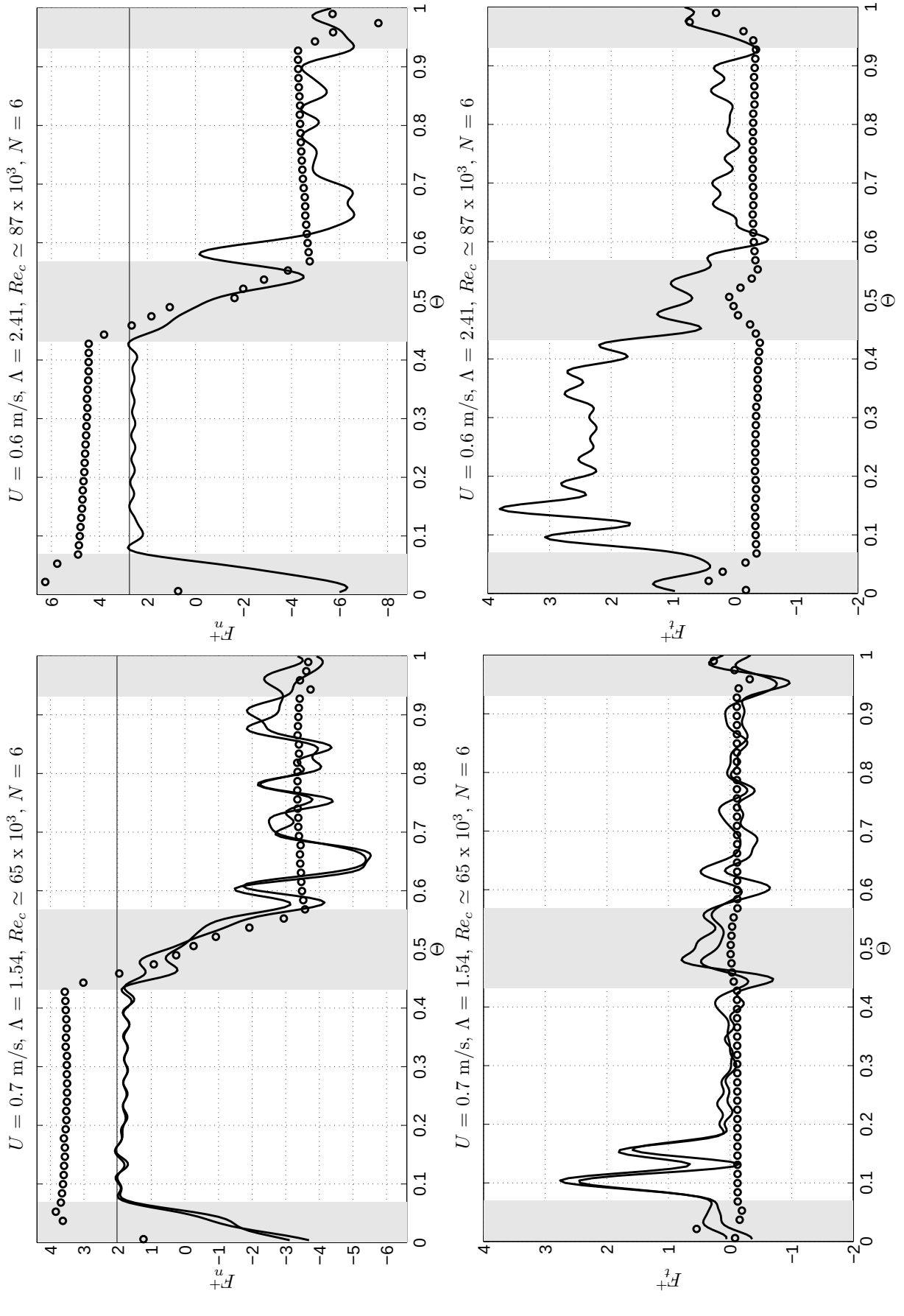
$U = 0.6$ m/s, $\Lambda = 2.41$, $Re_c \simeq 87$ x 10^3, $N = 6$
F_n^+
Θ
$U = 0.6$ m/s, $\Lambda = 2.41$, $Re_c \simeq 87$ x 10^3, $N = 6$
F_t^+
Θ
$U = 0.7$ m/s, $\Lambda = 1.54$, $Re_c \simeq 65$ x 10^3, $N = 6$
F_n^+
Θ
$U = 0.7$ m/s, $\Lambda = 1.54$, $Re_c \simeq 65$ x 10^3, $N = 6$
F_t^+
Θ

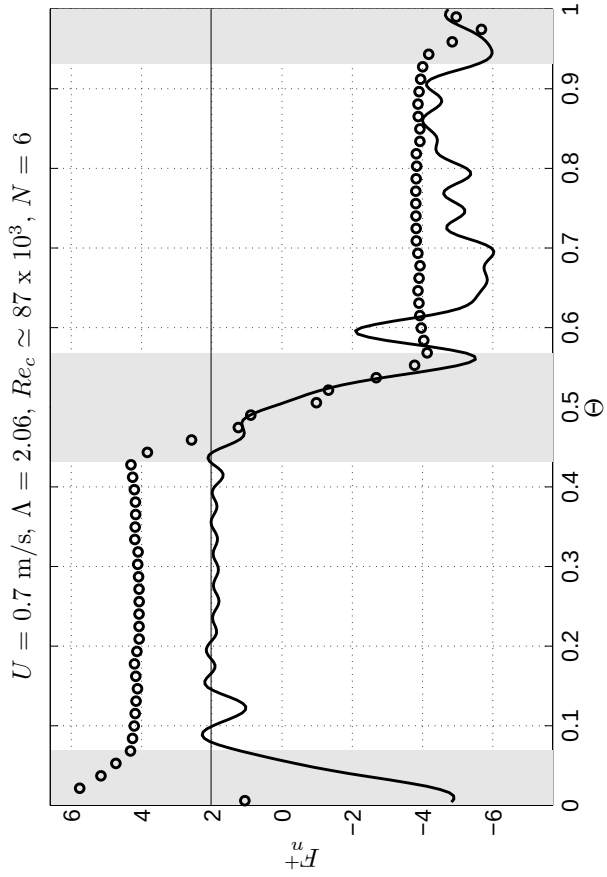
$U = 0.7$ m/s, $\Lambda = 2.06$, $Re_c \simeq 87$ x 10^3, $N = 6$
F_n^+
Θ

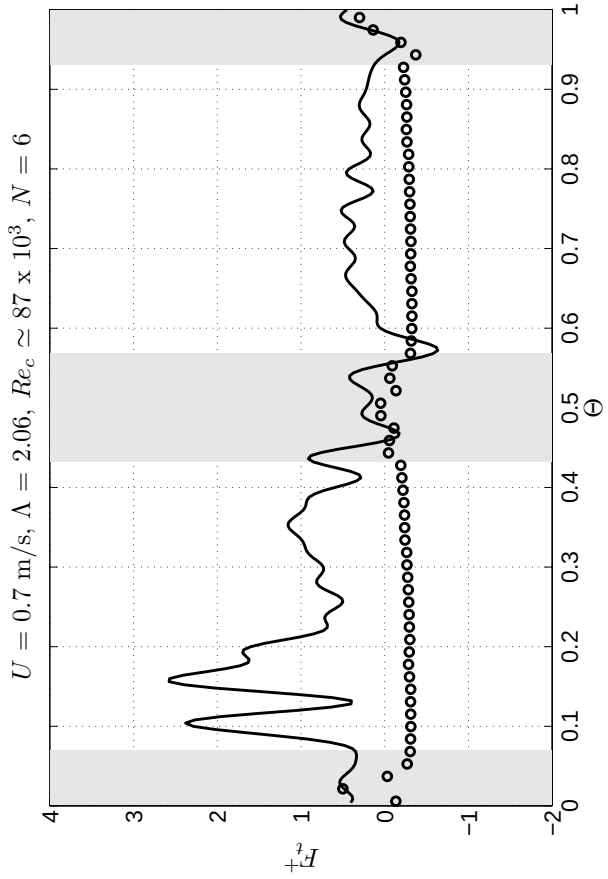
$U = 0.7$ m/s, $\Lambda = 2.06$, $Re_c \simeq 87$ x 10^3, $N = 6$
F_t^+
Θ

A.2.2 Three blades

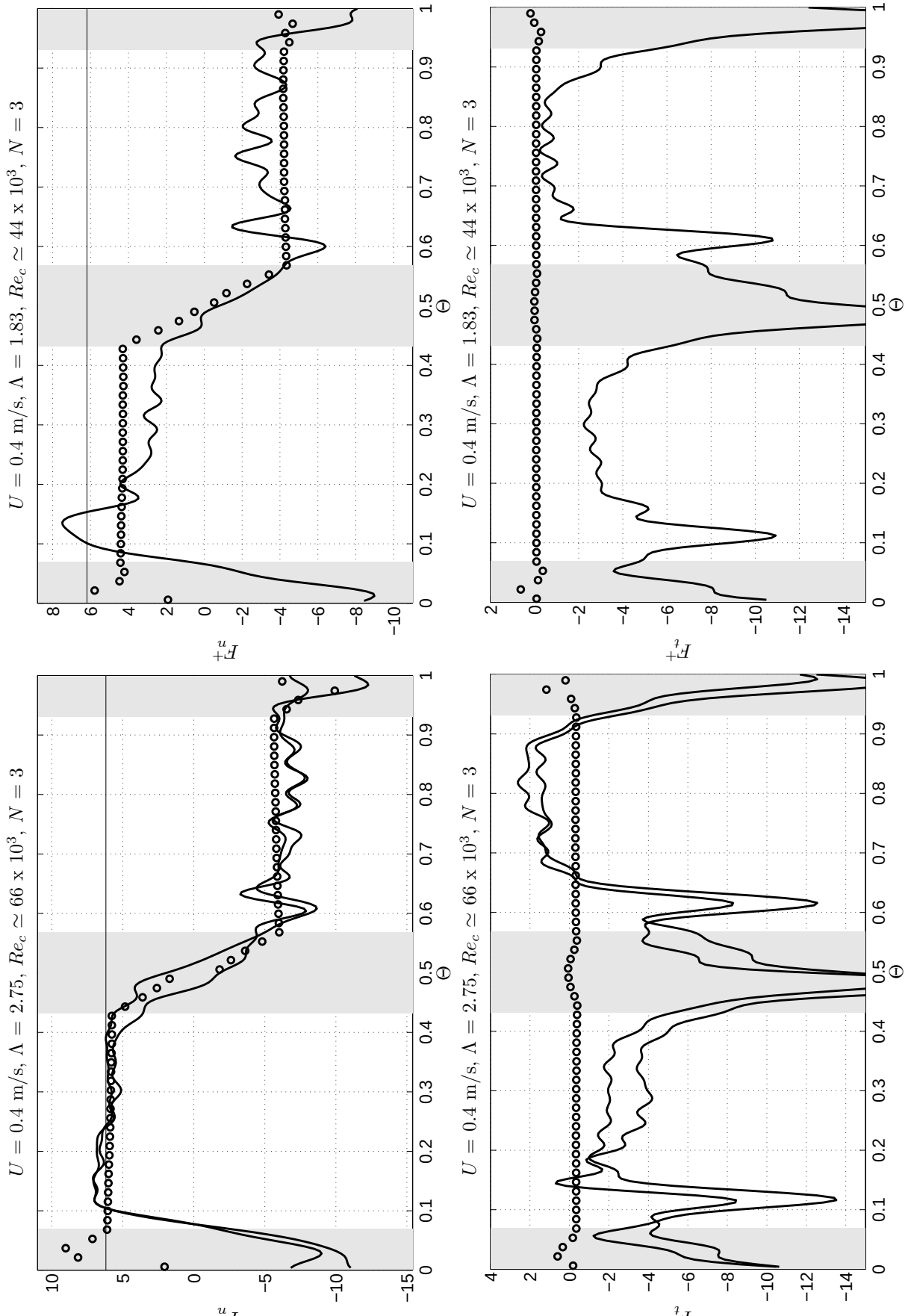

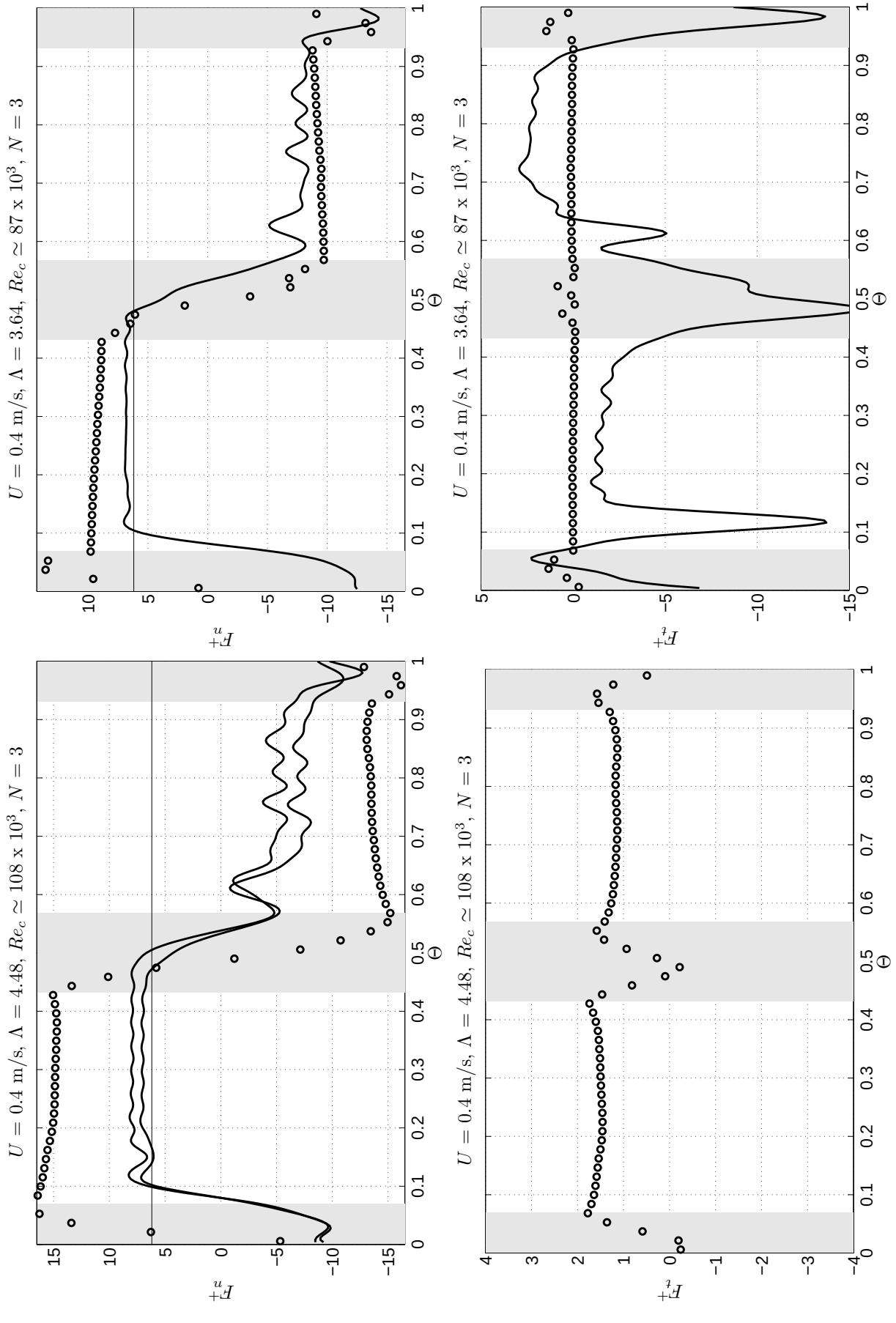
$U = 0.4$ m/s, $\Lambda = 3.64$, $Re_c \simeq 87$ x 10^3, $N = 3$
F_n^+
Θ
$U = 0.4$ m/s, $\Lambda = 3.64$, $Re_c \simeq 87$ x 10^3, $N = 3$
F_t^+
Θ
$U = 0.4$ m/s, $\Lambda = 4.48$, $Re_c \simeq 108$ x 10^3, $N = 3$
F_n^+
Θ
$U = 0.4$ m/s, $\Lambda = 4.48$, $Re_c \simeq 108$ x 10^3, $N = 3$
F_t^+
Θ

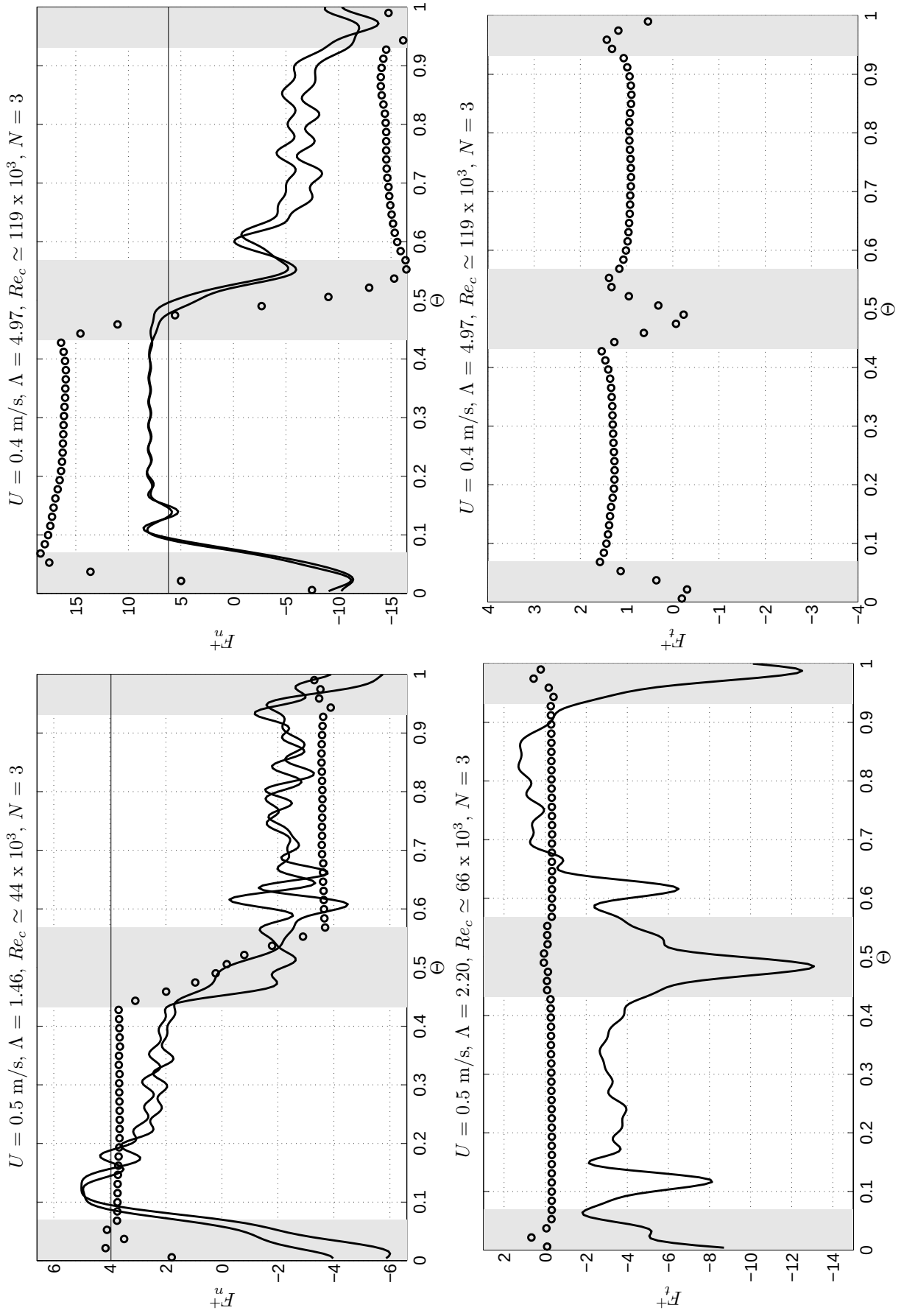
$U = 0.5$ m/s, $\Lambda = 1.46$, $Re_c \simeq 44$ x 10^3, $N = 3$
$U = 0.4$ m/s, $\Lambda = 4.97$, $Re_c \simeq 119$ x 10^3, $N = 3$
$U = 0.5$ m/s, $\Lambda = 2.20$, $Re_c \simeq 66$ x 10^3, $N = 3$
$U = 0.4$ m/s, $\Lambda = 4.97$, $Re_c \simeq 119$ x 10^3, $N = 3$
F_n^+
F_t^+
Θ

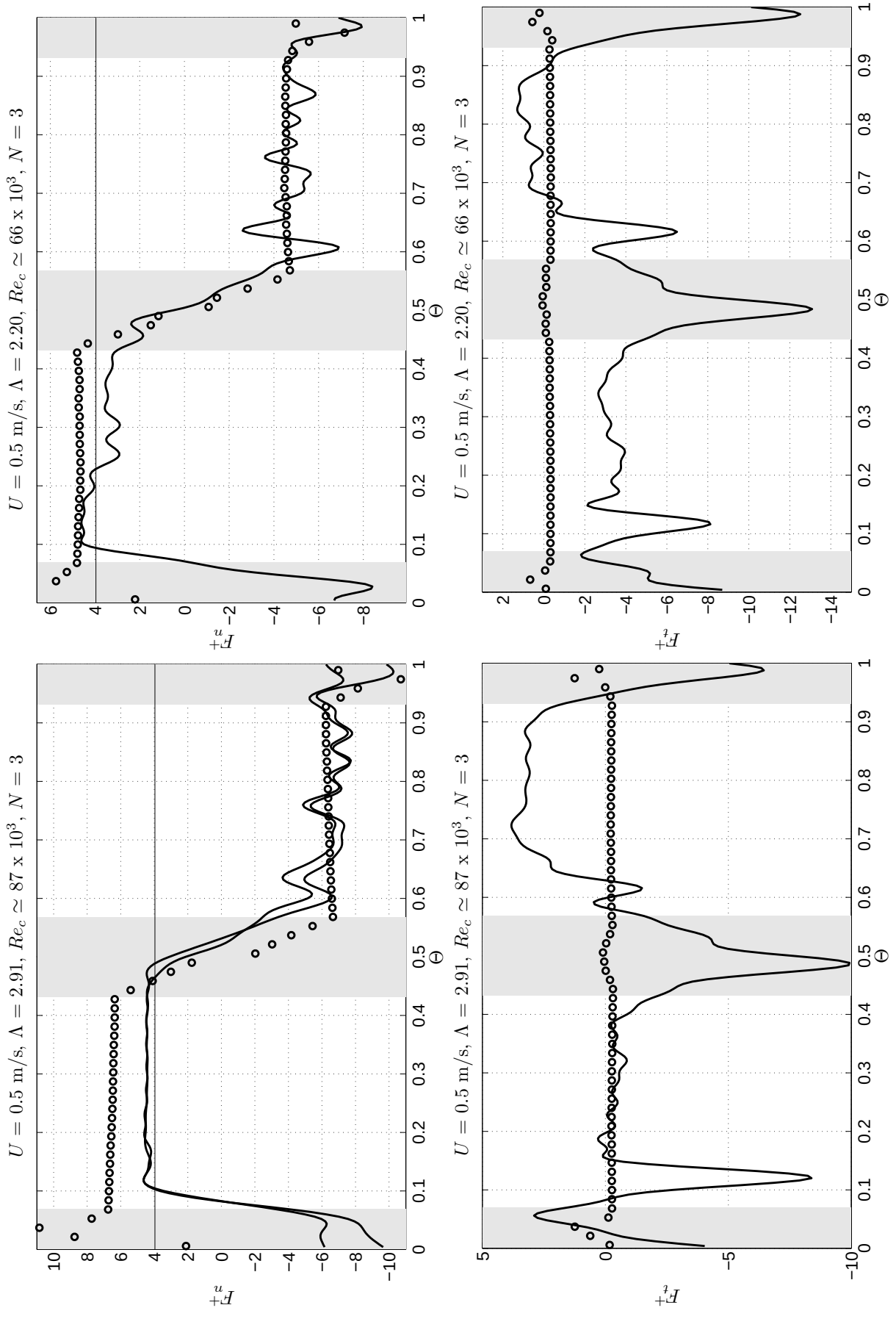
$U = 0.5$ m/s, $\Lambda = 2.20$, $Re_c \simeq 66$ x 10^3, $N = 3$
$U = 0.5$ m/s, $\Lambda = 2.91$, $Re_c \simeq 87$ x 10^3, $N = 3$
F_n^+
F_t^+
Θ

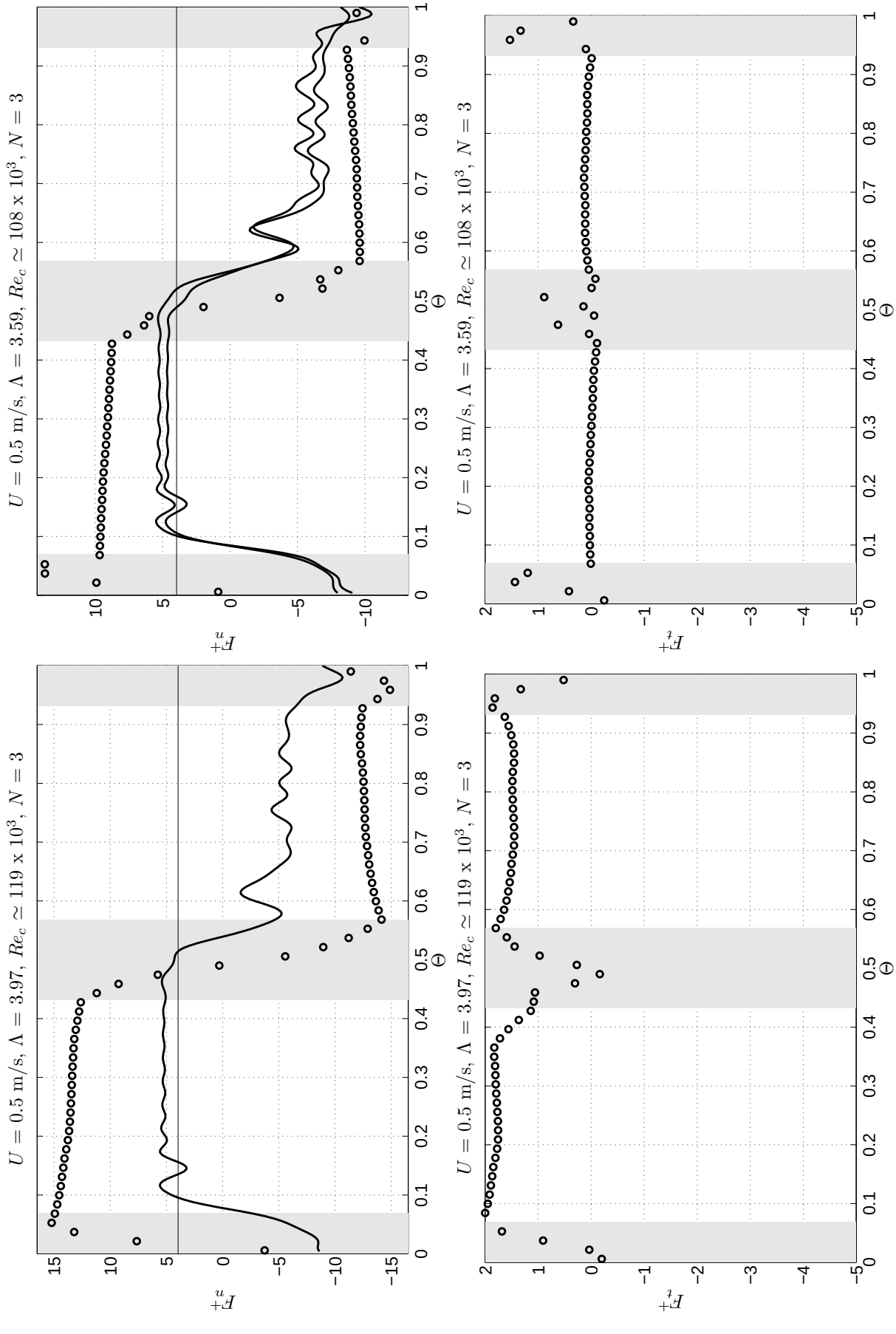
$U = 0.5$ m/s, $\Lambda = 3.59$, $Re_c \simeq 108$ x 10^3, $N = 3$
F_n^+
Θ
$U = 0.5$ m/s, $\Lambda = 3.59$, $Re_c \simeq 108$ x 10^3, $N = 3$
F_t^+
Θ
$U = 0.5$ m/s, $\Lambda = 3.97$, $Re_c \simeq 119$ x 10^3, $N = 3$
F_n^+
Θ
$U = 0.5$ m/s, $\Lambda = 3.97$, $Re_c \simeq 119$ x 10^3, $N = 3$
F_t^+
Θ

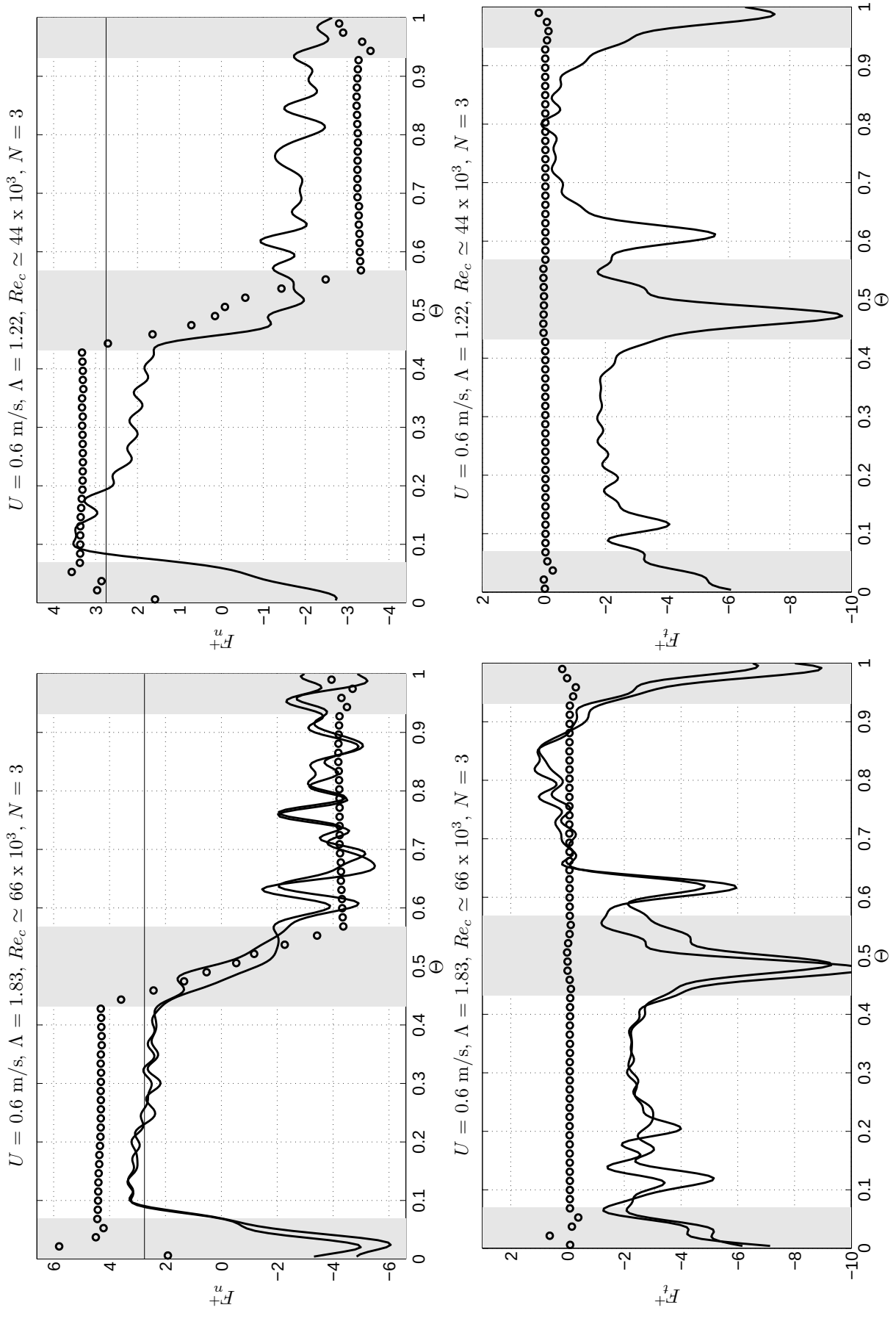
$U = 0.6$ m/s, $\Lambda = 1.22$, $Re_c \simeq 44$ x 10^3, $N = 3$
F_n^+
Θ
$U = 0.6$ m/s, $\Lambda = 1.22$, $Re_c \simeq 44$ x 10^3, $N = 3$
F_t^+
Θ
$U = 0.6$ m/s, $\Lambda = 1.83$, $Re_c \simeq 66$ x 10^3, $N = 3$
F_n^+
Θ
$U = 0.6$ m/s, $\Lambda = 1.83$, $Re_c \simeq 66$ x 10^3, $N = 3$
F_t^+
Θ

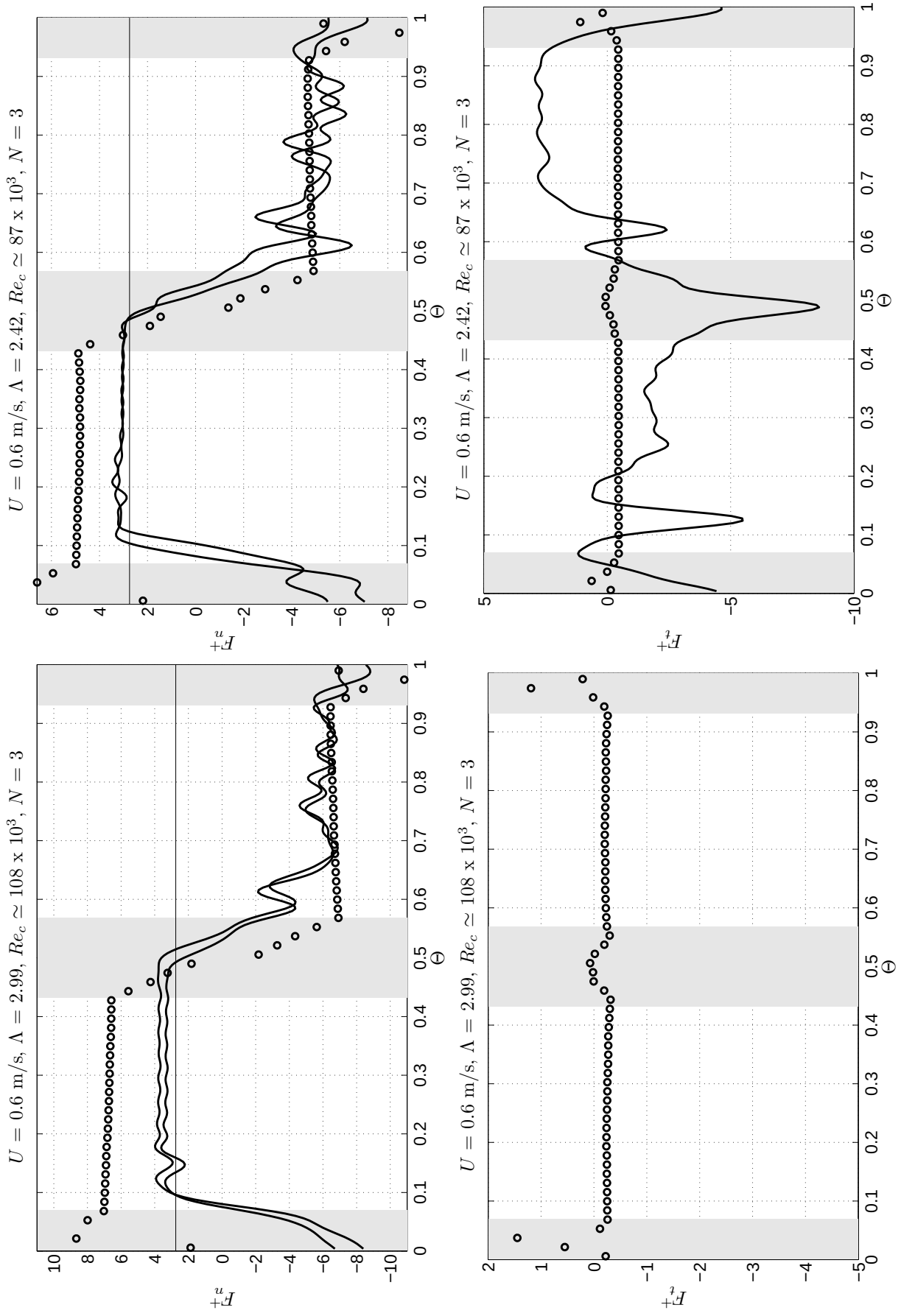
$U = 0.6$ m/s, $\Lambda = 2.42$, $Re_c \simeq 87$ x 10^3, $N = 3$
F_n^+
Θ
$U = 0.6$ m/s, $\Lambda = 2.42$, $Re_c \simeq 87$ x 10^3, $N = 3$
F_t^+
Θ
$U = 0.6$ m/s, $\Lambda = 2.99$, $Re_c \simeq 108$ x 10^3, $N = 3$
F_n^+
Θ
$U = 0.6$ m/s, $\Lambda = 2.99$, $Re_c \simeq 108$ x 10^3, $N = 3$
F_t^+
Θ

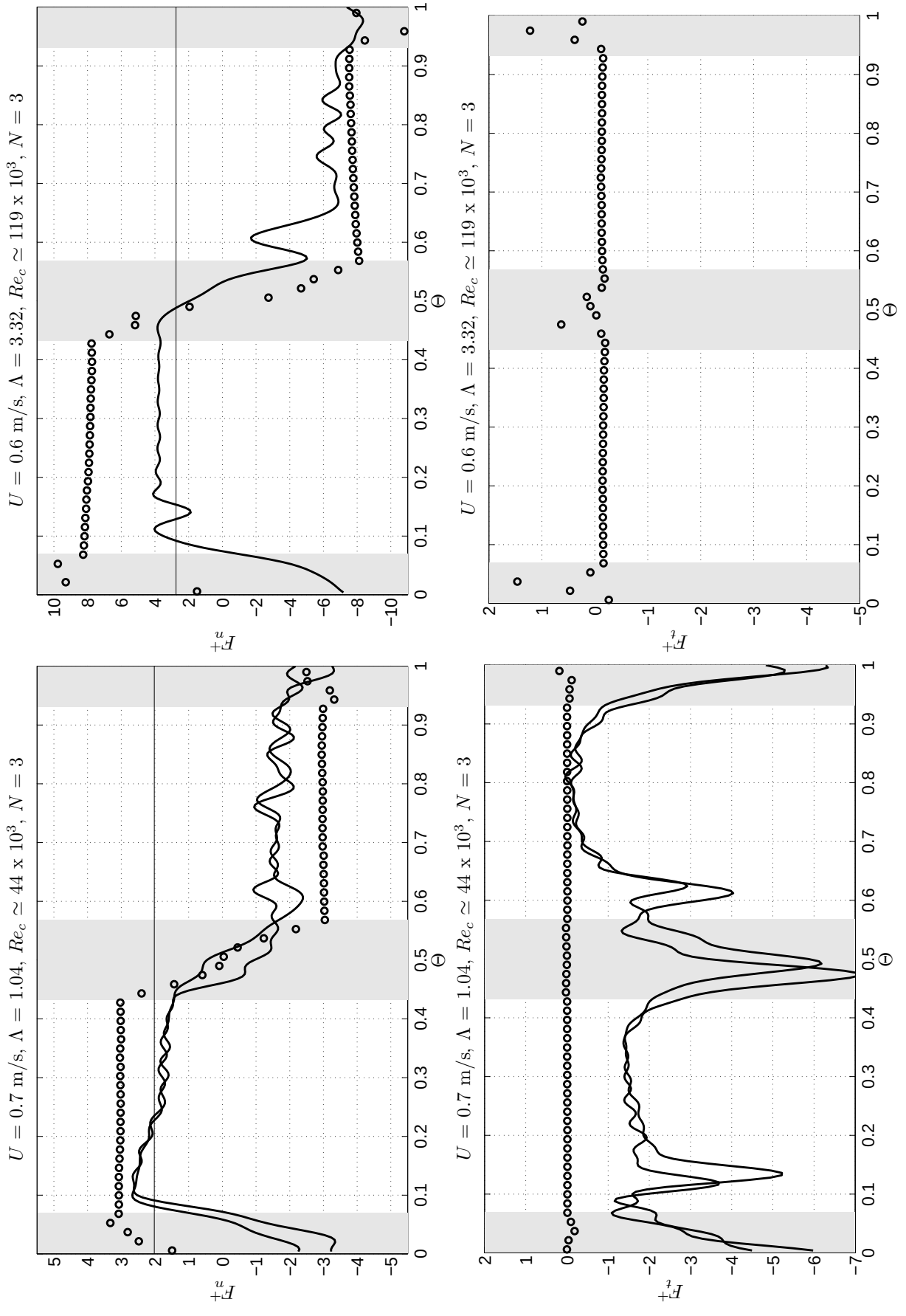
$U = 0.6$ m/s, $\Lambda = 3.32$, $Re_c \simeq 119$ x 10^3, $N = 3$
F_n^+
Θ
$U = 0.6$ m/s, $\Lambda = 3.32$, $Re_c \simeq 119$ x 10^3, $N = 3$
F_t^+
Θ
$U = 0.7$ m/s, $\Lambda = 1.04$, $Re_c \simeq 44$ x 10^3, $N = 3$
F_n^+
Θ
$U = 0.7$ m/s, $\Lambda = 1.04$, $Re_c \simeq 44$ x 10^3, $N = 3$
F_t^+
Θ

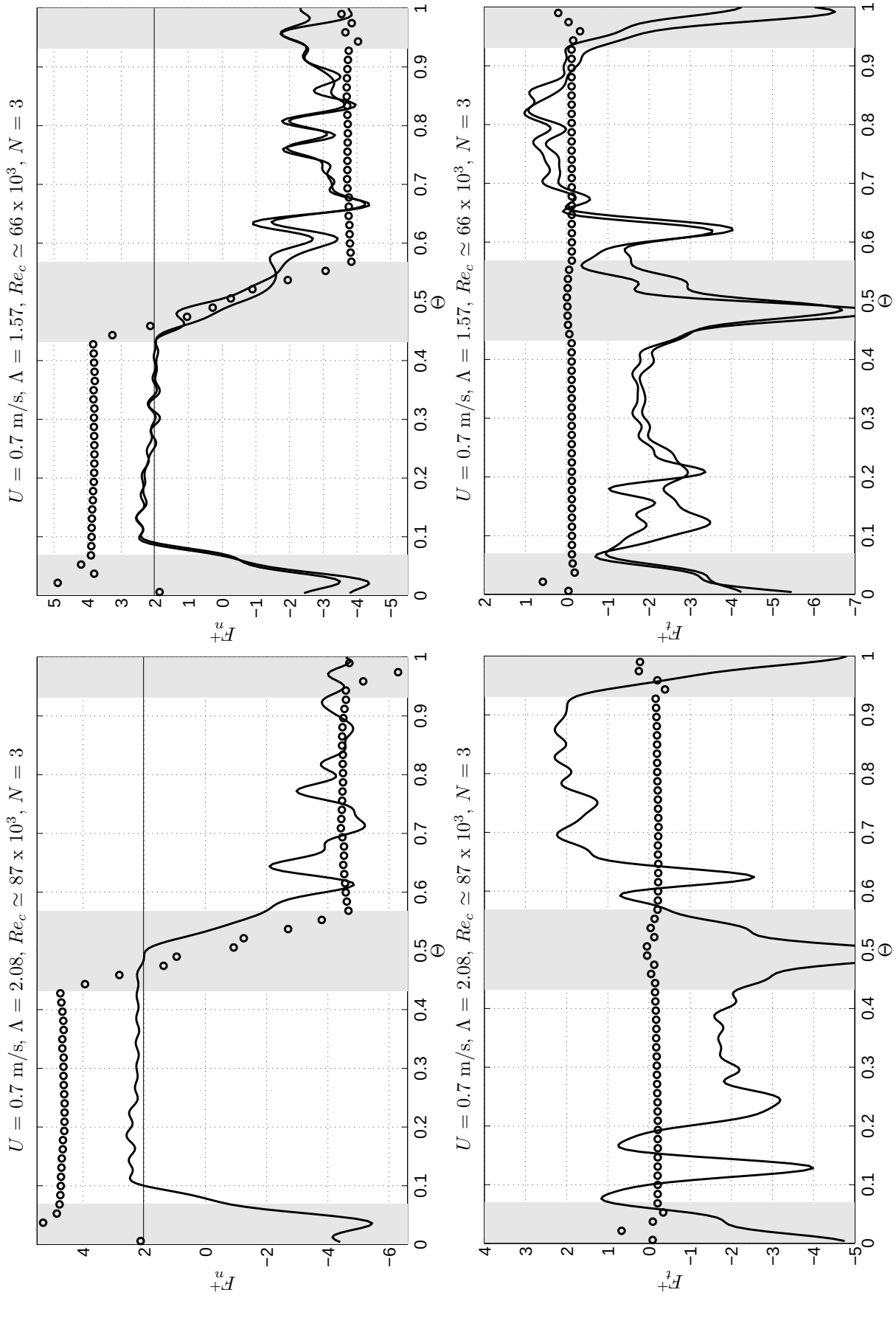
$U = 0.7$ m/s, $\Lambda = 1.57$, $Re_c \simeq 66$ x 10^3, $N = 3$
F_n^+
Θ
$U = 0.7$ m/s, $\Lambda = 1.57$, $Re_c \simeq 66$ x 10^3, $N = 3$
F_t^+
Θ
$U = 0.7$ m/s, $\Lambda = 2.08$, $Re_c \simeq 87$ x 10^3, $N = 3$
F_n^+
Θ
$U = 0.7$ m/s, $\Lambda = 2.08$, $Re_c \simeq 87$ x 10^3, $N = 3$
F_t^+
Θ